# GEOMETRIC AND ELECTRONIC CONTROL OF THE MAGNETIC PROPERTIES OF FIRST-ROW TRANSITION METAL COMPLEXES

A Dissertation

by

TOBY JOHN WOODS

Submitted to the Office of Graduate and Professional Studies of
Texas A&M University
in partial fulfillment of the requirements for the degree of

DOCTOR OF PHILOSOPHY

| | |
|---|---|
| Chair of Committee, | Kim R. Dunbar |
| Committee Members, | Francois P. Gabbai |
| | Timothy R. Hughbanks |
| | Donald G. Naugle |
| Head of Department, | Simon W. North |

August 2016

Major Subject: Chemistry

# ABSTRACT

The realization that $[Mn_{12}(CH_3COO)_{16}(H_2O)_4O_{12}]\bullet 2CH_3COOH\bullet 2H_2O$ ($Mn_{12}OAc$) displayed magnetic hysteresis, a phenomenon usually associated with permanent bulk magnets, was a truly remarkable discovery since $Mn_{12}OAc$ is a zero-dimensional molecular system in which there is no magnetic interplay between individual $Mn_{12}OAc$ units. In essence, every $Mn_{12}OAc$ molecule behaves as a tiny bar magnet of 1 nm in size, capable of maintaining its magnetization even after removal of the magnetizing field. The term Single Molecule Magnet (SMM) was introduced to describe molecules that displayed hysteresis behavior similar to $Mn_{12}OAc$. In the intervening years, many new examples of molecules that display SMM properties have been discovered but success at increasing the operating temperature has been limited. Despite these challenges, interest in this field remains high due to the potential applications of these materials as elements in magnetic storage devices as well as in spintronics and quantum computing. In an effort to better understand the relationships between molecular structure, spin, anisotropy, and SMM behavior and, ideally, to discover new SMMs with enhanced properties, this work focuses on exploring the use of two ligand types that have been underexplored in the field of molecular magnetism – radical bridging ligands and fluoride as a bridging ligand. A series of dinuclear compounds in which two transition metal centers are bridged by the radical anion form of the tetrazine-based ligand bmtz (bmtz = 3,6-bis(2'-pyrimidyl)-1,2,4,5-tetrazine) have been synthesized; the complexes

exhibit the desired strong metal-radical magnetic exchange coupling and SMM behavior. In an effort to expand the library of molecular magnets that contain unsupported fluoride bridges, a series of mixed-valence metal-fluoride cages were prepared and studied. Single crystal X-ray diffraction experiments revealed that these cages resemble a classic Keggin ion in structure but with the oxide bridges of the Keggin ion being replaced by fluoride bridges. Further studies using single crystal neutron diffraction methods have revealed that a small percentage of the bridging fluoride ligands are actually $[OH]^-$ ligands. Finally, an investigation into how careful control of the molecular geometry can affect the magnetic behavior of a series of mononuclear cobalt compounds was undertaken.

# DEDICATION

For my father

# ACKNOWLEDGEMENTS

I would like to thank my advisor, Prof. Kim R. Dunbar, for the mentorship and support she has given me during my career at Texas A&M. I am grateful for her willingness to let me pursue experimental techniques that are far from standard practice in a synthetic inorganic chemistry group, such as neutron diffraction, and for teaching me how to approach problem solving from a chemist's perspective.

Thank you as well to my committee members: Prof. Timothy Hughbanks, Prof. Francois Gabbai, and Prof. Donald Naugle. I appreciate the support you have provided me during my Ph.D. studies.

I was very fortunate to have the opportunity to work with two amazing people during my visits to national laboratories to conduct research. Dr. Yu-Sheng Chen at the Advanced Photon Source taught me how to make the most effective use of synchrotron X-rays and was invaluable in the performance of the X-ray Anomalous Dispersion experiments presented in Chapter IV. Dr. Xiaoping Wang of the Spallation Neutron Source taught me what I know about single crystal neutron diffraction while I was at Oak Ridge National Laboratory performing the neutron diffraction experiments presented in Chapter IV. He also taught me a few tricks that are useful not only for refining crystal structures from neutron diffraction data but also for refining crystal structures from X-ray diffraction data.

I would like to thank all of the members of the Dunbar group, past and present. Dr. Hanhua Zhao, Dr. Maria Fernanda Ballesteros Rivas, Dr. Silvia Gomez-Coca, Dr.

Mohamed Saber, Dr. Dawid Pinkowicz, Dr. Helen Chifotides, Dr. Yuan-Zhu Zhang, Dr. Ian Giles, Dr. Heather Southerland, Dr. Zhongyue Zhang, Dr. Bruno Pena, Dr. Zhanyong Li, Dr. Amanda David, Dr. Andrew Brown, Sarah Lane, Francisco Birk, Ryan Coll, Jill Ellengarger, Carolyn Gunthardt, David Kempe, Agustin Millet, Sayan Saha, Codi Sanders, Kelsey Schulte, Zhe Shen, Haomiao Xie, and Xuan Zhang – it has been a pleasure to work with all of you and I wish you the best in the future. I am also indebted to my undergraduate research advisor, Dr. Jamie Manson, for getting me interested in crystallography and magnetic materials. My exposure to research while working with Dr. M. is the reason I decided to pursue graduate studies in chemistry.

Finally, I would like to thank my wife for all of her patience and support, especially during the writing of this dissertation. You have helped immensely with maintaining balance in my life!

# NOMENCLATURE

| | |
|---|---|
| AC | Alternating Current |
| bmtz | 3,6-bis(2'-pyrimidyl)-1,2,4,5-tetrazine |
| DC | Direct Current |
| DMF | *N,N*-dimethylformamide |
| EPR | Electron Paramagnetic Resonance |
| EtOH | ethanol |
| ICP-MS | Inductively Coupled Plasma Mass Spectrometry |
| $L_4^2$ | $N^1$,$N^2$-dimethyl-$N^1$,$N^2$-bis-(pyridin-2-ylmethyl)ethane-1,2-diamine |
| NAA | Neutron Activation Analysis |
| MeOH | methanol |
| SMM | Single Molecule Magnet |
| TBP | trigonal bi-pyramidal |
| TGA | thermogravimetric analysis |
| THF | tetrahydrofuran |
| tmphen | 3,4,7,8-tetramethyl-1,10-phenanthroline |
| TPMA | tris(2-pyridylmethyl)amine |
| tren | tris(2-aminoethyl)amine |
| ZFS | Zero Field Splitting |

TABLE OF CONTENTS

Page

LIST OF FIGURES

Page

LIST OF TABLES

# CHAPTER I

# INTRODUCTION

In 1980 Lis synthesized the compound $[Mn_{12}(CH_3COO)_{16}(H_2O)_4O_{12}]\bullet 2CH_3COOH\bullet 2H_2O$, hereafter referred to as $Mn_{12}OAc$, as part of a study of mixed-valence Mn carboxylates.[1] The structure of $Mn_{12}OAc$, Figure 1, was described by Lis as "resembling a snow-flake" and consists of a cubane-like core composed of four oxo-bridged high spin $Mn^{IV}$ ions with a ring of eight high spin $Mn^{III}$ ions surrounding the cubane core. The core and outer ring are connected by a series of $\mu_3$-oxo bridges that also serve to connect the $Mn^{III}$ ions in the outer ring. Bridging acetate ligands complete the coordination sphere of the outer ring. Additionally, four of the $Mn^{III}$ ions are coordinated to a water molecule. Lis postulated that if magnetic exchange interactions were occurring between all twelve Mn ions through the oxygen atoms that " . . . such a complicated dodecameric unit should have interesting magnetic properties."

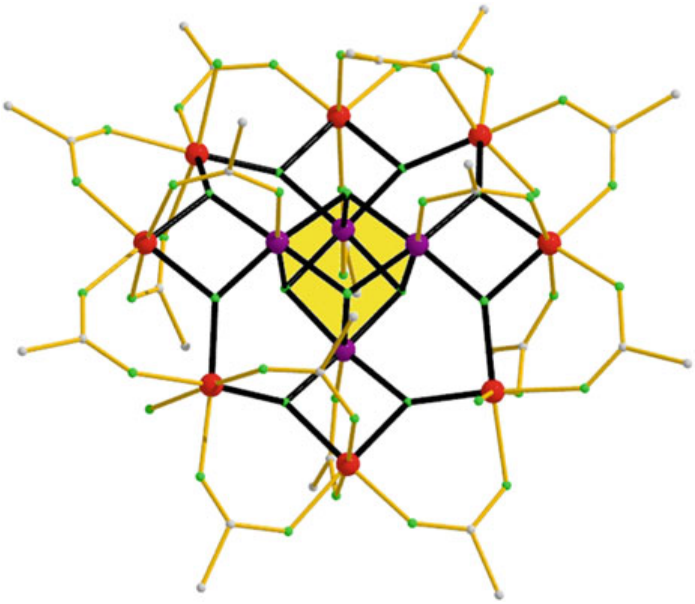

**Figure 1.** Depiction of the molecular structure of $[Mn_{12}(CH_3COO)_{16}(H_2O)_4O_{12}]\bullet 2CH_3COOH\bullet 2H_2O$. Hydrogen atoms are omitted for the sake of clarity. Color code: $Mn^{III}$, red; $Mn^{IV}$, purple; O, green; C, gold. Reproduced with permission of Springer from reference 2, copyright 2014.

It was not until 1991 that researchers realized how interesting $Mn_{12}OAc$ was in terms of its magnetic properties. In that year Caneschi, Gatteschi, and Sessoli performed magnetic and EPR studies of $Mn_{12}OAc$.[3] DC magnetization and EPR experiments confirmed the S = 10 ground state determined by Lis and that the $M_S$ = +/- 10 components of the zero field split ground state lie lowest in energy; in other words, the axial zero field splitting term (D) is negative. Most interesting were the results of the AC susceptibility experiments. Above 8 K the real component of the susceptibility ($\chi'$) increases as the temperature is lowered, as would be expected for a molecular system. Below 8 K, $\chi'$ decreases abruptly while the imaginary component of the susceptibility ($\chi''$) increases in magnitude, reaches a maximum, and then decreases to zero again. The

frequency of the maximum in $\chi''$ was observed to be frequency dependent, a phenomenon that had been previously observed in superparamagnets and spin glasses, where there is a frequency-dependent freezing of the magnetization, but whose origin could not be explained in this molecular system.

Two years later a report of more detailed magnetic susceptibility studies of $Mn_{12}OAc$ by the Hendrickson group[4] and an almost simultaneous report by the Novak group[5] appeared in the literature and provided an explanation for the observed frequency dependence of $\chi''$ in $Mn_{12}OAc$. Of particular importance was the observation by the Novak group of an open hysteresis loop at temperatures below 2.8 K. An open hysteresis loop is traditionally only observed for bulk magnets; no evidence of long range magnetic order was observed in the magnetization, susceptibility, or specific heat measurements, confirming the molecular nature of the observed hysteresis loop. Further confirmation of the molecular nature of the relaxation process in $Mn_{12}OAc$ was provided when additional magnetization measurements showed the presence of steps in the hysteresis loops at low temperature (Figure 2) that could only be explained as quantum tunneling of the magnetization, a molecular phenomenon.[6,7] The work of Friedman and Sarachik further expounded on the idea of quantum tunneling of the magnetization, showing that the observed steps in the hysteresis loop are fully consistent with a model of thermally assisted quantum tunneling, in which the tunneling is occurring between thermally populated excited states.[8] In the following years the term Single Molecule Magnets (SMMs) began to be widely used in the literature to describe molecules that displayed this slow relaxation behavior.

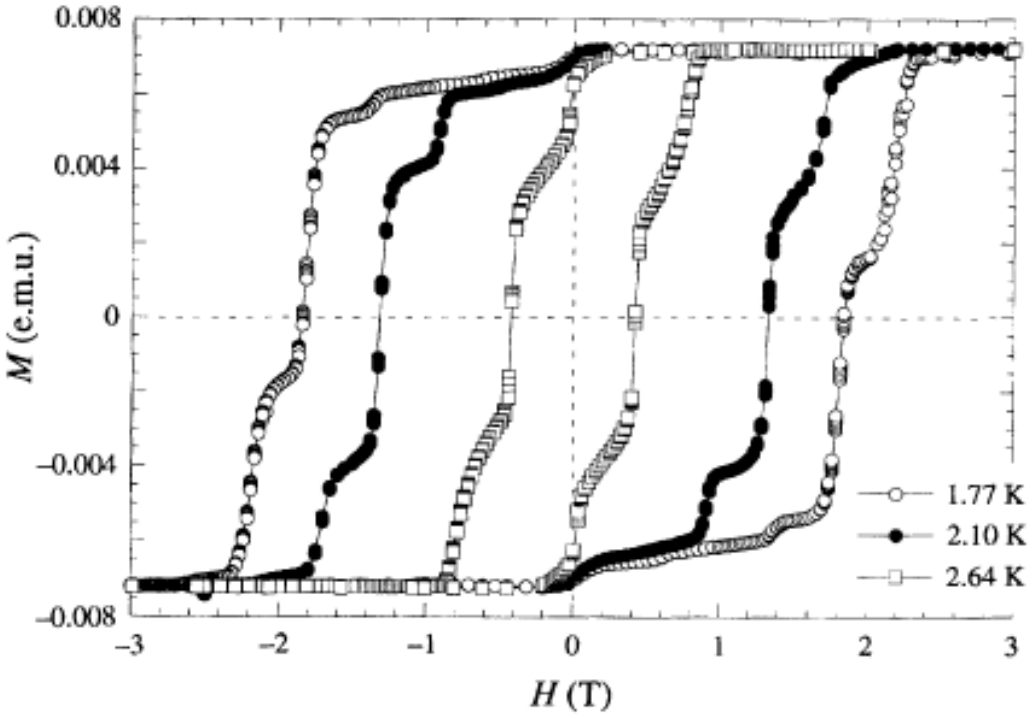


**Figure 2.** Hysteresis loops for a single crystal of $Mn_{12}OAc$ at various temperatures, showing the steps characteristic of quantum tunneling of the magnetization. Reprinted by permission from Macmillan Publishers Ltd: Nature, reference 6, copyright 1996.

Before continuing with a history of the progress in the field of SMMs a discussion of the methods of identifying and classifying SMM behavior is warranted. The magnetic bistability of SMMs is a consequence of the existence of a thermal barrier to the reversal of the spin from the +(−) $M_S$ state to the −(+) $M_S$ state, Figure 3. The effective height of this barrier, $U_{eff}$, was postulated to be governed by the equations:

$$U_{eff} = S^2|D|$$

$$U_{eff} = (S^2 - 1/4)\,|D|$$

for integer and non-integer spin ground states, respectively, where S is the total spin ground state and D is the axial zero field splitting (ZFS) parameter.

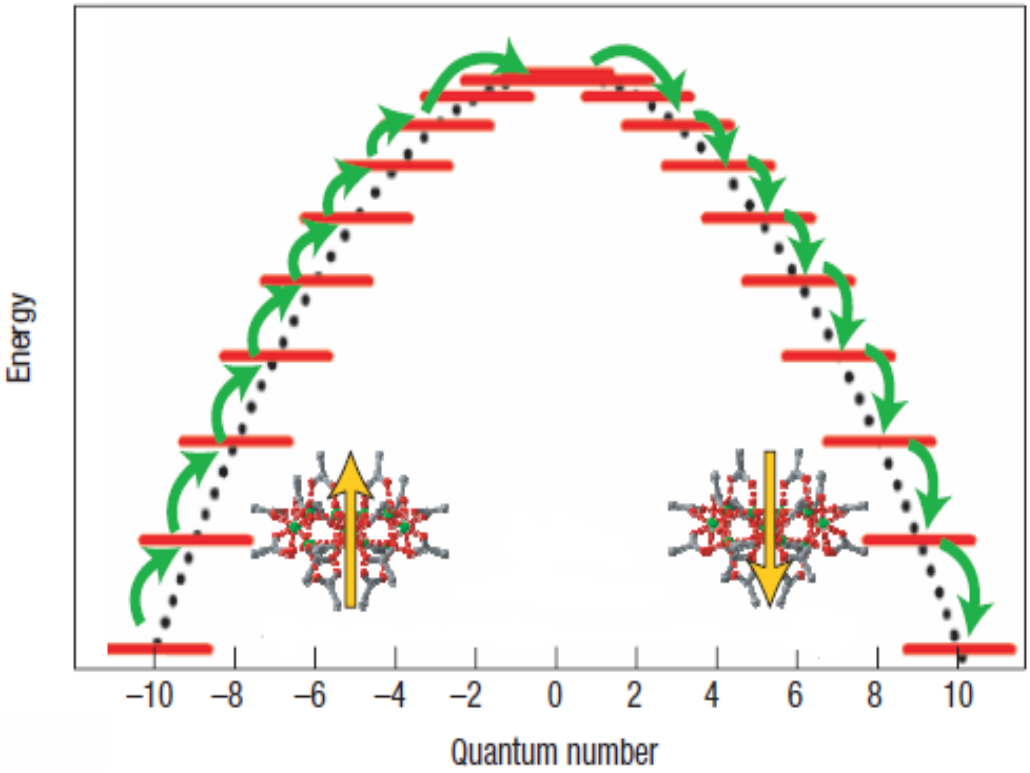


**Figure 3.** Representation of the energy barrier to spin reversal in a SMM with an S = 10 spin ground state. Reprinted by permission from Macmillan Publishers Ltd: Nature Materials, reference 9, copyright 2008.

The magnitude of D is the preference for the spin to align along a certain direction in the molecular reference frame and is commonly determined by evaluation of a ZFS Hamiltonian of the form:

$$\widehat{H} = gS\beta H + D\left(\hat{S}_z^2 - \frac{1}{3}\hat{S}^2\right) + E(\hat{S}_x^2 - \hat{S}_y^2)$$

The first term in this Hamiltonian describes the Zeeman interaction in an applied field where $g$ is the electronic g factor, $S$ is the spin state, β is the Bohr magneton, and $H$ is the applied field. The second and third terms describe the axial and rhombic ZFS terms, respectively, where $\hat{S}$ is the spin operator. The D parameter has not only a magnitude,

but also a sign. If D is negative, the $M_S$ states of largest magnitude will lie lowest in energy in zero field; this situation is frequently referred to as easy-axis anisotropy since the spins have a preference to align with the z axis. If D is positive, the lowest value $M_S$ state(s) will lie lowest in energy; this situation is frequently referred to as easy-plane anisotropy since the spins have a preference to align in the xy plane. Rhombic anisotropy can have a dramatic effect on SMM properties and will be discussed in more detail later.

Observation of a magnetic hysteresis loop, especially if steps due to quantum tunneling are present, is the most definitive way of establishing a molecule's SMM behavior. The highest temperature at which an open hysteresis loop can be observed is commonly referred to as the blocking temperature ($T_B$). Another method that can be used to determine if a molecule should be classified as an SMM is AC susceptibility; this was discussed briefly above when presenting $Mn_{12}OAc$. When measuring AC susceptibility the sample is subjected to a magnetic field oscillating at a frequency ν. If the sample behaves as a simple paramagnet the AC susceptibility remains a real quantity. If, on the other hand, the molecules in the sample behave as SMMs the AC susceptibility becomes a complex quantity with $\chi'$ representing the real component of the susceptibility and $\chi''$ representing the imaginary, or out-of-phase, component. Phenomenologically, the imaginary component can be thought of as the percentage of the spins that cannot traverse up and over the thermal barrier and relax back down on the other side of the barrier at a rate that is equal to or greater than the applied AC frequency. This has the effect of trapping the spins on one side of the barrier and gives

rise to non-zero values of χ''. Plots of χ' and χ'' for $[Mn(L_{N5Me})(H_2O)]_2[Mo(CN_7)]\bullet 6H_2O$ are shown in Figure 4 as a representative example.

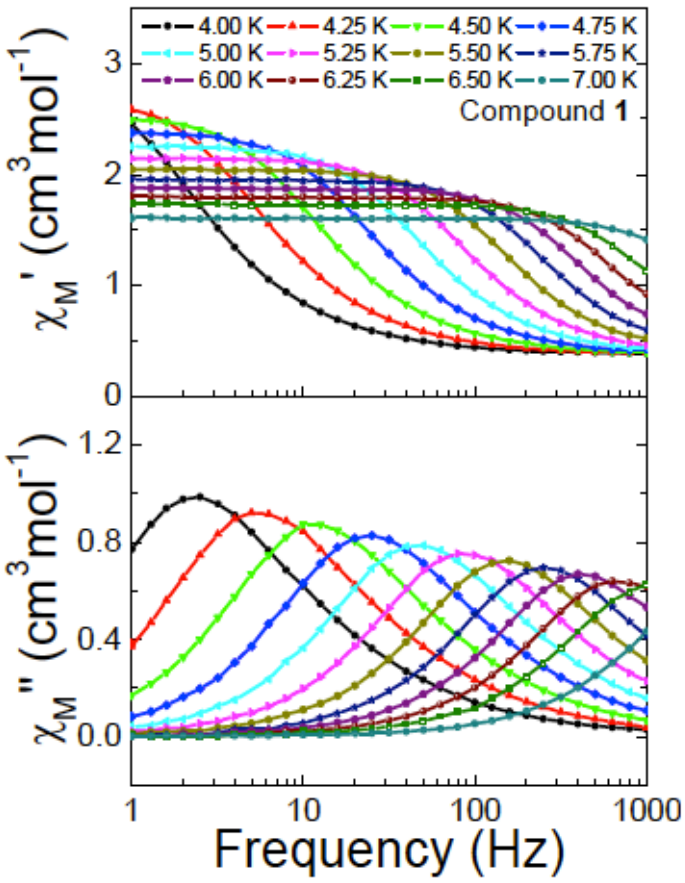


**Figure 4.** Frequency dependence of χ' and χ'' for $[Mn(L_{N5Me})(H_2O)]_2[Mo(CN_7)]\bullet 6H_2O$. Reprinted with permission from reference 10, Copyright 2013 American Chemical Society.

The frequency of the maxima in χ'' are related to the relaxation time, τ, by:

$$\tau = \frac{1}{2\pi\nu}$$

The relaxation time, and hence the maxima in χ'', are temperature- and frequency-dependent for an SMM. The values of τ obtained at various combinations of temperature and frequency will obey the Arrhenius law:

$$\tau = \tau_o e^{U_{eff}/k_b T}$$

where $\tau_o$ is the pre-exponential factor, $k_b$ is the Boltzmann constant, and $T$ is the temperature. When plotted as $\ln(1/\tau)$ vs. $1/T$ the slope of the line will be equal to $-U_{eff}/k_b$ and the y-intercept can be used to determine $\tau_o$. This method of reporting $U_{eff}$ is the most common in the literature today. As a benchmark, when $Mn_{12}OAc$ is analyzed in this way the resulting parameters are $U_{eff}/k_b$ = 64.1 K, D = -0.46 $cm^{-1}$, and an open hysteresis loop is visible up to 3.5 K.

In the years following the discovery of SMM behavior in $Mn_{12}OAc$, many other derivatives of this molecule were reported that retain the $Mn_{12}$ core but which are based on numerous other carboxylate derivatives.[11] Other reports of SMMs in this time frame were also manganese carboxylate complexes, with nuclearities as high as $Mn_{84}$ being reported,[12] but none of these derivatives surpassed the performance of the original $Mn_{12}OAc$. Compounds with other metal ions were also investigated, with complexes of $V_4$,[13] $Mn_4$,[14] $Fe_4$,[15,16] $Fe_8$,[17] $Fe_9$,[18,19] $Fe_{10}$,[20] $Co_4$,[21] $Co_6$,[22] $Ni_{12}$,[23] $Ni_{21}$,[24] $MnMo_6$,[25] and CuTb[26] being reported. In 2006 Powell and co-workers reported a $Mn_{19}$ complex with a record S = 83/2 ground state but SMM behavior was observed only below 0.5 K.[27] It was not until 2007 when Brechin and co-workers reported $[Mn^{III}_6O_2(sao)_6(O_2CPh)_2(EtOH)_4]$ ($saoH_2$ = salicylaldoxime or 2-hydroxybenzaldehyde oxime) that a barrier and blocking temperature above that of $Mn_{12}OAc$ was realized.[28]

This $Mn_6$ complex has a modest S = 12 ground state with D = -0.43 $cm^{-1}$ and yet shows hysteresis up to 4.5 K and a $U_{eff}/k_b$ value of 86.4 K.

Up to this point, researchers had been trying to increase the operating temperature of SMMs by increasing S, which was a reasonable approach given that the S term is squared in the expression for $U_{eff}$. In 2007 Oliver Waldmann published a report in which he pointed out the fact that the effective barrier does not increase with S as $S^2$ but rather as $S^{0.29}$.[29] He suggested that increasing the spin of the individual spin carriers is a more appropriate approach to realize larger energy barriers, as well as increasing D. Also in 2007, Ruiz and co-workers presented a theoretical investigation of the effects of electronic structure on D for a pair of $Mn_6$ molecules and $Mn_{12}OAc$.[30] Their results show that as the ground spin state gets larger, the magnitude of D becomes smaller. The main conclusion from their paper was that the magnitude of $U_{eff}$ is mainly determined by the strength of spin-orbit coupling and trying to independently maximize D and S is impossible since the two parameters are inversely related. The Neese group reached similar conclusions by performing *ab initio* calculations on $Fe^{II}$ complexes in either a trigonal bipyramidal (TBP) or square-based pyramid coordination environment.[31] Hill and co-workers provided additional evidence that the underlying physics of SMM behavior is perhaps more complicated than was originally thought when they proposed the use of a double-exponential function of the form:

$$\left(\frac{1}{\tau}\right) = \left(\frac{1}{\tau_{o1}}\right) e^{-U_1/k_bT} + \left(\frac{1}{\tau_{o2}}\right) e^{-U_2/k_bT}$$

to explain the non-linearity that was being observed in some Arrhenius plots.[32] In their equation, $U_1$ represents relaxation within the spin ground state and $U_2$ represents relaxation via excited spin states.

The concept of designing SMMs by attempting to control anisotropy as put forth by Waldmann, Ruiz, and Neese was demonstrated by Ishikawa and co-workers in 2003, albeit for lanthanide complexes instead of transition metals.[33] These authors rationalized that, if an appropriate ligand field could be generated around a single lanthanide ion, the sublevel with the largest $J_z$ component would lie lowest in energy, akin to a large negative D value in transition metal complexes. He found such a complex in the literature, $(Bu_4N)[Pc_2Tb]$ (Pc = dianion of phthalocyanine), and observed maxima in $\chi''$ at temperatures as high as 40 K, much higher than that observed for any transition metal complex. Arrhenius analysis of the AC behavior of $(Bu_4N)[Pc_2Tb]$ yielded a $U_{eff}/k_b$ value of 322 K, much higher than what had been observed previously in transition metal complexes. This discovery was an early indication that controlling the anisotropy of a single metal ion was a viable method for designing new SMMs with higher blocking temperatures. Lanthanide complexes remain a promising route to higher temperature SMMs, currently holding the records for the highest observed $U_{eff}$ and the highest observed $T_B$. At 20 K, the pentagonal bipyramidal complex $[Dy(Cy_3PO)_2(H_2O)_5]Br_3 \bullet 2(Cy_3PO) \bullet 2H_2O \bullet 2EtOH$ ($Cy_3PO$ = tricyclohexylphosphine oxide) is the current record holder for $T_B$[34] with another pentagonal bipyramidal complex, [Dy(bbpen)Br] ($H_2$bbpen = N,N′-bis(2-hydroxybenzyl)-N,N′-bis(2-methylpyridyl)ethylenediamine), the current record holder for the highest effective

barrier with $U_{eff}/k_b$ = 1025 K.[35]

The first example of a mononuclear transition metal SMM was reported in 2010, namely K[(tpa$^{Mes}$)Fe].[36] From DC magnetization experiments the Long group determined that D = -39.6 cm$^{-1}$ and E = -0.4 cm$^{-1}$, in line with the anisotropy prerequisites for SMM behavior. Initial investigation of the AC susceptibility of this complex revealed a lack of SMM behavior. If, however, the AC susceptibility is measured in the presence of a 1500 Oe static DC field, strong out-of-phase signals are observed. From the Arrhenius analysis the value of $U_{eff}/k_b$ was determined to be 58.8 K. The lack of an AC signal in the absence of a DC field was attributed to fast quantum tunneling through the barrier. The effect of applying a DC field on relaxation dynamics is illustrated in Figure 5. In zero DC field the +2 and –2 states are degenerate in energy. For a truly axial system with 3-fold symmetry tunneling between these two levels is forbidden but transverse anisotropy, as quantified by E, allows for tunneling pathways to become operative.[37,38] By applying a static DC field the degeneracy of the +$M_S$ and –$M_S$ states is broken, effectively shutting down the tunneling pathway and allowing thermal relaxation to be observed.

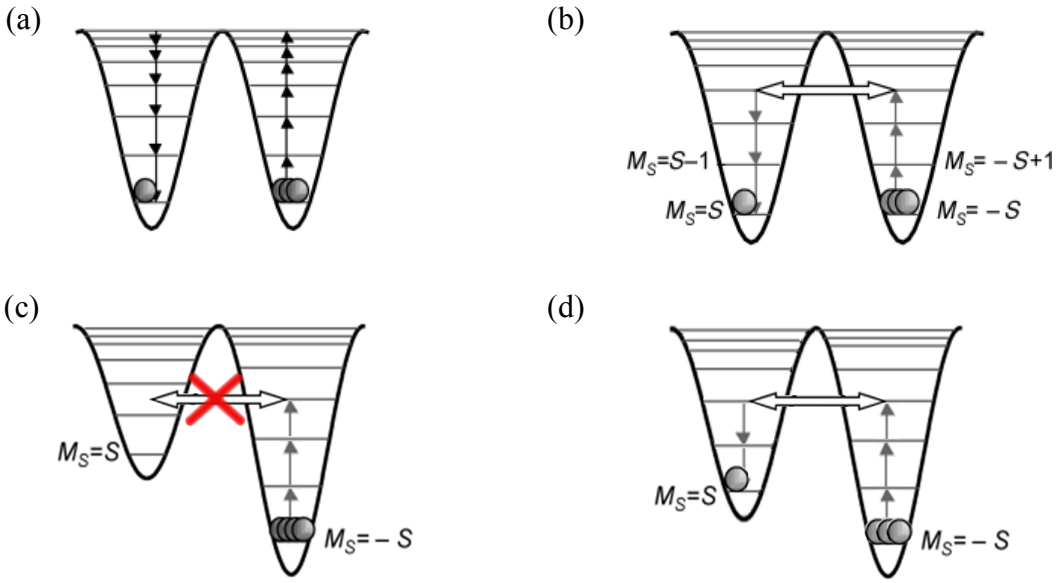


**Figure 5.** Possible relaxation mechanisms for SMMs. (a) thermal, or Orbach, relaxation over the barrier. (b) thermally assisted quantum tunneling. (c) application of a static DC field distorts the energy wells, lifting the degeneracy between states and minimizing quantum tunneling. (d) distortion of the energy wells by a DC field can bring states of different $M_S$ into resonance, increasing the probability of quantum tunneling. Adapted with permission from reference 39, copyright 2003, Wiley-VCH Verlag GmbH & Co KGaA, Weinheim.

It should be mentioned that, in addition to E, a transverse field can also be generated by dipolar fields from neighboring molecules or hyperfine fields from nuclear spins.[38] An excellent example of the importance of dipolar fields from neighboring molecules was demonstrated by Glaser and co-workers in a 2015 report on a series of $[Mn^{III}_6Cr^{III}]^{3+}$ compounds.[40] The $[Mn_6Cr]^{3+}$ complex could be crystallized as a $[BPh_4]^-$, $[Cr^{III}(CN)_6]^{3-}$, or lactate salt. All three salts display open hysteresis loops below 2 K. The lactate salt is unique in that quantum tunneling is completely suppressed, even at temperatures as low as 0.3 K. The authors attribute the suppression of quantum tunneling to the perfect alignment of the $C_3$ axes of neighboring molecules in the lactate

salt, which is not the case in the other salts (Figure 6). The perfect alignment of the $C_3$ axes eliminates all transverse dipolar fields in the lactate salt. The authors calculated the dipole field components felt by a given molecule to corroborate this hypothesis. They found that for the lactate salt, the dipole field is described by $H_x = 0$, $H_y = 0$, and $H_z = 3.7$ mT. For the $[BPh_4]^-$ salt the dipole field is described by $H_x = 3.34$, $H_y = 4.78$, and $H_z = -10.0$ mT.

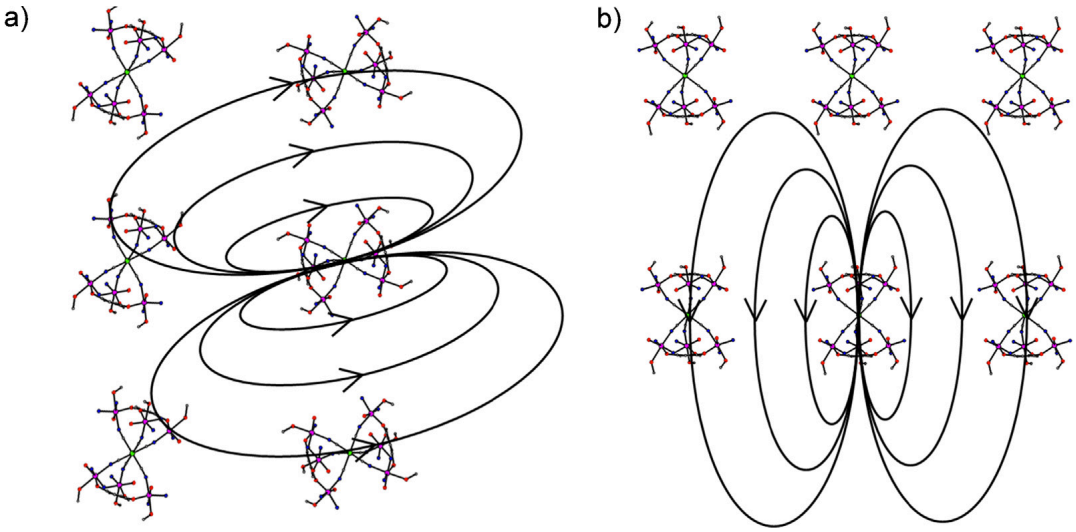


**Figure 6.** Influence of the relative orientation of the SMMs in the crystal structure on the stray field components experienced by neighboring SMMs. (a) In the non-collinear arrangement, the neighboring SMM experiences non-zero stray-field components $H_x$, $H_y$, and $H_z$ in its own molecular coordinate system. (b) In a collinear arrangement, the neighboring molecule only experiences a non-zero stray field component $H_z$, while the transversal components $H_x$ and $H_y$ are zero. Reprinted from reference 40 with permission from Elsevier.

In the years since K[(tpa$^{Mes}$)Fe] was identified as the first mononuclear transition metal SMM, there have been numerous reports of other mononuclear transition metal SMMs. Many of them require the application of a static DC field for slow relaxation to

be observed. The most notable are the ones that do not require a DC field, such as $(Ph_4P)_2[Co^{II}(SPh)_4]$,[41] $(HNEt_3)[Co^{II}Co^{III}{}_3L_6)$ ($H_2L$ = *R*-4-bromo-2((2-hydroxy-1-phenylethylimino)methyl)phenol),[42] $(Ph_4P)_2[Co^{II}C_3S_5)_2]$,[43] a $Co^{II}$ pseudo-clathrochelate,[44] $(HNEt_3)_2[Co^{II}(L^{2-})_2]$ ($H_2L$ = 1,2-bis(methanesulfonamido)benzene),[45] $[Co\{(NtBu)_3SMe\}_2]$[46] and the linear $[K(crypt\text{-}222)][Fe^{I}(C(SiMe_3)_3)_2]$.[47]

While these smaller molecules have led to some impressive blocking temperatures, perhaps their most important contribution to the field has been the ability to perform theoretical investigations of these molecules because of their small size. In 2013 Ruiz and co-workers used $Fe^{II}(NH_3)_x$ model complexes to assemble a comprehensive table of molecular geometries and spin states, predicting the sign and magnitude of D for different combinations of geometry and d electron count (Table 1).[48] In this same paper they provide a more general recipe for synthesizing molecules with large, negative D values. Their approach was to consider molecular geometries and d electron counts that result in a degenerate ground state. The molecular geometry was allowed to distort in a Jahn-Teller fashion, the orbital energies re-computed, and then the sign and magnitude of D was calculated. The important outcome of this analysis is that the sign and magnitude of D is largely dependent on the character of the first excitation for the Jahn-Teller split orbitals (Figure 7). If the first transition is between orbitals of the same $m_l$ value the contribution to $D_{zz}$ will be negative; the smaller the energy gap between the orbitals the larger the magnitude of D will be.

**Table 1.** Estimation of the D values for high spin mononuclear transition metal complexes with different electronic configurations and coordination modes using ammonia ligands (using the molecular orbitals of $Fe^{II}(NH_3)_x$ models)[a]. Reprinted with permission from reference 48, Copyright 2013 American Chemical Society.


[a]Green and blue squares indicate large and small negative values, in that order, while red and orange represent large and small positive values, respectively. Cases with more than one color indicate that the nondistorted structure has a zero D value, and different options are possible depending on the symmetry of the Jahn-Teller distortion.

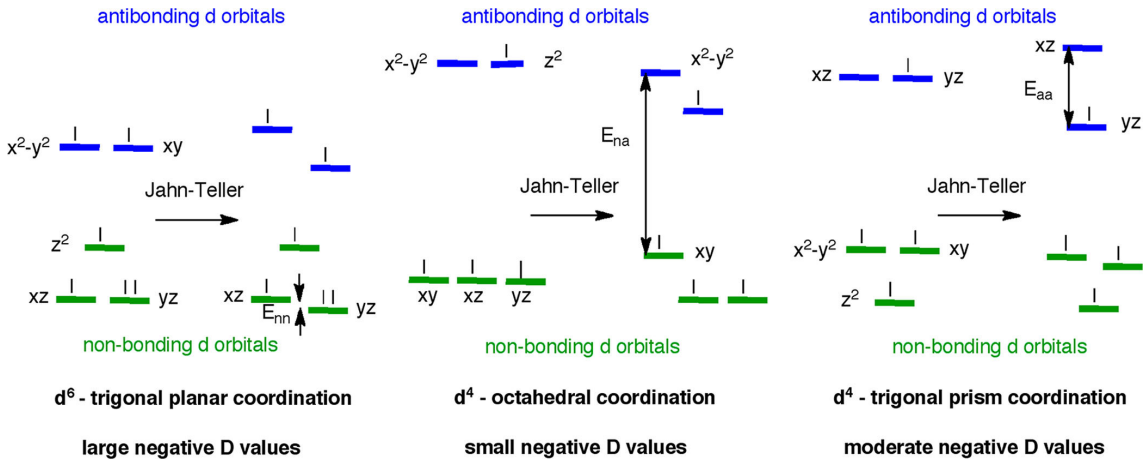


**Figure 7.** Splitting of the d orbitals due to the Jahn-Teller effect for three cases with negative D values: $d^6$ trigonal planar coordination (left), $d^4$ octahedral coordination (middle), and $d^4$ trigonal prism coordination (right). The energy difference indicated by the arrow in each case corresponds to the first excitation that leads to the main contribution to $D_{zz}$. The smaller the excitation energy, the larger the magnitude of D becomes. Reprinted with permission from reference 48, Copyright 2013 American Chemical Society.

In another study, Ruiz and co-workers showed that entanglement of the electron and nuclear spin of $Co^{II}$ can have a profound effect on the relaxation properties,[49] a finding that has prompted researchers to attempt to synthesize SMMs with nuclear spin-free metals and ligand sets.[43,50] Theoretical calculations have also been used to explain the unique magnetic properties of some of these smaller molecules. For example, *ab initio* calculations revealed that the large anisotropy of [K(crypt-222)][$Fe^{I}(C(SiMe_3)_3)_2$][47] is due, in large part, to very strong $4s - 3_{dz}{}^2$ mixing, resulting in the $d_z{}^2$ orbital lying lowest in energy.

Researchers have also come to realize that in these smaller molecules relaxation processes other than quantum tunneling and Orbach processes need to be considered, as

evidenced by distinct curvature of the Arrhenius plot. It is becoming more common in the literature to perform the fitting of the Arrhenius plot with the equation:[51]

$$\tau^{-1} = AH^2T + \frac{B_1}{1 + B_2H^2} + CT^n + \tau_o^{-1}\exp\left(-U_{eff}/k_bT\right)$$

where the first term represents a direct process, the second term correlates to the zero-field tunneling process, the third term represents a Raman relaxation process, and the final term represents the thermal Orbach relaxation process. In this report the authors admit that the physical meaning of the coefficients *A* and *C* is not easily understood because these values depend on properties such as the crystal density, the speed of sound in the solid, and the strength of the interaction of the spin system with phonons. Regardless, the values of *A* and *C* can be used on a relative scale to compare the preference for these relaxation mechanisms among different complexes.

Mononuclear SMMs have provided impressive results but by no means should the search for new SMMs be limited to mononuclear entities. Fast quantum tunneling remains a problem in many mononuclear SMMs; one reason could be due to the limitations on the spin ground state in mononuclear complexes. The tunneling probability between two states $M_S$ and $M_S$' at a constant field sweep rate is given by:[40]

$$P_{M_SM_S'} = 1 - exp\left[-\frac{\pi\Delta^2_{M_SM_S'}}{2\hbar g\mu_B|M_S - M_S'|\mu_o\, dH_z/dt}\right]$$

where Δ is the tunnel splitting between the two states; thus larger values of Δ lead to larger values of *P*, increasing the probability of observing quantum tunneling. The tunnel splitting is related to the rhombicity of the crystal field by:[40]

$$\Delta \propto \left(\frac{E_{S_t}}{D_{S_t}}\right)^{S_t}$$

which has two important implications. First, the rhombic ZFS term should be kept as small as possible. This is most easily achieved by designing molecules with at least 3-fold symmetry, forcing E to be zero (or at least close to zero if only small perturbations away from 3-fold symmetry are present). An elegant example of the importance of 3-fold symmetry was recently demonstrated for the series of complexes $[Dy(EFID)_3(X)]$ (EFID = 1-(1-ethyl-1*H*-indol-3-yl)-4,4,4-trifluorobutane-1,3-dione), X = $H_2O$, DMF, DMSO, triphenylphosphine oxide).[52] The $H_2O$ analog, in which the symmetry about the $Dy^{III}$ ion closest to the ideal $C_{3v}$, displays SMM behavior in zero DC field and a slight opening in the hysteresis loop at 1.8 K with no obvious transition to a quantum tunneling regime. The DMF and DMSO analogs, in which the coordinated solvent molecule further distorts the geometry about the $Dy^{III}$ ion, show SMM behavior only in the presence of a 2000 Oe DC field. The triphenylphosphine analog, the most distorted of the family, did not show SMM behavior at any of the DC fields investigated. Second, the tunneling probability becomes exponentially smaller with larger spin states. Higher spin states can only be achieved by synthesizing exchange coupled polynuclear compounds or by designing mononuclear systems that incorporate organic radical ligands ferromagnetically coupled to transition metal centers. A balance is therefore needed, in which the ground state spin value is maximized but the molecule remains small enough that symmetry and anisotropy can be controlled, for the rational design of high-temperature SMMs to be successful.

In addition to increasing the spin ground state, the use of organic radicals in designing SMMs is also advantageous in that the exchange coupling in radical systems is, in general, stronger than in systems with diamagnetic ligands.[53] This helps to isolate the spin ground state from excited states, thus preventing relaxation pathways via these low-lying excited states.[54-57] The topic of radical ligands in magnetic materials will be further developed in Chapter II.

While by no means all-inclusive, the preceding survey of the emergence and growth of the field of Single Molecule Magnetism nonetheless provides the foundation on which the work presented herein was based. More in-depth discussions of the principles and ideas presented here are included, where appropriate, in the individual chapters of this dissertation. Chapter II presents a series of dinuclear first-row transition metal compounds bridged by the bmtz ligand in both the neutral and radical forms, with strong magnetic exchange coupling observed in the radical analogs. Chapter III describes a family of isostructural mononuclear $Co^{II}$ compounds in which the effects of symmetry and crystal packing on the magnetic properties are examined. Chapter IV is a continuation of work started by Dr. Xinyi Wang while he was a postdoctoral researcher in the Dunbar lab. New information gained by synchrotron X-ray and neutron diffraction experiments on a series of transition metal fluoride cages is presented.

# CHAPTER II

# BMTZ COMPLEXES OF DIVALENT FIRST-ROW TRANSITION METALS[*]

## Introduction

Magnetic properties of molecule-based materials are dictated by three primary factors, *viz*., dimensionality, the magnitude of the exchange coupling, and degree of anisotropy. A building block or modular approach allows one to control the dimensionality of paramagnetic compounds with M-X-M linkages (X = bridging atom or ligand) in order to circumvent 3-D architectures; the possibilities are 2-D and 1-D motifs or discrete molecules (0-D) depending on the choice of ligands. A majority of the reported molecular magnets are based on transition or rare earth metal ions as the sole spin carriers with only diamagnetic ligands, but the incorporation of organic radicals that participate in direct exchange interactions leads to materials with enhanced magnetic, electronic, and redox properties. If the radical serves as a bridging ligand between two paramagnetic metal centers, a magnetic ground state is achieved regardless of whether exchange coupling is antiferromagnetic or ferromagnetic. If the metal and radical spins couple ferromagnetically, a high spin ground state will result due to the parallel alignment of all of the spins in the system. Conversely, if antiferromagnetic interactions dominate, a ferrimagnetic ground state of at least S = 1/2 will result; the

[*] Part of the data reported in this chapter is reprinted with permission from Woods, T. J.; Ballesteros-Rivas, M. F.; Ostrovsky, S. M.; Palii, A. V.; Reu, O. S.; Klokishner, S. I.; Dunbar, K. R. *Chem. Eur. J.* **2015**, *21*, 10302, copyright 2015 Wiley-VCH Verlag GmbH&Co. KGaA, Weinheim.

spin ground state will be even higher if metal ions with greater than S = 1/2 ground states are bridged by an S = 1/2 radical.

One of the earliest examples of an organic radical-based magnet is $V(TCNE)_x \bullet nCH_2Cl_2$ ($x \approx 2$, $n \approx ½$, TCNE = tetracyanoethylene) which is extraordinary in that it exhibits spontaneous magnetization above room temperature.[58] Another seminal discovery is the first single chain magnet (SCM), $[Co(hfac)_2(NITPhOMe)]$ (hfac = hexafluoroacetylacetonate, NITPhOMe = 4'-methoxy-phenyl-4,4,5,5-tetramethylimidazoline-1-oxyl-3-oxide) in which the $Co^{II}$ units are connected via nitronyl nitroxide radicals.[59]

Research in the area of molecular magnetic materials, particularly SMMs, is a very active and growing topic due to the potential applications in high-density data storage,[60] spintronics,[61,62] and quantum computing.[62,63] SMMs are well suited to these applications due to the existence of a bistable ground state in these molecules below a certain blocking temperature which enables these molecules to behave as tiny bar magnets of precisely defined size and shape. One of the major challenges facing this field is the temperature required for this phenomenon to be observed. To date, the blocking temperatures are in the range of liquid helium cryogenics. One of the hurdles for achieving higher temperature SMM behavior in large polynuclear complexes is that predicting and maximizing global anisotropy in these molecules is challenging owing to the general lack of control over the arrangement of the easy axes of the individual ions. An entirely different approach that is experiencing considerable success is the design of low nuclearity complexes with specific combinations of geometry, coordination

number, and a specific electronic configuration in order to promote strong single ion anisotropy. A natural limitation of this strategy is that the total spin of the system, which also has some bearing on $T_B$, is limited for these smaller nuclearity compounds. Nevertheless, one can increase the total spin of the system by incorporating radical ligands into the molecule. For example, organic radicals in the nitroxide and verdazyl families have been used to synthesize SMMs.[64] In addition to increasing the total spin of the system, organic radical bridges have the added advantage of increasing the magnitude of the magnetic exchange coupling,[56,65-69] which leads to higher blocking temperatures.[56,65,66,70] Pioneering work involving semiquinone,[71] nitroxide,[72] and verdazyl[73] radicals paved the way for the current interest in the subject for the design of new generations of SMMs.[64] A particularly notable example of the use of radical bridging ligands is the work of Long and coworkers who reported that the $N_2^{3-}$ radical bridged compound $[K(18\text{-crown-6})]\{[(Me_3Si)_2N]_2(THF)Gd\}_2(\mu\text{-}\eta^2\text{:}\eta^2\text{-}N_2)$ exhibits a superexchange coupling constant of J = -27 $cm^{-1}$ between $Gd^{III}$ ions, the strongest coupling observed to date between these 4f spin centers.[65] The $Tb^{III}$ analog of the same complex exhibits magnetic hysteresis up to 14 K,[66] a blocking temperature that has only very recently been surpassed by the observation of magnetic hysteresis at 20 K in $[Dy(Cy_3PO)_2(H_2O)_5]Br_3 \bullet 2(Cy_3PO) \bullet 2H_2O \bullet 2EtOH$ ($Cy_3PO$ = tricyclohexylphosphine oxide).[34]

Since the report of $[Co_4(hmp)_4(MeOH)_4Cl_4]$, the first $Co^{II}$ complex to display SMM behavior,[21] only a few reports of multinuclear $Co^{II}$ exchange-coupled SMM systems have appeared in the literature.[22,74-81] The existence of mononuclear cobalt

SMMs coordinated to terminal radical ligands[82-90] inspired us to expand on this concept by using the tetrazine-based ligand 3,6-bis(2'-pyrimidyl)-1,2,4,5-tetrazine (bmtz), a ligand that is known to exist as a stable radical anion, to prepare dinuclear $Co^{II}$ SMM complexes and then to expand the scope to include $Fe^{II}$ and $Ni^{II}$. The magnetic orbital of bmtz is localized on the π* orbital of the tetrazine ring nitrogen atoms (Figure 8), an ideal orbital for realizing strong magnetic coupling between metal centers.[91] Although the radical has been reported by Kaim *et al*., to exist in compounds of $Cu^{I}$,[92] $Ru^{(0/I/II)}$,[93] $Re^{I}$,[94] and $Os^{(0/I/II/III)}$[93] its use has not been extended to the area of molecular magnets.

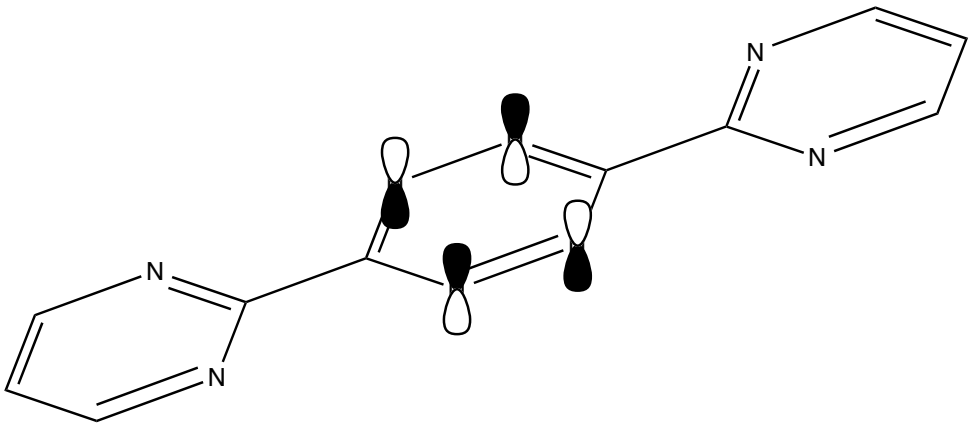


**Figure 8.** Singly occupied radical orbital of bmtz.

**Iron Complexes of the bmtz Ligand**

**Experimental Section**

The reagents tris-(2-pyridylmethyl)amine (TPMA),[95] $[Fe(CH_3CN)_6](BF_4)_2$,[96] $Fe(CF_3SO_3)_2$,[97] and bmtz[91] were prepared by literature procedures. $Cp_2Co$ (Aldrich) was used as received. The $CH_3CN$ was pre-dried by storage over 3 Å molecular sieves and

distilled over 3 Å molecular sieves prior to use. The $Et_2O$ was purified using an MBRAUN solvent purification system and then stored over 3 Å molecular sieves in the dry box. Syntheses of the bmtz complexes were performed in an MBRAUN dry box under an $N_2$ atmosphere. Elemental analyses were performed by Atlantic Microlabs, Inc., Norcross, GA. Magnetic measurements were conducted in the temperature range of 1.8 to 350 K using a Quantum Design MPMS-XL SQUID magnetometer equipped with a 7T superconducting magnet. The diamagnetic contribution of the plastic bag used as the sample holder was subtracted from the raw data. Core diamagnetism of the sample was accounted for using Pascal's constants.[98] Mossbauer measurements on $[\{Fe(TPMA)\}_2\text{-}\mu\text{-}bmtz^{\bullet-}](CF_3SO_3)_3$ and $[\{Fe(TPMA)\}_2\text{-}\mu\text{-}bmtz](CF_3SO_3)_4$ were performed by Heather Stout and Dr. Catalina Achim at Carnegie Mellon University. The Mossbauer samples were prepared by grinding the complex to a fine powder using a mortar and pestle, placing the powder in a Delrin® Mossbauer cup, and covering the sample with mineral oil (Aldrich) to create a suspension. The SQUID measurement on the Mossbauer sample of $[\{Fe(TPMA)\}_2\text{-}\mu\text{-}bmtz^{\bullet-}](CF_3SO_3)_3$ was performed in a home-made Delrin® sample holder. The contribution of the sample holder to the measured susceptibility was determined by direct measurement of the empty sample holder using the same measurement sequence that was used to measure the sample in the SQUID, allowing a point-by-point subtraction to be performed. The contribution of the mineral oil to the measured susceptibility was accounted for by determining the temperature-dependent gram susceptibility of mineral oil by direct measurement in the Delrin® sample holder, allowing a point-by-point subtraction to be performed. A portion of the

Mossbauer sample was transferred to the SQUID sample holder in the dry box. The mass of compound and mineral oil in the SQUID sample was determined by assuming the mass ratio of compound:oil was the same in the SQUID sample as in the Mossbauer sample.

*Syntheses*

**[{Fe(TPMA)}$_2$-μ-bmtz$^{\bullet-}$](BF$_4$)$_3$•CH$_3$CN.** Quantities of $Cp_2Co$ (0.0120 g, 0.0634 mmol) and bmtz (0.0200 g, 0.0840 mmol) were stirred in $CH_3CN$ (5 mL) until the solution was red-orange. Solid TPMA (0.0310 g, 0.107 mmol) was then added to the solution and stirred for one minute after which time solid $[Fe(CH_3CN)_6](BF_4)_2$ (0.0460 g, 0.0967 mmol) was added, resulting in a red solution. The reaction was stirred for one day and $Et_2O$ vapor was diffused into the reaction solution. Red X-ray quality crystals formed over the course of two days. Yield: 0.0223 g (37%). Analysis calculated (found) for $[\{Fe(TPMA)\}_2(bmtz)](BF_4)_3$ ($C_{46}H_{43}N_{16}B_3F_{12}Fe_2$): C: 46.35% (45.53%), H: 3.64% (3.61%), N: 18.80% (18.78%).

**[{Fe(TPMA)}$_2$-μ-bmtz](BF$_4$)$_4$•2CH$_3$CN.** Quantities of $[Fe(CH_3CN)_6](BF_4)_2$ (0.0260 g, 0.0546 mmol) and TPMA (0.0145 g, 0.0499 mmol) were stirred in $CH_3CN$ (5 mL) to give a clear, reddish solution. To this solution was added bmtz (0.0090 g, 0.038 mmol) in $CH_3CN$ (5 mL), which resulted in a slight color change to darker red with some solid bmtz being suspended in solution. The reaction was stirred overnight, filtered, and $Et_2O$ vapor was diffused into the filtrate to give blue X-ray quality crystals. This reaction was never repeated and no yield was ever obtained.

**[{Fe(TPMA)}$_2$-μ-bmtz$^{\bullet-}$](CF$_3$SO$_3$)$_3$•CH$_3$CN**. Quantities of $Cp_2Co$ (0.0094 g, 0.050 mmol) and bmtz (0.0250 g, 0.105 mmol) were stirred in $CH_3CN$ (5 mL) until the solution was orange. Solid TPMA (0.0290 g, 0.100 mmol) was then added to the solution and stirred until all of the TPMA dissolved, at which point solid $Fe(CF_3SO_3)_2$ (0.0340 g, 0.0961 mmol) was added to the reaction. The resulting red-orange solution was stirred overnight and then $Et_2O$ vapor was diffused into the reaction solution, which led to the formation of X-ray quality red crystals. Yield: 0.0149 g (20%). Analysis calculated (found) for [{Fe(TPMA)}$_2$(bmtz)](CF$_3$SO$_3$)$_3$•CH$_3$CN ($C_{51}H_{45}N_{17}O_9F_9S_3Fe_2$): C: 43.17% (42.47%), H: 3.20% (3.01%), N: 16.78% (16.94%).

**[{Fe(TPMA)}$_2$-μ-bmtz](CF$_3$SO$_3$)$_4$•4CH$_3$CN.** A quantity of $Fe(CF_3SO_3)_2$ (0.0170 g, 0.0480 mmol) was dissolved in $CH_3CN$ (5 mL) to give a clear, colorless solution. In a separate vessel, TPMA (0.0145 g, 0.0499 mmol) and bmtz (0.0130 g, 0.0546 mmol) were placed in $CH_3CN$ (5 mL) to produce a pink solution with solid bmtz present as a suspension. The two solutions were mixed to produce a green solution and then stirred for two days. Diffusion of $Et_2O$ vapor into the reaction solution produced blue X-ray quality crystals. Yield: 0.0292 g (72%). Analysis calculated (found) for [{Fe(TPMA)}$_2$(bmtz)](CF$_3$SO$_3$)$_4$•2CH$_3$CN ($C_{54}H_{48}N_{18}O_{12}F_{12}S_4Fe_2$): C: 40.31% (40.09%), H: 3.01% (2.94%), N: 15.67% (15.40%).

*X-ray Crystallographic Measurements*

Single crystal X-ray data were collected on a Bruker APEXII (Mo $K_\alpha$) diffractometer equipped with a CCD detector for all crystals. A suitable crystal was affixed to either a nylon loop or a MiTeGen® MicroLoop with Paratone® oil and placed

in a cold stream of $N_{2(g)}$ at 110 K. For the spin crossover complex [{Fe(TPMA)}$_2$-μ-bmtz$^{\bullet-}$]$(CF_3SO_3)_3$ data were also collected at 150 and 210 K. The frames were integrated with the Bruker APEXII software package[99] and a semi-empirical absorption correction was applied using SADABS as contained within the Bruker APEXII software suite. The structures were solved using SHELXT[100] and refined using SHELXL-2014[101] as implemented in ShelXle, a graphical interface for the SHELX suite of programs.[102] The remaining non-hydrogen atoms were located by alternating cycles of least-squares refinements and difference Fourier maps. All hydrogen atoms were placed in calculated positions. The final refinements were carried out with anisotropic thermal parameters for all non-hydrogen atoms except as otherwise noted. For [{Fe(TPMA)}$_2$-μ-bmtz$^{\bullet-}$]$(BF_4)_3$, one of the $[BF_4]^-$ anions and the $CH_3CN$ solvent molecule were found to be disordered about inversion centers and were modeled with a fixed 50% occupancy. For the crystal of [{Fe(TPMA)}$_2$-μ-bmtz$^{\bullet-}$]$(CF_3SO_3)_3$ measured at 110 K, one of the $[CF_3SO_3]^-$ anions and the $CH_3CN$ solvent molecule were found to be disordered about inversion centers and were modeled with a fixed 50% occupancy. For the crystal of [{Fe(TPMA)}$_2$-μ-bmtz$^{\bullet-}$]$(CF_3SO_3)_3$ measured at 150 K one of the $[CF_3SO_3]^-$ anions and the $CH_3CN$ solvent molecule were found disordered about inversion centers and were modeled with a fixed 50% occupancy. For the crystal of [{Fe(TPMA)}$_2$-μ-bmtz$^{\bullet-}$]$(CF_3SO_3)_3$ measured at 210 K the $CH_3CN$ solvent molecule was disordered about an inversion center and was modeled with a fixed 50% occupancy. One of the $[CF_3SO_3]^-$ anions was found to be disordered over two positions, both of which were further disordered about an inversion center. The occupancy of each position was set at 50% to

account for the inversion center and then the ratio of the two positions was allowed to freely refine. Similarity restraints of the thermal parameters were required for the disordered $[CF_3SO_3]^-$ anion to achieve a satisfactory convergence of the site occupancy ratio. Convergence was reached with a ratio of 0.38:0.62 between the two positions. Further pertinent details of the X-ray refinements are given in Table 2.

**Table 2.** Crystal and structural refinement data for $Fe^{II}$ bmtz complexes.

| | | |
|---|---|---|
| Identification code | $[\{Fe(TPMA)\}_2bmtz](BF_4)_3$ | $[\{Fe(TPMA)\}_2bmtz](BF_4)_4$ |
| Empirical formula | $C_{48}H_{45}B_3N_{17}F_{12}Fe_2$ | $C_{50}H_{48}B_4N_{18}F_{16}Fe_2$ |
| Formula weight | 1232.14 | 1360.00 |
| Temperature/K | 110.15 | 110.15 |
| Crystal system | triclinic | triclinic |
| Space group | P-1 | P-1 |
| a/Å | 8.442(4) | 9.372(3) |
| b/Å | 9.963(5) | 10.372(4) |
| c/Å | 16.198(8) | 14.914(5) |
| α/° | 92.966(7) | 74.431(4) |
| β/° | 97.599(7) | 85.362(5) |
| γ/° | 101.206(7) | 78.273(5) |
| Volume/$Å^3$ | 1320.4(12) | 1366.8(9) |
| Z | 1 | 1 |
| $\varrho_{calc}g/cm^3$ | 1.550 | 1.652 |
| $\mu/mm^{-1}$ | 0.646 | 0.643 |
| F(000) | 627.0 | 690.0 |
| Crystal size/$mm^3$ | | 0.23 × 0.048 × 0.03 |
| Radiation | MoKα (λ = 0.71073 Å) | MoKα (λ = 0.71073 Å) |
| 2Θ range for data collection/° | 2.544 to 43.93 | 4.152 to 49.62 |
| Index ranges | $-8 \le h \le 8, -10 \le k \le 10, -17 \le l \le 17$ | $-11 \le h \le 10, -12 \le k \le 12, -17 \le l \le 17$ |
| Reflections collected | 9525 | 12759 |
| Independent reflections | 3221 [$R_{int}$ = 0.0534, $R_{sigma}$ = 0.0611] | 4650 [$R_{int}$ = 0.0585, $R_{sigma}$ = 0.0750] |
| Data/restraints/parameters | 3221/10/407 | 4650/0/407 |
| Goodness-of-fit on $F^2$ [c] | 1.100 | 0.967 |
| Final R indexes [I>=2σ (I)] | $R_1$[a] = 0.0622, $wR_2$[b] = 0.1500 | $R_1$[a] = 0.0476, $wR_2$[b] = 0.1031 |
| Final R indexes [all data] | $R_1$[a] = 0.0822, $wR_2$[b] = 0.1625 | $R_1$[a] = 0.0766, $wR_2$[b] = 0.1176 |
| Largest diff. peak/hole / e $Å^{-3}$ | 1.67/-0.28 | 0.48/-0.39 |

**Table 2** Continued

| | | |
|---|---|---|
| Identification code | $[\{Fe(TPMA)\}_2bmtz](CF_3SO_3)_3$ | $[\{Fe(TPMA)\}_2bmtz](CF_3SO_3)_3$ |
| Empirical formula | $C_{51}H_{44}N_{17}O_9F_9S_3Fe_2$ | $C_{51}H_{45}N_{17}O_9F_9S_3Fe_2$ |
| Formula weight | 1417.91 | 1418.92 |
| Temperature/K | 110.15 | 150.0 |
| Crystal system | triclinic | triclinic |
| Space group | P-1 | P-1 |
| a/Å | 8.592(8) | 8.666(3) |
| b/Å | 10.373(10) | 10.328(3) |
| c/Å | 16.974(16) | 17.061(5) |
| α/° | 88.534(11) | 88.606(4) |
| β/° | 80.818(11) | 80.521(4) |
| γ/° | 78.526(11) | 78.909(4) |
| Volume/$Å^3$ | 1464(2) | 1478.0(7) |
| Z | 1 | 1 |
| $\varrho_{calc}g/cm^3$ | 1.609 | 1.594 |
| $\mu/mm^{-1}$ | 0.702 | 0.696 |
| F(000) | 722.0 | 723.0 |
| Crystal size/$mm^3$ | 1.6 × 0.106 × 0.02 | 0.176 × 0.133 × 0.032 |
| Radiation | MoKα (λ = 0.71073 Å) | MoKα (λ = 0.71073 Å) |
| 2Θ range for data collection/° | 2.43 to 44.04 | 4.018 to 50.228 |
| Index ranges | $-9 \le h \le 9, -10 \le k \le 10, -17 \le l \le 16$ | $-10 \le h \le 10, -12 \le k \le 12, -20 \le l \le 20$ |
| Reflections collected | 8103 | 14481 |
| Independent reflections | 3548 [$R_{int} = 0.0557$, $R_{sigma} = 0.0769$] | 5236 [$R_{int} = 0.0465$, $R_{sigma} = 0.0579$] |
| Data/restraints/parameters | 3548/19/460 | 5236/19/461 |
| Goodness-of-fit on $F^{2\ c}$ | 1.100 | 1.045 |
| Final R indexes [I>=2σ (I)] | $R_1{}^a = 0.0647$, $wR_2{}^b = 0.1767$ | $R_1{}^a = 0.0471$, $wR_2{}^b = 0.1073$ |
| Final R indexes [all data] | $R_1{}^a = 0.0935$, $wR_2{}^b = 0.1929$ | $R_1{}^a = 0.0760$, $wR_2{}^b = 0.1204$ |
| Largest diff. peak/hole / e $Å^{-3}$ | 0.76/-0.55 | 0.82/-0.39 |

**Table 2** Continued

| Identification code | [{Fe(TPMA)}$_2$bmtz](CF$_3$SO$_3$)$_3$ | [{Fe(TPMA)}$_2$bmtz](CF$_3$SO$_3$)$_4$ |
|---|---|---|
| Empirical formula | $C_{51}H_{45}N_{17}O_9F_9S_3Fe_2$ | $C_{58}H_{54}N_{20}O_{12}F_{12}S_4Fe_2$ |
| Formula weight | 1418.92 | 1691.14 |
| Temperature/K | 210.0 | 110.15 |
| Crystal system | triclinic | monoclinic |
| Space group | P-1 | $P2_1/n$ |
| a/Å | 8.728(4) | 14.327(2) |
| b/Å | 10.402(5) | 17.238(3) |
| c/Å | 16.954(8) | 14.900(2) |
| α/° | 88.417(7) | 90 |
| β/° | 80.275(7) | 110.813(2) |
| γ/° | 78.758(7) | 90 |
| Volume/Å$^3$ | 1488.0(13) | 3439.7(9) |
| Z | 1 | 2 |
| $\varrho_{calc}$g/cm$^3$ | 1.583 | 1.6327 |
| μ/mm$^{-1}$ | 0.691 | 0.652 |
| F(000) | 723.0 | 1727.4 |
| Crystal size/mm$^3$ | 0.12 × 0.103 × 0.02 | |
| Radiation | MoKα (λ = 0.71073 Å) | Mo Kα (λ = 0.71073 Å) |
| 2Θ range for data collection/° | 3.992 to 46.55 | 3.38 to 51.26 |
| Index ranges | -9 ≤ h ≤ 9, -11 ≤ k ≤ 11, -18 ≤ l ≤ 18 | -17 ≤ h ≤ 17, -20 ≤ k ≤ 20, -18 ≤ l ≤ 18 |
| Reflections collected | 12508 | 34116 |
| Independent reflections | 4291 [$R_{int}$ = 0.0717, $R_{sigma}$ = 0.0860] | 6472 [$R_{int}$ = 0.0422, $R_{sigma}$ = 0.0326] |
| Data/restraints/parameters | 4291/57/462 | 6472/0/488 |
| Goodness-of-fit on F$^{2\ c}$ | 0.996 | 1.040 |
| Final R indexes [I>=2σ (I)] | $R_1{}^a$ = 0.0530, $wR_2{}^b$ = 0.1063 | $R_1{}^a$ = 0.0412, $wR_2{}^b$ = 0.0900 |
| Final R indexes [all data] | $R_1{}^a$ = 0.0932, $wR_2{}^b$ = 0.1239 | $R_1{}^a$ = 0.0539, $wR_2{}^b$ = 0.0987 |
| Largest diff. peak/hole / e Å$^{-3}$ | 0.39/-0.30 | 1.05/-0.75 |

$^a R_1 = \Sigma \big| \, |F_o| - |F_c| \, \big| / \Sigma |F_o|$. $^b wR_2 = \{\Sigma [w(F_o^2 - F_c^2)^2] / \Sigma w(F_o^2)^2]\}^{1/2}$. $^c$Goodness-of-fit $= \{\Sigma [w(F_o^2 - F_c^2)^2]/(n-p)\}^{1/2}$, where $n$ is the number of reflections and $p$ is the total number of parameters refined.

## Results and Discussion

*Syntheses*

As a general note, the syntheses of all of the dinuclear bmtz complexes presented herein were performed with an excess of bmtz. Stoichiometric amounts led to similar color changes throughout the course of the reaction but little to no crystalline product was obtained from the reaction.

**[{Fe(TPMA)}$_2$-μ-bmtz$^{\bullet-}$](BF$_4$)$_3$•CH$_3$CN.** Unlike the $Co^{II}$ and $Ni^{II}$ analogs, no spontaneous reduction of bmtz was observed. The product was isolated from a reaction of *in situ* generated [Fe(TPMA)(solv)$_x$](BF$_4$)$_2$ with the neutral form of bmtz in the presence of $Cp_2Co$.

**[{Fe(TPMA)}$_2$-μ-bmtz](BF$_4$)$_4$•2CH$_3$CN.** This compound was prepared by reacting a solution of *in situ* generated [Fe(TPMA)(solv)$_x$](BF$_4$)$_2$ with the neutral form of bmtz.

**[{Fe(TPMA)}$_2$-μ-bmtz$^{\bullet-}$](CF$_3$SO$_3$)$_3$•CH$_3$CN.** This compound was prepared by reacting a solution of *in situ* generated [Fe(TPMA)(solv)$_x$](CF$_3$SO$_3$)$_2$ with the neutral form of bmtz in the presence of $Cp_2Co$.

**[{Fe(TPMA)}$_2$-μ-bmtz](CF$_3$SO$_3$)$_4$•4CH$_3$CN.** This compound was prepared by reacting a solution of *in situ* generated [Fe(TPMA)(solv)$_x$](CF$_3$SO$_3$)$_2$ with the neutral form of bmtz.

*Single Crystal X-ray Diffraction*

**[{Fe(TPMA)}$_2$-μ-bmtz$^{\bullet-}$](BF$_4$)$_3$•CH$_3$CN.** The cationic unit of [{Fe(TPMA)}$_2$-μ-bmtz$^{\bullet-}$](BF$_4$)$_3$ consists of two $[Fe(TPMA)]^{2+}$ fragments bridged by a bmtz ligand in the radical anion form. Only one of the $Fe^{II}$ ions is crystallographically unique and resides in a

distorted octahedral coordination environment. The geometrical constraints of the ligand lead to $N_{py}$-Fe-$N_{amine}$ angles for the $[Fe(TPMA)]^{2+}$ fragment in the range 74.47(19) - 77.80(19)°, much more acute than the expected 90° angles for an ideal octahedral coordination geometry. The Fe-N bond lengths also vary significantly from 2.055(5) to 2.294(5) Å. This distortion is best described as a meridional elongation in which the Fe1-N1, Fe1-N3, and Fe1-N7 bonds form one meridian of the octahedron spanning from the bmtz pyrimidine ring to the bridgehead amine N atom of TPMA and one of the pyridine rings of TPMA with an average bond length of 2.26 Å. The Fe1-N2, Fe1-N4, and Fe1-N5 bonds form the other meridian of the octahedron with an average bond length of 2.12 Å.

Evidence for the radical anion oxidation state of the bmtz ligand was gleaned from the tetrazine N-N bond lengths. At 1.392(7) Å, the N5-N6 distance is consistent with previous reports of the radical anion state of bmtz and significantly longer than the 1.33 Å expected for the neutral form of the ligand.[92] In addition, charge balance requires the cationic framework to have a 3+ charge, consistent with two $Fe^{II}$ centers and one ligand radical. The thermal ellipsoid plot of $[\{Fe(TPMA)\}_2$-μ-$bmtz^{\bullet-}](BF_4)_3$ is displayed in Figure 9 and Table 3 contains a compilation of bond distances and angles.

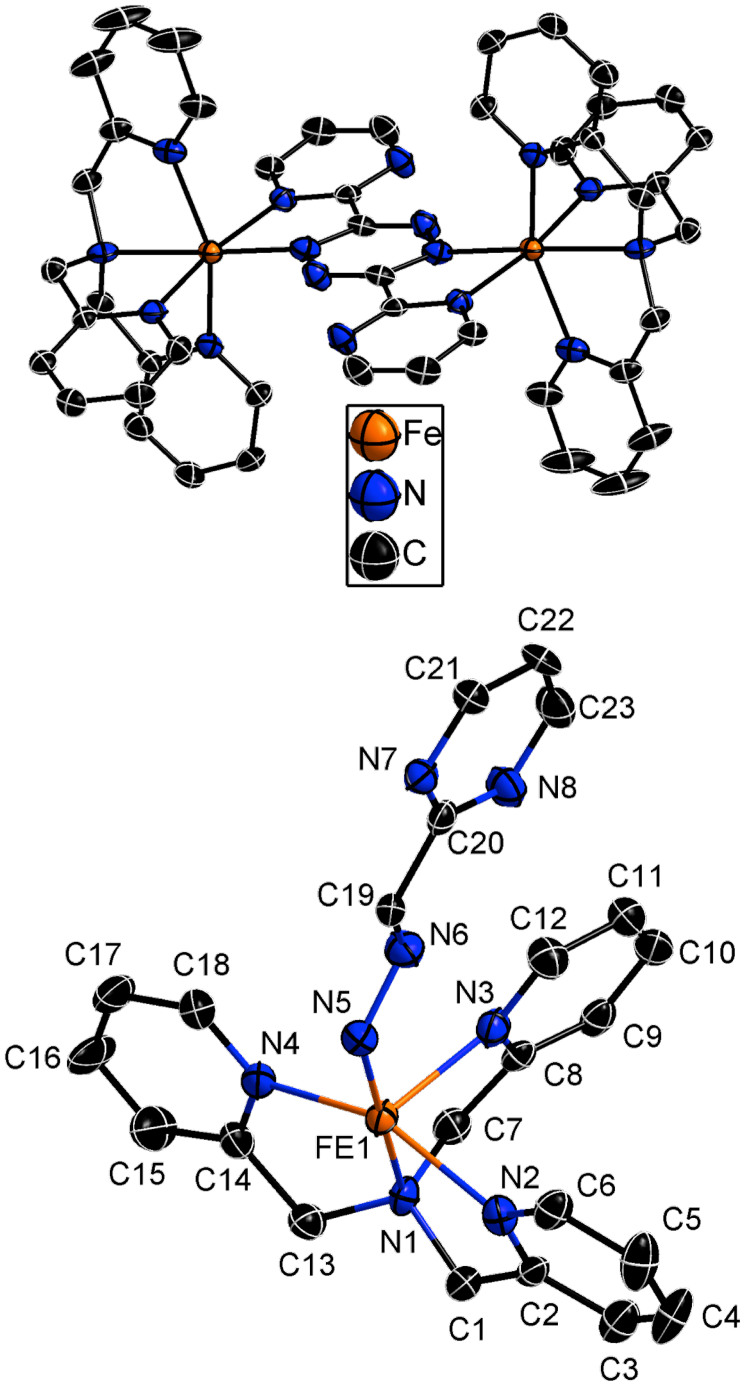


**Figure 9.** Thermal ellipsoid plot and atom numbering scheme of the asymmetric unit for the cationic unit of $[\{Fe(TPMA)\}_2\text{-}\mu\text{-}bmtz^{\bullet-}](BF_4)_3$. Thermal ellipsoids are drawn at the 50% probability level. H atoms were omitted for the sake of clarity.

**Table 3.** Bond distances and angles for [{Fe(TPMA)}$_2$-μ-bmtz$^{\bullet-}$](BF$_4$)$_3$.

| Atom | Atom | Length/Å | Atom | Atom | Length/Å |
|---|---|---|---|---|---|
| Fe1 | N1 | 2.268(5) | N7 | C21 | 1.332(8) |
| Fe1 | N2 | 2.155(5) | C8 | C9 | 1.380(9) |
| Fe1 | N3 | 2.202(5) | N8 | C20 | 1.333(8) |
| Fe1 | N4 | 2.146(5) | N8 | C23 | 1.342(8) |
| Fe1 | N5 | 2.055(5) | C9 | C10 | 1.385(9) |
| Fe1 | N7[1] | 2.294(5) | C10 | C11 | 1.364(9) |
| N1 | C1 | 1.475(8) | C11 | C12 | 1.378(9) |
| N1 | C7 | 1.490(8) | C15 | C14 | 1.373(9) |
| N1 | C13 | 1.487(8) | C15 | C16 | 1.361(11) |
| C1 | C2 | 1.505(9) | C14 | C13 | 1.498(9) |
| N2 | C2 | 1.349(7) | C16 | C17 | 1.358(11) |
| N2 | C6 | 1.350(8) | C17 | C18 | 1.375(10) |
| C2 | C3 | 1.384(9) | C19 | N5[1] | 1.363(8) |
| N3 | C8 | 1.350(8) | C19 | C20 | 1.482(9) |
| N3 | C12 | 1.349(8) | C21 | C22 | 1.381(9) |
| C3 | C4 | 1.366(10) | C22 | C23 | 1.372(9) |
| N4 | C14 | 1.360(8) | B1 | F1 | 1.379(9) |
| N4 | C18 | 1.329(8) | B1 | F2 | 1.359(8) |
| C4 | C5 | 1.362(10) | B1 | F3 | 1.410(8) |
| N5 | N6 | 1.392(7) | B1 | F4 | 1.381(9) |
| N5 | C19[1] | 1.363(8) | N9 | C24 | 1.122(19) |
| C5 | C6 | 1.392(9) | C24 | C25 | 1.47(2) |
| N6 | C19 | 1.301(8) | B3 | F5 | 1.365(19) |
| C7 | C8 | 1.503(9) | B3 | F6 | 1.372(15) |
| N7 | Fe1[1] | 2.294(5) | B3 | F7 | 1.398(14) |
| N7 | C20 | 1.336(8) | B3 | F8 | 1.375(19) |

[1]1-X, 1-Y, 1-Z

| Atom | Atom | Atom | Angle/° | Atom | Atom | Atom | Angle/° |
|---|---|---|---|---|---|---|---|
| N1 | Fe1 | N7[1] | 108.58(18) | N1 | C7 | C8 | 113.6(5) |
| N2 | Fe1 | N1 | 77.22(18) | C20 | N7 | Fe1[1] | 113.7(4) |
| N2 | Fe1 | N3 | 85.02(19) | C21 | N7 | Fe1[1] | 130.5(4) |

**Table 3** Continued

| Atom | Atom | Atom | Angle/° | Atom | Atom | Atom | Angle/° |
|---|---|---|---|---|---|---|---|
| N2 | Fe1 | N7[1] | 92.13(18) | C21 | N7 | C20 | 115.4(5) |
| N3 | Fe1 | N1 | 77.80(19) | N3 | C8 | C7 | 116.7(5) |
| N3 | Fe1 | N7[1] | 172.30(19) | N3 | C8 | C9 | 122.5(6) |
| N4 | Fe1 | N1 | 74.47(19) | C9 | C8 | C7 | 120.7(6) |
| N4 | Fe1 | N2 | 149.5(2) | C20 | N8 | C23 | 115.2(6) |
| N4 | Fe1 | N3 | 99.84(19) | C8 | C9 | C10 | 119.2(6) |
| N4 | Fe1 | N7[1] | 86.24(19) | C11 | C10 | C9 | 118.8(6) |
| N5 | Fe1 | N1 | 175.8(2) | C10 | C11 | C12 | 119.5(6) |
| N5 | Fe1 | N2 | 106.0(2) | N3 | C12 | C11 | 122.8(6) |
| N5 | Fe1 | N3 | 99.7(2) | C16 | C15 | C14 | 119.9(7) |
| N5 | Fe1 | N4 | 102.8(2) | N4 | C14 | C15 | 120.8(6) |
| N5 | Fe1 | N7[1] | 74.16(19) | N4 | C14 | C13 | 116.5(5) |
| C1 | N1 | Fe1 | 108.5(4) | C15 | C14 | C13 | 122.6(6) |
| C1 | N1 | C7 | 112.6(5) | N1 | C13 | C14 | 110.0(5) |
| C1 | N1 | C13 | 111.7(5) | C17 | C16 | C15 | 119.1(7) |
| C7 | N1 | Fe1 | 107.4(4) | C16 | C17 | C18 | 119.7(7) |
| C13 | N1 | Fe1 | 107.8(4) | N4 | C18 | C17 | 121.8(7) |
| C13 | N1 | C7 | 108.7(5) | N5[1] | C19 | C20 | 114.4(6) |
| N1 | C1 | C2 | 112.8(5) | N6 | C19 | N5[1] | 127.8(6) |
| C2 | N2 | Fe1 | 117.1(4) | N6 | C19 | C20 | 117.7(6) |
| C2 | N2 | C6 | 118.5(5) | N7 | C20 | C19 | 115.7(6) |
| C6 | N2 | Fe1 | 123.2(4) | N8 | C20 | N7 | 127.3(6) |
| N2 | C2 | C1 | 115.3(5) | N8 | C20 | C19 | 117.0(6) |
| N2 | C2 | C3 | 121.6(6) | N7 | C21 | C22 | 122.6(6) |
| C3 | C2 | C1 | 122.8(6) | C23 | C22 | C21 | 116.7(6) |
| C8 | N3 | Fe1 | 115.2(4) | N8 | C23 | C22 | 122.7(6) |
| C12 | N3 | Fe1 | 126.8(4) | F1 | B1 | F3 | 108.1(6) |
| C12 | N3 | C8 | 117.2(6) | F1 | B1 | F4 | 109.2(6) |
| C4 | C3 | C2 | 119.2(7) | F2 | B1 | F1 | 110.6(6) |
| C14 | N4 | Fe1 | 117.3(4) | F2 | B1 | F3 | 108.1(5) |
| C18 | N4 | Fe1 | 123.8(5) | F2 | B1 | F4 | 112.1(6) |
| C18 | N4 | C14 | 118.6(6) | F4 | B1 | F3 | 108.5(5) |
| C5 | C4 | C3 | 120.2(6) | N9 | C24 | C25 | 177(2) |

**Table 3** Continued

| Atom | Atom | Atom | Angle/° | Atom | Atom | Atom | Angle/° |
|---|---|---|---|---|---|---|---|
| N6 | N5 | Fe1 | 123.0(4) | F5 | B3 | F6 | 108.5(14) |
| C19[1] | N5 | Fe1 | 121.5(4) | F5 | B3 | F7 | 109.4(14) |
| C19[1] | N5 | N6 | 115.3(5) | F5 | B3 | F8 | 111.7(17) |
| C4 | C5 | C6 | 118.7(6) | F6 | B3 | F7 | 107.1(12) |
| N2 | C6 | C5 | 121.8(6) | F6 | B3 | F8 | 109.5(14) |
| C19 | N6 | N5 | 116.9(5) | F8 | B3 | F7 | 110.5(14) |

[1]1-X, 1-Y, 1-Z

**[{Fe(TPMA)}$_2$-μ-bmtz](BF$_4$)$_4$•2CH$_3$CN.** The cationic unit of [{Fe(TPMA)}$_2$-μ-bmtz](BF$_4$)$_4$ consists of two $[Fe(TPMA)]^{2+}$ fragments bridged by a bmtz ligand in the neutral form. Only one of the Fe ions is crystallographically unique and resides in a distorted octahedral coordination environment. The geometrical constraints of the ligand lead to $N_{py}$-Fe-$N_{amine}$ angles for the $[Fe(TPMA)]^{2+}$ fragment in the range 81.06(12) – 84.49(12)°, much more acute than the expected 90° angles for an ideal octahedral coordination geometry. The Fe-N bond lengths also vary significantly from 1.877(3) to 2.025(3) Å. This distortion is best described as a trigonal or facial distortion in which the Fe1-N1, Fe1-N2, and Fe1-N5 bonds form one face of the octahedron spanning from the bmtz tetrazine ring to the bridgehead amine N atom of TPMA and one of the pyridine rings of TPMA with an average bond length of 1.94 Å. The Fe1-N3, Fe1-N4, and Fe1-N7a bonds comprise the other face of the octahedron with an average bond length of 2.01 Å.

Evidence for the neutral oxidation state of the bmtz ligand is derived from the tetrazine N-N bond lengths. At 1.356(4) Å, the N5-N6 distance is much shorter than that observed in the radical form of bmtz and is consistent with previous reports of the neutral form.[92] In addition, charge balance requires the cationic framework to have a 4+ charge, consistent with two $Fe^{II}$ centers and one neutral ligand. The thermal ellipsoid plot of $[\{Fe(TPMA)\}_2\text{-}\mu\text{-}bmtz^{\bullet-}](BF_4)_4$ is displayed in Figure 10 and Table 4 lists bond distances and angles.

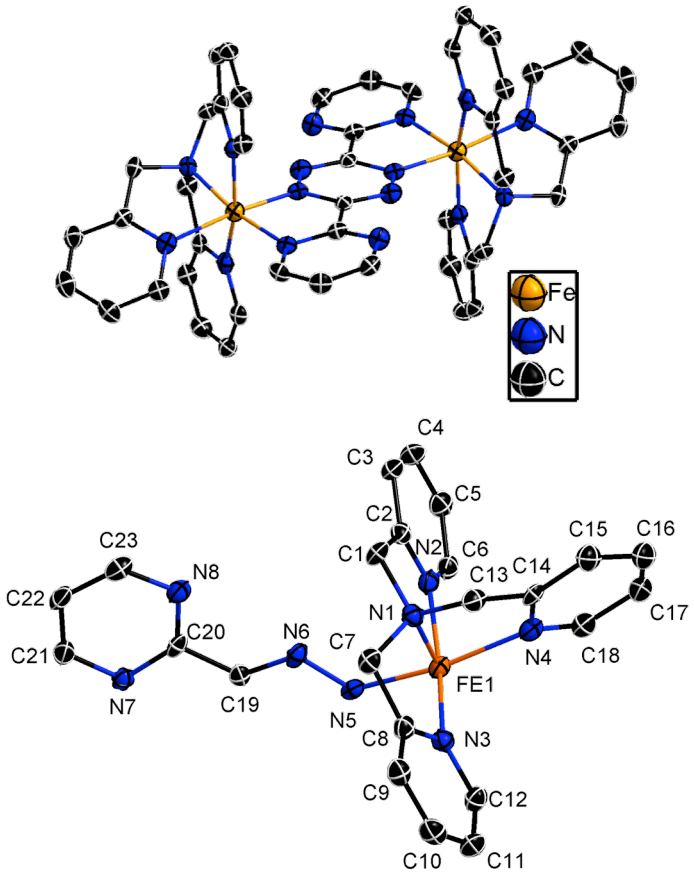


**Figure 10.** Thermal ellipsoid plot and atom numbering scheme of the asymmetric unit for the cationic unit of $[\{Fe(TPMA)\}_2\text{-}\mu\text{-}bmtz^{\bullet-}](BF_4)_4$. Thermal ellipsoids are drawn at the 50% probability level. H atoms were omitted for the sake of clarity.

**Table 4.** Bond distances and angles for [{Fe(TPMA)}$_2$-μ-bmtz$^{\bullet-}$](BF$_4$)$_4$.

| Atom | Atom | Length/Å | Atom | Atom | Length/Å |
|---|---|---|---|---|---|
| Fe1 | N1 | 1.981(3) | C4 | C5 | 1.374(5) |
| Fe1 | N2 | 1.967(3) | N5 | N6 | 1.356(4) |
| Fe1 | N3 | 2.001(3) | N5 | C19[1] | 1.354(4) |
| Fe1 | N4 | 2.025(3) | C5 | C6 | 1.384(5) |
| Fe1 | N5 | 1.877(3) | N6 | C19 | 1.313(4) |
| Fe1 | N7[1] | 2.014(3) | N7 | Fe1[1] | 2.014(3) |
| F1 | B1 | 1.375(5) | N7 | C20 | 1.361(4) |
| B1 | F2 | 1.397(5) | N7 | C21 | 1.357(4) |
| B1 | F3 | 1.384(5) | C7 | C8 | 1.499(5) |
| B1 | F4 | 1.388(5) | N8 | C20 | 1.322(4) |
| N1 | C1 | 1.491(4) | N8 | C23 | 1.336(4) |
| N1 | C7 | 1.501(4) | C8 | C9 | 1.381(5) |
| N1 | C13 | 1.499(4) | N9 | C24 | 1.140(7) |
| C1 | C2 | 1.496(5) | C9 | C10 | 1.369(5) |
| B2 | F5 | 1.392(5) | C10 | C11 | 1.381(5) |
| B2 | F6 | 1.376(5) | C11 | C12 | 1.373(5) |
| B2 | F7 | 1.372(5) | C14 | C13 | 1.476(5) |
| B2 | F8 | 1.396(5) | C14 | C15 | 1.374(5) |
| N2 | C2 | 1.357(4) | C15 | C16 | 1.382(5) |
| N2 | C6 | 1.345(4) | C16 | C17 | 1.371(6) |
| C2 | C3 | 1.382(5) | C17 | C18 | 1.378(5) |
| N3 | C8 | 1.364(4) | C19 | N5[1] | 1.354(4) |
| N3 | C12 | 1.342(4) | C19 | C20 | 1.459(5) |
| C3 | C4 | 1.381(5) | C21 | C22 | 1.366(5) |
| N4 | C14 | 1.346(4) | C22 | C23 | 1.368(5) |
| N4 | C18 | 1.348(4) | C24 | C25 | 1.457(8) |

[1]1-X, 1-Y, 1-Z

| Atom | Atom | Atom | Angle/° | Atom | Atom | Atom | Angle/° |
|---|---|---|---|---|---|---|---|
| N1 | Fe1 | N3 | 81.06(12) | C12 | N3 | C8 | 117.1(3) |
| N1 | Fe1 | N4 | 83.51(12) | C4 | C3 | C2 | 119.7(3) |
| N1 | Fe1 | N7[1] | 169.63(11) | C14 | N4 | Fe1 | 113.5(2) |

**Table 4** Continued

| Atom | Atom | Atom | Angle/° | Atom | Atom | Atom | Angle/° |
|---|---|---|---|---|---|---|---|
| N2 | Fe1 | N1 | 84.49(12) | C14 | N4 | C18 | 117.2(3) |
| N2 | Fe1 | N3 | 165.54(12) | C18 | N4 | Fe1 | 128.1(2) |
| N2 | Fe1 | N4 | 82.59(12) | C5 | C4 | C3 | 119.2(3) |
| N2 | Fe1 | N7[1] | 105.29(12) | N6 | N5 | Fe1 | 124.8(2) |
| N3 | Fe1 | N4 | 96.16(12) | C19[1] | N5 | Fe1 | 118.4(2) |
| N3 | Fe1 | N7[1] | 89.12(11) | C19[1] | N5 | N6 | 116.5(3) |
| N5 | Fe1 | N1 | 96.27(12) | C4 | C5 | C6 | 119.0(3) |
| N5 | Fe1 | N2 | 87.75(12) | C19 | N6 | N5 | 117.4(3) |
| N5 | Fe1 | N3 | 93.36(12) | N2 | C6 | C5 | 122.3(3) |
| N5 | Fe1 | N4 | 170.32(12) | C20 | N7 | Fe1[1] | 113.5(2) |
| N5 | Fe1 | N7[1] | 80.91(12) | C21 | N7 | Fe1[1] | 131.7(2) |
| N7[1] | Fe1 | N4 | 100.95(12) | C21 | N7 | C20 | 113.6(3) |
| F1 | B1 | F2 | 109.0(3) | C8 | C7 | N1 | 106.9(3) |
| F1 | B1 | F3 | 110.2(3) | C20 | N8 | C23 | 114.9(3) |
| F1 | B1 | F4 | 109.2(3) | N3 | C8 | C7 | 114.4(3) |
| F3 | B1 | F2 | 109.1(3) | N3 | C8 | C9 | 121.7(3) |
| F3 | B1 | F4 | 109.2(3) | C9 | C8 | C7 | 123.9(3) |
| F4 | B1 | F2 | 110.1(3) | C10 | C9 | C8 | 119.9(4) |
| C1 | N1 | Fe1 | 109.4(2) | C9 | C10 | C11 | 119.0(3) |
| C1 | N1 | C7 | 113.3(3) | C12 | C11 | C10 | 118.6(4) |
| C1 | N1 | C13 | 111.9(3) | N4 | C14 | C13 | 115.2(3) |
| C7 | N1 | Fe1 | 106.2(2) | N4 | C14 | C15 | 122.5(3) |
| C13 | N1 | Fe1 | 108.9(2) | C15 | C14 | C13 | 122.3(3) |
| C13 | N1 | C7 | 106.9(3) | C14 | C13 | N1 | 111.2(3) |
| N1 | C1 | C2 | 109.9(3) | N3 | C12 | C11 | 123.7(4) |
| F5 | B2 | F8 | 107.9(4) | C14 | C15 | C16 | 120.0(4) |
| F6 | B2 | F5 | 108.2(4) | C17 | C16 | C15 | 117.7(4) |
| F6 | B2 | F8 | 108.9(4) | C16 | C17 | C18 | 119.9(4) |
| F7 | B2 | F5 | 111.3(4) | N4 | C18 | C17 | 122.6(4) |
| F7 | B2 | F6 | 111.3(4) | N5[1] | C19 | C20 | 113.5(3) |
| F7 | B2 | F8 | 109.1(4) | N6 | C19 | N5[1] | 126.1(3) |
| C2 | N2 | Fe1 | 113.6(2) | N6 | C19 | C20 | 120.3(3) |
| C6 | N2 | Fe1 | 127.7(2) | N7 | C20 | C19 | 112.6(3) |

**Table 4** Continued

| Atom | Atom | Atom | Angle/° | Atom | Atom | Atom | Angle/° |
|---|---|---|---|---|---|---|---|
| C6 | N2 | C2 | 118.6(3) | N8 | C20 | N7 | 128.4(3) |
| N2 | C2 | C1 | 116.3(3) | N8 | C20 | C19 | 119.0(3) |
| N2 | C2 | C3 | 121.2(3) | N7 | C21 | C22 | 122.3(3) |
| C3 | C2 | C1 | 122.5(3) | C21 | C22 | C23 | 118.1(3) |
| C8 | N3 | Fe1 | 112.8(2) | N8 | C23 | C22 | 122.7(3) |
| C12 | N3 | Fe1 | 130.1(2) | N9 | C24 | C25 | 177.9(5) |

[1]1-X, 1-Y, 1-Z

**[{Fe(TPMA)}$_2$-μ-bmtz$^{\bullet-}$](CF$_3$SO$_3$)$_3$•CH$_3$CN.** The cationic unit of [{Fe(TPMA)}$_2$-μ-bmtz$^{\bullet-}$](CF$_3$SO$_3$)$_3$ consists of two [Fe(TPMA)]$^{2+}$ fragments bridged by a bmtz ligand in the radical anion form. Only one of the Fe ions is crystallographically unique and resides in a distorted octahedral coordination environment that exhibits no major changes over the 110 – 210 K temperature range investigated. The geometrical constraints of the ligand lead to an average $N_{py}$-Fe-$N_{amine}$ angle for the [Fe(TPMA)]$^{2+}$ fragment of 76.4°, which is more acute than the expected 90° angles for an ideal octahedral coordination geometry. Table 5 lists the key bond lengths for the three temperatures that were investigated.

**Table 5.** Variation of pertinent bond lengths for $[\{Fe(TPMA)\}_2\text{-}\mu\text{-}bmtz^{\bullet-}](CF_3SO_3)_3$ across the temperature range investigated.

| | **110 K** | **150 K** | **210 K** |
|---|---|---|---|
| TZ N-N[a] | 1.382(8) Å | 1.386(4) Å | 1.387(5) Å |
| Fe-$N_{py}$[b] | 2.17 Å | 2.17 Å | 2.16 Å |
| Fe-$N_{tz}$[c] | 2.066(6) Å | 2.078(3) Å | 2.058(4) Å |
| Fe-$N_{pm}$[d] | 2.233(7) Å | 2.255(3) Å | 2.247(4) Å |
| Fe-$N_{am}$[e] | 2.263(6) Å | 2.260(3) Å | 2.244(4) Å |

[a] Tetrazine N-N distance.
[b] Average bond distance between Fe and the TPMA pyridine N atoms.
[c] Bond distance between Fe and the tetrazine N atom of bmtz.
[d] Bond distance between Fe and the pyrimidine N atom of bmtz.
[e] Bond distance between Fe and the bridgehead amine N atom of TPMA.

Evidence for the radical anion oxidation state of the bmtz ligand is found in the tetrazine N-N bond lengths. At an average of 1.385 Å, the tetrazine N-N distance is consistent with previous reports of the radical anion state of bmtz and significantly longer than the 1.33 Å expected for the neutral form of the ligand.[92] In addition, charge balance requires the cationic framework to have a 3+ charge, consistent with two $Fe^{II}$ centers and one ligand radical. The thermal ellipsoid plot of $[\{Fe(TPMA)\}_2\text{-}\mu\text{-}bmtz^{\bullet-}](CF_3SO_3)_3$ at 110 K is displayed in Figure 11 and Table 6 lists bond distances and angles.

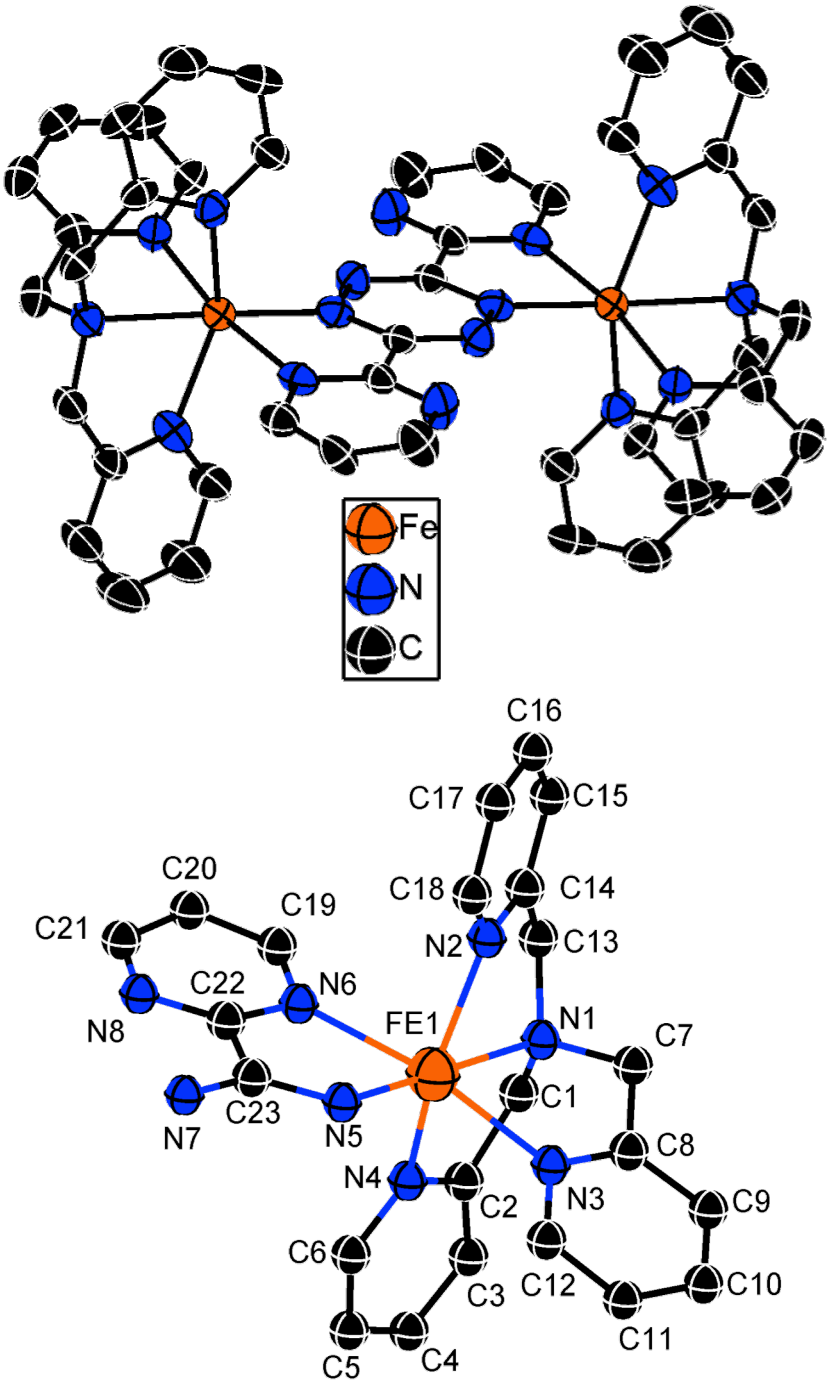


**Figure 11.** Thermal ellipsoid plot and atom numbering scheme of the asymmetric unit for the cationic unit of $[\{Fe(TPMA)\}_2\text{-}\mu\text{-}bmtz^{\bullet-}](CF_3SO_3)_3$. Thermal ellipsoids are drawn at the 50% probability level. H atoms were omitted for the sake of clarity.

**Table 6.** Bond distances and angles for [{Fe(TPMA)}$_2$-μ-bmtz$^{\bullet-}$](CF$_3$SO$_3$)$_3$ at 110 K.

| Atom | Atom | Length/Å | Atom | Atom | Length/Å |
|---|---|---|---|---|---|
| Fe1 | N1 | 2.263(6) | N6 | C19 | 1.354(10) |
| Fe1 | N2 | 2.146(6) | N6 | C22 | 1.353(9) |
| Fe1 | N4 | 2.155(6) | C7 | C8 | 1.495(11) |
| Fe1 | N3 | 2.194(7) | N7 | N5[1] | 1.382(8) |
| Fe1 | N5 | 2.066(6) | N7 | C23 | 1.310(9) |
| Fe1 | N6 | 2.233(7) | N8 | C21 | 1.321(10) |
| N1 | C1 | 1.471(9) | N8 | C22 | 1.302(10) |
| N1 | C7 | 1.483(9) | C8 | C9 | 1.411(11) |
| N1 | C13 | 1.469(9) | C9 | C10 | 1.368(11) |
| C1 | C2 | 1.504(11) | C10 | C11 | 1.374(11) |
| N2 | C14 | 1.332(10) | C12 | C11 | 1.392(11) |
| N2 | C18 | 1.369(10) | C15 | C14 | 1.371(11) |
| C2 | N4 | 1.339(10) | C15 | C16 | 1.395(12) |
| C2 | C3 | 1.391(11) | C14 | C13 | 1.493(11) |
| N4 | C6 | 1.334(9) | C16 | C17 | 1.362(13) |
| C4 | C3 | 1.374(12) | C17 | C18 | 1.376(12) |
| C4 | C5 | 1.374(13) | C19 | C20 | 1.362(11) |
| N3 | C8 | 1.337(10) | C20 | C21 | 1.367(11) |
| N3 | C12 | 1.354(10) | C22 | C23 | 1.490(11) |
| F1A | C1A | 1.326(9) | C26 | N1B | 1.34(3) |
| F2A | C1A | 1.356(9) | C26 | C24 | 1.43(3) |
| F3A | C1A | 1.337(9) | F1B | C1B | 1.324(10) |
| C1A | S1A | 1.793(8) | F2B | C1B | 1.355(10) |
| S1A | O1A | 1.452(6) | F3B | C1B | 1.338(10) |
| S1A | O2A | 1.444(6) | C1B | S1B | 1.788(10) |
| S1A | O3A | 1.409(6) | S1B | O1B | 1.451(8) |
| N5 | N7[1] | 1.382(8) | S1B | O2B | 1.445(8) |
| N5 | C23 | 1.338(9) | S1B | O3B | 1.413(7) |
| C5 | C6 | 1.378(11) | | | |

[1]-X, 1-Y, -Z

**Table 6** Continued

| Atom | Atom | Atom | Angle/° | Atom | Atom | Atom | Angle/° |
|---|---|---|---|---|---|---|---|
| N2 | Fe1 | N1 | 73.8(2) | N7[1] | N5 | Fe1 | 123.9(5) |
| N2 | Fe1 | N4 | 148.9(3) | C23 | N5 | Fe1 | 120.8(5) |
| N2 | Fe1 | N3 | 101.6(2) | C23 | N5 | N7[1] | 115.2(6) |
| N2 | Fe1 | N6 | 87.4(2) | C4 | C5 | C6 | 118.8(8) |
| N4 | Fe1 | N1 | 77.5(2) | C19 | N6 | Fe1 | 131.1(5) |
| N4 | Fe1 | N3 | 83.7(2) | C22 | N6 | Fe1 | 115.1(5) |
| N4 | Fe1 | N6 | 90.2(2) | C22 | N6 | C19 | 113.8(7) |
| N3 | Fe1 | N1 | 77.7(2) | N4 | C6 | C5 | 122.7(8) |
| N3 | Fe1 | N6 | 170.4(2) | N1 | C7 | C8 | 112.8(6) |
| N5 | Fe1 | N1 | 175.6(2) | C23 | N7 | N5[1] | 116.7(6) |
| N5 | Fe1 | N2 | 103.1(2) | C22 | N8 | C21 | 115.7(7) |
| N5 | Fe1 | N4 | 106.2(2) | N3 | C8 | C7 | 117.5(7) |
| N5 | Fe1 | N3 | 100.0(2) | N3 | C8 | C9 | 122.3(7) |
| N5 | Fe1 | N6 | 74.6(2) | C9 | C8 | C7 | 120.0(7) |
| N6 | Fe1 | N1 | 108.2(2) | C10 | C9 | C8 | 118.2(8) |
| C1 | N1 | Fe1 | 109.1(4) | C9 | C10 | C11 | 119.8(8) |
| C1 | N1 | C7 | 113.1(6) | N3 | C12 | C11 | 121.0(7) |
| C7 | N1 | Fe1 | 106.0(4) | C10 | C11 | C12 | 119.8(8) |
| C13 | N1 | Fe1 | 107.3(4) | C14 | C15 | C16 | 118.6(8) |
| C13 | N1 | C1 | 112.6(6) | N2 | C14 | C15 | 122.8(8) |
| C13 | N1 | C7 | 108.4(6) | N2 | C14 | C13 | 116.3(7) |
| N1 | C1 | C2 | 113.6(6) | C15 | C14 | C13 | 120.9(8) |
| C14 | N2 | Fe1 | 117.4(5) | N1 | C13 | C14 | 110.5(6) |
| C14 | N2 | C18 | 118.2(7) | C17 | C16 | C15 | 119.4(8) |
| C18 | N2 | Fe1 | 123.8(5) | C16 | C17 | C18 | 119.4(8) |
| N4 | C2 | C1 | 116.4(7) | N2 | C18 | C17 | 121.7(8) |
| N4 | C2 | C3 | 122.5(7) | N6 | C19 | C20 | 122.4(8) |
| C3 | C2 | C1 | 121.0(8) | C19 | C20 | C21 | 116.8(8) |
| C2 | N4 | Fe1 | 117.0(5) | N8 | C21 | C20 | 123.1(8) |
| C6 | N4 | Fe1 | 123.9(6) | N6 | C22 | C23 | 114.0(7) |
| C6 | N4 | C2 | 118.2(7) | N8 | C22 | N6 | 127.7(7) |
| C3 | C4 | C5 | 119.6(8) | N8 | C22 | C23 | 118.2(7) |
| C4 | C3 | C2 | 118.2(8) | N5 | C23 | C22 | 115.0(7) |

**Table 6** Continued

| Atom | Atom | Atom | Angle/° | Atom | Atom | Atom | Angle/° |
|---|---|---|---|---|---|---|---|
| C8 | N3 | Fe1 | 114.4(5) | N7 | C23 | N5 | 128.1(7) |
| C8 | N3 | C12 | 118.9(7) | N7 | C23 | C22 | 116.9(7) |
| C12 | N3 | Fe1 | 126.1(5) | N1B | C26 | C24 | 127(4) |
| F1A | C1A | F2A | 105.9(7) | F1B | C1B | F2B | 106.1(17) |
| F1A | C1A | F3A | 108.9(7) | F1B | C1B | F3B | 109.2(16) |
| F1A | C1A | S1A | 112.1(5) | F1B | C1B | S1B | 112.4(14) |
| F2A | C1A | S1A | 111.5(6) | F2B | C1B | S1B | 109.4(10) |
| F3A | C1A | F2A | 107.8(6) | F3B | C1B | F2B | 105.1(12) |
| F3A | C1A | S1A | 110.4(6) | F3B | C1B | S1B | 114.1(13) |
| O1A | S1A | C1A | 102.0(4) | O1B | S1B | C1B | 101.7(12) |
| O2A | S1A | C1A | 103.3(4) | O2B | S1B | C1B | 101.7(9) |
| O2A | S1A | O1A | 114.3(4) | O2B | S1B | O1B | 113.6(13) |
| O3A | S1A | C1A | 104.3(4) | O3B | S1B | C1B | 106.1(8) |
| O3A | S1A | O1A | 114.1(3) | O3B | S1B | O1B | 116.7(11) |
| O3A | S1A | O2A | 116.4(4) | O3B | S1B | O2B | 114.5(10) |

[1]-X, 1-Y, -Z

**[{Fe(TPMA)}$_2$-μ-bmtz](CF$_3$SO$_3$)$_4$•4CH$_3$CN.** The cationic unit of [{Fe(TPMA)}$_2$-μ-bmtz](CF$_3$SO$_3$)$_4$ consists of two [Fe(TPMA)]$^{2+}$ fragments bridged by a bmtz ligand in the neutral form. Only one of the Fe ions is crystallographically unique and resides in a distorted octahedral coordination environment. As in the other compounds, the $N_{py}$-Fe-$N_{amine}$ angles for the [Fe(TPMA)]$^{2+}$ fragment in the range of 81.58(9) – 84.56(8)° are less than the expected 90° angles due to the geometric constraints of the ligand. The Fe-N bond lengths do not vary much in this complex, from 1.889(2) to 2.011(2) Å.

The tetrazine N5-N31 bond distance of 1.349(4) Å is much shorter that that observed for the radical form of bmtz and is consistent with previous reports of the

neutral bridging form.[92] In addition, charge balance dictates that the cationic framework has a 4+ charge, consistent with two $Fe^{II}$ centers and one neutral ligand. The thermal ellipsoid plot of [{Fe(TPMA)}$_2$-μ-bmtz](CF$_3$SO$_3$)$_4$ is displayed in Figure 12 and Table 7 lists bond distances and angles.

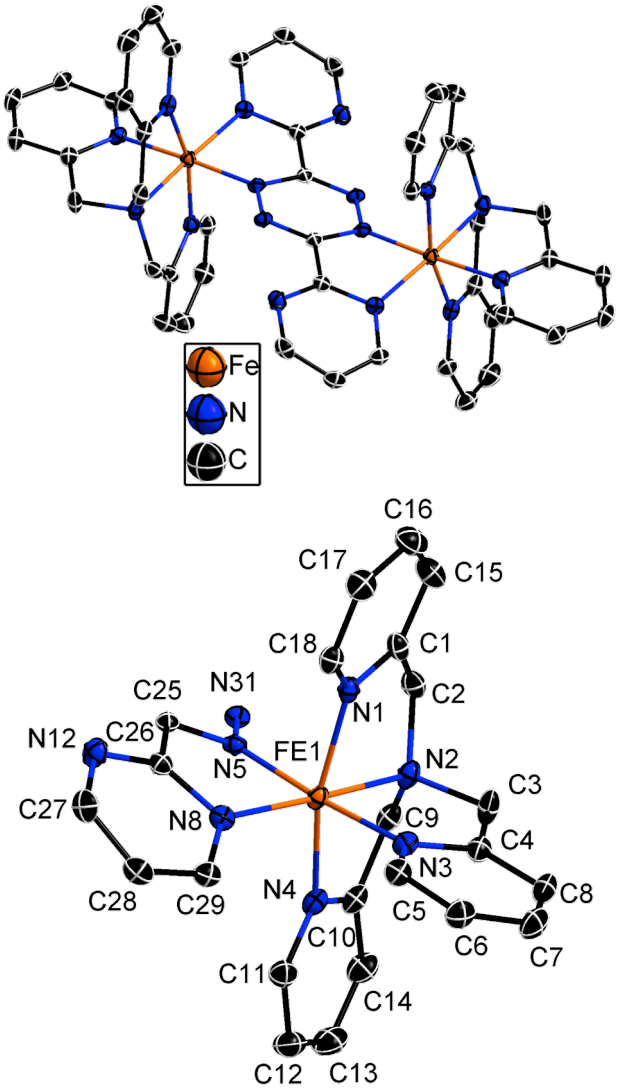


**Figure 12.** Thermal ellipsoid plot and atom numbering scheme of the asymmetric unit for the cationic unit of [{Fe(TPMA)}$_2$-μ-bmtz](CF$_3$SO$_3$)$_4$. Thermal ellipsoids are drawn at the 50% probability level. H atoms were omitted for the sake of clarity.

**Table 7.** Bond distances and angles for [{Fe(TPMA)}$_2$-μ-bmtz](CF$_3$SO$_3$)$_4$.

| Atom | Atom | Length/Å | Atom | Atom | Length/Å |
|---|---|---|---|---|---|
| Fe1 | N1 | 1.979(2) | N5 | C25 | 1.368(3) |
| Fe1 | N2 | 1.998(2) | N5 | N31 | 1.349(3) |
| Fe1 | N3 | 1.995(2) | C28 | C27 | 1.381(4) |
| Fe1 | N4 | 1.985(2) | C28 | C29 | 1.374(4) |
| Fe1 | N5 | 1.889(2) | C27 | N12 | 1.334(3) |
| Fe1 | N8 | 2.011(2) | N8 | C26 | 1.354(3) |
| S1 | O1 | 1.427(2) | N8 | C29 | 1.349(3) |
| S1 | O2 | 1.423(2) | C26 | C25 | 1.458(3) |
| S1 | O3 | 1.438(2) | C26 | N12 | 1.321(3) |
| S1 | C19 | 1.804(3) | C25 | N31[1] | 1.313(3) |
| S2 | O4 | 1.418(3) | N14 | C21 | 1.139(5) |
| S2 | O5 | 1.420(2) | N15 | C23 | 1.128(4) |
| S2 | O6 | 1.410(3) | C1 | C2 | 1.503(4) |
| S2 | C24 | 1.793(3) | C1 | C15 | 1.378(4) |
| F1 | C19 | 1.335(4) | C3 | C4 | 1.488(4) |
| F2 | C19 | 1.324(4) | C4 | C8 | 1.386(4) |
| F3 | C19 | 1.323(4) | C5 | C6 | 1.374(4) |
| F4 | C24 | 1.326(4) | C6 | C7 | 1.379(4) |
| F5 | C24 | 1.301(5) | C7 | C8 | 1.377(4) |
| F6 | C24 | 1.323(4) | C9 | C10 | 1.494(4) |
| N1 | C1 | 1.355(3) | C10 | C14 | 1.386(4) |
| N1 | C18 | 1.349(3) | C11 | C12 | 1.374(4) |
| N2 | C2 | 1.492(3) | C12 | C13 | 1.381(4) |
| N2 | C3 | 1.507(3) | C13 | C14 | 1.379(4) |
| N2 | C9 | 1.494(3) | C15 | C16 | 1.383(4) |
| N3 | C4 | 1.349(3) | C16 | C17 | 1.376(4) |
| N3 | C5 | 1.349(3) | C17 | C18 | 1.379(4) |
| N4 | C10 | 1.353(3) | C20 | C21 | 1.448(6) |
| N4 | C11 | 1.344(3) | C22 | C23 | 1.448(5) |

[1]2-X, 2-Y, 2-Z

**Table 7** Continued

| Atom | Atom | Atom | Angle/° | Atom | Atom | Atom | Angle/° |
|---|---|---|---|---|---|---|---|
| N2 | Fe1 | N1 | 83.02(9) | C29 | N8 | C26 | 114.4(2) |
| N3 | Fe1 | N1 | 86.29(8) | C25 | C26 | N8 | 112.2(2) |
| N3 | Fe1 | N2 | 84.56(8) | N12 | C26 | N8 | 127.9(2) |
| N4 | Fe1 | N1 | 164.32(9) | N12 | C26 | C25 | 119.5(2) |
| N4 | Fe1 | N2 | 81.58(9) | C26 | C25 | N5 | 113.5(2) |
| N4 | Fe1 | N3 | 89.33(9) | N31[1] | C25 | N5 | 126.6(2) |
| N5 | Fe1 | N1 | 88.17(8) | N31[1] | C25 | C26 | 119.4(2) |
| N5 | Fe1 | N2 | 96.87(9) | C26 | N12 | C27 | 115.4(2) |
| N5 | Fe1 | N3 | 174.07(9) | C2 | C1 | N1 | 115.0(2) |
| N5 | Fe1 | N4 | 96.57(9) | C15 | C1 | N1 | 121.6(2) |
| N8 | Fe1 | N1 | 96.88(8) | C15 | C1 | C2 | 123.4(2) |
| N8 | Fe1 | N2 | 177.11(9) | C1 | C2 | N2 | 108.0(2) |
| N8 | Fe1 | N3 | 98.31(8) | C4 | C3 | N2 | 112.9(2) |
| N8 | Fe1 | N4 | 98.65(9) | C3 | C4 | N3 | 116.4(2) |
| N8 | Fe1 | N5 | 80.25(8) | C8 | C4 | N3 | 122.3(2) |
| O2 | S1 | O1 | 114.78(18) | C8 | C4 | C3 | 121.2(2) |
| O3 | S1 | O1 | 114.61(13) | C6 | C5 | N3 | 122.6(2) |
| O3 | S1 | O2 | 115.58(15) | C7 | C6 | C5 | 119.1(3) |
| C19 | S1 | O1 | 103.16(18) | C8 | C7 | C6 | 119.1(3) |
| C19 | S1 | O2 | 102.68(16) | C7 | C8 | C4 | 118.9(3) |
| C19 | S1 | O3 | 103.58(13) | C10 | C9 | N2 | 106.9(2) |
| O5 | S2 | O4 | 113.80(17) | C9 | C10 | N4 | 115.2(2) |
| O6 | S2 | O4 | 113.5(2) | C14 | C10 | N4 | 121.4(3) |
| O6 | S2 | O5 | 116.39(17) | C14 | C10 | C9 | 123.4(2) |
| C24 | S2 | O4 | 102.67(18) | C12 | C11 | N4 | 122.6(3) |
| C24 | S2 | O5 | 104.95(15) | C13 | C12 | C11 | 119.0(3) |
| C24 | S2 | O6 | 103.51(18) | C14 | C13 | C12 | 119.0(3) |
| C1 | N1 | Fe1 | 113.47(17) | C13 | C14 | C10 | 119.5(3) |
| C18 | N1 | Fe1 | 127.70(18) | C16 | C15 | C1 | 119.4(3) |
| C18 | N1 | C1 | 118.6(2) | C17 | C16 | C15 | 119.1(3) |
| C2 | N2 | Fe1 | 106.86(15) | C18 | C17 | C16 | 119.3(3) |
| C3 | N2 | Fe1 | 110.65(15) | C17 | C18 | N1 | 122.0(3) |
| C3 | N2 | C2 | 109.9(2) | F1 | C19 | S1 | 111.6(2) |

**Table 7** Continued

| Atom | Atom | Atom | Angle/° | Atom | Atom | Atom | Angle/° |
|---|---|---|---|---|---|---|---|
| C9 | N2 | Fe1 | 107.48(15) | F2 | C19 | S1 | 110.5(2) |
| C9 | N2 | C2 | 112.9(2) | F2 | C19 | F1 | 108.2(3) |
| C9 | N2 | C3 | 109.0(2) | F3 | C19 | S1 | 111.5(3) |
| C4 | N3 | Fe1 | 114.57(17) | F3 | C19 | F1 | 107.6(3) |
| C5 | N3 | Fe1 | 127.71(18) | F3 | C19 | F2 | 107.3(3) |
| C5 | N3 | C4 | 117.6(2) | C25[1] | N31 | N5 | 117.7(2) |
| C10 | N4 | Fe1 | 113.86(17) | N8 | C29 | C28 | 121.6(2) |
| C11 | N4 | Fe1 | 127.51(18) | C20 | C21 | N14 | 179.5(4) |
| C11 | N4 | C10 | 118.5(2) | C22 | C23 | N15 | 179.9(4) |
| C25 | N5 | Fe1 | 115.41(16) | F4 | C24 | S2 | 111.3(2) |
| N31 | N5 | Fe1 | 128.34(16) | F5 | C24 | S2 | 112.2(3) |
| N31 | N5 | C25 | 115.6(2) | F5 | C24 | F4 | 107.3(3) |
| C29 | C28 | C27 | 118.0(2) | F6 | C24 | S2 | 112.8(2) |
| N12 | C27 | C28 | 121.9(2) | F6 | C24 | F4 | 106.4(3) |
| C26 | N8 | Fe1 | 112.54(16) | F6 | C24 | F5 | 106.5(3) |
| C29 | N8 | Fe1 | 133.08(18) | | | | |

[1]2-X, 2-Y, 2-Z

*Magnetic Measurements*

**[{Fe(TPMA)}$_2$-μ-bmtz$^{\bullet-}$](BF$_4$)$_3$•CH$_3$CN.** Static DC magnetic measurements on crushed single crystals of [{Fe(TPMA)}$_2$-μ-bmtz$^{\bullet-}$](BF$_4$)$_3$ were conducted between 1.8 and 300 K. The 300 K χT value of 6.64 emu K mol$^{-1}$ is consistent with the 6.68 emu K mol$^{-1}$ expected for two high-spin Fe$^{II}$ centers (S = 2 with g = 2.05) and one bmtz radical (S = 1/2 with g = 2.00). The value of χT slowly increases until ~30 K, after which temperature it begins to decrease rapidly until reaching a minimum of 5.84 emu K mol$^{-1}$ at 2.0 K (Figure 13a). The plot of M vs. H at 1.8 K (Figure 13b) saturates at a value of 5

$\mu_B$, much lower than expected for any reasonable spin ground state. The expected saturation value is either 7 $\mu_B$ for an S = 7/2 ground state resulting from antiferromagnetic coupling between the $Fe^{II}$ ions and the bmtz radical or 9 $\mu_B$ for an S = 9/2 ground state resulting from ferromagnetic coupling between the $Fe^{II}$ ions and the bmtz radical. A plot of reduced magnetization (Figure 13c) displays significant splitting of the isofield lines, suggestive of a high degree of anisotropy or low-lying excited states. This behavior is similar to what is observed for [{Co(TPMA)}$_2$-μ-bmtz$^{\bullet-}$](CF$_3$SO$_3$)$_3$, in which the coupling between the $Co^{II}$ ions and the radical was determined by theoretical crystal field calculations to be antiferromagnetic with a coupling constant of J = -62.5 cm$^{-1}$. Similarly to the situation encountered for [{Co(TPMA)}$_2$-μ-bmtz$^{\bullet-}$](CF$_3$SO$_3$)$_3$, no satisfactory fits to the magnetic data could be achieved with PHI[103] but it appears that the exchange coupling is antiferromagnetic and of the same order of magnitude as in [{Co(TPMA)}$_2$-μ-bmtz$^{\bullet-}$](CF$_3$SO$_3$)$_3$. Akin to the $^4T_1$ ground state of high spin $Co^{II}$, the ground state of high spin $Fe^{II}$ is $^5T_2$. This suggests that the inability to fit the magnetic data with a Hamiltonian in terms of J, D, and g is a consequence of D not being an appropriate parameter for a system of this type, which contains first-order angular momentum, and higher-level calculations, similar to those used for [{Co(TPMA)}$_2$-μ-bmtz$^{\bullet-}$](CF$_3$SO$_3$)$_3$, will need to be performed to understand the single ion anisotropy responsible for the observed DC magnetic properties of [{Fe(TPMA)}$_2$-μ-bmtz$^{\bullet-}$](BF$_4$)$_3$.

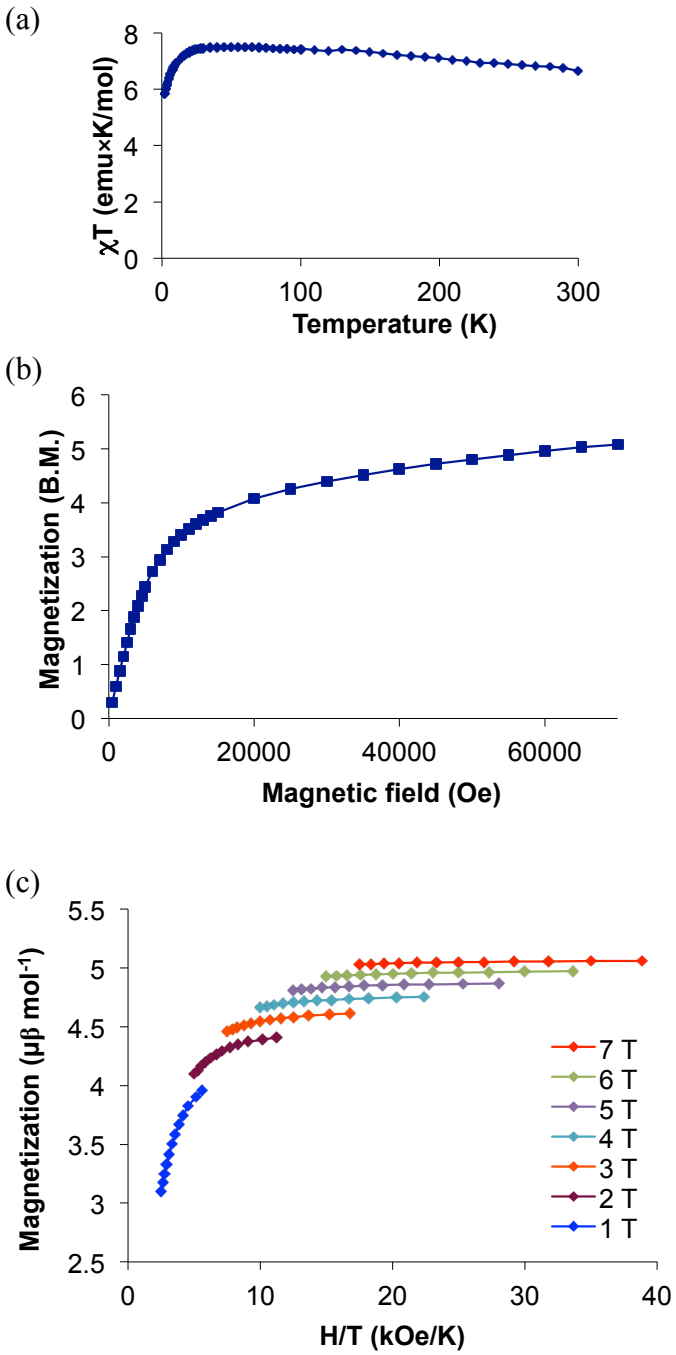


**Figure 13.** DC magnetic properties of [{Fe(TPMA)}$_2$-μ-bmtz$^{\bullet-}$](BF$_4$)$_3$. (a) χT product under a 1000 Oe field. (b) plot of M vs. H at 1.8 K. (c) temperature and field dependence of the magnetization. The solid lines are merely guides for the eye.

Dynamic AC magnetic measurements of [{Fe(TPMA)}$_2$-μ-bmtz$^{\bullet-}$](BF$_4$)$_3$ in zero applied DC field revealed the absence of an out-of-phase signal, but in a 400 Oe DC field a very strong χ'' signal is observed (Figure 14a). At low temperatures, the maxima in χ'' are below the accessible frequency range of the SQUID magnetometer but have the general appearance of being frequency independent. The maxima in χ'' become frequency dependent at higher temperatures, indicative of an Orbach relaxation process. The Cole-Cole plot (Figure 14b) was fit with CC-FIT[104] to extract the values of τ and α. The τ values were used to construct an Arrhenius plot that shows two distinct regions (Figure 14c). The low temperature region exhibits non-linear behavior consistent with quantum tunneling. The linear region between 2.9 and 4.7 K, where relaxation is via an Orbach process,[105] was used to extract an energy barrier of 42 K with $\tau_o = 9.8 \times 10^{-9}$ s. The α values from 2.9 to 4.7 K are between 0.32 and 0.12, indicating a gradual transition between the tunneling and thermal regimes.

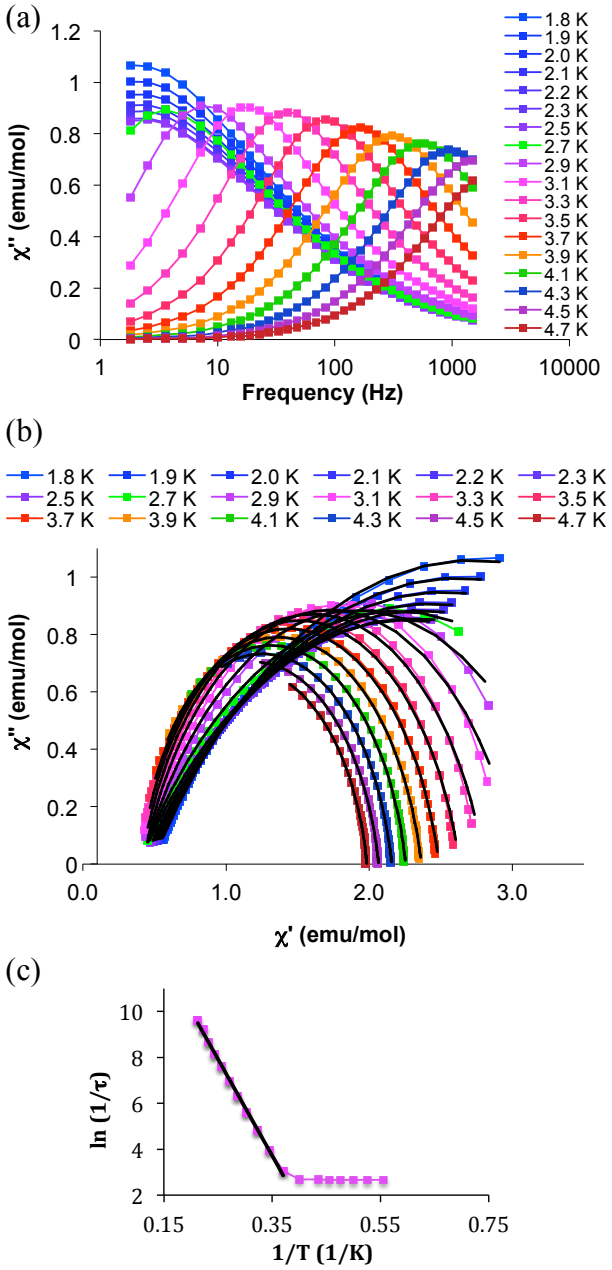


**Figure 14.** AC magnetic data for [{Fe(TPMA)}$_2$-μ-bmtz$^{\bullet-}$](BF$_4$)$_3$. (a) frequency dependence of χ'' collected in a 400 Oe DC field. Solid lines are guides for the eye. (b) Cole-Cole plot. The colored points and lines are experimental data and guides for the eye, respectively. The solid black lines are the results of fitting the data with CC-FIT as discussed in the main text. (c) Arrhenius plot. The black line is a linear regression fit to the data which resulted in a barrier height of 42 K with $\tau_o$ = 9.8 x $10^{-9}$ s as discussed in the main text.

**[{Fe(TPMA)}$_2$-μ-bmtz](BF$_4$)$_4$•2CH$_3$CN.** No magnetic characterization of [{Fe(TPMA)}$_2$-μ-bmtz$^{\bullet-}$](BF$_4$)$_4$ was performed due to the similarity in bond lengths between this complex and [{Fe(TPMA)}$_2$-μ-bmtz$^{\bullet-}$](CF$_3$SO$_3$)$_4$, which was shown to consist of diamagnetic low-spin Fe$^{II}$ centers (*vide infra*).

**[{Fe(TPMA)}$_2$-μ-bmtz$^{\bullet-}$](CF$_3$SO$_3$)$_3$•CH$_3$CN.** Static DC magnetic measurements on crushed single crystals of [{Fe(TPMA)}$_2$-μ-bmtz$^{\bullet-}$](CF$_3$SO$_3$)$_3$ were conducted between 1.8 and 300 K (Figure 15). In contrast to the behavior observed for [{Fe(TPMA)}$_2$-μ-bmtz$^{\bullet-}$](BF$_4$)$_3$, in which the Fe$^{II}$ ions are high spin at all temperatures, this complex undergoes an abrupt spin crossover transition at 150 K. This is only the second Fe$^{II}$ complex to display spin crossover behavior when coordinated directly to a radical ligand[106] and, to the best of our knowledge, is the first example of a dinuclear Fe$^{II}$ spin crossover complex containing a radical bridging ligand. The 300 K χT value of 5.03 emu K mol$^{-1}$ is lower than the 6.68 emu K mol$^{-1}$ expected for an uncoupled system consisting of two high-spin Fe$^{II}$ centers (S = 2 with g = 2.05) and one bmtz radical (S = 1/2 with g = 2.00). The value of χT gradually rises until 200 K, at which temperature the transition to low-spin Fe$^{II}$ commences. The spin transition is quite abrupt and is complete at ~130 K; there is no hysteresis between warming and cooling cycles. The value of χT at 130 K is 2.41 emu K mol$^{-1}$, higher than the 0.38 emu K mol$^{-1}$ expected for a complete spin transition to low-spin Fe$^{II}$ with the bmtz radical as the only spin carrier. This behavior, taken together with the low value of χT at 300 K, is indicative of a mixed system in which the high spin state is never fully achieved for both Fe$^{II}$ ions at high temperatures. The low spin state is not fully achieved at low temperatures, either.

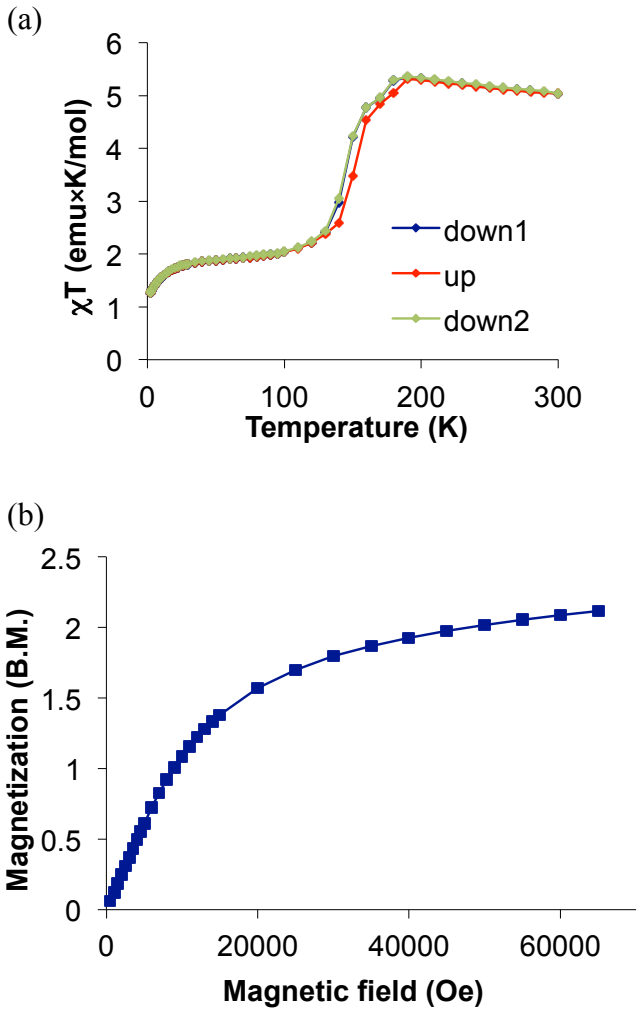


**Figure 15.** DC magnetic properties of $[\{Fe(TPMA)\}_2\text{-}\mu\text{-}bmtz^{\bullet-}](CF_3SO_3)_3$. (a) χT product under a 1000 Oe field. The blue and green "down" traces represent measurements during cooling from 300 to 2 K. The red "up" trace represents a measurement taken while warming from 2 to 300 K. The solid lines are guides for the eye. (b) plot of M vs. H at 1.8 K. The solid line is a guide for the eye.

The system is best described as a mixture of high spin and low spin $Fe^{II}$, with the ratio between the two spin states varying with temperature. Using the observed behavior of χT with temperature and taking 3.15 emu K $mol^{-1}$ as the expected value of χT for one high-spin $Fe^{II}$ center and 0.38 emu K $mol^{-1}$ as the expected value of χT for the bmtz

radical, the ratio of high spin to low spin $Fe^{II}$ at 300 K is found to be 0.79:0.21. At 70 K, after the spin transition is complete and $\chi T$ is approximately constant, the $\chi T$ value is 1.93 emu K $mol^{-1}$. This corresponds to a high spin to low spin ratio of 0.25:0.75. There is a further decrease in $\chi T$ at temperatures below 20 K that could be due to either antiferromagnetic coupling between the remaining high-spin $Fe^{II}$ ions and the bmtz radical, ZFS of the high-spin $Fe^{II}$ ions, or the completion of the spin transition to the low spin state.

To gain further insight into the nature of the spin transition Heather Stout and Dr. Catalina Achim at Carnegie Mellon University performed Mossbauer measurements on this complex. At 4.2 K, the Mossbauer results show a high spin to low spin ratio of 0.23:0.74, which eliminates the possibility of the completion of the spin transition to the low spin state as being the reason for the decrease in $\chi T$ below 20 K. At 120 K, the high spin to low spin ratio was found to be 0.25:0.71 and at 200 K, 0.37:0.67. The ratio at 120 K is in reasonable agreement with the ratio obtained from the $\chi T$ measurement. The agreement is not good at 200 K. The Mossbauer measurement shows little increase in the high spin $Fe^{II}$ concentration between 120 and 200 K, while the susceptibility data show an increase from 25% to 79% high spin $Fe^{II}$. One hypothesis for the discrepancy is that the Mossbauer measurement was performed in mineral oil, which freezes at about 250 K. The frozen mineral oil could have been exerting a pressure on the sample, favoring the low spin state. To test this hypothesis the DC susceptibility of the Mossbauer sample, still suspended in mineral oil, was measured. The sample was cooled to 2 K in zero DC field to freeze the mineral oil. Susceptibility data were then

measured from 2 K to 230 K and back down to 2 K. Temperatures above 230 K were not measured to ensure the mineral oil remained frozen. The results, shown in Figure 16, are much more consistent with the Mossbauer results. At 120 K the χT value is consistent with a high spin to low spin ratio of 0.35:0.65 and at 200 K the ratio is 0.43:0.57. This is convincing evidence that the frozen mineral oil is trapping the sample in the low spin state.

While spin crossover in mononuclear $Fe^{II}$ complexes is well established, spin crossover in dinuclear $Fe^{II}$ complexes is more rare.[107] Anion-dependence of the spin crossover has been previously observed in $Fe^{II}$ complexes[108,109] and in a mononuclear $Mn^{III}$ complex.[110] Both $[\{Fe(TPMA)\}_2\text{-}\mu\text{-}bmtz^{\bullet-}](BF_4)_3$ and $[\{Fe(TPMA)\}_2\text{-}\mu\text{-}bmtz^{\bullet-}](CF_3SO_3)_3$ display numerous, complex hydrogen bonding networks including the formation of rings of molecules and chains of molecules. Comparing the 210 K and 110 K crystal structures of the $[CF_3SO_3]^-$ salt, there is a disorder-to-order transition of one of the $[CF_3SO_3]^-$ anions as the temperature is lowered, which could perturb the hydrogen bonding network. This type of behavior leading to spin crossover behavior has been previously observed in a mononuclear $Mn^{III}$ complex.[110]

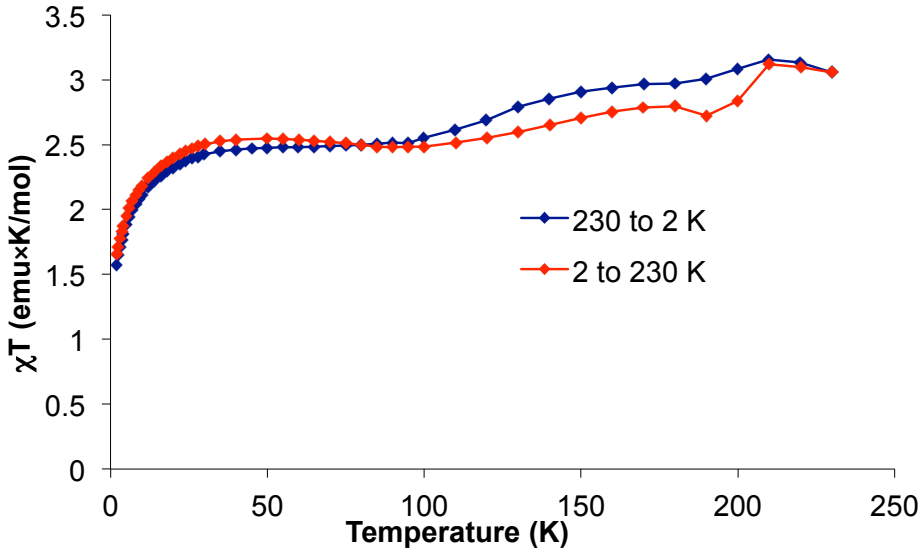


**Figure 16.** χT product of the post-Mossbauer SQUID measurement of [{Fe(TPMA)}$_2$-μ-bmtz$^{\bullet-}$](CF$_3$SO$_3$)$_3$ under a 2000 Oe field, depicting both the warming and cooling cycles. The solid lines are guides for the eye.

Dynamic AC magnetic measurements of [{Fe(TPMA)}$_2$-μ-bmtz$^{\bullet-}$](CF$_3$SO$_3$)$_3$ in zero applied DC field revealed no out-of-phase signal, but in a 400 Oe DC field a very strong χ'' signal is observed (Figure 17a). The Cole-Cole plot (Figure 17b) was fit to a modified Debye function[111,112] to extract the values of τ and α. The τ values were used to construct an Arrhenius plot that shows two distinct regions (Figure 17c). The low temperature region exhibits non-linear behavior consistent with quantum tunneling. The linear region between 2.6 and 3.4 K, where relaxation is via an Orbach process,[105] was used to extract an energy barrier of 36 K with $\tau_o = 3.2 \times 10^{-9}$ s. The α values from 2.6 to 3.4 K are between 0.20 and 0.06, which, along with the gradual slope of the Arrhenius plot, indicate a gradual transition between the tunneling regime and the thermal regime.

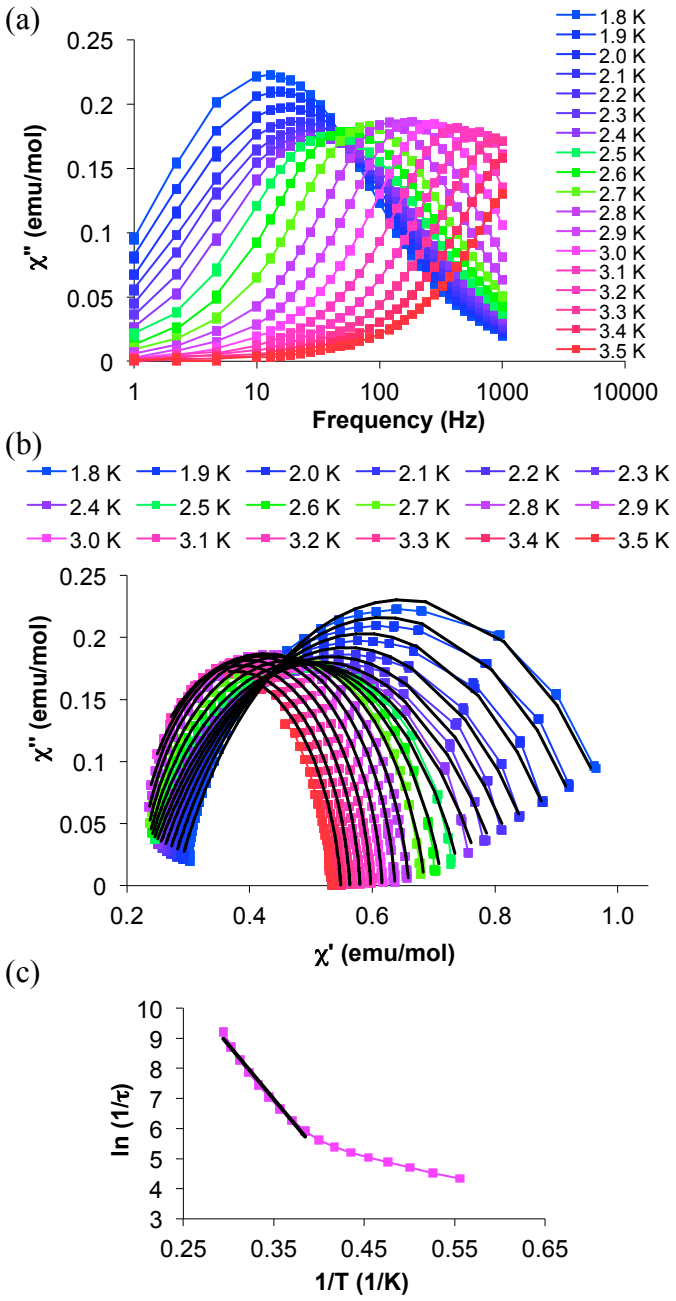


**Figure 17.** AC magnetic measurements for [{Fe(TPMA)}$_2$-μ-bmtz$^{\bullet-}$](CF$_3$SO$_3$)$_3$. (a) frequency dependence of χ'' collected in an 400 Oe DC field. Solid lines are guides for the eye. (b) Cole-Cole plot. The colored points and lines are experimental data and guides for the eye, respectively. The solid black lines are the results of fitting the data with a modified Debye function as discussed in the main text. (c) Arrhenius plot. The black line is a linear regression fit to the data which resulted in the barrier height of 36 K with $\tau_o = 3.2 \times 10^{-9}$ s as discussed in the main text.

**[{Fe(TPMA)}$_2$-μ-bmtz](CF$_3$SO$_3$)$_4$•4CH$_3$CN.** Static DC magnetic measurements on crushed single crystals of [{Fe(TPMA)}$_2$-μ-bmtz$^{\bullet-}$](CF$_3$SO$_3$)$_4$ were conducted between 1.8 and 350 K (Figure 18). The maximum value of χT, 0.15 emu K mol$^{-1}$, was observed at 350 K, indicating that this complex consists of predominantly diamagnetic low-spin Fe$^{II}$ at all temperatures below 350 K. This is consistent with the results of Mossbauer measurements, which showed a high spin to low spin ratio of 0.04:0.96 at 4.2 K.

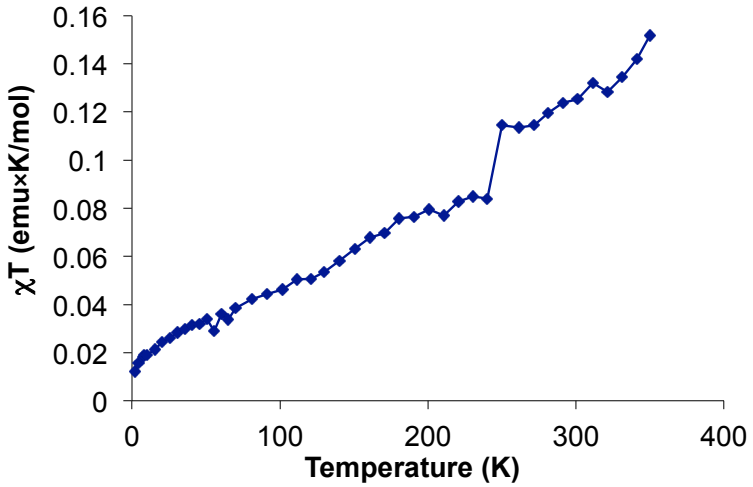


**Figure 18.** χT product of [{Fe(TPMA)}$_2$-μ-bmtz](CF$_3$SO$_3$)$_4$ under a 5000 Oe field. The solid line is a guide for the eye.

## Cobalt Complexes of the bmtz Ligand

### Experimental Section

TPMA was synthesized by literature procedure[95] with the addition of a final re-crystallization from boiling hexane. [Co(CH$_3$CN)$_6$](CF$_3$SO$_3$)$_2$[97] and bmtz[91] were prepared by literature procedures. Synthesis of the complex was performed in an MBRAUN dry box under an N$_2$ atmosphere. The CH$_3$CN was pre-dried by storage over

3 Å molecular sieves and then distilled from 3 Å molecular sieves prior to use. The $Et_2O$ was purified using an MBRAUN solvent purification system and then stored over 3 Å molecular sieves in the dry box. Elemental analysis was performed by Atlantic Microlabs, Inc., Norcross, GA. Magnetic measurements were conducted in the temperature range of 1.8 to 300 K using a Quantum Design MPMS-XL SQUID magnetometer equipped with a 7T superconducting magnet. The diamagnetic contribution of the plastic bag used as a sample holder was subtracted from the raw data. Core diamagnetism of the sample was accounted for using Pascal's constants.[98]

*Synthesis*

**$[\{Co(TPMA)\}_2$-μ-bmtz$^{\bullet-}](CF_3SO_3)_3 \bullet CH_3CN$.** To a red solution of $[Co(CH_3CN)_6](CF_3SO_3)_2$ (0.0280 g, 0.05 mmol) in $CH_3CN$ (3 mL) was added a solution containing TPMA (0.0290 g, 0.1 mmol), bmtz (0.0200 g, 0.08 mmol) and $Cp_2Co$ (0.0090 g, 0.047 mmol). The resulting dark red solution was stirred for 24 h and filtered. Red X-ray quality crystals were obtained after three days by slow diffusion of $Et_2O$ vapor into the filtrate. Yield: 0.0270 g (45%) based on $[Co(CH_3CN)_6](CF_3SO_3)_2$. Analysis calculated (found) for $[\{Co(TPMA)\}_2(bmtz)](CF_3SO_3)_3 \bullet CH_3CN$ ($C_{51}H_{45}N_{17}O_9F_9S_3Co_2$): C: 42.99% (42.99%), H: 3.18% (3.01%), N: 16.71% (16.74%).

*Single Crystal X-Ray Diffraction*

Single crystal X-ray data for $[\{Co(TPMA)\}_2$-μ-bmtz$^{\bullet-}](CF_3SO_3)_3$ was collected on a Bruker APEXII diffractometer equipped with a CCD detector. A red crystal was affixed to a nylon loop with Paratone® oil and placed in a cold stream of $N_{2(g)}$ at 150 K. The frames were integrated with the Bruker APEXII software package[99] and a semi-

empirical absorption correction was applied using SADABS as contained within the Bruker APEXII software suite. The structure was solved using SHELXS[100] and refined using SHELXL-2014[101] as implemented within ShelXle, a graphical interface for the SHELX suite of programs.[102] The remaining non-hydrogen atoms were located by alternating cycles of least-squares refinements and difference Fourier maps. All hydrogen atoms were placed in calculated positions. The final refinements were carried out with anisotropic thermal parameters for all non-hydrogen atoms. One of the $[CF_3SO_3]^-$ anions and the $CH_3CN$ molecule were disordered about inversion centers. The $CH_3CN$ molecule was modeled with a fixed 50% occupancy. The occupancy of the disordered $[CF_3SO_3]^-$ molecule was allowed to refine and converged to a 0.78:0.22 occupancy ratio for the two possible orientations of the $[CF_3SO_3]^-$ molecule. Further pertinent details of the X-ray refinements are given in Table 8. CCDC: 1011899.

**Table 8.** Crystal and structural refinement data for $[\{Co(TPMA)\}_2bmtz](CF_3SO_3)_3$.

| | |
|---|---|
| Empirical formula | $C_{51}H_{45}Co_2F_9N_{17}O_9S_3$ |
| Formula weight | 1425.08 |
| Temperature/K | 150(2) |
| Crystal system | triclinic |
| Space group | P-1 |
| a/Å | 8.950(6) |
| b/Å | 9.941(7) |
| c/Å | 16.385(11) |
| α/° | 92.020(9) |
| β/° | 98.068(8) |
| γ/° | 97.876(9) |
| Volume/Å$^3$ | 1427.5(17) |
| Z | 1 |
| $\varrho_{calc}$g/cm$^3$ | 1.658 |
| μ/mm$^{-1}$ | 0.793 |
| F(000) | 725.0 |
| Crystal size/mm$^3$ | 0.080 × 0.053 × 0.050 |
| Radiation | MoKα (λ = 0.71073 Å) |
| 2Θ range for data collection/° | 4.142 to 48.802 |
| Index ranges | $-10 \le h \le 10$, $-11 \le k \le 11$, $-19 \le l \le 19$ |
| Reflections collected | 12938 |
| Independent reflections | 4703 [$R_{int}$ = 0.0724, $R_{sigma}$ = 0.0885] |
| Data/restraints/parameters | 4703/287/528 |
| Goodness-of-fit on $F^2$ [c] | 1.003 |
| Final R indexes [I>=2σ (I)] | $R_1$[a] = 0.0488, $wR_2$[b] = 0.1058 |
| Final R indexes [all data] | $R_1$[a] = 0.0772, $wR_2$[b] = 0.1216 |
| Largest diff. peak/hole / e Å$^{-3}$ | 0.48/-0.45 |

[a] $R_1 = \Sigma \left| \left| F_o \right| - \left| F_c \right| \right| / \Sigma \left| F_o \right|$. [b] $wR_2 = \{\Sigma [w(F_o^2 - F_c^2)^2] / \Sigma w(F_o^2)^2]\}^{1/2}$. [c] Goodness-of-fit $= \{\Sigma [w(F_o^2 - F_c^2)^2]/(n-p)\}^{1/2}$, where *n* is the number of reflections and *p* is the total number of parameters refined.

**Results and Discussion**

*Synthesis*

[{Co(TPMA)}$_2$-μ-bmtz$^{\bullet-}$](CF$_3$SO$_3$)$_3$•CH$_3$CN was prepared by reacting a solution of *in situ* generated [Co(TPMA)(solv)$_x$](CF$_3$SO$_3$)$_2$ with bmtz and Cp$_2$Co in CH$_3$CN. A reducing agent did not need to be added to form the radical complex; the bmtz ligand would spontaneously reduce itself during the course of the reaction, which was surprising to us. A perusal of the literature revealed that Kaim had noted the same result in the absence of an obvious reducing agent.[94] Higher yields and more crystalline material were obtained when Cp$_2$Co was included in the reaction. The cationic unit consists of two [Co(TPMA)]$^{2+}$ units bridged by a single bmtz radical ligand. The two cobalt fragments are arranged *anti* to each other across the bmtz ligand.

*Single Crystal X-ray Diffraction*

The single Co$^{II}$ ion in the asymmetric unit exhibits a distorted octahedral coordination geometry. The N$_{py}$-Co-N$_{amine}$ angles in the Co(TPMA) moiety range from 76.12(12) to 79.16(12)°, much more acute than the expected 90° angles for an ideal octahedral coordination geometry. The Co-N bond lengths also vary significantly, from 2.100(3) to 2.256(3) Å. This distortion is best described as a meridional elongation, in which the Co1-N8, Co1-N2, and Co1-N6 bonds form one meridian of the octahedron spanning from the bmtz pyrimidine ring to the bridgehead amine N atom of TPMA and one of the pyridine rings of TPMA with an average bond length of 2.21 Å. The Co1-N5, Co1-N4, and Co1-N10 bonds form the other meridian of the octahedron with an average bond length of 2.08 Å. Evidence for the radical anion form of the bmtz ligand is the N3-

N5a distance of 1.385(4) Å in the tetrazine ring, which is significantly longer than the ~1.33 Å expected for the neutral form of the ligand and consistent with previous reports of the radical anion.[92] Moreover, charge balance requires the cationic framework to have a 3+ charge, consistent with two $Co^{II}$ centers and one ligand radical. The intramolecular Co-Co separation is 6.80 Å with the closest intermolecular Co-Co contact being 8.95 Å. The thermal ellipsoid plot of $[Co(TPMA)(CH_3CN)](BF_4)_2$ is displayed in Figure 19 and Table 9 lists bond distances and angles.

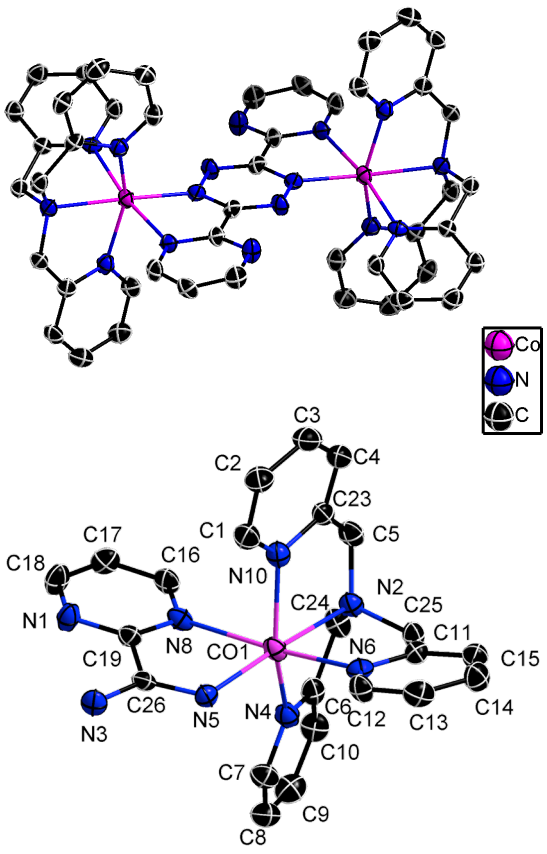


**Figure 19.** Thermal ellipsoid plot and atom numbering scheme of the asymmetric unit for the cationic unit of $[\{Co(TPMA)\}_2\text{-}\mu\text{-}bmtz^{\bullet-}](CF_3SO_3)_3$. Thermal ellipsoids are drawn at the 50% probability level. H atoms were omitted for the sake of clarity.

**Table 9.** Bond distances and angles for [{Co(TPMA)}$_2$-μ-bmtz$^{\bullet-}$](CF$_3$SO$_3$)$_3$.

| Atom | Atom | Length/Å | Atom | Atom | Length/Å |
|---|---|---|---|---|---|
| Co1 | N5 | 2.033(3) | N3 | N5[1] | 1.385(4) |
| Co1 | N10 | 2.100(3) | N5 | C26 | 1.337(5) |
| Co1 | N4 | 2.101(4) | N5 | N3[1] | 1.386(4) |
| Co1 | N6 | 2.158(3) | N2 | C5 | 1.471(5) |
| Co1 | N2 | 2.208(3) | N2 | C24 | 1.476(5) |
| Co1 | N8 | 2.256(3) | N2 | C25 | 1.483(5) |
| N1 | C19 | 1.329(5) | N4 | C7 | 1.339(5) |
| N1 | C18 | 1.332(5) | N4 | C6 | 1.353(5) |
| F1A | C1A | 1.340(5) | N6 | C11 | 1.343(5) |
| F2A | C1A | 1.325(5) | N6 | C12 | 1.359(5) |
| F3A | C1A | 1.333(5) | N8 | C19 | 1.331(5) |
| C1A | S1A | 1.811(5) | N8 | C16 | 1.347(5) |
| S1A | O3A | 1.431(3) | C1D | N10 | 1.345(5) |
| S1A | O2A | 1.431(3) | C1D | C1 | 1.364(6) |
| S1A | O1A | 1.439(3) | C1 | C3 | 1.386(6) |
| F1C | C1C | 1.342(7) | C3 | C4 | 1.369(6) |
| F2C | C1C | 1.328(7) | C4 | C23 | 1.373(6) |
| F3C | C1C | 1.336(7) | C5 | C23 | 1.507(6) |
| C1C | S1C | 1.817(7) | C6 | C10 | 1.376(6) |
| S1C | O3C | 1.436(5) | C6 | C24 | 1.504(5) |
| S1C | O2C | 1.437(5) | C7 | C8 | 1.375(6) |
| S1C | O1C | 1.445(6) | C8 | C9 | 1.383(6) |
| F1E | C1E | 1.341(7) | C9 | C10 | 1.374(6) |
| F2E | C1E | 1.328(7) | N10 | C23 | 1.346(5) |
| F3E | C1E | 1.335(7) | C11 | C15 | 1.377(5) |
| C1E | S1E | 1.815(7) | C11 | C25 | 1.499(5) |
| S1E | O3E | 1.435(6) | C12 | C13 | 1.381(5) |
| S1E | O2E | 1.436(6) | C13 | C14 | 1.386(6) |
| S1E | O1E | 1.443(6) | C14 | C15 | 1.379(6) |
| N7F | C1F | 1.15(5) | C16 | C17 | 1.361(5) |
| C1F | C2F | 1.467(14) | C17 | C18 | 1.375(5) |
| N3 | C26 | 1.314(5) | C19 | C26 | 1.490(5) |

[1]1-X, 1-Y, 1-Z

**Table 9** Continued

| Atom | Atom | Atom | Angle/° | Atom | Atom | Atom | Angle/° |
|---|---|---|---|---|---|---|---|
| N5 | Co1 | N10 | 104.99(13) | C26 | N5 | N3[1] | 116.4(3) |
| N5 | Co1 | N4 | 100.69(13) | C26 | N5 | Co1 | 120.1(2) |
| N10 | Co1 | N4 | 151.10(13) | N3[1] | N5 | Co1 | 123.4(2) |
| N5 | Co1 | N6 | 100.17(12) | C5 | N2 | C24 | 111.8(3) |
| N10 | Co1 | N6 | 86.89(13) | C5 | N2 | C25 | 112.8(3) |
| N4 | Co1 | N6 | 101.51(13) | C24 | N2 | C25 | 108.7(3) |
| N5 | Co1 | N2 | 176.47(12) | C5 | N2 | Co1 | 109.7(2) |
| N10 | Co1 | N2 | 78.47(12) | C24 | N2 | Co1 | 107.2(2) |
| N4 | Co1 | N2 | 76.12(12) | C25 | N2 | Co1 | 106.4(2) |
| N6 | Co1 | N2 | 79.16(12) | C7 | N4 | C6 | 117.9(4) |
| N5 | Co1 | N8 | 75.53(12) | C7 | N4 | Co1 | 125.1(3) |
| N10 | Co1 | N8 | 85.69(13) | C6 | N4 | Co1 | 116.5(3) |
| N4 | Co1 | N8 | 88.11(12) | C11 | N6 | C12 | 117.6(3) |
| N6 | Co1 | N8 | 170.11(12) | C11 | N6 | Co1 | 114.9(2) |
| N2 | Co1 | N8 | 105.68(11) | C12 | N6 | Co1 | 127.1(3) |
| C19 | N1 | C18 | 115.3(3) | C19 | N8 | C16 | 115.5(3) |
| F2A | C1A | F3A | 107.0(4) | C19 | N8 | Co1 | 112.1(2) |
| F2A | C1A | F1A | 108.0(3) | C16 | N8 | Co1 | 131.8(3) |
| F3A | C1A | F1A | 107.4(4) | N10 | C1D | C1 | 122.3(4) |
| F2A | C1A | S1A | 112.0(3) | C1D | C1 | C3 | 119.1(4) |
| F3A | C1A | S1A | 111.4(3) | C4 | C3 | C1 | 119.1(4) |
| F1A | C1A | S1A | 110.9(3) | C3 | C4 | C23 | 118.9(4) |
| O3A | S1A | O2A | 115.4(2) | N2 | C5 | C23 | 112.6(3) |
| O3A | S1A | O1A | 115.13(18) | N4 | C6 | C10 | 122.1(4) |
| O2A | S1A | O1A | 113.9(2) | N4 | C6 | C24 | 115.7(4) |
| O3A | S1A | C1A | 103.26(19) | C10 | C6 | C24 | 122.2(4) |
| O2A | S1A | C1A | 102.9(2) | N4 | C7 | C8 | 122.9(4) |
| O1A | S1A | C1A | 103.9(2) | C7 | C8 | C9 | 118.6(4) |
| F2C | C1C | F3C | 108.1(11) | C10 | C9 | C8 | 119.2(4) |
| F2C | C1C | F1C | 108.2(11) | C9 | C10 | C6 | 119.2(4) |
| F3C | C1C | F1C | 104.9(11) | C1D | N10 | C23 | 118.1(4) |
| F2C | C1C | S1C | 111.8(8) | C1D | N10 | Co1 | 123.2(3) |
| F3C | C1C | S1C | 112.4(8) | C23 | N10 | Co1 | 117.5(3) |

**Table 9** Continued

| Atom | Atom | Atom | Angle/° | Atom | Atom | Atom | Angle/° |
|---|---|---|---|---|---|---|---|
| F1C | C1C | S1C | 111.2(8) | N6 | C11 | C15 | 123.1(4) |
| O3C | S1C | O2C | 115.7(10) | N6 | C11 | C25 | 116.0(3) |
| O3C | S1C | O1C | 117.2(11) | C15 | C11 | C25 | 120.7(4) |
| O2C | S1C | O1C | 115.0(10) | N6 | C12 | C13 | 122.0(4) |
| O3C | S1C | C1C | 102.1(7) | C12 | C13 | C14 | 119.6(4) |
| O2C | S1C | C1C | 102.7(6) | C15 | C14 | C13 | 118.4(4) |
| O1C | S1C | C1C | 100.5(7) | C11 | C15 | C14 | 119.3(4) |
| F2E | C1E | F3E | 108(2) | N8 | C16 | C17 | 121.8(4) |
| F2E | C1E | F1E | 108(2) | C16 | C17 | C18 | 117.7(4) |
| F3E | C1E | F1E | 106(2) | N1 | C18 | C17 | 122.3(4) |
| F2E | C1E | S1E | 112.3(19) | N8 | C19 | N1 | 127.3(3) |
| F3E | C1E | S1E | 112(2) | N8 | C19 | C26 | 115.7(3) |
| F1E | C1E | S1E | 110.1(18) | N1 | C19 | C26 | 117.0(3) |
| O3E | S1E | O2E | 116(2) | N10 | C23 | C4 | 122.4(4) |
| O3E | S1E | O1E | 116(2) | N10 | C23 | C5 | 115.0(3) |
| O2E | S1E | O1E | 114.6(19) | C4 | C23 | C5 | 122.5(4) |
| O3E | S1E | C1E | 102.3(17) | N2 | C24 | C6 | 110.5(3) |
| O2E | S1E | C1E | 102.6(17) | N2 | C25 | C11 | 114.1(3) |
| O1E | S1E | C1E | 102.3(17) | N3 | C26 | N5 | 128.0(3) |
| N7F | C1F | C2F | 175(2) | N3 | C26 | C19 | 117.0(3) |
| C26 | N3 | N5[1] | 115.7(3) | N5 | C26 | C19 | 115.0(3) |

[1]1-X, 1-Y, 1-Z

*Magnetic Measurements*

The static DC magnetic properties of $[\{Co(TPMA)\}_2\text{-}\mu\text{-}bmtz^{\bullet-}](CF_3SO_3)_3$ were measured from 1.8-300 K in a 1000 Oe DC field (Figure 20a). The $\chi T$ value of 4.50 emu K $mol^{-1}$ at 300 K is slightly higher than the expected spin-only value of 4.13 emu K $mol^{-1}$ for an uncoupled system, suggesting that the orbital angular momentum is not

fully quenched in this complex. The $\chi T$ value exhibits a gradual increase from 300 K to ~45 K, below which temperature the value decreases rapidly to a value of 3.67 emu K $mol^{-1}$ at 2 K. At T = 1.8 K the magnetization as function of magnetic field does not saturate at 7 T (Figure 20b) and is lower than the value of 5 $\mu_B$ corresponding to the S = 5/2 pure spin ground state that arises from antiferromagnetic coupling of the $Co^{II}$ ions with the bmtz radical. This provides additional evidence that the orbital magnetic moment is not fully quenched giving rise to a significant single-ion anisotropy. Reduced magnetization data for this complex (Figure 20c) exhibit splitting of the isofield lines, consistent with an anisotropic system or low-lying excited states.

Attempts to fit the susceptibility and magnetization data with PHI,[103] which is based on a -2J spin Hamiltonian, were unsuccessful. The use of a single Co-radical exchange coupling term ($J_{Co\text{-}rad}$) led to fits that were unsatisfactory and with large correlations between the $J_{Co\text{-}rad}$ parameter and the $D_{Co}$ and $g_{Co}$ terms that were also treated as fitting parameters. If both a $J_{Co\text{-}rad}$ term and a $J_{Co\text{-}Co}$ superexchange term were included in the fitting routine, the two J terms were also highly correlated. The inability to fit the magnetic data with a simple spin Hamiltonian based on J, D, and g is not surprising due to the complicated electronic structure of the molecule that results from the anisotropic nature of the $Co^{II}$ ions. In order to obtain a deeper understanding of the electronic structure of this complex and the effects of the electronic structure on the observed magnetic properties we enlisted the help of the theoretician Sophia Klokishner and her research group.

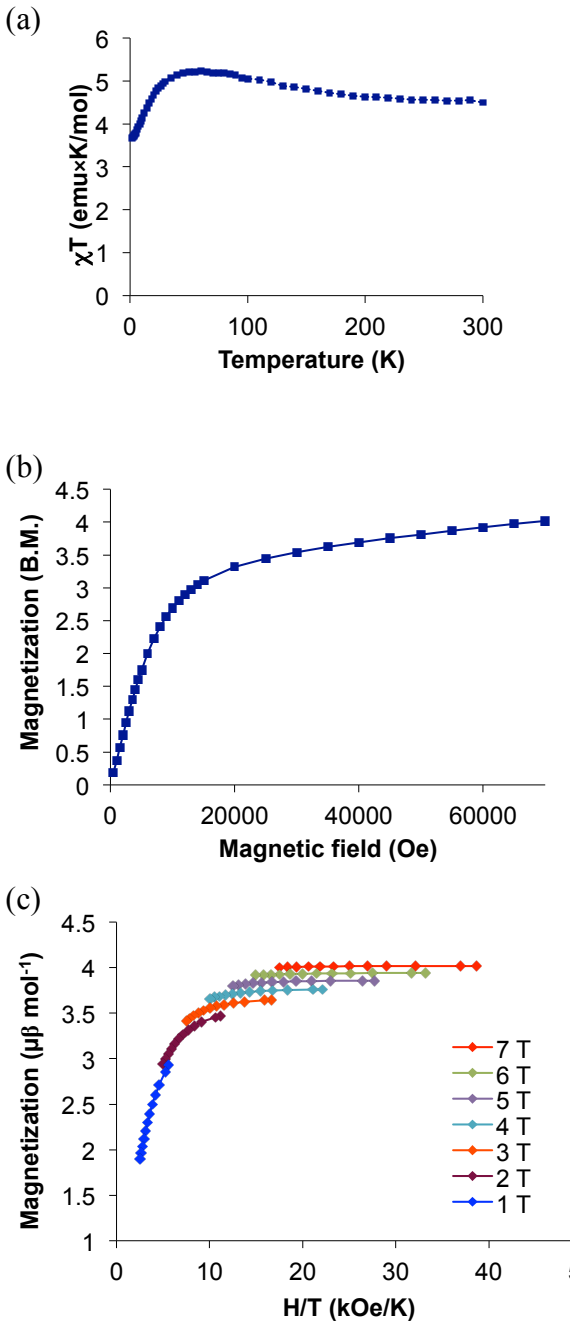


**Figure 20.** DC magnetic properties of [{Co(TPMA)}$_2$-μ-bmtz$^{\bullet-}$](CF$_3$SO$_3$)$_3$. (a) χT product under a 1000 Oe field. (b) plot of M vs. H at 1.8 K. (c) temperature and field dependence of the magnetization. Solid lines are guides for the eye.

The Klokishner group derived the following model Hamiltonian to explain the DC magnetic properties:

$$H = -\frac{3}{2}\lambda\kappa \sum_{i=1,2} \boldsymbol{l}_i \boldsymbol{s}_i + \Delta_{ax} \sum_{i=1,2} \left[ l_{Zi}^2 - \frac{1}{3} l(l+1) \right] + \Delta_{rh} \sum_{i=1,2} (l_{Xi}^2 - l_{Yi}^2) - 2J_{ex}(\boldsymbol{s}_1 \boldsymbol{s}_R + \boldsymbol{s}_R \boldsymbol{s}_2) + \mu_B \boldsymbol{H} \left[ \sum_{i=1,2} \left( -\frac{3}{2}\kappa \boldsymbol{l}_i + g_e \boldsymbol{s}_i \right) + g_e \boldsymbol{s}_R \right]$$

This Hamiltonian operates within the space representing a direct product of cubic $^4T_1$ terms (states with fictitious orbital angular momenta $l$ = 1) and the spin 1/2 states for the radical. The first term in $H$ describes the spin-orbital interaction within each $Co^{II}$ ion, index $i$ enumerates the $Co^{II}$ ions, λ is the spin-orbit coupling parameter and κ is the orbital reduction factor. The second and third terms account for the axial and rhombic components of the crystal field, where $\Delta_{ax}$ and $\Delta_{rh}$ are the corresponding crystal field parameters, and $l_{Zi}$, $l_{Xi}$, and $l_{Yi}$ are the components of the orbital angular momentum operator for the $Co^{II}$ ions. The complex is centrosymmetric and so the principal axes of the crystal field tensors for the $Co^{II}$ ions are parallel and the molecular frame axes $X$, $Y$, and $Z$ were chosen to be parallel to the crystallographic axes, with Z lying approximately along the Co-tetrazine-Co axis, Y being perpendicular to the bmtz plane, and X in the bmtz plane. The fourth term represents the isotropic exchange interaction between the $Co^{II}$ ions and the radical defined in the framework of the Lines model,[113] $J_{ex}$ is the exchange parameter. Finally, the last term represents the Zeeman interaction including both the orbital and spin components of the $Co^{II}$ ions, where $\mu_B$ is the Bohr magneton, $\boldsymbol{H}$ is the magnetic field and $g_e$ is the electronic Lande factor. For the

spin-orbit coupling parameter the typical value $\lambda = -180$ cm$^{-1}$ was used[114] while the four parameters $\Delta_{ax}$, $\Delta_{rh}$, $\kappa$, and $J_{ex}$ were allowed to vary in course of the fitting procedure. The theoretical $\chi$T and magnetization curves obtained with the set of the best-fit parameters $\Delta_{ax} = 1150$ cm$^{-1}$, $\Delta_{rh} = 280$ cm$^{-1}$, $\kappa = 0.757$ and $J_{ex} = -62.5$ cm$^{-1}$ are shown by solid lines in Figure 21a. This set of parameters reproduces the experimentally observed magnetic behavior of $[\{Co(TPMA)\}_2\text{-}\mu\text{-}bmtz^{\bullet-}](CF_3SO_3)_3$ quite well, with the agreement criteria being equal to 0.9% and 5.8% for $\chi$T vs. T and M vs. H, respectively. The temperature dependence of the main components of the $\chi$T tensor calculated with the best-fit parameters (Figure 21b) reveal that Z is the hard axis of magnetization. This result is similar to the situation of a positive zero field splitting parameter $D$ in the case of pure spin systems. At the same time, the large difference between the $\chi_{XX}T$ and $\chi_{YY}T$ components indicates the presence of strong rhombic anisotropy. At first glance, the use of four adjustable parameters may lead to concerns about over-parameterization. The parameter $J_{ex}$ is essentially uniquely determined by the position of the maximum in the $\chi$T vs. T curve, while the value of the parameter $\kappa$ was assumed to be constrained to the limits typical for a high-spin $Co^{II}$ ion in octahedral surroundings (from 0.6 to 0.9).[113] Taking into account that simultaneous fittings of $\chi$T vs. T and M vs. H were performed, one can assert with a high degree of confidence that the obtained set of the best-fit parameters is the only possible one.

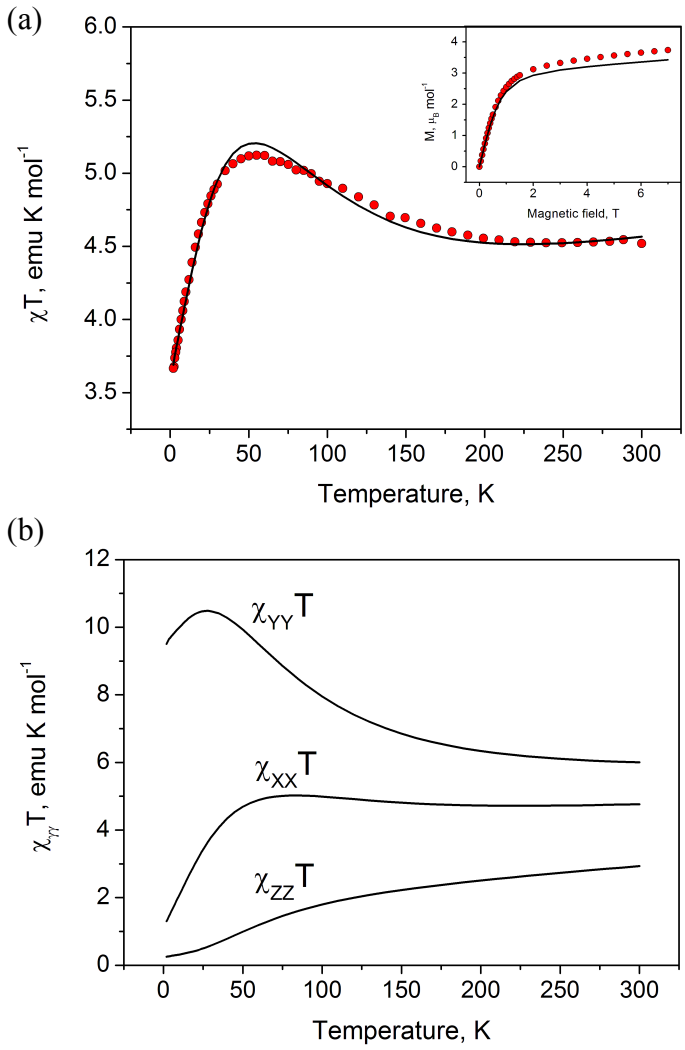


**Figure 21.** Fitted DC magnetic properties for $[\{Co(TPMA)\}_2\text{-}\mu\text{-}bmtz^{\bullet-}](CF_3SO_3)_3$. (a) red circles: experimental χT values. Solid line: theoretical curves using the best-fit parameters described in the main text. Inset: M vs. H at 1.8 K. (b) components of the χT tensor calculated with the parameters described in the main text.

At this point it is important to compare this approach with that used for the examination of the DC magnetic properties of the similar radical-bridged dinuclear $Co^{II}$ complex $[K(DME)_4][dmp_2Nin\{Co[N(SiMe_3)\}_2]$ ($dmp_2Nin^{2-}$ = bis-(2,6-dimethylphenyl)nindigo).[68] In the nindigo work, the energy spectrum of single $Co^{II}$ ions

was determined from *ab initio* calculation of the crystal field terms with subsequent mixing and splitting of these terms by spin-orbit coupling. In contrast, for the current Klokishner model, the energy spectrum was modeled with the aid of the simplified single-ion Hamiltonian which acts within the ground cubic $^4T_1$ terms of each $Co^{II}$ ion and contains the low-symmetry crystal field (axial and rhombic contributions) and spin-orbit coupling operators. In both of these approaches, the exchange coupling was treated in the framework of the Lines model,[113] neglecting the anisotropic orbitally-dependent exchange contributions. Klokishner's model also neglects the rather weak Co-Co superexchange and retains only the dominant Co-radical exchange term. In both approaches the exchange parameters were obtained from a fitting procedure. The authors of the nindigo complex obtained a very strong antiferromagnetic Co-radical direct exchange of $J$ = -132.74 $cm^{-1}$ (defined by the Hamiltonian $-JS_{Co} \bullet S_R$) and a much weaker ferromagnetic Co-Co superexchange interaction.[68]

Dynamic AC magnetic measurements of [{Co(TPMA)}$_2$-μ-bmtz$^{\bullet-}$](CF$_3$SO$_3$)$_3$ in a zero applied DC field revealed no out-of-phase signal but in an 800 Oe DC field a very strong χ'' signal (Figure 22a) is observed. At low temperatures the maxima in χ'' are frequency independent due to rapid quantum tunneling and become frequency dependent at higher temperatures, indicative of an Orbach relaxation process. This is consistent with [{Co(TPMA)}$_2$-μ-bmtz$^{\bullet-}$](CF$_3$SO$_3$)$_3$ belonging to a class of SMMs that display field induced slow magnetic relaxation with axial and strong rhombic anisotropy.[115-119]

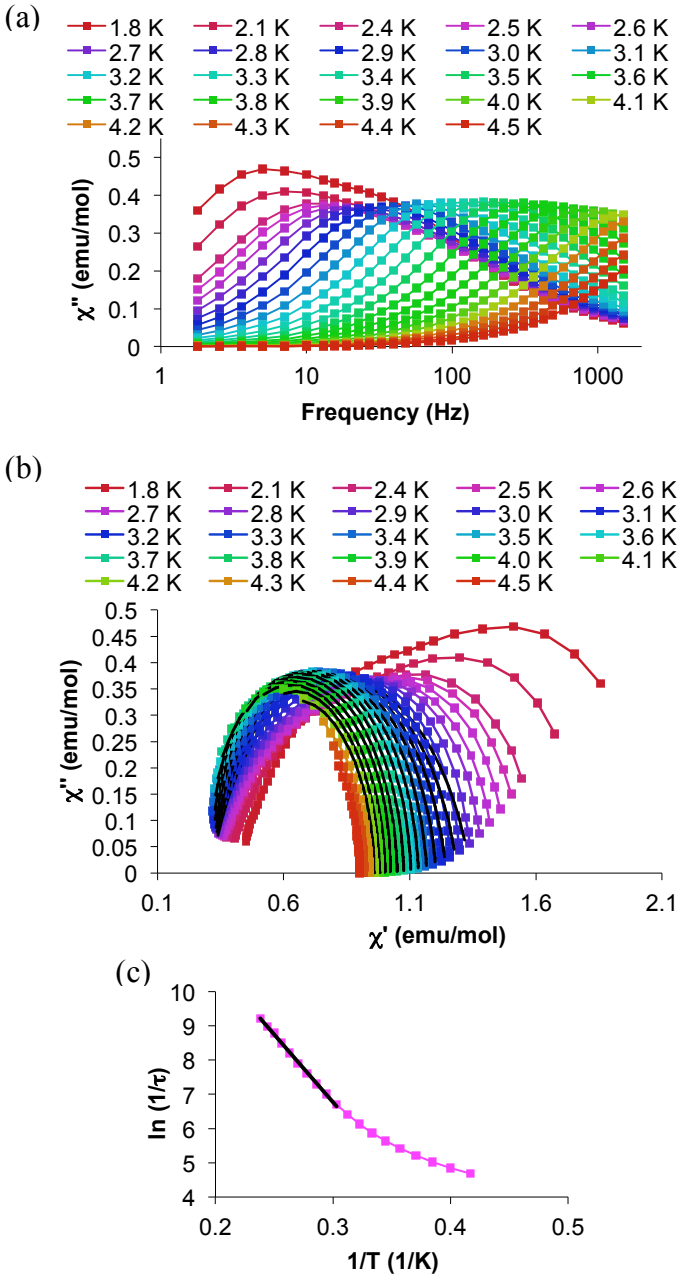


**Figure 22.** AC magnetic measurements for $[\{Co(TPMA)\}_2\text{-}\mu\text{-}bmtz^{\bullet-}](CF_3SO_3)_3$. (a) frequency dependence of $\chi''$ collected in an 800 Oe DC field. Solid lines are guides for the eye. (b) Cole-Cole plot. The colored points and lines are experimental data and guides for the eye, respectively. The solid black lines are the results of fitting the data to a modified Debye function as discussed in the main text. (c) Arrhenius plot. The black line is a linear regression fit to the data which resulted in the barrier height of 39 K with $\tau_o = 8.1 \times 10^{-9}$ s as discussed in the main text.

The Cole-Cole plot (Figure 22b) was fit to a modified Debye function[111,112] to extract the values of $\tau$ and $\alpha$. The $\tau$ values were used to construct an Arrhenius plot that shows two distinct regions (Figure 22c). The low temperature region exhibits non-linear behavior consistent with quantum tunneling. The linear region between 3.3 and 4.2 K, where relaxation is via an Orbach process,[105] was used to extract an energy barrier of 39 K with $\tau_o$ = 8.1 x $10^{-9}$ s, a slightly higher barrier than the 33 K barrier reported for $[K(DME)_4]$ $[dmp_2Nin\{Co[N(SiMe_3)\}_2]$.[68] The $\alpha$ values between 3.3 and 4.2 K are less than 0.12, indicating a narrow distribution of relaxation times.

**Nickel Complexes of the bmtz Ligand**

**Experimental Section**

The reagents TPMA,[95] $[Ni(CH_3CN)_6](BF_4)_2$,[96] $Ni(CF_3SO_3)_2$,[97] and bmtz[91] were prepared by literature procedures. The ligand $L_4^2$•4HCl ($L_4^2$ = $N^1$,$N^2$-dimethyl-$N^1$,$N^2$-bis-(pyridin-2-ylmethyl)ethane-1,2-diamine) was synthesized by Xinyi Wang, a former postdoctoral researcher in the Dunbar group. The reagents $Cp^*_2Co$ (Aldrich), $Cp_2Co$ (Aldrich), $NiCl_2$•$6H_2O$ (J.T. Baker), $TlPF_6$ (Strem), and tris(2-aminoethyl)amine (tren) (Strem) were used as received. The $CH_3CN$ was pre-dried by storage over 3 Å molecular sieves and distilled from 3Å molecular sieves prior to use. The $Et_2O$ was purified using an MBRAUN solvent purification system and then stored over 3 Å molecular sieves in the dry box. Propionitrile and butyronitrile were distilled from 3 Å molecular sieves under an Argon atmosphere and stored in an MBRAUN dry box over 3 Å molecular sieves. Syntheses of the bmtz complexes were performed in an MBRAUN dry box under an $N_2$ atmosphere. Synthesis of $[Ni(L_4^2)(CH_3CN)_2](PF_6)_2$•$2CH_3CN$ was

performed in air with ACS grade solvents that were used as received. Elemental analyses were performed by Atlantic Microlabs, Inc., Norcross, GA. Magnetic measurements were conducted in the temperature range of 1.8 to 300 K using a Quantum Design MPMS-XL SQUID magnetometer equipped with a 7T superconducting magnet. The diamagnetic contribution of the plastic bag used as the sample holder was subtracted from the raw data. Core diamagnetism of the sample was accounted for using Pascal's constants.[98]

*Syntheses*

**[{Ni(TPMA)}$_2$-μ-bmtz$^{\bullet-}$](BF$_4$)$_3$•2CH$_3$CN.** To a pink suspension of bmtz (0.0160 g, 0.07 mmol) in $CH_3CN$ (5 mL) was added $Cp^*_2Co$ (0.0100 g, 0.03 mmol). After stirring the reaction mixture for 30 minutes, an orange solution was obtained and $[Ni(CH_3CN)_6][BF_4]_2$ (.0478 g, 0.1 mmol) and TPMA (0.0290 g, 0.1 mmol) in $CH_3CN$ (5mL) were added. The resulting brown solution was stirred for 24 h and filtered. Brown X-ray quality crystals were obtained after three days by slow diffusion of $Et_2O$ vapor into the filtrate. Yield: 0.0215 g (34%). Analysis calculated (found) for $[\{Ni(TPMA)\}_2(bmtz)](BF_4)_3$ ($C_{46}H_{42}N_{16}B_3F_{12}Ni_2$): C: 46.17% (45.61%), H: 3.54% (3.62%), N: 18.73% (18.70%).

**[{Ni(tren)}$_2$-μ-bmtz$^{\bullet-}$](BF$_4$)$_3$•3CH$_3$CN.** A solution of tren (0.0595 g, 0.407 mmol) in $CH_3CN$ (9 mL) was added to a stirring solution of $[Ni(CH_3CN)_6](BF_4)_2$ (0.1851 g, 0.3867 mmol) in $CH_3CN$ (12.5 mL) to give a purple/pink solution. This $(Ni(tren)(solv)_x](BF_4)_2$ solution was added to a stirring pink suspension of bmtz (0.0463g, 0.194 mmol) in $CH_3CN$ (22.5 mL). The reaction solution was a clear, reddish-

orange color after combining the two solutions. The reaction was allowed to stir for 16 hours and then the solvent was removed under vacuum. The resulting dark red solid was re-dissolved in 10 mL of $CH_3CN$ and filtered to remove a small amount of orange solid. The dark red-orange filtrate was layered over toluene. Red X-ray quality crystals formed in one week. Yield: 0.0204 g (10%).

**[{Ni(TPMA)}$_2$-μ-bmtz$^{\bullet-}$](CF$_3$SO$_3$)$_3$•CH$_3$CN.** To a pink suspension of bmtz (0.0160 g, 0.07 mmol) in $CH_3CN$ (5 mL) was added $Cp_2Co$ (0.0008 g, 0.04 mmol). After the reaction mixture was stirred for 30 minutes, the resulting orange solution was treated with solid $Ni(CF_3SO_3)_2$ (0.0356 g, 0.100 mmol) and TPMA (0.0290 g, 0.100 mmol). The resulting red solution was stirred for 24 h and filtered. Red X-ray quality crystals were obtained after three days by slow diffusion of $Et_2O$ vapor into the filtrate. Yield: 0.0264 g (37%). Analysis calculated (found) for $[\{Ni(TPMA)\}_2bmtz](CF_3SO_3)_3$ ($C_{49}H_{42}N_{16}O_9F_9S_3Ni_2$): C: 42.54% (42.13%), H: 3.06% (3.21%), N: 16.20% (16.50%).

**[Ni(L$_4^2$)(CH$_3$CN)$_2$](PF$_6$)$_2$•2CH$_3$CN.** $NiCl_2$•$6H_2O$ (0.2760 g, 1.161 mmol) was dissolved in 10 mL of MeOH and stirred for 20 minutes to yield a clear green solution. $L_4^2$•4HCl (0.4853 g, 1.166 mmol) was placed in MeOH (10 mL) and stirred for 10 minutes to yield a tan suspension, at which time the $NiCl_2$ solution was rapidly added with a glass Pasteur pipet to the stirring suspension of $L_4^2$•4HCl to give a cloudy green solution. The solution was refluxed at atmospheric pressure for one hour to yield a clear, blue-green solution. After cooling, the solution was gravity filtered through Whatman filter paper to remove a small amount of insoluble white powder, most likely excess ligand. While stirring the blue-green solution, $Et_2O$ was added until a green-blue

powder precipitated. The powder was collected by gravity filtration and washed with 2 x 15 mL of $Et_2O$. Yield: 0.4146 g. This intermediate was not characterized further but is presumed to be $NiCl_2(L_4^2)$. To a solution of $NiCl_2(L_4^2)$ (0.1000 g, 0.2524 mmol) in $CH_3CN$ (5 mL) was added solid $TlPF_6$ (0.0910 g, 0.260 mmol). The blue solution became cloudy upon addition of the $TlPF_6$. The suspension was stirred for one hour, during which time the color changed from blue to purple, and then gravity filtered to remove TlCl. A purple solid was precipitated by slow addition of $Et_2O$. Yield: 0.0960 g (55%). Recrystallization from $CH_3CN/Et_2O$ gave large purple X-ray quality crystals that were shown to be $[Ni(L_4^2)(CH_3CN)_2](PF_6)_2 \bullet 2CH_3CN$ by single crystal X-ray diffraction.

**$[\{Ni(L_4^2)\}_2$-μ-bmtz$^{\bullet-}](PF_6)_3 \bullet 2CH_3CN$.** Quantities of bmtz (0.0250 g, 0.105 mmol) and $Cp_2Co$ (0.0094 g, 0.050 mmol) were stirred in $CH_3CN$ (5 mL) for two hours to give a clear, reddish-orange solution. $[Ni(L_4^2)(CH_3CN)_2](PF_6)_2$ (0.0760 g, 0.108 mmol) was then added and the resulting red solution was stirred for one day. Diffusion of $Et_2O$ vapor into the reaction solution produced red X-ray quality crystals. Yield: 0.0188 g (26%) Analysis calculated (found) for $[\{Ni(L_4^2)\}_2(bmtz)](PF_6)_3 \bullet 2CH_3CN$ ($C_{46}H_{56}N_{18}P_3F_{18}Ni_2$): C: 39.09% (39.51%), H: 3.99% (3.88%), N: 17.84% (17.56%).

*X-ray Crystallographic Measurements*

Single crystal X-ray data were collected on a Bruker APEXII (Mo $K_\alpha$) diffractometer equipped with a CCD detector for all crystals except $[\{Ni(TPMA)\}_2$-μ-bmtz$^{\bullet-}](CF_3SO_3)_3 \bullet CH_3CN$, which was collected on a Bruker GADDS (Cu $K_\alpha$) diffractometer equipped with a Hi-Star MWPC detector. A suitable crystal was affixed

to either a nylon loop or a MiTeGen® MicroLoop with Paratone® oil and placed in a cold stream of $N_{2(g)}$ at 110 K. The frames were integrated with the Bruker APEXII software package[99] and a semi-empirical absorption correction was applied using SADABS as contained within the Bruker APEXII software suite. The structure was solved using SHELXT[100] and refined using SHELXL-2014[101] as implemented in ShelXle, a graphical interface for the SHELX suite of programs.[102] The remaining non-hydrogen atoms were located by alternating cycles of least-squares refinements and difference Fourier maps. All hydrogen atoms were placed in calculated positions. The final refinements were carried out with anisotropic thermal parameters for all non-hydrogen atoms except as otherwise noted. For $[\{Ni(TPMA)\}_2\text{-}\mu\text{-}bmtz^{\bullet-}](BF_4)_3\bullet 2CH_3CN$ one of the tetrafluoroborate anions and both of the acetonitrile molecules were disordered about inversion centers and were modeled with a fixed 50% occupancy in each orientation. The crystal of $[\{Ni(tren)\}_2\text{-}\mu\text{-}bmtz^{\bullet-}](BF_4)_3\bullet 3CH_3CN$ chosen for the structural study was found to be non-merohedrally twinned and was refined as a two-component twin with the twin fractions refining to 0.731 and 0.269. For $[\{Ni(TPMA)\}_2\text{-}\mu\text{-}bmtz^{\bullet-}](CF_3SO_3)_3\bullet CH_3CN$ one of the $[CF_3SO_3]^-$ anions was found on a general position and disordered over two orientations. The occupancy of the two positions was allowed to refine and converged to a 0.486:0.514 occupancy ratio for the two orientations of the $[CF_3SO_3]^-$ anion. The other $[CF_3SO_3]^-$ anion and the $CH_3CN$ molecule are disordered about inversion centers and were modeled with a fixed 50% occupancy. For $[\{Ni(L_4^2)\}_2\text{-}\mu\text{-}bmtz^{\bullet-}](PF_6)_3\bullet 2CH_3CN$ both $[PF_6]^-$ anions reside on general positions and were found disordered about two positions. The occupancies of

the two positions were allowed to refine and converged to 0.760:0.240 and 0.574:0.426 occupancy ratios for the two orientations of the $[PF_6]^-$ anions. Similarity restraints on the thermal parameters were required to achieve a satisfactory convergence and one of the anions could not be successfully refined anisotropically. The $L_4^2$ ligand exhibited whole ligand disorder over two orientations. The occupancy of the two orientations was allowed to refine and converged to a 0.654:0.346 ratio for the two orientations. The ligand could not be successfully refined anisotropically. Significant residual electron density remained after assignment of the main molecule and anions. This residual density had the appearance of $CH_3CN$ molecules but could not be successfully refined as such. The PLATON program SQUEEZE[120] was used to remove this residual density. The number of electrons removed by SQUEEZE is consistent with two $CH_3CN$ molecules for every Ni-bmtz dinuclear unit, which is corroborated by the results of elemental analysis. Further pertinent details of the X-ray refinements are given in Table 10. CCDC: 1021285 ($[\{Ni(TPMA)\}_2\text{-}\mu\text{-}bmtz^{\bullet-}](BF_4)_3 \bullet 2CH_3CN$).

**Table 10.** Crystal and structural refinement data for $Ni^{II}$ bmtz complexes.

| Identification code | $[\{Ni(TPMA)\}_2bmtz](BF_4)_3$ | $[\{Ni(tren)\}_2bmtz](BF_4)_3$ |
|---|---|---|
| Empirical formula | $C_{50}H_{48}B_3F_{12}N_{18}Ni_2$ | $C_{28}H_{51}B_3N_{19}F_{12}Ni_2$ |
| Formula weight | 1278.91 | 1031.72 |
| Temperature/K | 110(2) | 150.15 |
| Crystal system | triclinic | triclinic |
| Space group | P-1 | P-1 |
| a/Å | 8.6413(18) | 9.443(8) |
| b/Å | 9.835(2) | 15.694(12) |
| c/Å | 16.092(3) | 16.863(13) |
| α/° | 91.898(2) | 65.528(10) |
| β/° | 98.419(2) | 81.318(11) |
| γ/° | 101.109(2) | 77.965(11) |
| Volume/$Å^3$ | 1324.9(5) | 2219(3) |
| Z | 1 | 2 |
| $\varrho_{calc}g/cm^3$ | 1.603 | 1.544 |
| $\mu/mm^{-1}$ | 0.810 | 0.947 |
| F(000) | 653.0 | 1062.0 |
| Crystal size/$mm^3$ | 0.126 × 0.110 × 0.052 | 0.085 × 0.063 × 0.041 |
| Radiation | MoKα (λ = 0.71073 Å) | MoKα (λ = 0.71073 Å) |
| 2Θ range for data collection/° | 2.564 to 52.74 | 4.422 to 45.706 |
| Index ranges | $-10 \le h \le 10, -12 \le k \le 12, -20 \le l \le 20$ | $-10 \le h \le 10, -15 \le k \le 17, 0 \le l \le 18$ |
| Reflections collected | 14063 | 6057 |
| Independent reflections | 5361 [$R_{int} = 0.0210$, $R_{sigma} = 0.0261$] | 6057 [$R_{int} = 0.0000$, $R_{sigma} = 0.0885$] |
| Data/restraints/parameters | 5361/111/435 | 6057/0/581 |
| Goodness-of-fit on $F^{2\ c}$ | 1.054 | 1.023 |
| Final R indexes [I>=2σ (I)] | $R_1{}^a = 0.0480$, $wR_2{}^b = 0.1171$ | $R_1{}^a = 0.0633$, $wR_2{}^b = 0.1489$ |
| Final R indexes [all data] | $R_1{}^a = 0.0529$, $wR_2{}^b = 0.1202$ | $R_1{}^a = 0.0980$, $wR_2{}^b = 0.1699$ |
| Largest diff. peak/hole / e $Å^{-3}$ | 1.13/-0.78 | 1.12/-0.64 |

**Table 10** Continued

| | | |
|---|---|---|
| Identification code | $[\{Ni(TPMA)\}_2bmtz](CF_3SO_3)_3$ | $[\{Ni(TPMA)\}_2bmtz](CF_3SO_3)_3$ |
| Empirical formula | $C_{51}H_{45}N_{17}O_9F_9S_3Ni_2$ | $C_{51}H_{47}N_{17}O_9F_9S_3Ni_2$ |
| Formula weight | 1424.61 | 1426.65 |
| Temperature/K | 110.15 | 110.15 |
| Crystal system | triclinic | triclinic |
| Space group | P-1 | P-1 |
| a/Å | 8.7701(6) | 8.873(16) |
| b/Å | 10.4280(7) | 15.90(3) |
| c/Å | 15.8794(11) | 22.88(4) |
| α/° | 93.488(4) | 108.240(14) |
| β/° | 97.857(4) | 97.428(15) |
| γ/° | 94.656(4) | 97.088(14) |
| Volume/Å$^3$ | 1430.05(17) | 2994(9) |
| Z | 1 | 2 |
| $\varrho_{calc}$g/cm$^3$ | 1.6541 | 1.582 |
| μ/mm$^{-1}$ | 2.741 | 0.831 |
| F(000) | 724.6 | 1458.0 |
| Crystal size/mm$^3$ | 0.11 × 0.06 × 0.01 | 0.165 × 0.112 × 0.06 |
| Radiation | Cu Kα (λ = 1.54178 Å) | MoKα (λ = 0.71073 Å) |
| 2Θ range for data collection/° | 5.64 to 117.9 | 2.738 to 33.514 |
| Index ranges | $-9 \le h \le 9, -11 \le k \le 11, -17 \le l \le 17$ | $-7 \le h \le 7, -12 \le k \le 12, 0 \le l \le 18$ |
| Reflections collected | 16653 | 3322 |
| Independent reflections | 4051 [$R_{int}$ = 0.1382, $R_{sigma}$ = 0.0907] | 3322 [$R_{int}$ = 0.0000, $R_{sigma}$ = 0.1316] |
| Data/restraints/parameters | 4051/0/394 | 3322/0/377 |
| Goodness-of-fit on F$^{2\ c}$ | 1.132 | 1.569 |
| Final R indexes [I>=2σ (I)] | $R_1{}^a$ = 0.0679, $wR_2{}^b$ = 0.1734 | $R_1{}^a$ = 0.1185, $wR_2{}^b$ = 0.2678 |
| Final R indexes [all data] | $R_1{}^a$ = 0.0850, $wR_2{}^b$ = 0.1824 | $R_1{}^a$ = 0.1674, $wR_2{}^b$ = 0.2953 |
| Largest diff. peak/hole / e Å$^{-3}$ | 0.98/-1.01 | 1.05/-0.78 |

**Table 10** Continued

| | | |
|---|---|---|
| Identification code | $[Ni(L_4^2)(CH_3CN)_2](PF_6)_2$ | $[\{Ni(L_4^2)\}_2bmtz](PF_6)_3$ |
| Empirical formula | $C_{24}H_{34}N_8F_{12}P_2Ni$ | $C_{46}H_{56}N_{18}F_{18}P_3Ni_2$ |
| Formula weight | 783.24 | 1413.41 |
| Temperature/K | 110.15 | 110.15 |
| Crystal system | orthorhombic | monoclinic |
| Space group | Pnna | $P2_1/n$ |
| a/Å | 13.4474(8) | 12.527(4) |
| b/Å | 13.6085(8) | 17.011(5) |
| c/Å | 17.3805(10) | 13.926(4) |
| α/° | 90 | 90 |
| β/° | 90 | 99.811(4) |
| γ/° | 90 | 90 |
| Volume/Å$^3$ | 3180.6(3) | 2924.1(14) |
| Z | 4 | 2 |
| $\varrho_{calc}$g/cm$^3$ | 1.636 | 1.605 |
| μ/mm$^{-1}$ | 0.813 | 0.835 |
| F(000) | 1600.0 | 1442.0 |
| Crystal size/mm$^3$ | 0.363 × 0.269 × 0.155 | 1.385 × 0.564 × 0.190 |
| Radiation | MoKα (λ = 0.71073 Å) | MoKα (λ = 0.71073 Å) |
| 2Θ range for data collection/° | 3.802 to 55.788 | 3.814 to 51.576 |
| Index ranges | $-17 \le h \le 17, -17 \le k \le 17, -22 \le l \le 22$ | $-15 \le h \le 15, -20 \le k \le 20, -16 \le l \le 16$ |
| Reflections collected | 36365 | 29491 |
| Independent reflections | 3798 [$R_{int}$ = 0.0418, $R_{sigma}$ = 0.0206] | 5581 [$R_{int}$ = 0.0516, $R_{sigma}$ = 0.0390] |
| Data/restraints/parameters | 3798/0/217 | 5581/63/349 |
| Goodness-of-fit on F$^2$ [c] | 1.086 | 1.087 |
| Final R indexes [I>=2σ (I)] | $R_1$[a] = 0.0347, $wR_2$[b] = 0.1038 | $R_1$[a] = 0.0827, $wR_2$[b] = 0.1892 |
| Final R indexes [all data] | $R_1$[a] = 0.0383, $wR_2$[b] = 0.1072 | $R_1$[a] = 0.0944, $wR_2$[b] = 0.1954 |
| Largest diff. peak/hole / e Å$^{-3}$ | 0.42/-0.65 | 0.98/-0.73 |

[a] $R_1 = \Sigma \big| \, |F_o| - |F_c| \, \big| / \Sigma |F_o|$. [b] $wR_2 = \{\Sigma [w(F_o^2 - F_c^2)^2] / \Sigma w(F_o^2)^2]\}^{1/2}$. [c] Goodness-of-fit $= \{\Sigma [w(F_o^2 - F_c^2)^2]/(n-p)\}^{1/2}$, where $n$ is the number of reflections and $p$ is the total number of parameters refined.

## Results and Discussion

*Syntheses*

As a general note, the syntheses of all of the dinuclear bmtz complexes presented herein were performed with an excess of bmtz. If bmtz is used in stoichiometric amounts, the color changes throughout the course of the reaction are similar but no crystalline product is obtained from the reaction.

**[{Ni(TPMA)}$_2$-μ-bmtz$^{\bullet-}$](BF$_4$)$_3$•2CH$_3$CN.** This compound was prepared by reacting a solution of *in situ* generated [Ni(TPMA)(solv)$_x$](BF$_4$)$_2$ with the neutral form of bmtz. During the course of the reaction, the bmtz ligand was spontaneously reduced to the radical anion form. Higher yields of crystalline material were obtained by adding the reducing agent $Cp^*_2Co$ to the reaction mixture.

**[{Ni(tren)}$_2$-μ-bmtz$^{\bullet-}$](BF$_4$)$_3$•3CH$_3$CN.** A solution of *in situ* generated [Ni(tren)(solv)$_x$](BF$_4$)$_2$ was reacted with the neutral form of bmtz. During the course of the reaction the bmtz ligand was spontaneously reduced to the radical anion form. The crystallization of this complex proved to be irreproducible. Numerous attempts with the same synthetic conditions that led to the initial crystallization of the complex were performed, as were variations in solution concentration, scale of the reaction, and precipitation with other crystallizing solvents. In one such trial, orange crystals of poor X-ray quality were obtained but the unit cell was different than the expected unit cell for [{Ni(tren)}$_2$-μ-bmtz$^{\bullet-}$](BF$_4$)$_3$•3CH$_3$CN. The crystal did not diffract well enough for a full structure solution but it appears that the product is a different solvate of the [{Ni(tren)}$_2$-μ-bmtz$^{\bullet-}$](BF$_4$)$_3$ radical complex.

**[{Ni(TPMA)}$_2$-μ-bmtz$^{\bullet-}$](CF$_3$SO$_3$)$_3$•CH$_3$CN.** This compound was synthesized in a manner identical to the $[BF_4]^-$ salt reported above.

**[Ni(L$_4^2$)(CH$_3$CN)$_2$](PF$_6$)$_2$•2CH$_3$CN.** Contrary to the synthesis of the TPMA and tren compounds, this solvated intermediate was isolated to facilitate the use of the dry box for synthesis of the dinuclear $Ni^{II}$ bmtz complex. The HCl salt of $L_4^2$ was reacted with $NiCl_2$ in MeOH to produce a product that is presumed to be $NiCl_2(L_4^2)$. $TlPF_6$ was used to replace the chloride ions with hexafluorophosphate anions to facilitate coordination to bmtz. Re-crystallization of this product from $CH_3CN/Et_2O$ produced anhydrous and acid free $[Ni(L_4^2)(CH_3CN)_2](PF_6)_2•2CH_3CN$ that was suitable for use in the dry box as a precursor for forming dinuclear bmtz complexes.

**[{Ni(L$_4^2$)}$_2$-μ-bmtz$^{\bullet-}$](PF$_6$)$_3$•2CH$_3$CN.** The synthesis of this complex was performed in a manner similar to the TPMA and tren analogs. The pre-formed $[Ni(L_4^2)(CH_3CN)_2]^{2+}$ precursor was reacted with bmtz in the presence of $Cp_2Co$ to produce the desired $[\{Ni(L_4^2)\}_2\text{-}\mu\text{-bmtz}^{\bullet-}](PF_6)_3$ complex.

*Single Crystal X-ray Diffraction*

**[{Ni(TPMA)}$_2$-μ-bmtz$^{\bullet-}$](BF$_4$)$_3$•2CH$_3$CN.** The cationic unit of $[\{Ni(TPMA)\}_2\text{-}\mu\text{-bmtz}^{\bullet-}](BF_4)_3$ consists of two $[Ni(TPMA)]^{2+}$ fragments bridged by a bmtz ligand in the radical anion form. Only one of the Ni ions is crystallographically unique and resides in a distorted octahedral coordination environment. The geometrical constraints of the ligand lead to $N_{py}$-Ni-$N_{amine}$ angles for the $[Ni(TPMA)]^{2+}$ fragment in the range 77.94(10) - 81.52(9)°, much more acute than the expected 90° angles for an ideal octahedral coordination geometry. The Ni-N bond lengths also vary significantly from

2.035(2) to 2.236(3) Å. This distortion is best described as a meridional elongation in which the Ni1-N1, Ni1-N3, and Ni1-N5 bonds form one meridian of the octahedron spanning from the bmtz pyrimidine ring to the bridgehead amine N atom of TPMA and one of the pyridine rings of TPMA with an average bond length of 2.16 Å. The Ni1-N2, Ni1-N4, and Ni1-N7 bonds form the other meridian of the octahedron with an average bond length of 2.07 Å.

Evidence for the radical anion oxidation state of the bmtz ligand is derived from the tetrazine N-N bond lengths. At 1.381(3) Å, the N7-N8a distance is consistent with previous reports of the radical anion state of bmtz and significantly longer than the 1.33 Å expected for the neutral form of the ligand.[92] In addition, charge balance requires the cationic framework to have a 3+ charge, consistent with two $Ni^{II}$ centers and one ligand radical. The thermal ellipsoid plot of $[\{Ni(TPMA)\}_2\text{-}\mu\text{-}bmtz^{\bullet-}](BF_4)_3$ is displayed in Figure 23 and Table 11 lists bond distances and angles. There is evidence of π-π stacking between the pyrimidine rings of bmtz and the pyridine rings of TPMA (Figure 24). The shortest atom-to-atom contact between these rings is 3.38 Å, which is within the accepted range of distances for π-π stacking interactions.[121] The intramolecular Ni-Ni separation is 6.81 Å, with the closest intermolecular Ni-Ni distance being 8.64 Å.

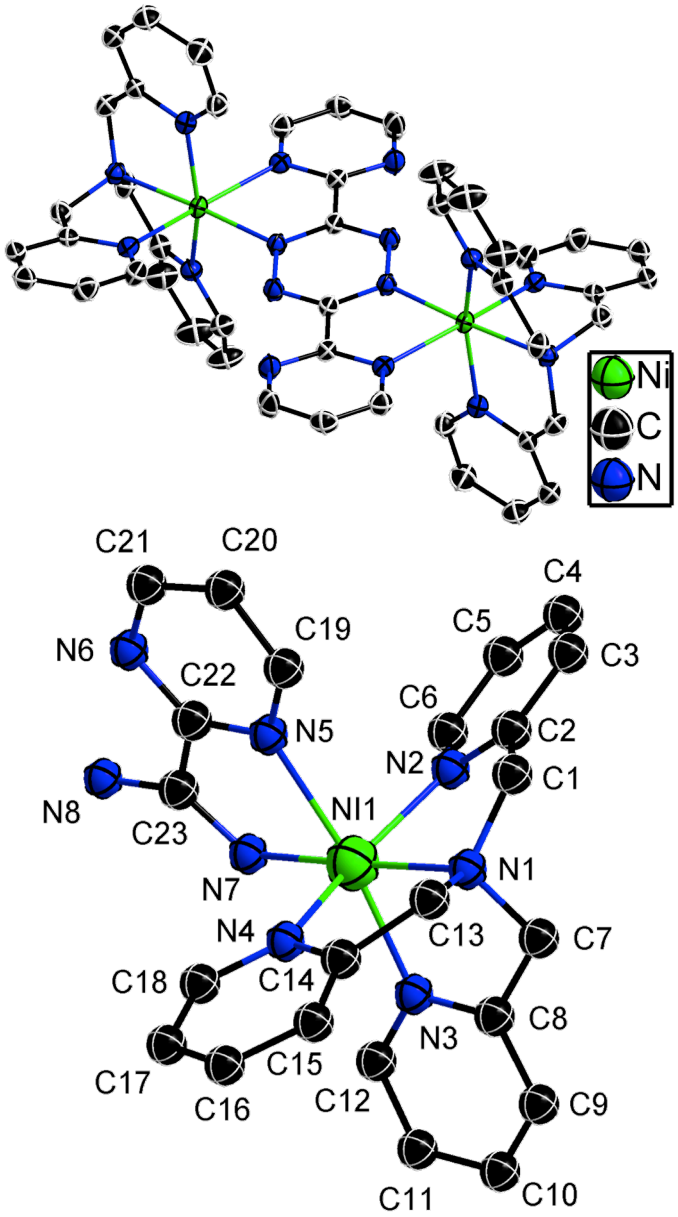


**Figure 23.** Thermal ellipsoid plot and atom labeling scheme for the asymmetric unit of $[\{Ni(TPMA)\}_2\text{-}\mu\text{-}bmtz^{\bullet-}]^{3+}$ in $[\{Ni(TPMA)\}_2\text{-}\mu\text{-}bmtz^{\bullet-}](BF_4)_3$. Thermal ellipsoids are drawn at the 50% probability level. H atoms were omitted for the sake of clarity.

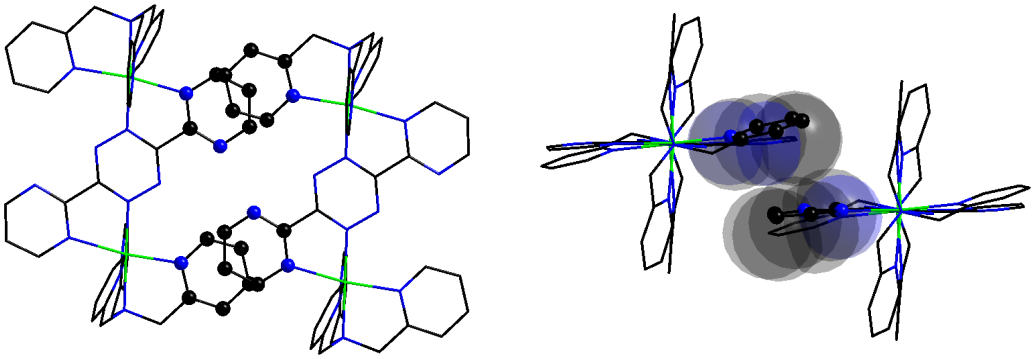

**Figure 24.** Plots emphasizing the π-π stacking interactions in [{Ni(TPMA)}$_2$-μ-bmtz$^{\bullet-}$](BF$_4$)$_3$.

**Table 11.** Bond distances and angles for [{Ni(TPMA)}$_2$-μ-bmtz$^{\bullet-}$](BF$_4$)$_3$.

| Atom | Atom | Length/Å | Atom | Atom | Length/Å |
|---|---|---|---|---|---|
| Ni1 | N7 | 2.035(2) | N6 | C21 | 1.333(4 |
| Ni1 | N4 | 2.081(2) | N8 | C23 | 1.317(4) |
| Ni1 | N2 | 2.084(3) | N8 | N7$^1$ | 1.381(3) |
| Ni1 | N3 | 2.122(3) | C8 | C9 | 1.386(4) |
| Ni1 | N1 | 2.124(2) | C9 | C10 | 1.375(5) |
| Ni1 | N5 | 2.236(3) | C11 | C12 | 1.377(4) |
| B1_1 | F1_1 | 1.384(4) | C11 | C10 | 1.383(5) |
| B1_1 | F2_1 | 1.386(4) | C15 | C14 | 1.383(4) |
| B1_1 | F4_1 | 1.389(4) | C15 | C16 | 1.389(5) |
| B1_1 | F3_1 | 1.398(4) | C16 | C17 | 1.378(5) |
| C1 | N1 | 1.474(4) | C17 | C18 | 1.383(5) |
| C1 | C2 | 1.512(4) | C19 | C20 | 1.378(5) |
| N1 | C13 | 1.482(4) | C20 | C21 | 1.381(5) |
| N1 | C7 | 1.486(4) | C22 | C23 | 1.487(4) |
| C2 | N2 | 1.343(4) | C14 | C13 | 1.502(4) |
| C2 | C3 | 1.377(5) | B1_2 | F4_2 | 1.378(6) |
| N2 | C6 | 1.343(4) | B1_2 | F2_2 | 1.388(6) |
| C3 | C4 | 1.380(5) | B1_2 | F1_2 | 1.388(6) |
| N3 | C8 | 1.343(4) | B1_2 | F3_2 | 1.415(6) |
| N3 | C12 | 1.351(4) | N1_3 | C1_3 | 0.799(9) |
| C4 | C5 | 1.379(5) | C1_3 | C2_3 | 1.584(11) |

**Table 11** Continued

| Atom | Atom | Length/Å | Atom | Atom | Length/Å |
|---|---|---|---|---|---|
| N4 | C18 | 1.341(4) | C2_3 | H2A_3 | 0.9800 |
| N4 | C14 | 1.347(4) | C2_3 | H2B_3 | 0.9800 |
| C5 | C6 | 1.375(5) | C2_3 | H2C_3 | 0.9800 |
| N5 | C22 | 1.338(4) | N1_4 | C1_4 | 0.815(10) |
| N5 | C19 | 1.343(4) | C1_4 | C2_4 | 1.590(11) |
| N7 | C23 | 1.335(4) | C2_4 | H2A_4 | 0.9800 |
| N7 | N8[1] | 1.381(3) | C2_4 | H2B_4 | 0.9800 |
| C7 | C8 | 1.499(4) | C2_4 | H2C_4 | 0.9800 |
| N6 | C22 | 1.324(4) | | | |

[1]1-X, 1-Y, -Z

| Atom | Atom | Atom | Angle/° | Atom | Atom | Atom | Angle/° |
|---|---|---|---|---|---|---|---|
| N7 | Ni1 | N4 | 101.93(10) | N1 | C7 | C8 | 113.0(2) |
| N7 | Ni1 | N2 | 98.74(10) | C22 | N6 | C21 | 115.4(3) |
| N4 | Ni1 | N2 | 157.43(10) | N2 | C6 | C5 | 122.7(3) |
| N7 | Ni1 | N3 | 98.14(10) | C23 | N8 | N7[1] | 115.7(2) |
| N4 | Ni1 | N3 | 86.61(10) | N3 | C8 | C9 | 122.2(3) |
| N2 | Ni1 | N3 | 99.40(10) | N3 | C8 | C7 | 116.6(3) |
| N7 | Ni1 | N1 | 176.50(10) | C9 | C8 | C7 | 121.0(3) |
| N4 | Ni1 | N1 | 81.52(9) | C10 | C9 | C8 | 119.4(3) |
| N2 | Ni1 | N1 | 77.94(10) | C12 | C11 | C10 | 119.0(3) |
| N3 | Ni1 | N1 | 81.42(9) | C9 | C10 | C11 | 118.8(3) |
| N7 | Ni1 | N5 | 75.86(9) | C14 | C15 | C16 | 118.9(3) |
| N4 | Ni1 | N5 | 89.49(9) | C17 | C16 | C15 | 119.1(3) |
| N2 | Ni1 | N5 | 86.83(9) | C16 | C17 | C18 | 119.0(3) |
| N3 | Ni1 | N5 | 172.02(9) | N4 | C18 | C17 | 122.3(3) |
| N1 | Ni1 | N5 | 104.90(9) | N5 | C19 | C20 | 121.9(3) |
| F1_1 | B1_1 | F2_1 | 109.5(3) | C19 | C20 | C21 | 117.0(3) |
| F1_1 | B1_1 | F4_1 | 109.5(3) | N6 | C21 | C20 | 122.6(3) |
| F2_1 | B1_1 | F4_1 | 109.9(3) | N6 | C22 | N5 | 127.7(3) |
| F1_1 | B1_1 | F3_1 | 108.4(3) | N6 | C22 | C23 | 116.5(3) |
| F2_1 | B1_1 | F3_1 | 111.1(3) | N5 | C22 | C23 | 115.8(2) |

**Table 11** Continued

| Atom | Atom | Atom | Angle/° | Atom | Atom | Atom | Angle/° |
|---|---|---|---|---|---|---|---|
| F4_1 | B1_1 | F3_1 | 108.4(3) | N8 | C23 | N7 | 127.9(3) |
| N1 | C1 | C2 | 110.1(2) | N8 | C23 | C22 | 117.3(3) |
| C1 | N1 | C13 | 112.8(2) | N7 | C23 | C22 | 114.8(2) |
| C1 | N1 | C7 | 108.1(2) | N4 | C14 | C15 | 122.0(3) |
| C13 | N1 | C7 | 112.1(2) | N4 | C14 | C13 | 116.2(3) |
| C1 | N1 | Ni1 | 107.56(18) | C15 | C14 | C13 | 121.5(3) |
| C13 | N1 | Ni1 | 108.49(18) | N1 | C13 | C14 | 112.4(2) |
| C7 | N1 | Ni1 | 107.55(18) | N3 | C12 | C11 | 122.6(3) |
| N2 | C2 | C3 | 122.3(3) | F4_2 | B1_2 | F2_2 | 108.9(6) |
| N2 | C2 | C1 | 116.2(3) | F4_2 | B1_2 | F1_2 | 112.8(6) |
| C3 | C2 | C1 | 121.5(3) | F2_2 | B1_2 | F1_2 | 112.7(5) |
| C6 | N2 | C2 | 118.2(3) | F4_2 | B1_2 | F3_2 | 102.9(5) |
| C6 | N2 | Ni1 | 126.7(2) | F2_2 | B1_2 | F3_2 | 117.0(7) |
| C2 | N2 | Ni1 | 114.0(2) | F1_2 | B1_2 | F3_2 | 102.1(5) |
| C2 | C3 | C4 | 118.9(3) | N1_3 | C1_3 | C2_3 | 174.0(16) |
| C8 | N3 | C12 | 117.9(3) | C1_3 | C2_3 | H2A_3 | 109.5 |
| C8 | N3 | Ni1 | 113.1(2) | C1_3 | C2_3 | H2B_3 | 109.5 |
| C12 | N3 | Ni1 | 128.3(2) | H2A_3 | C2_3 | H2B_3 | 109.5 |
| C5 | C4 | C3 | 119.2(3) | C1_3 | C2_3 | H2C_3 | 109.5 |
| C18 | N4 | C14 | 118.6(3) | H2A_3 | C2_3 | H2C_3 | 109.5 |
| C18 | N4 | Ni1 | 126.6(2) | H2B_3 | C2_3 | H2C_3 | 109.5 |
| C14 | N4 | Ni1 | 114.22(19) | N1_4 | C1_4 | C2_4 | 142.9(13) |
| C6 | C5 | C4 | 118.7(3) | C1_4 | C2_4 | H2A_4 | 109.5 |
| C22 | N5 | C19 | 115.3(3) | C1_4 | C2_4 | H2B_4 | 109.5 |
| C22 | N5 | Ni1 | 112.86(19) | H2A_4 | C2_4 | H2B_4 | 109.5 |
| C19 | N5 | Ni1 | 131.7(2) | C1_4 | C2_4 | H2C_4 | 109.5 |
| C23 | N7 | N8[1] | 116.4(2) | H2A_4 | C2_4 | H2C_4 | 109.5 |
| C23 | N7 | Ni1 | 120.25(19) | H2B_4 | C2_4 | H2C_4 | 109.5 |
| N8[1] | N7 | Ni1 | 123.32(18) | | | | |

[1]1-X, 1-Y, -Z

**[{Ni(tren)}$_2$-μ-bmtz$^{\bullet-}$](BF$_4$)$_3$•3CH$_3$CN.** The cationic unit of [{Ni(tren)}$_2$-μ-bmtz$^{\bullet-}$](BF$_4$)$_3$ consists of two [Ni(tren)]$^{2+}$ fragments bridged by a bmtz ligand in the radical anion form. The asymmetric unit consists of two independent halves of the dinuclear molecule, with each half molecule residing on an inversion center. The Ni ions reside in distorted octahedral coordination environments. The geometrical constraints of the ligand lead to $N_{bridgehead}$-Ni-$N_{NH2}$ angles for the [Ni(tren)]$^{2+}$ fragments in the range of 82.5(2) - 83.9(2)°, more acute than the expected 90° angles for a perfect octahedral coordination geometry but less distorted than the aforementioned TPMA analog. These acute angles result in the projection of the $Ni^{II}$ ion out of the mean N3 plane formed by the $NH_2$ arms of the tren ligand by 0.250 Å. The Ni-N bond lengths also vary significantly from 2.074(6) to 2.134(6) Å. This distortion is best described as a meridional elongation in which the Ni1-N15, Ni1-N14, and Ni1-N9 bonds form one meridian of the octahedron spanning from the bmtz pyrimidine ring to the bridgehead amine N atom of TPMA and to the tetrazine N atom with an average bond length of 2.09 Å. The Ni1-N10, Ni1-N11, and Ni1-N12 bonds form the other meridian of the octahedron with an average bond length of 2.11 Å.

Evidence for the radical anion oxidation state of the bmtz ligand is found in the tetrazine N-N bond lengths, which are 1.389(8) Å for both N13-N14 and N5-N6. Charge balance also requires the cationic framework to have a 3+ charge, which is consistent with a ligand radical. The thermal ellipsoid plot of [{Ni(tren)}$_2$-μ-bmtz$^{\bullet-}$](BF$_4$)$_3$ is displayed in Figure 25 and Table 12 lists bond distances and angles. There is the appearance of π-π stacking between the pyrimidine rings of bmtz in adjacent

molecules (Figure 26) but the shortest atom-to-atom contact between these rings is 4.94 Å, much longer than what is traditionally considered for π-π stacking interactions,[121] rendering a discussion of π-π stacking interactions inappropriate for this complex. The intramolecular Ni-Ni separation is 6.89 Å, with the closest intermolecular Ni-Ni distance being 8.74 Å.

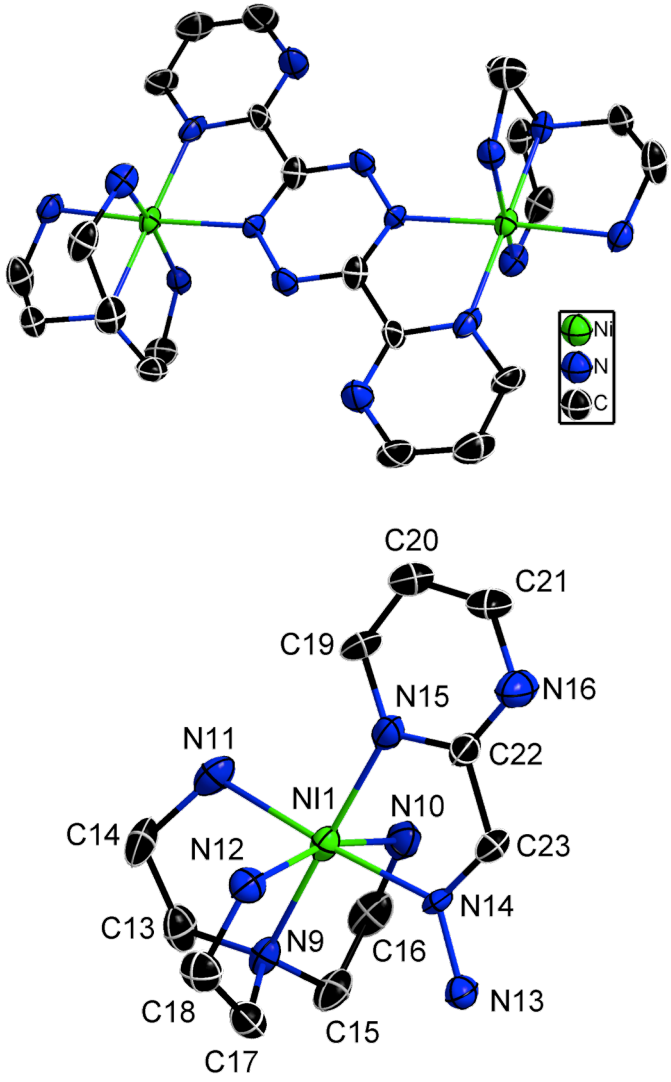


**Figure 25.** Thermal ellipsoid plot of the cationic unit of $[\{Ni(tren)\}_2\text{-}\mu\text{-}bmtz^{\bullet-}](BF_4)_3$ and atom labeling scheme of the asymmetric unit. Thermal ellipsoids are drawn at the 50% probability level. H atoms were omitted for the sake of clarity.

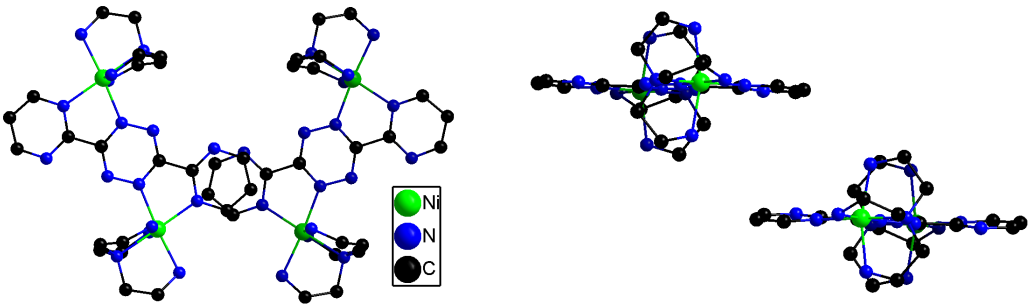


**Figure 26.** Intermolecular packing arrangement in [{Ni(tren)}$_2$-μ-bmtz$^{\bullet-}$](BF$_4$)$_3$.

**Table 12.** Bond distances and angles for [{Ni(tren)}$_2$-μ-bmtz$^{\bullet-}$](BF$_4$)$_3$.

| Atom | Atom | Length/Å | Atom | Atom | Length/Å |
|---|---|---|---|---|---|
| Ni1 | N9 | 2.092(6) | Ni2 | N1 | 2.074(6) |
| Ni1 | N10 | 2.102(6) | Ni2 | N2 | 2.102(6) |
| Ni1 | N11 | 2.100(6) | Ni2 | N3 | 2.134(6) |
| Ni1 | N12 | 2.113(6) | Ni2 | N4 | 2.096(6) |
| Ni1 | N14 | 2.083(6) | Ni2 | N6 | 2.089(6) |
| Ni1 | N15 | 2.094(6) | Ni2 | N7 | 2.092(6) |
| F1 | B2 | 1.365(11) | F2 | B2 | 1.375(12) |
| N9 | C13 | 1.485(9) | N1 | C1 | 1.473(10) |
| N9 | C15 | 1.470(9) | N1 | C3 | 1.504(9) |
| N9 | C17 | 1.470(9) | N1 | C5 | 1.480(10) |
| F9 | B3 | 1.312(12) | N2 | C4 | 1.483(10) |
| N10 | C16 | 1.480(10) | N3 | C6 | 1.475(10) |
| F10 | B3 | 1.304(12) | F3 | B2 | 1.365(11) |
| N11 | C14 | 1.468(10) | N4 | C7 | 1.475(10) |
| F11 | B3 | 1.272(13) | N5 | N6 | 1.389(8) |
| N12 | C18 | 1.474(10) | N5 | C8$^2$ | 1.323(9) |
| F12 | B2 | 1.326(13) | N6 | C8 | 1.323(9) |
| N13 | N14 | 1.389(8) | N7 | C9 | 1.339(9) |
| N13 | C23$^1$ | 1.318(9) | N7 | C10 | 1.331(10) |
| N14 | C23 | 1.335(9) | N8 | C9 | 1.326(10) |
| N15 | C19 | 1.346(9) | N8 | C12 | 1.333(11) |
| N15 | C22 | 1.335(9) | F8 | B3 | 1.318(11) |
| N16 | C21 | 1.326(10) | C1 | C7 | 1.515(11) |

**Table 12** Continued

| Atom | Atom | Length/Å | Atom | Atom | Length/Å |
|---|---|---|---|---|---|
| N16 | C22 | 1.333(9) | C3 | C4 | 1.506(12) |
| C13 | C14 | 1.492(11) | C5 | C6 | 1.510(11) |
| C15 | C16 | 1.497(11) | C8 | N5[2] | 1.323(9) |
| C17 | C18 | 1.522(11) | C8 | C9 | 1.504(10) |
| C19 | C20 | 1.369(12) | C10 | C11 | 1.383(12) |
| C20 | C21 | 1.380(12) | C11 | C12 | 1.352(13) |
| C22 | C23 | 1.475(10) | N18 | C27 | 1.135(10) |
| C23 | N13[1] | 1.318(9) | C26 | C27 | 1.450(12) |
| B1 | F4 | 1.373(13) | N19 | C29 | 1.142(13) |
| B1 | F5 | 1.306(11) | C28 | C29 | 1.451(15) |
| B1 | F6 | 1.336(12) | N17 | C25 | 1.135(12) |
| B1 | F7 | 1.335(11) | C24 | C25 | 1.460(14) |

[1]1-X, 1-Y, 1-Z; [2]2-X, 2-Y, 1-Z

| Atom | Atom | Atom | Angle/° | Atom | Atom | Atom | Angle/° |
|---|---|---|---|---|---|---|---|
| N9 | Ni1 | N10 | 83.4(2) | N2 | Ni2 | N3 | 92.2(3) |
| N9 | Ni1 | N11 | 82.6(2) | N4 | Ni2 | N2 | 93.0(3) |
| N9 | Ni1 | N12 | 83.0(2) | N4 | Ni2 | N3 | 164.8(3) |
| N9 | Ni1 | N15 | 178.8(2) | N6 | Ni2 | N2 | 175.1(3) |
| N10 | Ni1 | N12 | 164.2(2) | N6 | Ni2 | N3 | 87.0(2) |
| N11 | Ni1 | N10 | 94.1(3) | N6 | Ni2 | N4 | 89.0(2) |
| N11 | Ni1 | N12 | 92.1(2) | N6 | Ni2 | N7 | 77.3(2) |
| N14 | Ni1 | N9 | 101.9(2) | N7 | Ni2 | N2 | 98.1(3) |
| N14 | Ni1 | N10 | 86.9(2) | N7 | Ni2 | N3 | 98.2(3) |
| N14 | Ni1 | N11 | 175.5(2) | N7 | Ni2 | N4 | 95.2(3) |
| N14 | Ni1 | N12 | 88.0(2) | C1 | N1 | Ni2 | 104.8(4) |
| N14 | Ni1 | N15 | 77.0(2) | C1 | N1 | C3 | 111.2(6) |
| N15 | Ni1 | N10 | 96.1(2) | C1 | N1 | C5 | 112.4(6) |
| N15 | Ni1 | N11 | 98.5(2) | C3 | N1 | Ni2 | 109.9(5) |
| N15 | Ni1 | N12 | 97.4(2) | C5 | N1 | Ni2 | 105.9(5) |
| C13 | N9 | Ni1 | 109.6(4) | C5 | N1 | C3 | 112.1(6) |
| C15 | N9 | Ni1 | 105.1(4) | C4 | N2 | Ni2 | 107.9(5) |

**Table 12** Continued

| Atom | Atom | Atom | Angle/° | Atom | Atom | Atom | Angle/° |
|---|---|---|---|---|---|---|---|
| C15 | N9 | C13 | 111.8(6) | C6 | N3 | Ni2 | 109.4(5) |
| C15 | N9 | C17 | 112.3(6) | C7 | N4 | Ni2 | 109.6(5) |
| C17 | N9 | Ni1 | 104.7(4) | C8[2] | N5 | N6 | 113.7(6) |
| C17 | N9 | C13 | 112.8(6) | N5 | N6 | Ni2 | 125.6(4) |
| C16 | N10 | Ni1 | 108.7(4) | C8 | N6 | Ni2 | 117.2(5) |
| C14 | N11 | Ni1 | 108.2(5) | C8 | N6 | N5 | 117.1(6) |
| C18 | N12 | Ni1 | 109.4(4) | C9 | N7 | Ni2 | 115.8(5) |
| C23[1] | N13 | N14 | 115.5(6) | C10 | N7 | Ni2 | 127.9(5) |
| N13 | N14 | Ni1 | 126.1(4) | C10 | N7 | C9 | 116.2(7) |
| C23 | N14 | Ni1 | 116.9(4) | C9 | N8 | C12 | 115.1(8) |
| C23 | N14 | N13 | 117.0(5) | N1 | C1 | C7 | 111.1(6) |
| C19 | N15 | Ni1 | 127.3(5) | N1 | C3 | C4 | 112.8(7) |
| C22 | N15 | Ni1 | 116.2(5) | N2 | C4 | C3 | 108.8(6) |
| C22 | N15 | C19 | 116.5(7) | N1 | C5 | C6 | 110.3(7) |
| C21 | N16 | C22 | 116.7(7) | N3 | C6 | C5 | 111.8(6) |
| N9 | C13 | C14 | 113.5(6) | N4 | C7 | C1 | 109.1(6) |
| N11 | C14 | C13 | 109.5(6) | N5[2] | C8 | C9 | 116.7(6) |
| N9 | C15 | C16 | 110.1(6) | N6 | C8 | N5[2] | 129.2(7) |
| N10 | C16 | C15 | 110.0(6) | N6 | C8 | C9 | 114.1(6) |
| N9 | C17 | C18 | 109.9(6) | N7 | C9 | C8 | 114.9(7) |
| N12 | C18 | C17 | 111.1(6) | N8 | C9 | N7 | 126.6(7) |
| N15 | C19 | C20 | 121.0(8) | N8 | C9 | C8 | 118.5(7) |
| C19 | C20 | C21 | 118.3(8) | N7 | C10 | C11 | 121.2(8) |
| N16 | C21 | C20 | 121.5(8) | C12 | C11 | C10 | 117.4(8) |
| N15 | C22 | C23 | 115.2(7) | N8 | C12 | C11 | 123.3(9) |
| N16 | C22 | N15 | 126.1(7) | N18 | C27 | C26 | 179.6(12) |
| N16 | C22 | C23 | 118.7(6) | F1 | B2 | F2 | 106.0(8) |
| N13[1] | C23 | N14 | 127.5(6) | F12 | B2 | F1 | 111.0(9) |
| N13[1] | C23 | C22 | 117.8(7) | F12 | B2 | F2 | 113.2(9) |
| N14 | C23 | C22 | 114.6(6) | F12 | B2 | F3 | 108.2(9) |
| F5 | B1 | F4 | 105.3(10) | F3 | B2 | F1 | 110.0(7) |
| F5 | B1 | F6 | 109.0(9) | F3 | B2 | F2 | 108.5(9) |
| F5 | B1 | F7 | 114.7(9) | N19 | C29 | C28 | 178.6(13) |

**Table 12** Continued

| Atom | Atom | Atom | Angle/° | Atom | Atom | Atom | Angle/° |
|---|---|---|---|---|---|---|---|
| F6 | B1 | F4 | 104.4(9) | N17 | C25 | C24 | 179.1(11) |
| F7 | B1 | F4 | 111.8(9) | F9 | B3 | F8 | 115.9(10) |
| F7 | B1 | F6 | 111.1(8) | F10 | B3 | F9 | 103.2(10) |
| N1 | Ni2 | N2 | 83.2(3) | F10 | B3 | F8 | 114.4(9) |
| N1 | Ni2 | N3 | 82.5(2) | F11 | B3 | F9 | 104.7(11) |
| N1 | Ni2 | N4 | 83.9(2) | F11 | B3 | F10 | 108.7(11) |
| N1 | Ni2 | N6 | 101.5(2) | F11 | B3 | F8 | 109.4(10) |
| N1 | Ni2 | N7 | 178.5(2) | | | | |

[1]1-X, 1-Y, 1-Z; [2]2-X, 2-Y, 1-Z

**[{Ni(TPMA)}$_2$-μ-bmtz$^{\bullet-}$](CF$_3$SO$_3$)$_3$•CH$_3$CN.** The cationic unit of [{Ni(TPMA)}$_2$-μ-bmtz$^{\bullet-}$](CF$_3$SO$_3$)$_3$ consists of two [Ni(TPMA)]$^{2+}$ fragments bridged by a bmtz ligand in the radical anion form. Only one of the Ni ions is crystallographically unique and resides in a distorted octahedral coordination environment. The geometrical constraints of the ligand lead to $N_{py}$-Ni-$N_{amine}$ angles for the [Ni(TPMA)]$^{2+}$ fragment in the range 80.56(15) - 82.21(15)°. The Ni-N bond lengths also vary significantly from 2.070(4) to 2.136(4) Å. This distortion can also be described as a meridional elongation but is different than what is observed for [{Ni(TPMA)}$_2$-μ-bmtz$^{\bullet-}$](BF$_4$)$_3$, [{Co(TPMA)}$_2$-μ-bmtz$^{\bullet-}$](CF$_3$SO$_3$)$_3$, and [{Fe(TPMA)}$_2$-μ-bmtz$^{\bullet-}$](BF$_4$)$_3$. In the present case a pyridine N atom of TPMA is positioned trans to the bmtz tetrazine ring N atom. In all other bmtz radical complexes with TPMA, the bridgehead amine nitrogen atom of TPMA is trans to the tetrazine ring N atom. In this complex, the Ni1-N1, Ni1-N3, and Ni1-N6 bonds form one meridian of the octahedron spanning from the bmtz pyrimidine ring to the

bridgehead amine N atom of TPMA and one of the pyridine rings of TPMA with an average bond length of 2.13 Å. The Ni1-N2, Ni1-N8, and Ni1-N4 bonds form the other meridian of the octahedron with an average bond length of 2.08 Å.

Evidence for the radical anion oxidation state of the bmtz ligand can be seen in the tetrazine N-N bond lengths. The N7-N8a distance of 1.388(5) Å is consistent with previous reports of the radical anion state of bmtz and is significantly longer than the ~1.33 Å expected for the neutral form of the ligand.[92] Charge balance is also consistent with a radical ligand. The thermal ellipsoid plot of $[\{Ni(TPMA)\}_2\text{-}\mu\text{-}bmtz^{\bullet-}](CF_3SO_3)_3$ is displayed in Figure 27 and Table 13 lists bond distances and angles. There is evidence of π-π stacking between the pyridine rings of TPMA. The shortest atom-to-atom contact between these rings is 3.41 Å which is within the accepted range of distances for π-π stacking interactions.[121] The intramolecular Ni-Ni separation is 6.86 Å, with the closest intermolecular Ni-Ni distance being 8.77 Å.

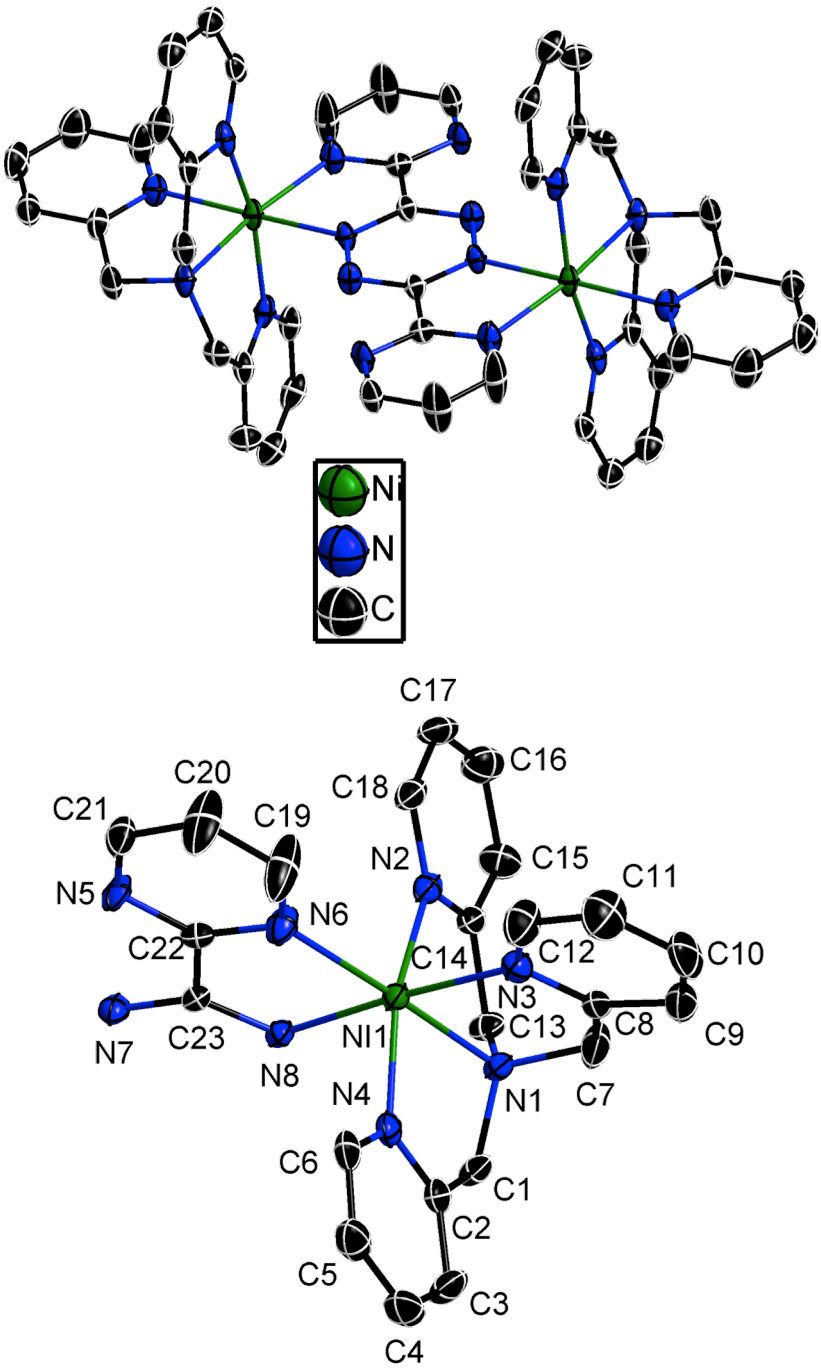


**Figure 27.** Thermal ellipsoid plot of the cationic unit of [{Ni(TPMA)}$_2$-μ-bmtz$^{\bullet-}$](CF$_3$SO$_3$)$_3$ and atom labeling scheme of the asymmetric unit. Thermal ellipsoids are drawn at the 50% probability level. H atoms were omitted for the sake of clarity.

**Table 13.** Bond distances and angles for [{Ni(TPMA)}$_2$-μ-bmtz$^{\bullet-}$](CF$_3$SO$_3$)$_3$.

| Atom | Atom | Length/Å | Atom | Atom | Length/Å |
|---|---|---|---|---|---|
| Ni1 | N1 | 2.111(4) | C14 | C13 | 1.518(6) |
| Ni1 | N2 | 2.083(4) | C14 | C15 | 1.389(7) |
| Ni1 | N3 | 2.136(4) | C17 | C16 | 1.373(8) |
| Ni1 | N4 | 2.089(4) | C17 | C18 | 1.386(7) |
| Ni1 | N6 | 2.129(4) | C16 | C15 | 1.392(7) |
| Ni1 | N8 | 2.070(4) | C19 | C20 | 1.375(8) |
| N1 | C1 | 1.497(6) | C20 | C21 | 1.360(8) |
| N1 | C7 | 1.496(6) | C22 | C23 | 1.486(6) |
| N1 | C13 | 1.484(6) | F1 | C30 | 1.458(16) |
| C1 | C2 | 1.509(7) | F2 | C30 | 1.190(14) |
| N2 | C14 | 1.335(6) | F3 | C30 | 1.326(14) |
| N2 | C18 | 1.352(6) | C30 | S1 | 1.934(10) |
| C2 | C3 | 1.394(7) | S1 | O1 | 1.465(13) |
| C2 | N4 | 1.341(7) | S1 | O2 | 1.620(11) |
| C3 | C4 | 1.393(8) | S1 | O3 | 1.535(11) |
| N3 | C8 | 1.337(6) | N9 | C24$^2$ | 1.257(17) |
| N3 | C12 | 1.343(7) | N9 | C24 | 1.257(17) |
| C4 | C5 | 1.368(8) | C24 | C26 | 1.095(18) |
| N4 | C6 | 1.328(6) | F4A | C27A | 0.957(14) |
| C5 | C6 | 1.380(7) | F5A | C27A | 1.86(2) |
| N5 | C21 | 1.326(6) | F6A | C27A | 1.292(16) |
| N5 | C22 | 1.336(6) | C27A | S2A | 2.080(15) |
| N6 | C19 | 1.323(7) | S2A | O4A | 1.419(11) |
| N6 | C22 | 1.338(6) | S2A | O5A | 1.594(12) |
| C7 | C8 | 1.502(7) | S2A | O6A | 1.347(9) |
| N7 | N8$^1$ | 1.388(5) | F4B | C27B | 1.420(18) |
| N7 | C23 | 1.321(6) | F5B | C27B | 1.259(17) |
| N8 | C23 | 1.324(6) | F6B | C27B | 1.590(18) |
| C8 | C9 | 1.378(7) | C27B | S2B | 1.658(15) |
| C9 | C10 | 1.384(8) | S2B | O4B | 1.591(10) |
| C10 | C11 | 1.371(9) | S2B | O5B | 1.324(12) |
| C12 | C11 | 1.366(8) | S2B | O6B | 1.368(10) |

**Table 13** Continued

[1]1-X, 1-Y, 1-Z; [2]-X, -Y, -Z

| Atom | Atom | Atom | Angle/° | Atom | Atom | Atom | Angle/° |
|---|---|---|---|---|---|---|---|
| N2 | Ni1 | N1 | 80.56(15) | C15 | C14 | N2 | 123.4(4) |
| N3 | Ni1 | N1 | 81.87(15) | C15 | C14 | C13 | 119.8(4) |
| N3 | Ni1 | N2 | 92.64(15) | C14 | C13 | N1 | 109.7(4) |
| N4 | Ni1 | N1 | 82.21(15) | C18 | C17 | C16 | 119.1(5) |
| N4 | Ni1 | N2 | 162.52(16) | C15 | C16 | C17 | 119.9(5) |
| N4 | Ni1 | N3 | 87.84(15) | C16 | C15 | C14 | 117.4(5) |
| N6 | Ni1 | N1 | 173.02(15) | C17 | C18 | N2 | 121.9(5) |
| N6 | Ni1 | N2 | 96.24(16) | C20 | C19 | N6 | 123.2(5) |
| N6 | Ni1 | N3 | 104.56(15) | C21 | C20 | C19 | 117.3(5) |
| N6 | Ni1 | N4 | 100.55(16) | C20 | C21 | N5 | 121.9(5) |
| N8 | Ni1 | N1 | 96.56(15) | N6 | C22 | N5 | 126.7(4) |
| N8 | Ni1 | N2 | 89.79(14) | C23 | C22 | N5 | 117.9(4) |
| N8 | Ni1 | N3 | 176.86(15) | C23 | C22 | N6 | 115.4(4) |
| N8 | Ni1 | N4 | 89.25(14) | N8 | C23 | N7 | 128.0(4) |
| N8 | Ni1 | N6 | 77.14(14) | C22 | C23 | N7 | 117.0(4) |
| C1 | N1 | Ni1 | 106.1(3) | C22 | C23 | N8 | 114.9(4) |
| C7 | N1 | Ni1 | 109.9(3) | F2 | C30 | F1 | 95.3(10) |
| C7 | N1 | C1 | 112.0(4) | F3 | C30 | F1 | 97.1(10) |
| C13 | N1 | Ni1 | 104.8(3) | F3 | C30 | F2 | 141.9(13) |
| C13 | N1 | C1 | 113.6(4) | S1 | C30 | F1 | 104.1(9) |
| C13 | N1 | C7 | 110.0(4) | S1 | C30 | F2 | 107.6(8) |
| C2 | C1 | N1 | 110.9(4) | S1 | C30 | F3 | 104.0(8) |
| C14 | N2 | Ni1 | 112.5(3) | O1 | S1 | C30 | 96.7(7) |
| C18 | N2 | Ni1 | 129.2(3) | O2 | S1 | C30 | 106.6(6) |
| C18 | N2 | C14 | 118.2(4) | O2 | S1 | O1 | 133.1(7) |
| C3 | C2 | C1 | 121.3(5) | O3 | S1 | C30 | 105.4(6) |
| N4 | C2 | C1 | 117.7(4) | O3 | S1 | O1 | 127.1(6) |
| N4 | C2 | C3 | 121.0(5) | O3 | S1 | O2 | 85.3(6) |
| C4 | C3 | C2 | 118.5(5) | C24[2] | N9 | C24 | 180.0 |
| C8 | N3 | Ni1 | 113.2(3) | C26 | C24 | N9 | 173.2(17) |
| C12 | N3 | Ni1 | 129.5(4) | F5A | C27A | F4A | 100.3(13) |

**Table 13** Continued

| Atom | Atom | Atom | Angle/° | Atom | Atom | Atom | Angle/° |
|---|---|---|---|---|---|---|---|
| C12 | N3 | C8 | 117.0(4) | F6A | C27A | F4A | 139.4(18) |
| C5 | C4 | C3 | 119.7(5) | F6A | C27A | F5A | 100.7(11) |
| C2 | N4 | Ni1 | 112.3(3) | S2A | C27A | F4A | 112.4(12) |
| C6 | N4 | Ni1 | 128.1(4) | S2A | C27A | F5A | 80.5(8) |
| C6 | N4 | C2 | 119.6(4) | S2A | C27A | F6A | 105.1(10) |
| C6 | C5 | C4 | 118.3(5) | O4A | S2A | C27A | 102.8(6) |
| C22 | N5 | C21 | 116.2(4) | O5A | S2A | C27A | 100.5(6) |
| C19 | N6 | Ni1 | 130.3(4) | O5A | S2A | O4A | 109.2(6) |
| C22 | N6 | Ni1 | 114.8(3) | O6A | S2A | C27A | 99.7(5) |
| C22 | N6 | C19 | 114.7(4) | O6A | S2A | O4A | 138.7(6) |
| C5 | C6 | N4 | 122.8(5) | O6A | S2A | O5A | 100.0(6) |
| C8 | C7 | N1 | 114.2(4) | F5B | C27B | F4B | 104.2(11) |
| C23 | N7 | N8[1] | 114.7(4) | F6B | C27B | F4B | 85.5(10) |
| N7[1] | N8 | Ni1 | 125.1(3) | F6B | C27B | F5B | 109.2(11) |
| C23 | N8 | Ni1 | 117.6(3) | S2B | C27B | F4B | 116.5(10) |
| C23 | N8 | N7[1] | 117.2(4) | S2B | C27B | F5B | 130.0(12) |
| C7 | C8 | N3 | 118.2(4) | S2B | C27B | F6B | 102.0(9) |
| C9 | C8 | N3 | 122.8(5) | O4B | S2B | C27B | 104.9(6) |
| C9 | C8 | C7 | 118.9(5) | O5B | S2B | C27B | 114.1(8) |
| C10 | C9 | C8 | 119.1(5) | O5B | S2B | O4B | 108.1(7) |
| C11 | C10 | C9 | 118.4(5) | O6B | S2B | C27B | 105.1(7) |
| C11 | C12 | N3 | 123.7(6) | O6B | S2B | O4B | 114.7(6) |
| C12 | C11 | C10 | 119.0(5) | O6B | S2B | O5B | 110.0(7) |
| C13 | C14 | N2 | 116.8(4) | | | | |

[1]1-X, 1-Y, 1-Z; [2]-X, -Y, -Z

This compound was only obtained once as a single crystal with this unit cell. All other synthetic attempts led to twinned crystals that could be indexed in the original unit cell but were multi-component twins that could not be solved in the original unit cell.

The crystals could also be indexed in a larger triclinic unit cell and refined as a two-component non-merohedral twin. The larger unit cell contains two half molecules in the asymmetric unit, both of which reside on inversion centers (Figure 28). One of the crystallographically independent Ni atoms also exhibits a meridional elongation that spans the three pyridine N atoms of TPMA with the other meridian consisting of the bridgehead amine N atom and the two coordinated N atoms of bmtz. The other crystallographically independent Ni atom is better described as a trigonal or facial distortion. One face of the octahedron that contains two pyridine N atoms of TPMA and the pyrimidine N atom of bmtz display elongated Ni-N bonds. The other face, formed by the remaining pyridine N atom and bridgehead amine N atom of TPMA along with the tetrazine N atom of bmtz consist of shortened Ni-N bonds. Table 14 lists bond distances and angles for $[\{Ni(TPMA)\}_2\text{-}\mu\text{-}bmtz^{\bullet-}](CF_3SO_3)_3$ as crystallized in the larger unit cell.

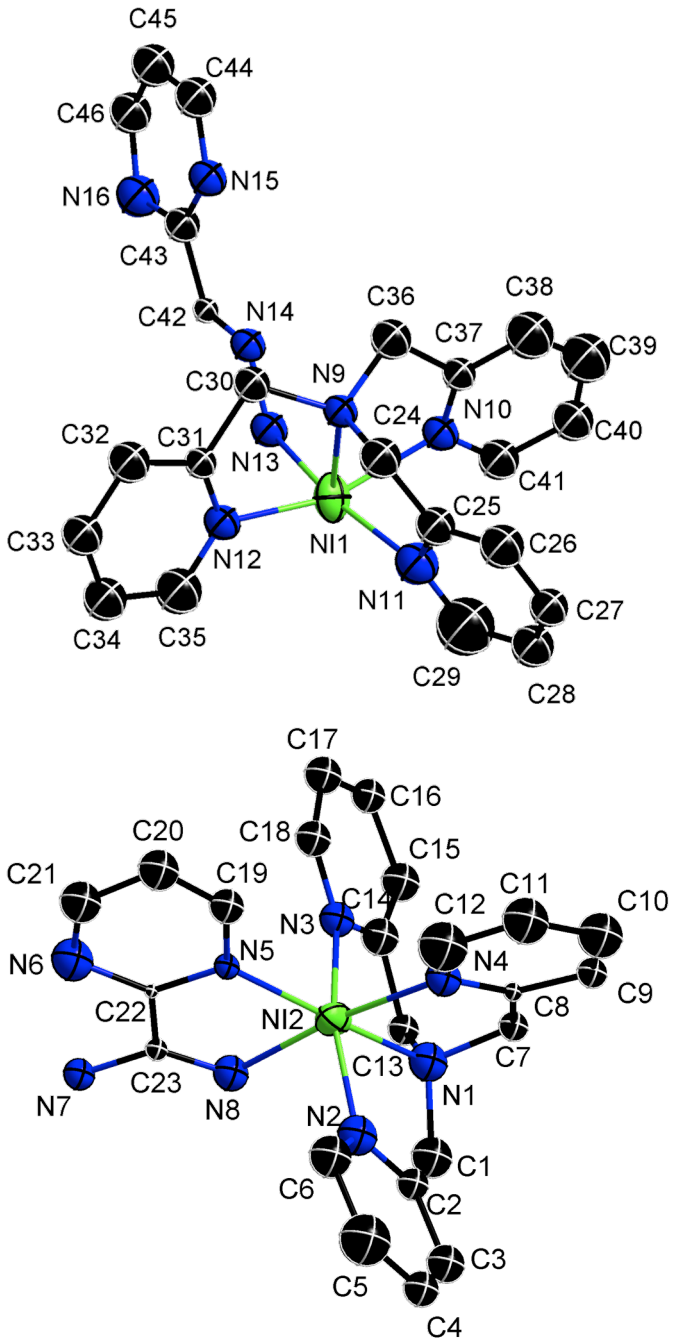


**Figure 28.** Atom numbering scheme of the asymmetric unit for the cationic unit of $[\{Ni(TPMA)\}_2\text{-}\mu\text{-}bmtz^{\bullet-}](CF_3SO_3)_3$ as crystallized in the larger unit cell. Thermal ellipsoids are drawn at the 50% probability level. H atoms were omitted for the sake of clarity.

**Table 14.** Bond distances and angles for [{Ni(TPMA)}$_2$-μ-bmtz$^{\bullet-}$](CF$_3$SO$_3$)$_3$ as crystallized in the larger unit cell.

| Atom | Atom | Length/Å | Atom | Atom | Length/Å |
|---|---|---|---|---|---|
| Ni1 | N9 | 2.10(2) | N8 | C23 | 1.28(3) |
| Ni1 | N10 | 2.14(3) | F8 | C52 | 1.29(6) |
| Ni1 | N12 | 2.11(3) | C8 | C9 | 1.42(3) |
| Ni1 | N11 | 2.12(3) | N9 | C24 | 1.55(4) |
| Ni1 | N13 | 2.03(3) | N9 | C30 | 1.54(3) |
| Ni1 | N16[1] | 2.08(3) | N9 | C36 | 1.49(4) |
| S1 | O7 | 1.40(2) | F9 | C52 | 1.35(6) |
| S1 | O8 | 1.51(3) | C9 | C10 | 1.40(4) |
| S1 | O9 | 1.44(3) | C10 | C11 | 1.38(4) |
| S1 | C50 | 1.67(4) | N10 | C37 | 1.29(4) |
| F1 | C49 | 1.40(6) | N10 | C41 | 1.37(4) |
| O1 | S3 | 1.49(3) | N12 | C31 | 1.30(3) |
| N1 | C1 | 1.50(3) | N12 | C35 | 1.33(4) |
| N1 | Ni2 | 2.09(3) | C12 | C11 | 1.49(4) |
| N1 | C7 | 1.51(3) | N11 | C25 | 1.40(4) |
| N1 | C13 | 1.47(3) | N11 | C29 | 1.37(4) |
| C1 | C2 | 1.42(4) | N13 | N14 | 1.42(3) |
| Ni2 | N2 | 2.04(3) | N13 | C42[1] | 1.39(3) |
| Ni2 | N3 | 2.11(3) | C13 | C14 | 1.50(4) |
| Ni2 | N4 | 2.14(3) | C14 | C15 | 1.36(4) |
| Ni2 | N5 | 2.15(2) | N14 | C42 | 1.34(3) |
| Ni2 | N8 | 2.06(3) | C15 | C16 | 1.45(4) |
| S2 | O4 | 1.44(3) | N15 | C43 | 1.37(4) |
| S2 | O5 | 1.49(2) | N15 | C44 | 1.33(4) |
| S2 | O6 | 1.46(2) | N16 | Ni1[1] | 2.08(3) |
| S2 | C49 | 1.68(6) | N16 | C43 | 1.37(4) |
| F2 | C49 | 1.33(5) | N16 | C46 | 1.37(4) |
| O2 | S3 | 1.37(3) | C16 | C17 | 1.32(4) |
| N2 | C2 | 1.36(3) | C17 | C18 | 1.36(4) |
| N2 | C6 | 1.37(4) | N17 | C47 | 1.12(4) |
| C2 | C3 | 1.44(4) | C19 | C20 | 1.32(4) |
| S3 | O3 | 1.42(3) | C20 | C21 | 1.44(4) |

**Table 14** Continued

| Atom | Atom | Length/Å | Atom | Atom | Length/Å |
|---|---|---|---|---|---|
| S3 | C52 | 1.99(6) | C23 | C22 | 1.47(4) |
| F3 | C49 | 1.34(6) | C24 | C25 | 1.46(4) |
| N3 | C14 | 1.31(4) | C25 | C26 | 1.35(4) |
| N3 | C18 | 1.32(3) | C28 | C27 | 1.38(4) |
| C3 | C4 | 1.37(4) | C28 | C29 | 1.42(4) |
| F4 | C50 | 1.38(4) | C27 | C26 | 1.31(4) |
| N4 | C8 | 1.30(3) | C30 | C31 | 1.53(4) |
| N4 | C12 | 1.39(4) | C31 | C32 | 1.41(4) |
| C4 | C5 | 1.36(4) | C32 | C33 | 1.42(4) |
| F5 | C50 | 1.31(4) | C33 | C34 | 1.34(4) |
| N5 | C19 | 1.29(3) | C34 | C35 | 1.45(4) |
| N5 | C22 | 1.33(3) | C36 | C37 | 1.56(4) |
| C5 | C6 | 1.50(4) | C37 | C38 | 1.32(4) |
| F6 | C50 | 1.42(4) | C38 | C39 | 1.38(4) |
| N6 | C21 | 1.34(4) | C39 | C40 | 1.31(4) |
| N6 | C22 | 1.37(3) | C40 | C41 | 1.37(4) |
| N7 | N8[2] | 1.36(3) | C42 | N13[1] | 1.39(3) |
| N7 | C23 | 1.35(3) | C42 | C43 | 1.45(4) |
| F7 | C52 | 1.21(6) | C44 | C45 | 1.37(4) |
| C7 | C8 | 1.43(3) | C45 | C46 | 1.33(4) |
| N8 | N7[2] | 1.36(3) | C47 | C48 | 1.44(5) |

[1]-X, 1-Y, -Z; [2]1-X, 1-Y, 1-Z

| Atom | Atom | Atom | Angle/° | Atom | Atom | Atom | Angle/° |
|---|---|---|---|---|---|---|---|
| N9 | Ni1 | N10 | 79.7(10) | C11 | C10 | C9 | 117(3) |
| N9 | Ni1 | N12 | 79.5(10) | C37 | N10 | Ni1 | 113(2) |
| N9 | Ni1 | N11 | 83.1(12) | C37 | N10 | C41 | 118(3) |
| N12 | Ni1 | N10 | 158.6(12) | C41 | N10 | Ni1 | 127(2) |
| N12 | Ni1 | N11 | 100.2(10) | C31 | N12 | Ni1 | 113(2) |
| N11 | Ni1 | N10 | 82.1(10) | C31 | N12 | C35 | 121(3) |
| N13 | Ni1 | N9 | 99.1(11) | C35 | N12 | Ni1 | 126(3) |
| N13 | Ni1 | N10 | 88.2(10) | N4 | C12 | C11 | 119(3) |

**Table 14** Continued

| Atom | Atom | Atom | Angle/° | Atom | Atom | Atom | Angle/° |
|---|---|---|---|---|---|---|---|
| N13 | Ni1 | N12 | 90.2(10) | C10 | C11 | C12 | 119(3) |
| N13 | Ni1 | N11 | 169.5(11) | C25 | N11 | Ni1 | 115(2) |
| N13 | Ni1 | N16[1] | 80.0(12) | C29 | N11 | Ni1 | 125(3) |
| N16[1] | Ni1 | N9 | 174.9(11) | C29 | N11 | C25 | 119(3) |
| N16[1] | Ni1 | N10 | 105.2(11) | N14 | N13 | Ni1 | 128(2) |
| N16[1] | Ni1 | N12 | 95.5(11) | C42[1] | N13 | Ni1 | 115(2) |
| N16[1] | Ni1 | N11 | 98.7(12) | C42[1] | N13 | N14 | 117(2) |
| O7 | S1 | O8 | 118.3(19) | N1 | C13 | C14 | 108(2) |
| O7 | S1 | O9 | 112.4(18) | N3 | C14 | C13 | 114(3) |
| O7 | S1 | C50 | 100.5(19) | N3 | C14 | C15 | 127(3) |
| O8 | S1 | C50 | 99(2) | C15 | C14 | C13 | 119(3) |
| O9 | S1 | O8 | 116.9(19) | C42 | N14 | N13 | 119(3) |
| O9 | S1 | C50 | 106(2) | C14 | C15 | C16 | 114(3) |
| C1 | N1 | Ni2 | 106(2) | C44 | N15 | C43 | 123(3) |
| C1 | N1 | C7 | 108(2) | C43 | N16 | Ni1[1] | 113(2) |
| C7 | N1 | Ni2 | 109.2(17) | C46 | N16 | Ni1[1] | 137(3) |
| C13 | N1 | C1 | 117(2) | C46 | N16 | C43 | 109(3) |
| C13 | N1 | Ni2 | 106.1(18) | C17 | C16 | C15 | 122(3) |
| C13 | N1 | C7 | 111(2) | C16 | C17 | C18 | 116(3) |
| C2 | C1 | N1 | 113(3) | N3 | C18 | C17 | 128(3) |
| N1 | Ni2 | N3 | 77.9(10) | N5 | C19 | C20 | 127(3) |
| N1 | Ni2 | N4 | 81.9(11) | C19 | C20 | C21 | 111(3) |
| N1 | Ni2 | N5 | 170.8(9) | N6 | C21 | C20 | 128(3) |
| N2 | Ni2 | N1 | 81.9(11) | N7 | C23 | C22 | 113(3) |
| N2 | Ni2 | N3 | 159.5(12) | N8 | C23 | N7 | 128(3) |
| N2 | Ni2 | N4 | 84.1(10) | N8 | C23 | C22 | 119(3) |
| N2 | Ni2 | N5 | 105.4(11) | N5 | C22 | N6 | 127(3) |
| N2 | Ni2 | N8 | 88.8(10) | N5 | C22 | C23 | 115(3) |
| N3 | Ni2 | N4 | 96.3(10) | N6 | C22 | C23 | 118(3) |
| N3 | Ni2 | N5 | 94.3(10) | C25 | C24 | N9 | 118(3) |
| N4 | Ni2 | N5 | 104.2(10) | N11 | C25 | C24 | 112(3) |
| N8 | Ni2 | N1 | 96.9(11) | C26 | C25 | N11 | 123(3) |
| N8 | Ni2 | N3 | 90.2(10) | C26 | C25 | C24 | 124(4) |

**Table 14** Continued

| Atom | Atom | Atom | Angle/° | Atom | Atom | Atom | Angle/° |
|---|---|---|---|---|---|---|---|
| N8 | Ni2 | N4 | 173.0(10) | C27 | C28 | C29 | 124(4) |
| N8 | Ni2 | N5 | 77.9(11) | C26 | C27 | C28 | 119(3) |
| O4 | S2 | O5 | 113.4(16) | C27 | C26 | C25 | 120(4) |
| O4 | S2 | O6 | 116.9(15) | N11 | C29 | C28 | 115(4) |
| O4 | S2 | C49 | 102(2) | C31 | C30 | N9 | 106(3) |
| O5 | S2 | C49 | 105(2) | N12 | C31 | C30 | 119(3) |
| O6 | S2 | O5 | 112.5(15) | N12 | C31 | C32 | 125(3) |
| O6 | S2 | C49 | 105(2) | C32 | C31 | C30 | 116(3) |
| C2 | N2 | Ni2 | 113(2) | C31 | C32 | C33 | 114(3) |
| C2 | N2 | C6 | 123(3) | C34 | C33 | C32 | 123(4) |
| C6 | N2 | Ni2 | 123(2) | C33 | C34 | C35 | 118(4) |
| C1 | C2 | C3 | 122(3) | N12 | C35 | C34 | 120(4) |
| N2 | C2 | C1 | 117(3) | N9 | C36 | C37 | 106(3) |
| N2 | C2 | C3 | 121(3) | N10 | C37 | C36 | 118(3) |
| O1 | S3 | C52 | 103(2) | N10 | C37 | C38 | 122(3) |
| O2 | S3 | O1 | 115.1(18) | C38 | C37 | C36 | 119(3) |
| O2 | S3 | O3 | 118(2) | C37 | C38 | C39 | 119(4) |
| O2 | S3 | C52 | 103(2) | C40 | C39 | C38 | 122(4) |
| O3 | S3 | O1 | 110.7(19) | C39 | C40 | C41 | 116(4) |
| O3 | S3 | C52 | 105(2) | N10 | C41 | C40 | 122(3) |
| C14 | N3 | Ni2 | 115(2) | N13[1] | C42 | C43 | 115(3) |
| C14 | N3 | C18 | 114(3) | N14 | C42 | N13[1] | 124(3) |
| C18 | N3 | Ni2 | 130(2) | N14 | C42 | C43 | 121(3) |
| C4 | C3 | C2 | 119(3) | N15 | C43 | N16 | 125(3) |
| C8 | N4 | Ni2 | 110(2) | N15 | C43 | C42 | 119(3) |
| C8 | N4 | C12 | 124(3) | N16 | C43 | C42 | 116(3) |
| C12 | N4 | Ni2 | 126(3) | N15 | C44 | C45 | 115(3) |
| C5 | C4 | C3 | 120(3) | C46 | C45 | C44 | 121(4) |
| C19 | N5 | Ni2 | 129(2) | C45 | C46 | N16 | 128(4) |
| C19 | N5 | C22 | 117(3) | N17 | C47 | C48 | 173(5) |
| C22 | N5 | Ni2 | 113.0(19) | F1 | C49 | S2 | 115(4) |
| C4 | C5 | C6 | 123(4) | F2 | C49 | F1 | 98(4) |
| C21 | N6 | C22 | 110(3) | F2 | C49 | S2 | 120(5) |

**Table 14** Continued

| Atom | Atom | Atom | Angle/° | Atom | Atom | Atom | Angle/° |
|---|---|---|---|---|---|---|---|
| N2 | C6 | C5 | 115(3) | F2 | C49 | F3 | 104(5) |
| C23 | N7 | N8[2] | 115(2) | F3 | C49 | F1 | 99(4) |
| C8 | C7 | N1 | 113(2) | F3 | C49 | S2 | 117(4) |
| N7[2] | N8 | Ni2 | 127(2) | F4 | C50 | S1 | 116(3) |
| C23 | N8 | Ni2 | 116(2) | F4 | C50 | F6 | 100(3) |
| C23 | N8 | N7[2] | 117(3) | F5 | C50 | S1 | 122(3) |
| N4 | C8 | C7 | 124(3) | F5 | C50 | F4 | 98(3) |
| N4 | C8 | C9 | 117(3) | F5 | C50 | F6 | 104(3) |
| C9 | C8 | C7 | 119(3) | F6 | C50 | S1 | 114(3) |
| C24 | N9 | Ni1 | 105.0(19) | F7 | C52 | S3 | 102(5) |
| C30 | N9 | Ni1 | 105.8(17) | F7 | C52 | F8 | 116(6) |
| C30 | N9 | C24 | 113(2) | F7 | C52 | F9 | 125(6) |
| C36 | N9 | Ni1 | 111(2) | F8 | C52 | S3 | 101(4) |
| C36 | N9 | C24 | 111(2) | F8 | C52 | F9 | 109(6) |
| C36 | N9 | C30 | 111(2) | F9 | C52 | S3 | 96(4) |
| C10 | C9 | C8 | 125(3) | | | | |

[1]-X, 1-Y, -Z; [2]1-X, 1-Y, 1-Z

**$[Ni(L_4^2)(CH_3CN)_2](PF_6)_2 \bullet 2CH_3CN$.** The cationic unit of $[Ni(L_4^2)(CH_3CN)_2](PF_6)_2$ consists of one $Ni^{II}$ ion in an octahedral coordination environment. The nickel coordination sphere is made up of four N atoms from the $L_4^2$ ligand and two N atoms from the coordinated $CH_3CN$ solvent molecules. The two $CH_3CN$ molecules adopt a cis orientation. The thermal ellipsoid plot of $[Ni(L_4^2)(CH_3CN)_2](PF_6)_2$ is displayed in Figure 29 and Table 15 lists bond distances and angles.

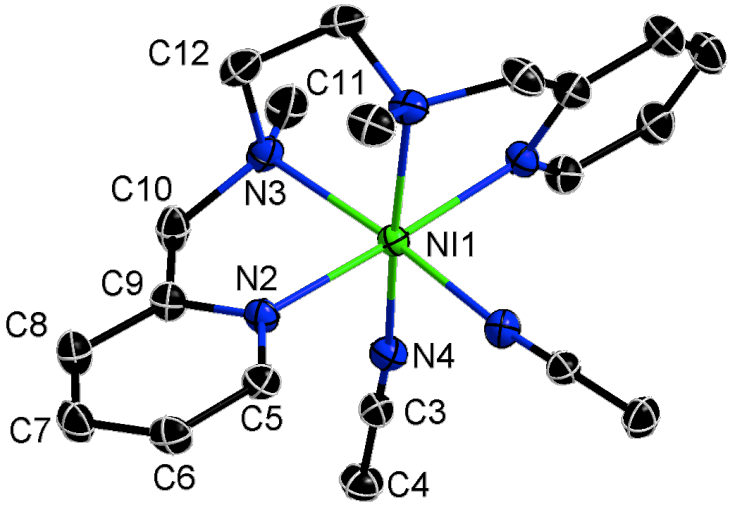


**Figure 29.** Thermal ellipsoid plot and atom labeling scheme of the asymmetric unit for the cation in $[Ni(L_4^2)(CH_3CN)_2](PF_6)_2$. Thermal ellipsoids are drawn at the 50% probability level. H atoms were omitted for the sake of clarity.

**Table 15.** Bond distances and angles for $[Ni(L_4^2)(CH_3CN)_2](PF_6)_2$.

| Atom | Atom | Length/Å | Atom | Atom | Length/Å |
|---|---|---|---|---|---|
| Ni1 | N2[1] | 2.0911(15) | N2 | C9 | 1.347(2) |
| Ni1 | N2 | 2.0911(16) | C3 | C4 | 1.453(3) |
| Ni1 | N3[1] | 2.1218(15) | C3 | N4 | 1.139(2) |
| Ni1 | N3 | 2.1219(15) | N3 | C10 | 1.480(2) |
| Ni1 | N4[1] | 2.0914(16) | N3 | C11 | 1.484(2) |
| Ni1 | N4 | 2.0914(16) | N3 | C12 | 1.493(2) |
| P1 | F1 | 1.5828(14) | N5 | C13 | 1.118(4) |
| P1 | F2 | 1.5918(16) | C5 | C6 | 1.379(3) |
| P1 | F3 | 1.6020(15) | C6 | C7 | 1.392(3) |
| P1 | F4 | 1.5899(14) | C7 | C8 | 1.382(3) |
| P1 | F5 | 1.5914(14) | C9 | C8 | 1.388(3) |
| P1 | F6 | 1.6099(14) | C9 | C10 | 1.504(3) |
| C2 | C13 | 1.452(5) | C12 | C12[1] | 1.509(4) |
| N2 | C5 | 1.349(2) | | | |

[1]+X, 1/2-Y, 3/2-Z

**Table 15** Continued

| Atom | Atom | Atom | Angle/° | Atom | Atom | Atom | Angle/° |
|---|---|---|---|---|---|---|---|
| $N2^1$ | Ni1 | N2 | 177.63(8) | F4 | P1 | F6 | 89.82(8) |
| $N2^1$ | Ni1 | N3 | 99.21(6) | F5 | P1 | F2 | 179.71(10) |
| N2 | Ni1 | N3 | 79.02(6) | F5 | P1 | F3 | 90.34(8) |
| $N2^1$ | Ni1 | $N3^1$ | 79.02(6) | F5 | P1 | F6 | 89.41(8) |
| N2 | Ni1 | $N3^1$ | 99.21(6) | C5 | N2 | Ni1 | 127.61(12) |
| $N2^1$ | Ni1 | N4 | 92.39(6) | C9 | N2 | Ni1 | 114.03(12) |
| $N2^1$ | Ni1 | $N4^1$ | 89.22(6) | C9 | N2 | C5 | 118.16(16) |
| N2 | Ni1 | $N4^1$ | 92.39(6) | N4 | C3 | C4 | 179.7(2) |
| N2 | Ni1 | N4 | 89.22(6) | C10 | N3 | Ni1 | 106.98(11) |
| $N3^1$ | Ni1 | N3 | 85.51(9) | C10 | N3 | C11 | 109.32(15) |
| $N4^1$ | Ni1 | N3 | 170.00(6) | C10 | N3 | C12 | 109.97(15) |
| N4 | Ni1 | $N3^1$ | 170.00(6) | C11 | N3 | Ni1 | 115.86(12) |
| N4 | Ni1 | N3 | 90.86(6) | C11 | N3 | C12 | 110.19(15) |
| $N4^1$ | Ni1 | $N3^1$ | 90.86(6) | C12 | N3 | Ni1 | 104.34(11) |
| N4 | Ni1 | $N4^1$ | 94.18(9) | C3 | N4 | Ni1 | 173.19(15) |
| F1 | P1 | F2 | 89.67(11) | N2 | C5 | C6 | 122.93(17) |
| F1 | P1 | F3 | 89.92(8) | C5 | C6 | C7 | 118.60(18) |
| F1 | P1 | F4 | 179.58(10) | C8 | C7 | C6 | 118.94(18) |
| F1 | P1 | F5 | 90.52(9) | N2 | C9 | C8 | 122.11(17) |
| F1 | P1 | F6 | 89.92(8) | N2 | C9 | C10 | 116.24(16) |
| F2 | P1 | F3 | 89.88(10) | C8 | C9 | C10 | 121.63(17) |
| F2 | P1 | F6 | 90.37(9) | C7 | C8 | C9 | 119.24(18) |
| F3 | P1 | F6 | 179.70(9) | N3 | C10 | C9 | 110.79(15) |
| F4 | P1 | F2 | 90.00(10) | N3 | C12 | $C12^1$ | 110.03(13) |
| F4 | P1 | F3 | 90.34(9) | N5 | C13 | C2 | 178.8(6) |
| F4 | P1 | F5 | 89.82(9) | | | | |

$^1$+X, 1/2-Y, 3/2-Z

**$[\{Ni(L_4^2)\}_2$-μ-bmtz$^{\bullet-}](PF_6)_3 \bullet 2CH_3CN$.** The cationic unit of $[\{Ni(L_4^2)\}_2$-μ-bmtz$^{\bullet-}](PF_6)_3$ consists of two $[Ni(TPMA)]^{2+}$ fragments bridged by a bmtz ligand in the radical anion

form. Only one of the Ni ions is crystallographically unique and resides in a distorted octahedral coordination environment. The geometrical constraints of the ligand lead to N-Ni-N angles for the $[Ni(L_4^2)]^{2+}$ fragment in the range 77.9(4) – 95.1(4)°. The Ni-N bond lengths also vary significantly from 2.028(4) to 2.185(7) Å.

The tetrazine N7-N8a distance of 1.385(6) Å is consistent with the radical anion state of bmtz[92] as is the cation:anion ratio. The thermal ellipsoid plot of $[\{Ni(L_4^2)\}_2$-μ-bmtz$^{\bullet-}](PF_6)_3$ is displayed in Figure 30 and Table 16 lists bond distances and angles. There is no evidence of π-π stacking for the cation. The intramolecular Ni-Ni separation is 6.76 Å, with the closest intermolecular Ni-Ni distance being 9.16 Å.

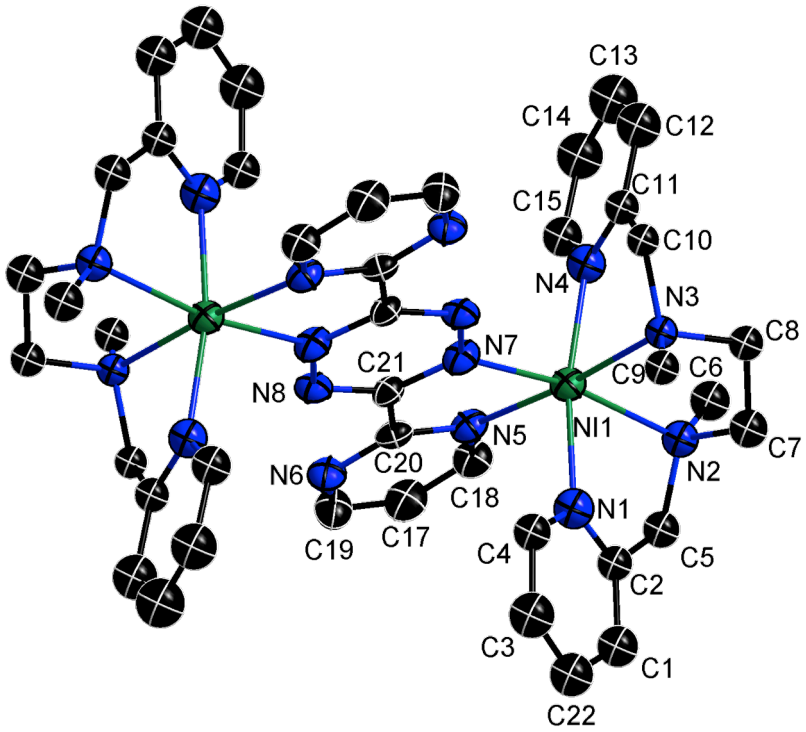


**Figure 30.** Thermal ellipsoid plot of the cation and atom labeling scheme for the asymmetric unit in $[\{Ni(L_4^2)\}_2$-μ-bmtz$^{\bullet-}](PF_6)_3$. Thermal ellipsoids are drawn at the 50% probability level. H atoms were omitted for the sake of clarity.

**Table 16.** Bond distances and angles for $[\{Ni(L_4^2)\}_2\text{-}\mu\text{-}bmtz^{\bullet-}](PF_6)_3$.

| Atom | Atom | Length/Å | Atom | Atom | Length/Å |
|---|---|---|---|---|---|
| Ni1 | N5 | 2.139(4) | C15B | N2B | 1.45(3) |
| Ni1 | N7 | 2.028(4) | C14B | N1B | 1.49(2) |
| Ni1 | N4A | 2.082(10) | C13B | C12B | 1.51(2) |
| Ni1 | N3A | 2.171(7) | C13B | N1B | 1.48(2) |
| Ni1 | N2A | 2.185(7) | C12B | N2B | 1.51(2) |
| Ni1 | N1A | 2.169(13) | C11B | C10B | 1.49(3) |
| Ni1 | N2B | 2.030(14) | C11B | N2B | 1.48(2) |
| Ni1 | N1B | 2.042(14) | C10B | C9B | 1.38(3) |
| Ni1 | N10B | 2.02(2) | C10B | N4B | 1.35(3) |
| Ni1 | N4B | 2.08(2) | C9B | C8B | 1.41(3) |
| N5 | C18 | 1.348(7) | C8B | C7B | 1.27(3) |
| N5 | C20 | 1.338(7) | C7B | C6B | 1.37(3) |
| N6 | C19 | 1.333(7) | C6B | N4B | 1.31(3) |
| N6 | C20 | 1.324(7) | C5B | C4B | 1.51(2) |
| N7 | $N8^1$ | 1.385(6) | C5B | N1B | 1.45(2) |
| N7 | C21 | 1.331(7) | C4B | C3B | 1.37(3) |
| N8 | $N7^1$ | 1.385(6) | C4B | N10B | 1.50(3) |
| N8 | C21 | 1.313(7) | C3B | C2B | 1.40(3) |
| C18 | C17 | 1.363(8) | C1B | N10B | 1.36(3) |
| C17 | C19 | 1.373(9) | P1A | F7A | 1.582(6) |
| C20 | C21 | 1.500(7) | P1A | $F7A^2$ | 1.582(6) |
| C22A | C3A | 1.363(16) | P1A | $F8A^2$ | 1.595(6) |
| C22A | C1A | 1.396(16) | P1A | F8A | 1.595(6) |
| C15A | C14A | 1.366(16) | P1A | F9A | 1.590(6) |
| C15A | N4A | 1.338(14) | P1A | $F9A^2$ | 1.590(6) |
| C14A | C13A | 1.367(18) | P1B | F7B | 1.561(13) |
| C13A | C12A | 1.387(16) | P1B | $F7B^2$ | 1.561(13) |
| C12A | C11A | 1.388(13) | P1B | $F8B^2$ | 1.570(14) |
| C11A | C10A | 1.504(12) | P1B | F8B | 1.570(14) |
| C11A | N4A | 1.354(13) | P1B | F9B | 1.603(13) |
| C10A | N3A | 1.468(11) | P1B | $F9B^2$ | 1.603(13) |
| C9A | N3A | 1.467(11) | P2A | F1A | 1.621(9) |
| C8A | C7A | 1.492(12) | P2A | F2A | 1.587(7) |

**Table 16** Continued

| Atom | Atom | Length/Å | Atom | Atom | Length/Å |
|---|---|---|---|---|---|
| C8A | N3A | 1.497(10) | P2A | F3A | 1.602(8) |
| C7A | N2A | 1.498(11) | P2A | F4A | 1.605(8) |
| C6A | N2A | 1.475(12) | P2A | F5A | 1.587(7) |
| C5A | C2A | 1.510(12) | P2A | F6A | 1.544(8) |
| C5A | N2A | 1.464(11) | P2B | F1B | 1.583(11) |
| C4A | C3A | 1.357(14) | P2B | F2B | 1.548(9) |
| C4A | N1A | 1.240(15) | P2B | F3B | 1.647(10) |
| C2A | C1A | 1.349(13) | P2B | F4B | 1.515(10) |
| C2A | N1A | 1.360(15) | P2B | F5B | 1.683(9) |
| C16B | C2B | 1.40(3) | P2B | F6B | 1.611(11) |
| C16B | C1B | 1.41(3) | | | |

[1]1-X, 1-Y, 1-Z; [2]1-X, 2-Y, 1-Z

| Atom | Atom | Atom | Angle/° | Atom | Atom | Atom | Angle/° |
|---|---|---|---|---|---|---|---|
| N5 | Ni1 | N3A | 174.7(2) | C10B | C9B | C8B | 112.8(18) |
| N5 | Ni1 | N2A | 101.5(2) | C7B | C8B | C9B | 127(2) |
| N5 | Ni1 | N1A | 90.1(4) | C8B | C7B | C6B | 116(2) |
| N7 | Ni1 | N5 | 77.12(17) | N4B | C6B | C7B | 119.5(19) |
| N7 | Ni1 | N4A | 96.3(3) | N1B | C5B | C4B | 109.9(14) |
| N7 | Ni1 | N3A | 99.2(2) | C3B | C4B | C5B | 123.3(16) |
| N7 | Ni1 | N2A | 168.7(2) | C3B | C4B | N10B | 123.8(17) |
| N7 | Ni1 | N1A | 90.6(4) | N10B | C4B | C5B | 112.8(15) |
| N7 | Ni1 | N2B | 171.5(5) | C4B | C3B | C2B | 120(2) |
| N7 | Ni1 | N1B | 96.8(4) | C3B | C2B | C16B | 120(2) |
| N7 | Ni1 | N4B | 89.3(6) | C15B | N2B | Ni1 | 120.2(12) |
| N4A | Ni1 | N5 | 98.5(3) | C15B | N2B | C12B | 110.3(15) |
| N4A | Ni1 | N3A | 77.9(4) | C15B | N2B | C11B | 110.8(15) |
| N4A | Ni1 | N2A | 95.1(4) | C12B | N2B | Ni1 | 101.9(10) |
| N4A | Ni1 | N1A | 170.0(5) | C11B | N2B | Ni1 | 106.6(11) |
| N3A | Ni1 | N2A | 82.8(3) | C11B | N2B | C12B | 105.7(14) |
| N1A | Ni1 | N3A | 93.8(4) | N10B | C1B | C16B | 131(2) |

**Table 16** Continued

| Atom | Atom | Atom | Angle/° | Atom | Atom | Atom | Angle/° |
|---|---|---|---|---|---|---|---|
| N1A | Ni1 | N2A | 78.1(4) | C14B | N1B | Ni1 | 112.3(11) |
| N2B | Ni1 | N5 | 98.6(4) | C13B | N1B | Ni1 | 104.2(10) |
| N2B | Ni1 | N1B | 89.0(6) | C13B | N1B | C14B | 110.5(14) |
| N2B | Ni1 | N4B | 83.3(7) | C5B | N1B | Ni1 | 108.8(11) |
| N1B | Ni1 | N5 | 165.6(5) | C5B | N1B | C14B | 109.3(13) |
| N1B | Ni1 | N4B | 102.4(7) | C5B | N1B | C13B | 111.6(14) |
| N10B | Ni1 | N5 | 85.4(6) | C4B | N10B | Ni1 | 111.0(12) |
| N10B | Ni1 | N7 | 91.8(6) | C1B | N10B | Ni1 | 139.9(16) |
| N10B | Ni1 | N2B | 95.2(7) | C1B | N10B | C4B | 109.0(17) |
| N10B | Ni1 | N1B | 81.7(7) | C10B | N4B | Ni1 | 110.4(14) |
| N10B | Ni1 | N4B | 175.6(8) | C6B | N4B | Ni1 | 125.7(15) |
| N4B | Ni1 | N5 | 90.6(6) | C6B | N4B | C10B | 123.7(19) |
| C18 | N5 | Ni1 | 131.1(4) | F7A$^{2}$ | P1A | F7A | 180.0 |
| C20 | N5 | Ni1 | 113.1(3) | F7A | P1A | F8A | 90.3(4) |
| C20 | N5 | C18 | 114.7(5) | F7A$^{2}$ | P1A | F8A | 89.7(4) |
| C20 | N6 | C19 | 115.9(5) | F7A | P1A | F8A$^{2}$ | 89.7(4) |
| N8$^{1}$ | N7 | Ni1 | 124.2(3) | F7A$^{2}$ | P1A | F8A$^{2}$ | 90.3(4) |
| C21 | N7 | Ni1 | 118.2(3) | F7A | P1A | F9A | 92.1(4) |
| C21 | N7 | N8$^{1}$ | 117.2(4) | F7A$^{2}$ | P1A | F9A | 87.9(4) |
| C21 | N8 | N7$^{1}$ | 114.5(4) | F7A | P1A | F9A$^{2}$ | 87.9(4) |
| N5 | C18 | C17 | 122.1(5) | F7A$^{2}$ | P1A | F9A$^{2}$ | 92.1(4) |
| C18 | C17 | C19 | 118.0(5) | F8A$^{2}$ | P1A | F8A | 180.0 |
| N6 | C19 | C17 | 121.7(6) | F9A | P1A | F8A | 89.2(4) |
| N5 | C20 | C21 | 114.6(5) | F9A$^{2}$ | P1A | F8A$^{2}$ | 89.1(4) |
| N6 | C20 | N5 | 127.5(5) | F9A$^{2}$ | P1A | F8A | 90.8(4) |
| N6 | C20 | C21 | 117.9(5) | F9A | P1A | F8A$^{2}$ | 90.8(4) |
| N7 | C21 | C20 | 113.9(4) | F9A | P1A | F9A$^{2}$ | 180.00(15) |
| N8 | C21 | N7 | 128.2(5) | F7B | P1B | F7B$^{2}$ | 180.0 |
| N8 | C21 | C20 | 117.8(5) | F7B | P1B | F8B | 93.1(10) |
| C3A | C22A | C1A | 119.4(11) | F7B | P1B | F8B$^{2}$ | 86.9(10) |
| N4A | C15A | C14A | 123.7(10) | F7B$^{2}$ | P1B | F8B$^{2}$ | 93.1(10) |
| C15A | C14A | C13A | 118.6(12) | F7B$^{2}$ | P1B | F8B | 86.9(10) |
| C14A | C13A | C12A | 119.6(12) | F7B$^{2}$ | P1B | F9B$^{2}$ | 90.7(9) |

**Table 16** Continued

| Atom | Atom | Atom | Angle/° | Atom | Atom | Atom | Angle/° |
|---|---|---|---|---|---|---|---|
| C13A | C12A | C11A | 118.5(10) | F7B | P1B | F9B$^2$ | 89.3(9) |
| C12A | C11A | C10A | 122.7(8) | F7B$^2$ | P1B | F9B | 89.3(9) |
| N4A | C11A | C12A | 121.9(9) | F7B | P1B | F9B | 90.7(9) |
| N4A | C11A | C10A | 115.4(8) | F8B$^2$ | P1B | F8B | 180.0 |
| N3A | C10A | C11A | 109.9(7) | F8B | P1B | F9B | 89.5(12) |
| C7A | C8A | N3A | 108.7(7) | F8B | P1B | F9B$^2$ | 90.5(12) |
| C8A | C7A | N2A | 112.2(8) | F8B$^2$ | P1B | F9B$^2$ | 89.5(12) |
| N2A | C5A | C2A | 110.5(7) | F8B$^2$ | P1B | F9B | 90.5(12) |
| N1A | C4A | C3A | 120.3(11) | F9B$^2$ | P1B | F9B | 180.0 |
| C15A | N4A | Ni1 | 127.1(8) | F2A | P2A | F1A | 87.4(5) |
| C15A | N4A | C11A | 117.6(9) | F2A | P2A | F3A | 89.9(4) |
| C11A | N4A | Ni1 | 115.3(7) | F2A | P2A | F4A | 87.5(4) |
| C4A | C3A | C22A | 119.4(11) | F2A | P2A | F5A | 170.8(5) |
| C10A | N3A | Ni1 | 106.0(5) | F3A | P2A | F1A | 86.4(5) |
| C10A | N3A | C8A | 108.5(7) | F3A | P2A | F4A | 174.6(5) |
| C9A | N3A | Ni1 | 115.8(5) | F4A | P2A | F1A | 88.8(5) |
| C9A | N3A | C10A | 109.4(6) | F5A | P2A | F1A | 83.4(5) |
| C9A | N3A | C8A | 109.8(6) | F5A | P2A | F3A | 89.2(4) |
| C8A | N3A | Ni1 | 107.0(5) | F5A | P2A | F4A | 92.7(4) |
| C1A | C2A | C5A | 121.0(8) | F6A | P2A | F1A | 175.9(5) |
| C1A | C2A | N1A | 119.0(9) | F6A | P2A | F2A | 92.5(5) |
| N1A | C2A | C5A | 119.9(9) | F6A | P2A | F3A | 89.6(5) |
| C7A | N2A | Ni1 | 104.0(5) | F6A | P2A | F4A | 95.3(5) |
| C6A | N2A | Ni1 | 118.5(6) | F6A | P2A | F5A | 96.6(5) |
| C6A | N2A | C7A | 108.2(7) | F1B | P2B | F3B | 90.7(6) |
| C5A | N2A | Ni1 | 105.9(5) | F1B | P2B | F5B | 88.5(6) |
| C5A | N2A | C7A | 109.5(7) | F1B | P2B | F6B | 169.1(7) |
| C5A | N2A | C6A | 110.3(7) | F2B | P2B | F1B | 91.4(7) |
| C2A | C1A | C22A | 117.5(10) | F2B | P2B | F3B | 87.4(6) |
| C4A | N1A | Ni1 | 125.2(10) | F2B | P2B | F5B | 174.9(7) |
| C4A | N1A | C2A | 124.1(12) | F2B | P2B | F6B | 96.5(7) |
| C2A | N1A | Ni1 | 109.5(8) | F3B | P2B | F5B | 87.5(6) |
| C2B | C16B | C1B | 116(2) | F4B | P2B | F1B | 92.0(7) |

**Table 16** Continued

| Atom | Atom | Atom | Angle/° | Atom | Atom | Atom | Angle/° |
|---|---|---|---|---|---|---|---|
| N1B | C13B | C12B | 108.7(15) | F4B | P2B | F2B | 93.0(6) |
| N2B | C12B | C13B | 109.1(15) | F4B | P2B | F3B | 177.3(7) |
| N2B | C11B | C10B | 112.3(16) | F4B | P2B | F5B | 92.1(6) |
| C9B | C10B | C11B | 123.6(18) | F4B | P2B | F6B | 95.1(7) |
| N4B | C10B | C11B | 117.6(17) | F6B | P2B | F3B | 82.2(6) |
| N4B | C10B | C9B | 118.6(18) | F6B | P2B | F5B | 82.9(7) |

[1]1-X, 1-Y, 1-Z; [2]1-X, 2-Y, 1-Z

*Magnetic Measurements*

**$[\{Ni(TPMA)\}_2$-μ-bmtz$^{\bullet-}](BF_4)_3 \bullet 2CH_3CN$.** The static DC magnetic properties of $[\{Ni(TPMA)\}_2$-μ-bmtz$^{\bullet-}](BF_4)_3$ were measured from 1.8-300 K in a 1000 Oe DC field (Figure 31). The χT value of 3.83 emu K mol$^{-1}$ at 300 K is significantly higher than the expected value of 2.80 emu K mol$^{-1}$ for two independent $Ni^{II}$ ions and one organic radical ($S_{Ni}$ = 1, $g_{Ni}$ = 2.2, $S_{bmtz}$ = 1/2, $g_{bmtz}$ = 2.0), an indication of strong coupling which is evident even at room temperature. The χT value increases continuously and reaches a broad maximum of 4.80 emu K mol$^{-1}$ at 40 K, consistent with a fully coupled S = 5/2 ground state with $g_{iso}$ = 2.1. Below 40 K, χT remains relatively constant until 15 K after which temperature it decreases precipitously. A plot of M vs. H at 1.8 K (Figure 31b) saturates at a value of 5 $\mu_B$, also consistent with an S = 5/2 ground state. Heather Stout and Dr. Catalina Achim performed EPR measurements on this compound as a glassy solution in 4:5 propionitrile:butyronitrile. The parameters $D_{Ni}$ = -3.0 cm$^{-1}$ and E/D = 0.33 were obtained from the EPR measurements. The susceptibility data were fit

using the program PHI.[103] The values of $D_{Ni}$ and $E_{Ni}$ were fixed at the EPR values and $g_{bmtz}$ was fixed at 2.004.[91] The best-fit parameters obtained from PHI are $J_{Ni\text{-}radical}$ = +147 $cm^{-1}$ and $g_{Ni}$ = 2.14, indicating that the coupling between the nickel and bmtz spin centers is indeed strong and ferromagnetic which is in accord with the orthogonality of the $e_g$ magnetic orbitals of $Ni^{II}$ and the $\pi^*$ radical orbital of bmtz. It is noted that this set of best-fit parameters does not reproduce the downturn of $\chi T$ at low temperatures very well, which is attributed to intermolecular interactions due to the $\pi$ stacking in the solid state. A mean-field approximation[122] in the form of a zJ' term was included to account for this interaction. The best-fit parameters including the mean field approximation are $J_{Ni\text{-}radical}$ = +147 $cm^{-1}$, zJ' = -0.02 $cm^{-1}$, and $g_{Ni}$ = 2.14. Strong ferromagnetic coupling between nickel centers and terminal verdazyl radicals has been observed in several cases with coupling constants of up to 188 $cm^{-1}$ being reported (-2J Hamiltonian).[123-125] There are two reports of dinuclear $Ni^{II}$ complexes featuring bridging radicals that display strong ferromagnetic coupling, but neither of them has been fully characterized. In {B.L.[Ni(hfac)$_2$]$_2$} (B.L. = 1,5-dimethyl-3-(4,6-dimethylpyrimidin-2-yl)-6-oxoverdazyl radical, hfac = hexafluoroacetylacetonate) the Ni-radical coupling has a magnitude of 110 $cm^{-1}$ (-2J Hamiltonian).[126] The salt [$Ni_2$(CTH)$_2$(*m*-Ph(SQ)$_2$)]($PF_6$)$_2$, (CTH = D,L-5,7,7,12,14,14-hexamethyl-1,4,8,11-tetraazacyclotetradecane, *m*-Ph(SQ)$_2$ = the diradical semiquinone form of 1,3-bis(3',4'-dihydroxy-5'-tert-butylphenyl)-5-tert-butyl-benzene) in which the radical bridge has two unpaired electrons (S = 1), displays a Ni-radical coupling estimated to be larger than +200 $cm^{-1}$.[127]

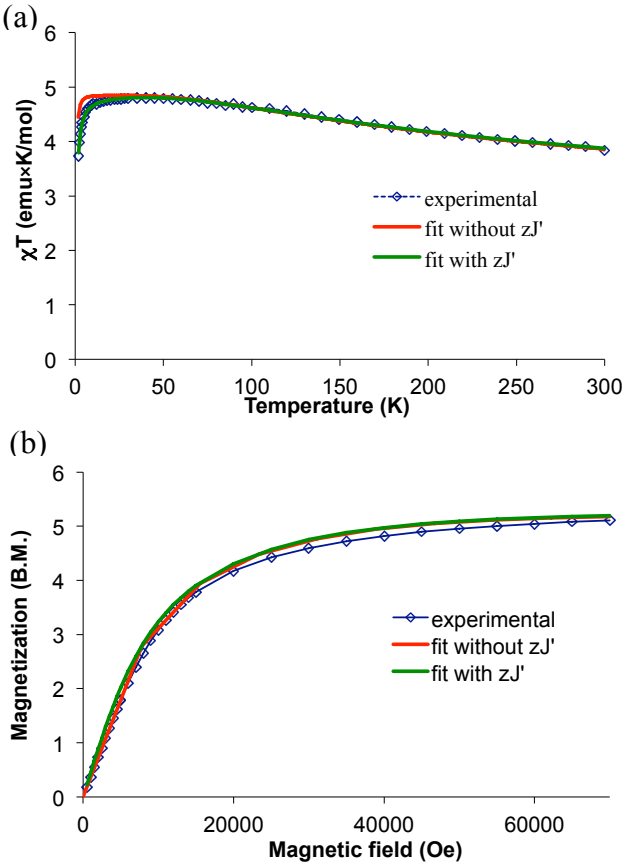


**Figure 31.** DC magnetic properties of [{Ni(TPMA)}$_2$-μ-bmtz$^{\bullet-}$](BF$_4$)$_3$. (a) χT product under a 1000 Oe field. The open blue diamonds are the data and the blue line is a guide for the eye. The solid red line is the result of the fitting that led to the parameters $J_{Ni\text{-}radical}$ = +147 cm$^{-1}$, and $g_{Ni}$ = 2.14 with $g_{bmtz}$ fixed at 2.004. The green line is the result of a simulation using the best-fit parameters with the inclusion of zJ' = -0.02 cm$^{-1}$. (b) plot of M vs. H at 1.8 K. The open blue diamonds are the data and the blue line is a guide for the eye. The solid red line is the result of the fitting without zJ'. The green line is the result of a simulation using the best-fit parameters with the inclusion of zJ' = -0.02 cm$^{-1}$.

Reports of Ni$^{II}$ based SMMs have lagged behind some of the other 3d metal ions in the literature but there is a growing number of examples in recent years.[2,128-131] Given that this new dinuclear Ni$^{II}$ compound exhibits a well isolated non-integer ground state of S = 5/2, we surmised that the quantum tunneling of the magnetization may be suppressed.[39] In the absence of an applied DC field, no out-of-phase (χ'') components of

the AC susceptibility data were observed above 1.8 K. In the presence of a 1000 Oe applied DC field one can observe the beginnings of a χ'' signal, but no maxima in χ'' were observed (Figure 32). The observed beginnings of an out-of-phase signal is likely due to the onset of SMM behavior at low temperatures, but, since no maximum in χ'' is observed, no firm conclusions can be made.

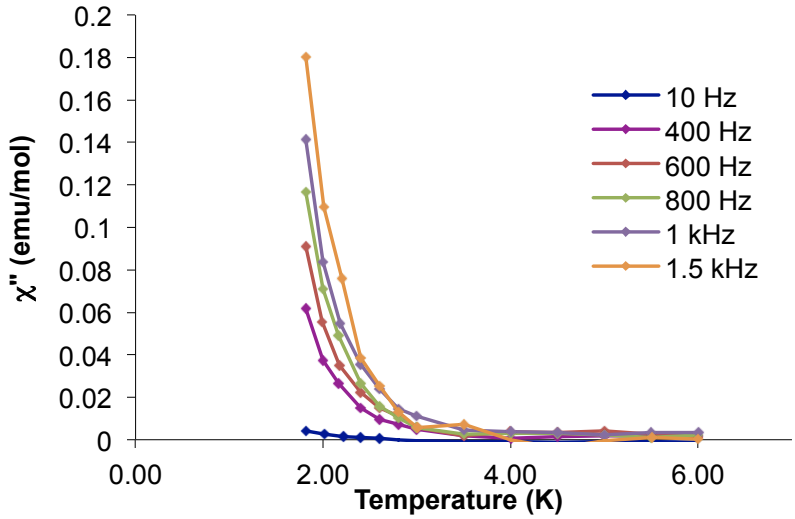


**Figure 32.** Out-of-phase susceptibility data for $[\{Ni(TPMA)\}_2\text{-}\mu\text{-}bmtz^{\bullet-}](BF_4)_3$ in a 1000 Oe applied DC field. The solid lines are guides for the eye.

**$[\{Ni(tren)\}_2\text{-}\mu\text{-}bmtz^{\bullet-}](BF_4)_3 \bullet 3CH_3CN$.** The static DC magnetic properties of $[\{Ni(tren)\}_2\text{-}\mu\text{-}bmtz^{\bullet-}](BF_4)_3$ were measured from 1.8-300 K in a 1000 Oe DC field (Figure 33a). The χT value of 3.79 emu K $mol^{-1}$ at 300 K is significantly higher than the expected value of 2.80 emu K $mol^{-1}$ for an uncoupled system of two $Ni^{II}$ ions and one organic radical ($S_{Ni}$ = 1, $g_{Ni}$ = 2.2, $S_{bmtz}$ = 1/2, $g_{bmtz}$ = 2.0), an indication of strong coupling which is evident even at room temperature. The χT value increases continuously and reaches a broad maximum of 4.89 emu K $mol^{-1}$ at 35 K, consistent

with a fully coupled S = 5/2 ground state with $g_{iso}$ = 2.05. Below 40 K, χT remains relatively constant until 15 K after which temperature it decreases precipitously. A plot of M vs. H at 1.8 K (Figure 33b) saturates at a value of 5.4 $\mu_B$, also consistent with an S = 5/2 ground state. The susceptibility data were fit using the program PHI,[103] leading to best-fit parameters from a simultaneous fitting of the χT vs. T and M vs. H data are $J_{Ni\text{-}radical}$ = +146 $cm^{-1}$, $D_{Ni}$ = -3.42 $cm^{-1}$, and $g_{Ni}$ = 2.11 with $g_{bmtz}$ fixed at 2.004,[91] indicating that the coupling between the nickel and bmtz spin centers is again strong and ferromagnetic. A similar set of fitting parameters can be obtained with a positive D value; based on the results of the EPR studies on $[\{Ni(TPMA)\}_2\text{-}\mu\text{-}bmtz^{\bullet-}](BF_4)_3$ it seems reasonable that D would also be negative for this complex. This set of parameters does not reproduce the shape of χT very well at low temperatures but it is reasonable if one considers the effect of π-π stacking interactions in the solid state, which influence the magnetic properties. As discussed above, the synthesis of this complex proved to be irreproducible therefore only this preliminary set of magnetic measurements is available. Simulating the χT curve with the above best-fit parameters and including an antiferromagnetic exchange term in the form of a mean-field approximation[122] to account for the intermolecular interactions produces the fit line shown in green in Figure 33a. The value of zJ' that best reproduces the downturn in χT is -0.02 $cm^{-1}$. In the absence of further magnetic characterization and EPR studies the best description of the system that can be deduced is that $J_{Ni\text{-}radical}$ = +146 $cm^{-1}$, $D_{Ni}$ = -3.42 $cm^{-1}$, $g_{Ni}$ = 2.11, and zJ' = -0.02 $cm^{-1}$. The effect of changing the capping ligand from the pyridine-based TPMA ligand to the amine-based tren ligand has little effect on the magnetic properties

of the system. Only preliminary AC measurements in a zero applied DC field were performed on this compound; no SMM behavior was observed.

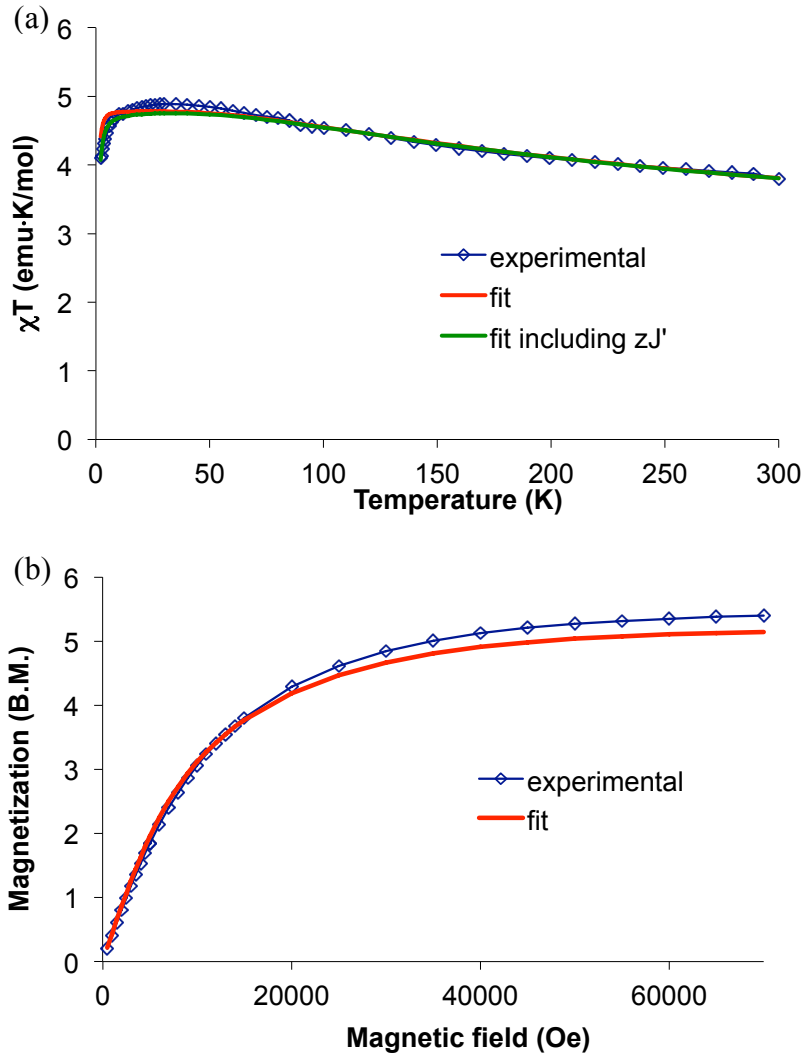


**Figure 33.** DC magnetic properties of $[\{Ni(tren)\}_2\text{-}\mu\text{-}bmtz^{\bullet-}](BF_4)_3$. (a) χT product under a 1000 Oe field. The open blue diamonds are the data and the blue line is a guide for the eye. The solid red line is the result of the fitting that led to the parameters $J_{Ni\text{-}radical} = +146\ cm^{-1}$, $D_{Ni} = -3.42\ cm^{-1}$, and $g_{Ni} = 2.11$ with $g_{bmtz}$ fixed at 2.004. The green line is the result of a simulation using the best-fit parameters with the inclusion of zJ' = $-0.02\ cm^{-1}$. (b) plot of M vs. H at 1.8 K. The open blue diamonds are the data and the blue line is a guide for the eye. The solid red line is the result of the fitting without zJ'.

**[{Ni(TPMA)}$_2$-μ-bmtz$^{\bullet-}$](CF$_3$SO$_3$)$_3$•CH$_3$CN.** The static DC magnetic properties of [{Ni(TPMA)}$_2$-μ-bmtz$^{\bullet-}$](CF$_3$SO$_3$)$_3$ were measured from 1.8-300 K in a 1000 Oe DC field (Figure 34a). The χT value of 4.68 emu K mol$^{-1}$ at 300 K is significantly higher than the expected value of 2.80 emu K mol$^{-1}$ for two Ni$^{II}$ paramagnetic ions and one organic radical ($S_{Ni}$ = 1, $g_{Ni}$ = 2.2, $S_{bmtz}$ = 1/2, $g_{bmtz}$ = 2.0) and is much higher than the value observed at 300 K for either [{Ni(TPMA)}$_2$-μ-bmtz$^{\bullet-}$](BF$_4$)$_3$ or [{Ni(tren)}$_2$-μ-bmtz$^{\bullet-}$](BF$_4$)$_3$. The χT value is constant until 45 K at which temperature it begins a gentle decrease followed by a more rapid decrease beginning at 5 K. The observed value of χT is consistent with a fully coupled S = 5/2 ground state with g = 2.07. A plot of M vs. H at 1.8 K (Figure 34b) saturates at a value of 4.7 $\mu_B$, also consistent with an S = 5/2 ground state. The lack of curvature in the χT data is indicative of extremely strong ferromagnetic coupling between the Ni$^{II}$ ions and the radical but renders a fitting of the data problematic. The best approach is to establish a lower bound for the exchange coupling parameter. The susceptibility and magnetization data were simulated using the program PHI.[103] In order to reproduce the lack of curvature in the susceptibility data, a $J_{Ni\text{-}radical}$ value of at least +600 cm$^{-1}$ was required. Any value of $J_{Ni\text{-}radical}$ greater than 600 cm$^{-1}$ also reproduces the lack of curvature but any value less than 600 cm$^{-1}$ does not, thus setting the lower limit on the value of $J_{Ni\text{-}radical}$. After setting a limit for $J_{Ni\text{-}radical}$, the parameters $D_{Ni}$ and $g_{Ni}$ were varied to achieve the best reproduction of the downturn in χT at low temperatures and the shape of the low-temperature magnetization curve. The best set of simulated parameters was found to be $D_{Ni}$ = 9.0 cm$^{-1}$ and $g_{Ni}$ = 2.10. $g_{bmtz}$ was fixed at 2.004[91] for all of the simulations. A negative $D_{Ni}$ value of approximately -9

$cm^{-1}$ reproduces the susceptibility data fairly well but the simulation of the magnetization data matches the experimental data much better with a positive D value. As with the previous $Ni^{II}$ complexes no SMM behavior was observed for $[\{Ni(TPMA)\}_2\text{-}\mu\text{-}bmtz^{\bullet-}](CF_3SO_3)_3$ even in the presence of an applied DC field.

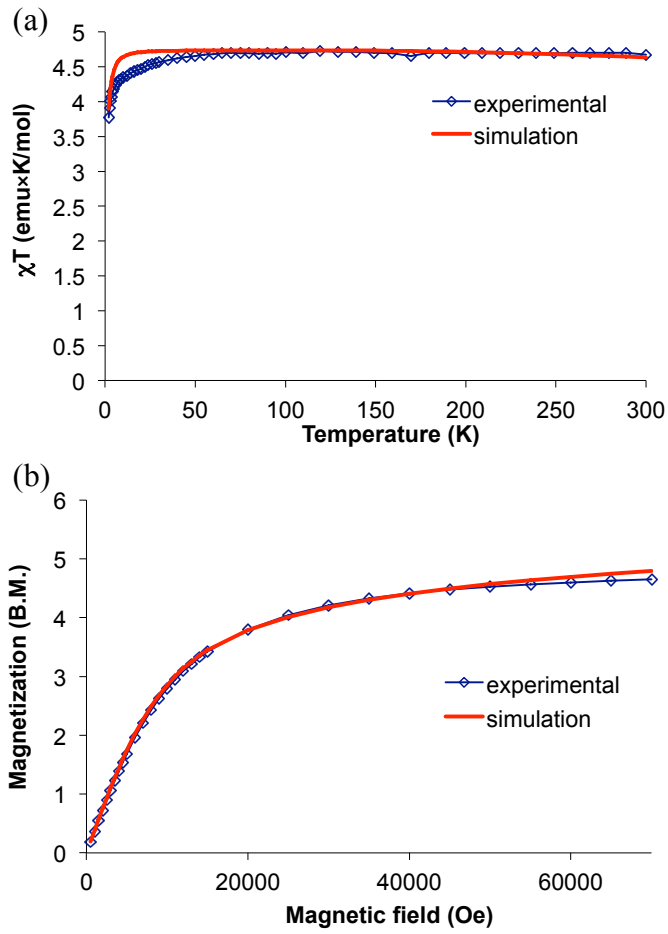


**Figure 34.** DC magnetic properties of $[\{Ni(TPMA)\}_2\text{-}\mu\text{-}bmtz^{\bullet-}](CF_3SO_3)_3$. (a) χT product under a 1000 Oe field. The open blue diamonds are the experimental data and the blue line is a guide for the eye. The solid red line is the result of the simulation using the parameters $J_{Ni\text{-}radical}$ = +600 $cm^{-1}$, $D_{Ni}$ = 9.0 $cm^{-1}$, $g_{Ni}$ = 2.10, and $g_{bmtz}$ = 2.004. (b) plot of M vs. H at 1.8 K. The open blue diamonds are the experimental data and the blue line is a guide for the eye. The solid red line is the result of the simulation.

As discussed earlier, the ability to reproducibly crystallize this complex in the original unit cell proved to be problematic. The static magnetic properties of $[\{Ni(TPMA)\}_2\text{-}\mu\text{-}bmtz^{\bullet-}](CF_3SO_3)_3$ as crystallized in the larger twinned unit cell were measured from 1.8-300 K in a 1000 Oe DC field. The data in Figure 35 reveal that the behavior of this compound is vastly different than what was observed for the original product with the smaller unit cell. The $\chi T$ value of 3.69 emu K $mol^{-1}$ at 300 K is significantly higher than that expected for an uncoupled system of two $Ni^{II}$ ions and a bmtz radical but is lower than the 4.68 emu K $mol^{-1}$ observed for the original compound. The value of $\chi T$ observed for the larger, twinned unit cell is similar to that observed for $[\{Ni(TPMA)\}_2\text{-}\mu\text{-}bmtz^{\bullet-}](BF_4)_3$ and $[\{Ni(tren)\}_2\text{-}\mu\text{-}bmtz^{\bullet-}](BF_4)_3$. In fact, the best-fit parameters from a simultaneous fitting of the $\chi T$ vs. T and M vs. H curves, $J_{Ni\text{-}radical}$ = +161 $cm^{-1}$, $D_{Ni}$ = -2.98 $cm^{-1}$, and $g_{Ni}$ = 2.06 with $g_{bmtz}$ fixed at 2.004,[91] are similar to those obtained for $[\{Ni(TPMA)\}_2\text{-}\mu\text{-}bmtz^{\bullet-}](BF_4)_3$ and $[\{Ni(tren)\}_2\text{-}\mu\text{-}bmtz^{\bullet-}](BF_4)_3$. No SMM behavior was observed for $[\{Ni(TPMA)\}_2\text{-}\mu\text{-}bmtz^{\bullet-}](CF_3SO_3)_3$ crystallized in the large unit cell even in the presence of an applied DC field.

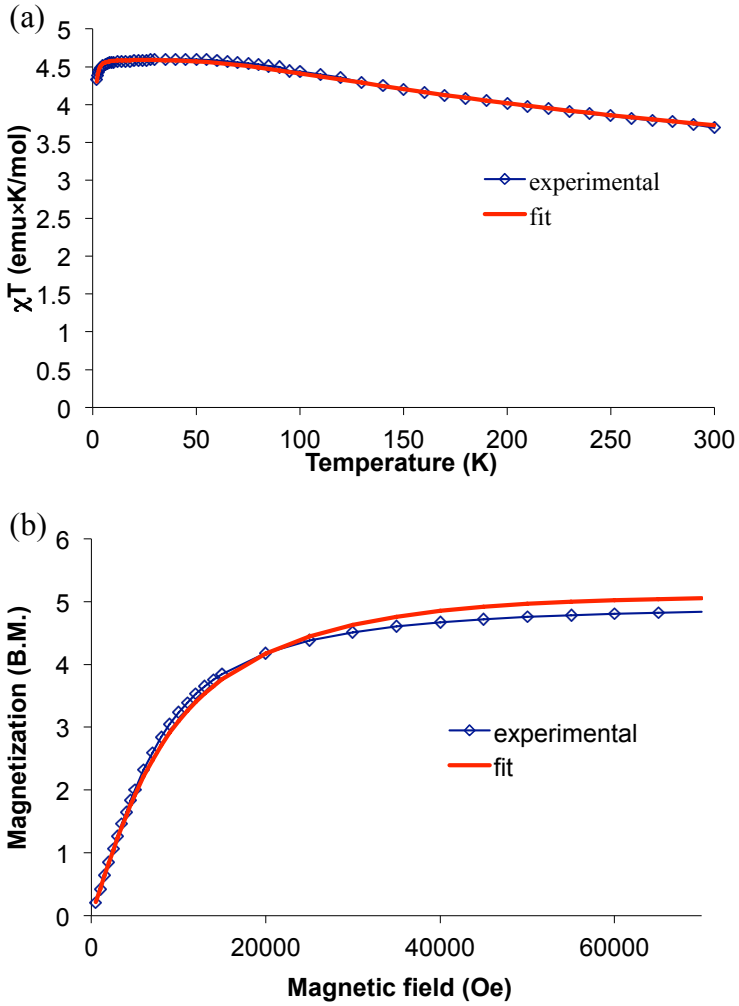


**Figure 35.** DC magnetic properties of $[\{Ni(TPMA)\}_2\text{-}\mu\text{-}bmtz^{\bullet-}](CF_3SO_3)_3$ as crystallized in the larger, twinned unit cell. (a) χT product under a 1000 Oe field. The open blue diamonds are the experimental data and the blue line is a guide for the eye. The solid red line is the result of the fitting that led to the parameters $J_{Ni\text{-}radical}$ = +161 $cm^{-1}$, $D_{Ni}$ = -2.98 $cm^{-1}$, and $g_{Ni}$ = 2.06 with $g_{bmtz}$ fixed at 2.004. (b) plot of M vs. H at 1.8 K. The open blue diamonds are the experimental data and the blue line is a guide for the eye. The solid red line is the result of the fitting.

We were initially surprised by the observation of the extremely large coupling constant in the original complex and attributed this to the different coordination geometries of $[\{Ni(TPMA)\}_2\text{-}\mu\text{-}bmtz^{\bullet-}](BF_4)_3$ and $[\{Ni(TPMA)\}_2\text{-}\mu\text{-}bmtz^{\bullet-}](CF_3SO_3)_3$.

Recall that in $[\{Ni(TPMA)\}_2\text{-}\mu\text{-}bmtz^{\bullet-}](BF_4)_3$ the bridgehead amine nitrogen atom of TPMA is trans to the tetrazine nitrogen atom of bmtz but in the $[CF_3SO_3]^-$ complex a pyridine nitrogen atom of TPMA is trans to the tetrazine nitrogen atom. This hypothesis is inconsistent, however, with the observed magnetic behavior of the salt $[\{Ni(TPMA)\}_2\text{-}\mu\text{-}bmtz^{\bullet-}](CF_3SO_3)_3$ when crystallized in the larger, twinned unit cell. The coordination geometry of TPMA is the same in both $[CF_3SO_3]^-$ complexes, regardless of the unit cell. The complex was crystallized in the larger unit cell on several occasions and the magnetic properties were measured twice and found to be very similar in both instances. The product was only isolated in the small unit cell one time and the measured magnetic properties led to the conclusion that the coupling constant $J_{Ni\text{-}radical}$ is at least +600 $cm^{-1}$. Without the ability to re-measure the magnetic properties of the small unit cell material to confirm the initial results, the reason for the difference in magnetic properties remains unclear.

**$[\{Ni(L_4^2)\}_2\text{-}\mu\text{-}bmtz^{\bullet-}](PF_6)_3 \bullet 2CH_3CN$.** The static DC magnetic properties of $[\{Ni(L_4^2)\}_2\text{-}\mu\text{-}bmtz^{\bullet-}](PF_6)_3$ were measured from 1.8-300 K in a 1000 Oe DC field (Figure 36a). The $\chi T$ value of 3.96 emu K $mol^{-1}$ at 300 K is significantly higher than the expected value of 2.80 emu K $mol^{-1}$ for an uncoupled system of two $Ni^{II}$ ions and one organic radical ($S_{Ni}$ = 1, $g_{Ni}$ = 2.2, $S_{bmtz}$ = 1/2, $g_{bmtz}$ = 2.0), an indication of strong coupling which is evident even at room temperature. The $\chi T$ value increases continuously until 12 K, at which temperature it begins to decrease quickly. A plot of M vs. H at 1.8 K (Figure 36b) saturates at a value of 5.2 $\mu_B$, also consistent with an S = 5/2 ground state. The susceptibility data were fit using the program PHI.[103] The best-fit

parameters obtained from a simultaneous fitting of the $\chi T$ vs. T and M vs. H data are $J_{Ni\text{-}radical} = +185\ cm^{-1}$, $D_{Ni} = -3.15\ cm^{-1}$, and $g_{Ni} = 2.13$ with $g_{bmtz}$ fixed at 2.004,[91] indicating that the coupling between the $Ni^{II}$ and bmtz spin carriers is strong and ferromagnetic. A similar set of fitting parameters can be obtained with a positive D value but, on the basis of the EPR studies for $[\{Ni(TPMA)\}_2\text{-}\mu\text{-}bmtz^{\bullet-}](BF_4)_3$, we have elected to report the negative D value for this complex. ANISOFIT2.0[132] was used to fit the reduced magnetization data (Figure 37) and led to best-fit parameters of $D = -0.6\ cm^{-1}$, $E = -6 \times 10^{-3}\ cm^{-1}$, and $g_{iso} = 2.10$, consistent with the results obtained from PHI. The lack of $\pi$-$\pi$ stacking interactions in the solid state is demonstrated by the fact that good fits to the magnetic data are obtained without the inclusion of a zJ' term. This observation also provides support for the inclusion of a zJ' term for the complexes where $\pi$-$\pi$ stacking is evident in the solid-state structure. No SMM behavior was observed for this complex even in the presence of an applied DC field.

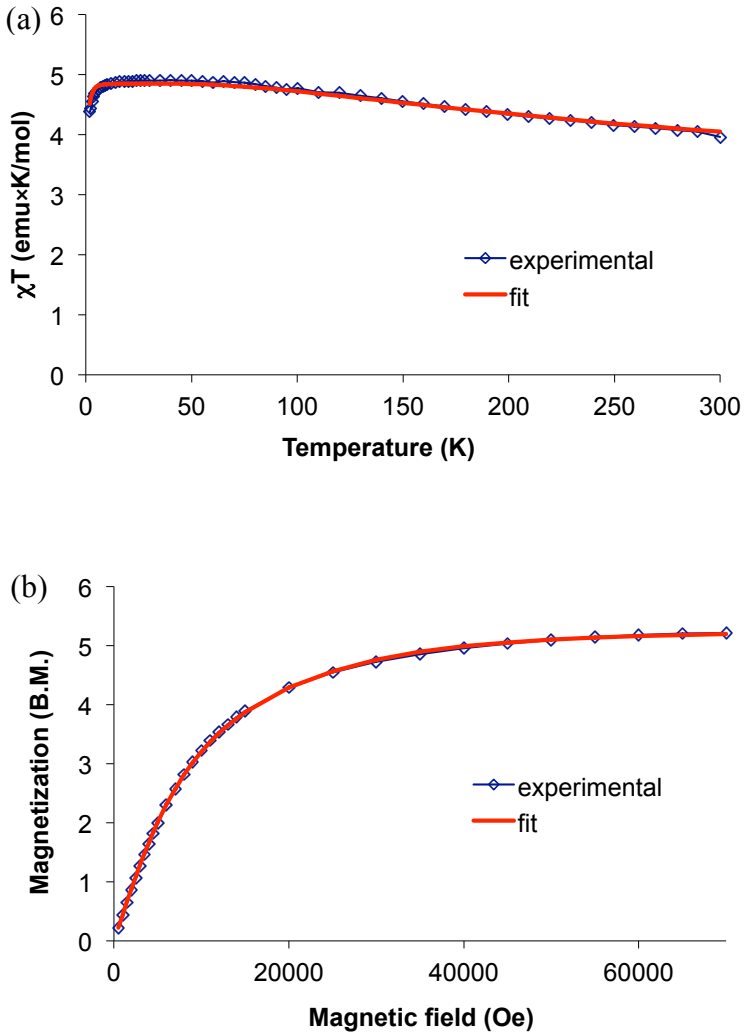


**Figure 36.** DC magnetic properties of $[\{Ni(L_4^2)\}_2\text{-}\mu\text{-bmtz}^{\bullet-}](PF_6)_3$. (a) χT product under a 1000 Oe field. The open blue diamonds are the experimental data and the blue line is a guide for the eye. The solid red line is the result of the fitting that led to the parameters $J_{Ni\text{-}radical}$ = +185 $cm^{-1}$, $D_{Ni}$ = -3.15 $cm^{-1}$, and $g_{Ni}$ = 2.13 with $g_{bmtz}$ fixed at 2.004. (b) plot of M vs. H at 1.8 K. The open blue diamonds are the experimental data and the blue line is a guide for the eye. The solid red line is the result of the fitting.

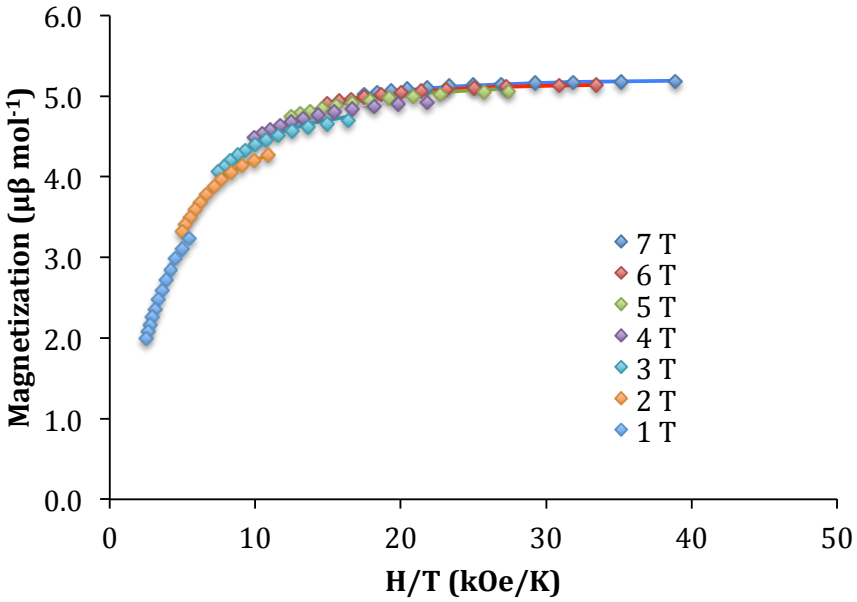


**Figure 37.** Temperature and field dependence of the magnetization for $[\{Ni(L_4^2)\}_2\text{-}\mu\text{-}bmtz^{\bullet-}](PF_6)_3$. Filled diamonds: experimental data. Solid lines: fitting of the experimental data using the parameters described in the main text for the ANISOFIT2.0 fitting.

## Conclusions

A series of dinuclear $M^{II}$ (M = Fe, Co, Ni) complexes bridged by bmtz have been synthesized. For all members of the series in which bmtz is in the radical form, there is evidence for strong coupling between the metal center and the radical. All of the $Ni^{II}$ complexes with $e_g$ magnetic orbitals show very strong ferromagnetic coupling owing to the orthogonality of the $e_g$ orbitals and the $\pi^*$ radical orbital of bmtz. The strength of the coupling is the same order of magnitude for all of the $Ni^{II}$ complexes (Table 17). One of the goals of this study was to determine if the nature of the capping ligand has any effect on the coupling strength. All of the capping ligands used were of the tetradentate N4 variety. The most electron-donating $L_4^2$ ligand yielded the strongest

coupling; detailed electronic structure calculations are needed to determine more definitively the nature of the electronic contributions to the magnetic behavior. Mixed donor ligands, such as tetradentate $N_2O_2$ ligands, would be a valuable addition to this study.

**Table 17.** Comparison of coupling constants for dinuclear $Ni^{II}$ bmtz radical complexes.

| Complex | J ($cm^{-1}$) |
|---|---|
| $[\{Ni(TPMA)\}_2\text{-}\mu\text{-}bmtz^{\bullet-}](BF_4)_3$ | 147 |
| $[\{Ni(tren)\}_2\text{-}\mu\text{-}bmtz^{\bullet-}](BF_4)_3$ | 146 |
| $[\{Ni(TPMA)\}_2\text{-}\mu\text{-}bmtz^{\bullet-}](CF_3SO_3)_3$ small unit cell | ≥600 |
| $[\{Ni(TPMA)\}_2\text{-}\mu\text{-}bmtz^{\bullet-}](CF_3SO_3)_3$ large unit cell | 161 |
| $[\{Ni(L_4^2)\}_2\text{-}\mu\text{-}bmtz^{\bullet-}](PF_6)_3$ | 185 |

The coupling in the $Co^{II}$ complex has been determined to be antiferromagnetic and it appears that the $Fe^{II}$ radical complexes are also antiferromagnetically coupled. This is not an unreasonable result considering that $Fe^{II}$ and $Co^{II}$ have $t_{2g}$ and $e_g$ magnetic orbitals, with direct overlap between the $t_{2g}$ and bmtz $\pi^*$ orbitals possible. The coupling between the metal center and bmtz radical in these complexes is not as strong as in the $Ni^{II}$ cases due to competition between ferromagnetic and antiferromagnetic interactions.

The $Fe^{II}$ complexes are the only members of this family that were able to be isolated with bmtz in its neutral form, with the large majority of the $Fe^{II}$ ions in the low spin state for both the $[BF_4]^-$ and $[CF_3SO_3]^-$ salts. This is not surprising, given the existence of low spin $Fe^{II}$ in $[\{Fe_5(bmtz)_5(CH_3CN)_{10}\} \subset SbF_6][SbF_6]_9$, in which bmtz is also in the neutral oxidation state.[133] Upon reduction of bmtz to the radical form the

ligand becomes a π-donor instead of a π-acceptor, weakening the ligand field enough to facilitate the transition to high spin $Fe^{II}$. For the $[BF_4]^-$ salt the $Fe^{II}$ centers remain high spin at all temperatures. In contrast the $[CF_3SO_3]^-$ salt is a spin crossover complex, albeit one in which spin crossover is incomplete. The difference in behavior between these two salts is attributed to the size of the different anions and a subtle disorder-order transition of one of the $[CF_3SO_3]^-$ anions.

# CHAPTER III

# A FAMILY OF ISOSTRUCTURAL MONONUCLEAR COBALT SINGLE MOLECULE MAGNETS

## Introduction

The search for compounds that exhibit SMM behavior continues but focus has shifted from the large spin ground state molecules synthesized in the early days of the field to smaller molecules, including mononuclear systems. This trend reflects the fact that controlling magnetic anisotropy, which is crucial for determining the energy barrier to spin reversal, is simplified when there is only one spin-bearing metal ion. In fact there are numerous reports in the literature regarding the SMM behavior of complexes containing a single lanthanide ion[134-136] and reports of SMM behavior for mononuclear $Co^{II}$ complexes are increasing rapidly.[87,118,137-142] The library of mononuclear $Co^{II}$ SMMs has recently been expanded to include a seven-coordinate pentagonal bipyramidal complex[143] and an eight-coordinate square antiprismatic complex.[144] The highest reported effective energy barrier to date for a mononuclear $Co^{II}$ complex is 322 $cm^{-1}$ for the four-coordinate $(HNEt_3)_2[Co^{II}(L^{2-})_2]$ ($H_2L$ = 1,2-bis(methanesulfonamido)benzene).[45] Several mononuclear iron complexes[47,51,145] and, very recently, mononuclear $Ni^{I}$ complexes[129,130] as well as a mononuclear $Ni^{II}$ SMM[131] have been reported. The results in this chapter describe our efforts to exploit the single-ion anisotropy of $Co^{II}$ in mononuclear complexes that have the potential for being used as secondary building units for heterometallic coordination complexes. In this approach,

the $Co^{II}$ ion is capped by an organic ligand to limit the dimensionality of the resulting complex, specifically the TPMA ligand. The series of mononuclear complexes of general formula $[Co(TPMA)X]^{n+}(Y)_m$ (X = $CH_3CN$, n = 2, Y = $[BF_4]^-$, m = 2; X = $[Cl]^-$, $[Br]^-$, $[I]^-$, n = 1, Y = $[Cl]^-$, $[Br]^-$, $[I]^-$, m = 1) were synthesized in which the $Co^{II}$ ion resides in a trigonal bipyramidal (TBP) environment with the axial ligand being $CH_3CN$, $[Cl]^-$, $[Br]^-$, or $[I]^-$, which should be easily replaced upon reaction with a suitable metal precursor. TPMA was chosen as the capping ligand to provide a rigid backbone for the cobalt center while still leaving an open coordination site for further chemistry to occur.

**Experimental Section**

The TPMA ligand was prepared by a literature procedure[95] with a final recrystallization from boiling hexanes being added. The salt $[Co(CH_3CN)_6](BF_4)_2$ was prepared by a literature procedure.[97] $CoCl_2$ (Strem), $CoCl_2 \bullet 6H_2O$ (Fisher Scientific), $CoBr_2$ (Alfa Aesar), and $CoI_2$ (Alfa Aesar) were used as received. $CoBr_2 \bullet 6H_2O$ was prepared by dissolving anhydrous $CoBr_2$ in distilled $H_2O$ followed by evaporation of the solvent to produce a microcrystalline pink-red solid.

The syntheses of $[Co(TPMA)(CH_3CN)](BF_4)_2$, the cubic phases of [Co(TPMA)Cl]Cl and [Co(TPMA)Br]Br, and [Co(TPMA)I]I were performed in an MBRAUN dry box under an $N_2$ atmosphere. The $CH_3CN$ was pre-dried by storage over 3 Å molecular sieves, distilled from 3 Å molecular sieves, and stored over 3 Å molecular sieves in the dry box. The $Et_2O$ was purified using an MBRAUN solvent purification system and then stored over 3 Å molecular sieves in the dry box. Toluene

was purified using an MBRAUN solvent purification system and then stored over 3 Å molecular sieves in the dry box.

Syntheses of the triclinic phases of [Co(TPMA)Cl]Cl and [Co(TPMA)Br]Br were performed under ambient air conditions using ACS grade solvents that were used as received without further purification. Elemental analyses were performed by Atlantic Microlabs, Inc., Norcross, GA. Thermogravimetric analyses (TGA) were performed with a Shimadzu TG-50 under a 20 mL/minute flow of $N_2$; an aluminum sample pan was used as the sample holder. The temperature was ramped from room temperature to 300 °C at 2 °C/minute. Infrared spectra were recorded on a Nicolet Nexus 470 FT-IR under an $N_2$ atmosphere as Nujol mulls on KBr plates. Magnetic measurements were conducted in the temperature range of 1.8 to 300 K using a Quantum Design MPMS-XL SQUID magnetometer equipped with a 7T superconducting magnet. The diamagnetic contribution of the plastic bag used as a sample holder was subtracted from the raw data and the core diamagnetism of the sample was accounted for using Pascal's constants.[98]

*Syntheses*

**[Co(TPMA)(CH$_3$CN)](BF$_4$)$_2$•CH$_3$CN**. [Co(CH$_3$CN)$_6$][BF$_4$]$_2$ (.0478 g, 0.0998 mmol) and TPMA (0.0290 g, 0.0999 mmol) were placed in a vial and 5 mL of $CH_3CN$ were added. The resulting red solution was stirred for 24 h and filtered. Red X-ray quality crystals were obtained by slow diffusion of $Et_2O$ vapor into the filtrate. Yield: 0.0493 g (82%). Analysis calculated (found) for [Co(TPMA)(CH$_3$CN)](BF$_4$)$_2$•CH$_3$CN ($C_{22}H_{24}N_6B_2F_8Co$): C: 43.68% (43.55%), H: 4.00% (3.95%), N: 13.89% (13.68%).

**[Co(TPMA)Cl]Cl•2.4$H_2O$ triclinic phase.** The triclinic phase of [Co(TPMACl]Cl was prepared by literature procedure;[146] a re-determination of the crystal structure in conjunction with TGA and IR analysis revealed that the published structure incorrectly reported the complex as anhydrous when it is in reality a hydrated salt. TPMA (0.0949 g, 0.327 mmol) was dissolved in 4.2 mL of MeOH to give a clear, colorless solution, which was added to solid $CoCl_2$•$6H_2O$ (0.0787 g, 0.331 mmol) to give a green solution. After stirring for one hour the MeOH was evaporated to yield a green residue, which was dissolved in a minimum volume of $CH_2Cl_2$ (~15 mL) to give a dark green solution. Gravity filtration through Whatman filter paper was performed to remove a small quantity of brown solid. Bulk green X-ray quality crystals were obtained by layering the clear, dark green filtrate with $Et_2O$. The stated water content in the formula is an average of the water content indicated by elemental analysis and TGA. Yield: 0.0892 g (59%). Analysis calculated (found) for [Co(TPMA)Cl]Cl•2.7$H_2O$ ($C_{18}H_{23.4}N_4Cl_2O_{2.7}Co$): C 46.11% (46.06%), H 5.03% (4.92%), N 11.95% (11.96%).

**[Co(TPMA)Cl]Cl cubic phase.** $CoCl_2$ (0.0333 g, 0.256 mmol) and TPMA (0.0761 g, 0.262 mmol) were placed in a vial and 6.0 mL of $CH_3CN$ were added. The resulting green solution was stirred for 24 hours and then filtered. Bulk green X-ray quality crystals were obtained by layering the green filtrate over toluene. Yield: 0.0401 g (37%). Analysis calculated (found) for [Co(TPMA)Cl]Cl ($C_{18}H_{18}N_4Cl_2Co$): C 51.45% (50.96%), H 4.32% (4.38%), N 13.33% (13.27%).

**[Co(TPMA)Br]Br•2.0$H_2O$ triclinic phase.** The triclinic phase of [Co(TPMABr]Br was prepared by substituting $CoBr_2$•$6H_2O$ for $CoCl_2$•$6H_2O$ in the reported synthesis for

the triclinic phase of [Co(TPMACl]Cl.[146] TPMA (0.0758 g, 0.261 mmol) was dissolved in 5.2 mL of MeOH to give a clear, colorless solution. The TPMA solution was added to solid $CoBr_2$•$6H_2O$ (0.0825 g, 0.252 mmol) to give a blue solution that was stirred for one hour. The MeOH was then evaporated to produce a dark blue-green residue, which was dissolved in the minimum amount of $CH_2Cl_2$ (~15 mL) to give a dark blue-green solution that was gravity filtered through Whatman filter paper to remove a small quantity of brown solid. Bulk green crystals were obtained by layering the blue-green solution with $Et_2O$. These crystals were found to be highly twinned and not suitable for X-ray structural determination. The product was recrystallized by layering $Et_2O$ on a solution of the crystals in 10 mL of $CH_2Cl_2$, which yielded bulk X-ray quality crystals. The stated water content in the formula is reported as an average of the water content obtained by elemental analysis and TGA. Recrystallized yield: 0.0661 g (47%). Analysis calculated (found) for [Co(TPMA)Br]Br•$2.7H_2O$ ($C_{18}H_{23.4}N_4Br_2O_{2.7}Co$): C 38.83% (39.07%), H 4.22% (3.98%), N 10.06% (9.81%).

**[Co(TPMA)Br]Br cubic phase.** $CoBr_2$ (0.0436 g, 0.199 mmol) and TPMA (0.0540 g, 0.186 mmol) were placed in a vial and 5.0 mL of $CH_3CN$ were added. The resulting blue-green solution was stirred for 24 hours and the solution was filtered through a fine glass frit. Bulk green X-ray quality crystals were obtained by layering the blue filtrate with $Et_2O$. Yield: 0.0418 g (44%). Analysis calculated (found) for [Co(TPMA)Br]Br ($C_{18}H_{18}N_4Br_2Co$): C 42.47% (42.73%), H 3.56% (3.66%), N 11.00% (10.93%).

**[Co(TPMA)I]I.** $CoI_2$ (0.0311 g, 0.0994 mmol) and TPMA (0.0290 g, 0.0999 mmol) were placed in a vial and 5.0 mL of $CH_3CN$ were added. The resulting blue-purple

solution was stirred for 24 hours after which time the solution was filtered through a fine glass frit. Bulk purple-pink X-ray quality crystals were obtained by layering the blue-purple filtrate with $Et_2O$. Yield: 0.0239 g (40%). Analysis calculated (found) for [Co(TPMA)I]I ($C_{18}H_{18}N_4I_2Co$): C 35.85% (36.10%), H 3.01% (3.06%), N 9.29% (9.18%).

*X-ray Crystallographic Measurements*

Single crystal X-ray data for $[Co(TPMA)(CH_3CN)](BF_4)_2$, [Co(TPMA)Cl]Cl (triclinic phase), [Co(TPMA)Cl]Cl (cubic phase), [Co(TPMA)Br]Br (cubic phase), and [Co(TPMA)I]I were collected on a Bruker APEXII (Mo $K_\alpha$) diffractometer equipped with a CCD detector. Suitable crystals were affixed to either a nylon loop or a MiTeGen® MicroLoop with Paratone® oil and placed in a cold stream of $N_{2(g)}$ at 110 K for all crystals except [Co(TPMA)I]I, which was collected at 150 K. The triclinic phase of [Co(TPMA)Br]Br was collected on a Bruker D8 Venture (Cu $K_\alpha$ Iμs microfocus) instrument equipped with a CMOS detector. A suitable crystal was affixed to a MiTeGen® MicroLoop with Paratone® oil and placed in a cold stream of $N_{2(g)}$ at 100 K. For all structures, the frames were integrated with the Bruker APEXII software package[99] and a semi-empirical absorption correction was applied using SADABS as contained within the Bruker APEXII software suite. The structure was solved using SHELXT[100] and refined using SHELXL-2014[101] as implemented in ShelXle, a graphical interface for the SHELX suite of programs.[102] The remaining non-hydrogen atoms were located by alternating cycles of least-squares refinements and difference Fourier maps. All hydrogen atoms were placed in calculated positions with the exception of the water

hydrogen atoms in the triclinic phases of [Co(TPMA)Cl]Cl and [Co(TPMA)Br]Br which were not assigned. The final refinements were carried out with anisotropic thermal parameters for all non-hydrogen atoms. Crystals of [Co(TPMA)I]I were invariably found to be non-merohedral twins. The crystal chosen for the structural study was refined as a two-domain twin with the twin fractions refining to 40.3% and 59.7%.

The outer-sphere halide ions in the triclinic phases of [Co(TPMA)Cl]Cl and [Co(TPMA)Br]Br were found to be disordered over multiple positions, as were the water molecules. For both halide derivatives one outer-sphere halide site was found to be fully occupied with the remaining sites being partially occupied. The water molecules were also refined over multiple partially occupied positions. For both of the triclinic halide crystals the total unit cell occupancy of the halide ion was constrained to a target value of 12.0 to balance the charge of the six $Co^{II}$ ions in the unit cell. The total unit cell occupancy of the water oxygen atoms was constrained to a target value of 12.0, resulting in a formula containing two water molecules per $[Co(TPMA)X]^{2+}$ molecule. Attempts to refine the water occupancy to the exact value determined by elemental analysis and TGA (*vide infra*) led to difficulties in convergence. CCDC: 1011895 ($[Co(TPMA)CH_3CN](BF_4)_2$, 1429142 ([Co(TPMA)Cl]Cl cubic phase), 1429144 ([Co(TPMA)Br]Br cubic phase), 1429143 ([Co(TPMA)I]I). Further pertinent details of the X-ray refinements are given in Table 18.

**Table 18.** Crystal and structural refinement data for [Co(TPMA)X] mononuclear compounds.

| Identification code | $[Co(TPMA)CH_3CN](BF_4)_2$ | [Co(TPMA)Cl]Cl |
|---|---|---|
| Empirical formula | $C_{22}H_{24}N_6B_2F_8Co$ | $C_{18}H_{18}N_4Cl_2Co$ |
| Formula weight | 605.02 | 420.19 |
| Temperature/K | 110.15 | 110.15 |
| Crystal system | monoclinic | cubic |
| Space group | $P2_1/c$ | $P2_13$ |
| a/Å | 18.536(12) | 12.394(3) |
| b/Å | 10.609(7) | 12.394(3) |
| c/Å | 14.294(9) | 12.394(3) |
| α/° | 90 | 90 |
| β/° | 110.734(7) | 90 |
| γ/° | 90 | 90 |
| Volume/$Å^3$ | 2629(3) | 1903.9(13) |
| Z | 4 | 4 |
| $\varrho_{calc}g/cm^3$ | 1.529 | 1.466 |
| $\mu/mm^{-1}$ | 0.734 | 1.190 |
| F(000) | 1228.0 | 860.0 |
| Crystal size/$mm^3$ | 0.23 × 0.211 × 0.195 | 0.222 × 0.182 × 0.166 |
| Radiation | MoKα (λ = 0.71073 Å) | MoKα (λ = 0.71073 Å) |
| 2Θ range for data collection/° | 4.502 to 54.984 | 4.648 to 54.96 |
| Index ranges | $-24 \le h \le 23, -13 \le k \le 13, -18 \le l \le 18$ | $-16 \le h \le 16, -16 \le k \le 16, -16 \le l \le 16$ |
| Reflections collected | 29487 | 22035 |
| Independent reflections | 6018 [$R_{int} = 0.0399, R_{sigma} = 0.0301$] | 1466 [$R_{int} = 0.0471, R_{sigma} = 0.0208$] |
| Data/restraints/parameters | 6018/0/354 | 1466/0/76 |
| Goodness-of-fit on $F^2$ [c] | 1.021 | 1.087 |
| Final R indexes [I>=2σ (I)] | $R_1$[a] = 0.0304, $wR_2$[b] = 0.0808 | $R_1$[a] = 0.0220, $wR_2$[b] = 0.0484 |
| Final R indexes [all data] | $R_1$[a] = 0.0381, $wR_2$[b] = 0.0858 | $R_1$[a] = 0.0246, $wR_2$[b] = 0.0495 |
| Largest diff. peak/hole / e $Å^{-3}$ | 0.32/-0.33 | 0.19/-0.20 |
| Flack parameter | | 0.015(7) |

**Table 18** Continued

| Identification code | [Co(TPMA)Cl]Cl | [Co(TPMA)Br]Br |
|---|---|---|
| Empirical formula | $C_{18}H_{18}N_4Cl_2CoO_2$ | $C_{18}H_{18}N_4CoBr_2$ |
| Formula weight | 457.59 | 509.11 |
| Temperature/K | 110.15 | 110.15 |
| Crystal system | triclinic | cubic |
| Space group | P-1 | $P2_13$ |
| a/Å | 11.591(3) | 12.626(4) |
| b/Å | 15.037(4) | 12.626(4) |
| c/Å | 19.998(5) | 12.626(4) |
| α/° | 90.464(3) | 90 |
| β/° | 103.773(3) | 90 |
| γ/° | 111.089(3) | 90 |
| Volume/Å$^3$ | 3141.7(13) | 2013(2) |
| Z | 6 | 4 |
| $\varrho_{calc}$g/cm$^3$ | 1.4511 | 1.680 |
| μ/mm$^{-1}$ | 1.083 | 4.831 |
| F(000) | 1406.9 | 1004.0 |
| Crystal size/mm$^3$ | 0.387 × 0.122 × 0.073 | 0.154 × 0.13 × 0.056 |
| Radiation | Mo Kα (λ = 0.71073 Å) | MoKα (λ = 0.71073 Å) |
| 2Θ range for data collection/° | 2.92 to 48.92 | 4.562 to 52.736 |
| Index ranges | -13 ≤ h ≤ 13, -17 ≤ k ≤ 17, -23 ≤ l ≤ 23 | -15 ≤ h ≤ 15, -15 ≤ k ≤ 15, -15 ≤ l ≤ 15 |
| Reflections collected | 29177 | 21852 |
| Independent reflections | 10358 [$R_{int}$ = 0.0498, $R_{sigma}$ = 0.0615] | 1388 [$R_{int}$ = 0.0823, $R_{sigma}$ = 0.0332] |
| Data/restraints/parameters | 10358/0/729 | 1388/0/76 |
| Goodness-of-fit on F$^2$ [c] | 0.996 | 1.066 |
| Final R indexes [I>=2σ (I)] | $R_1$[a] = 0.0695, $wR_2$[b] = 0.1715 | $R_1$[a] = 0.0279, $wR_2$[b] = 0.0626 |
| Final R indexes [all data] | $R_1$[a] = 0.0922, $wR_2$[b] = 0.1932 | $R_1$[a] = 0.0333, $wR_2$[b] = 0.0647 |
| Largest diff. peak/hole / e Å$^{-3}$ | 1.86/-1.21 | 0.47/-0.40 |
| Flack parameter | | 0.023(10) |

**Table 18** Continued

| | | |
|---|---|---|
| Identification code | [Co(TPMA)Br]Br | [Co(TPMA)I]I |
| Empirical formula | $C_{18}H_{18}N_4CoBr_2O_2$ | $C_{18}H_{18}N_4CoI_2$ |
| Formula weight | 541.11 | 603.09 |
| Temperature/K | 99.99 | 150.15 |
| Crystal system | triclinic | triclinic |
| Space group | P-1 | P-1 |
| a/Å | 11.7529(4) | 9.5710(14) |
| b/Å | 15.0871(5) | 14.259(2) |
| c/Å | 20.3000(7) | 16.834(3) |
| α/° | 90.7760(10) | 114.841(2) |
| β/° | 102.8730(10) | 100.240(2) |
| γ/° | 110.7960(10) | 91.620(2) |
| Volume/Å$^3$ | 3263.46(19) | 2037.8(5) |
| Z | 6 | 4 |
| $\varrho_{calc}$g/cm$^3$ | 1.652 | 1.966 |
| μ/mm$^{-1}$ | 10.651 | 3.880 |
| F(000) | 1602.0 | 1148.0 |
| Crystal size/mm$^3$ | 0.138 × 0.136 × 0.035 | 0.276 × 0.165 × 0.04 |
| Radiation | CuKα (λ = 1.54178 Å) | MoKα (λ = 0.71073 Å) |
| 2Θ range for data collection/° | 4.488 to 137.492 | 2.726 to 56.72 |
| Index ranges | -14 ≤ h ≤ 14, -17 ≤ k ≤ 18, -24 ≤ l ≤ 24 | -12 ≤ h ≤ 12, -19 ≤ k ≤ 17, 0 ≤ l ≤ 22 |
| Reflections collected | 97930 | 17761 |
| Independent reflections | 11855 [$R_{int}$ = 0.0521, $R_{sigma}$ = 0.0289] | 17761 [$R_{int}$ = ?, $R_{sigma}$ = 0.0553] |
| Data/restraints/parameters | 11855/2/730 | 17761/0/452 |
| Goodness-of-fit on F$^{2\ c}$ | 1.059 | 1.088 |
| Final R indexes [I>=2σ (I)] | $R_1{}^a$ = 0.0685, $wR_2{}^b$ = 0.1817 | $R_1{}^a$ = 0.0417, $wR_2{}^b$ = 0.1002 |
| Final R indexes [all data] | $R_1{}^a$ = 0.0805, $wR_2{}^b$ = 0.1951 | $R_1{}^a$ = 0.0525, $wR_2{}^b$ = 0.1070 |
| Largest diff. peak/hole / e Å$^{-3}$ | 2.29/-1.72 | 0.84/-1.16 |

$^a R_1 = \Sigma \big| \, |F_o| - |F_c| \, \big| / \Sigma |F_o|$. $^b wR_2 = \{\Sigma [w(F_o^2 - F_c^2)^2] / \Sigma w(F_o^2)^2]\}^{1/2}$. $^c$Goodness-of-fit = $\{\Sigma [w(F_o^2 - F_c^2)^2]/(n-p)\}^{1/2}$, where *n* is the number of reflections and *p* is the total number of parameters refined.

For [Co(TPMA)Cl]Cl, [Co(TPMA)Br]Br, and [Co(TPMA)I]I powder X-ray diffraction experiments were conducted on a Bruker D8-Focus ECO (Cu $K_\alpha$) Bragg-Brentano diffractometer at room temperature using a silicon zero-background sample holder to verify the phase purity of the bulk sample.

*Computational Details*

Single point calculations of the cationic $[Co(TPMA)X]^{n+}$ fragments were performed using the crystallographic geometries provided in the .cif files. The *ab initio* calculations were performed using the two-step approach implemented in the ORCA 3.0.3 program in which the spin-orbit coupling (SOC) and spin-spin coupling (SSC) relativistic effects are included *a posteriori*.[147] The electronic configuration of $Co^{II}$ is $d^7$, so the selected active space CAS(7,5) contains 7 electrons in the 5 essentially atomic d orbitals. To evaluate the effects of the dynamic correlations, N-Electron Valence Perturbation Theory (NEVPT2) was employed. The Karlsruhe polarized triple-z basis set (TZVP)[148] and the auxiliary def2-TZV/J basis set for resolution of identity (RI)[149] approximation were employed.

**Results and Discussion**

*Syntheses*

The series of compounds constitutes an isostructural family with only slight differences between the members of the family that, nevertheless, have a marked impact on the magnetic properties. In this vein, these compounds are excellent candidates for delving more deeply into the small structural differences that impact the magnetic properties of SMMs. The coordination sphere of the $Co^{II}$ ions in all of the complexes

consists of the four nitrogen atoms from the TPMA capping ligand and either one nitrogen atom from a coordinated $CH_3CN$ molecule or a coordinated halide ion, resulting in a TBP coordination environment. Using the empirical parameter τ, which ranges in value from 0 for a perfect square pyramid to 1 for a perfect trigonal bipyramid and is based on the relationships between the angles around the metal,[150] all members of this family are best described as almost perfect TBP molecules with the equatorial plane defined by the three pyridine N atoms of TPMA (Figure 38). The τ values were found to be 0.995 ($CH_3CN$), 1.000 (Cl triclinic and cubic), 1.000 (Br triclinic and cubic), and 1.000 (I).

All members of the family exhibit approximate $C_3$ symmetry, with the cubic phases having crystallographically imposed $C_3$ symmetry. As can be seen in Figure 39, if only the first coordination sphere is considered, the molecules have $C_{3v}$ symmetry. The mirror plane symmetry is broken by the slight tilt of the pyridine rings and non-planarity between the methyl carbon atoms connecting the pyridine rings to the bridgehead amine nitrogen atom.

It should be noted that, for the synthesis of the triclinic phase of the bromide analog, if a slight excess of TPMA is not used at least some of the product, as shown by single crystal X-ray diffraction, is $[Co(TPMA)Br]_2(CoBr_4)$.

Using $Et_2O$ as the precipitating solvent instead of toluene produces crystals of the cubic phase of [Co(TPMA)Cl]Cl but can also produce crystals of a triclinic phase or a mixture of the two. Attempts to control the phase that crystallizes from $Et_2O$ by varying solution concentration, amount of $Et_2O$ layered on the reaction solution, amount

of time the reaction is stirred before layering with $Et_2O$, or layering versus rapid precipitation with $Et_2O$ did not lead to a set of conditions that would reproducibly crystallize one phase over the other. Crystallizations from toluene preferentially formed the pure cubic phase as confirmed by powder X-ray diffraction (*vide infra*) and the literature method used to prepare the triclinic phase has reproducibly crystallized the desired triclinic phase.

Unlike the chloride complexes, precipitation of [Co(TPMA)Br]Br with $Et_2O$ in the dry box reproducibly crystallizes only the cubic phase. To isolate the triclinic phase, the reaction was performed in air starting from $CoBr_2 \bullet 6H_2O$. The phase purity of these two salts was verified by powder X-ray diffraction (*vide infra*).

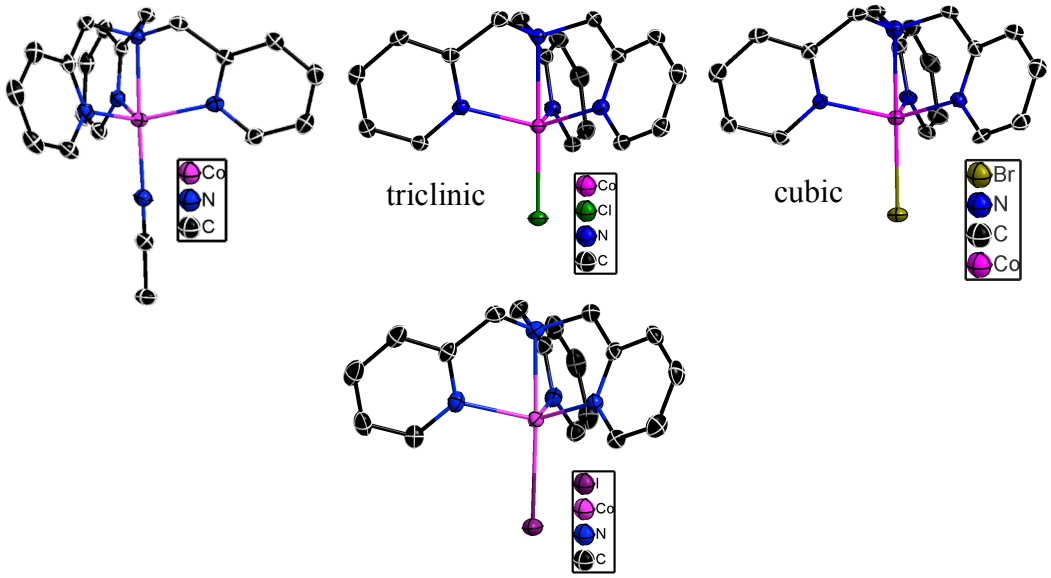


**Figure 38.** Thermal ellipsoid plots of the cationic unit of representative members of the $[Co(TPMA)X]^{1+/2+}$ family. Ellipsoids are drawn at the 50% probability level; H atoms were omitted for the sake of clarity.

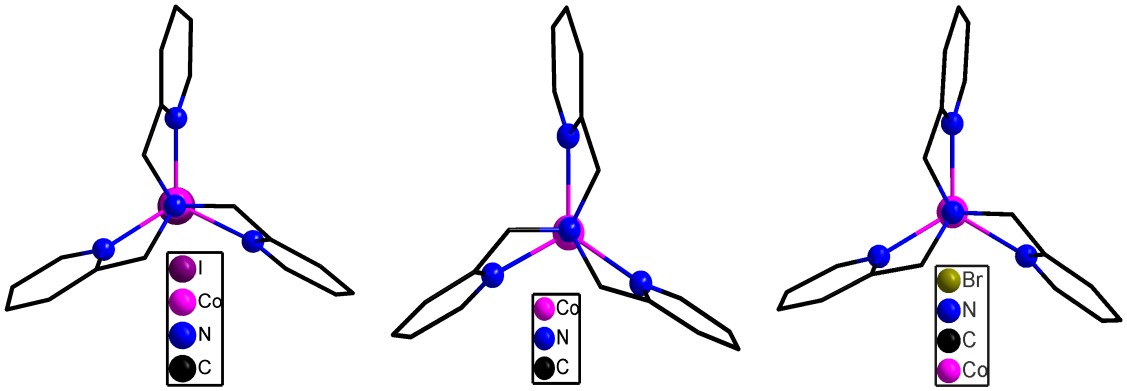


Triclinic
Iodide

Monoclinic
$CH_3CN$

Cubic
Bromide

**Figure 39.** View down the $C_3$ axis of representative members of the $[Co(TPMA)X]^{1+/2+}$ family.

*Single Crystal X-ray Diffraction*

**[Co(TPMA)(CH$_3$CN)](BF$_4$)$_2$•CH$_3$CN**. This molecule is distorted from an ideal TBP geometry with the average $N_{py}$-Co-$N_{amine}$ angle formed by coordination of the TPMA ligand being 78.9° which is much more acute than the expected 90° angle. This results in the $Co^{II}$ ion projecting out of the equatorial plane formed by the three pyridine nitrogen atoms of TPMA and toward the $CH_3CN$ nitrogen atom by 0.395 Å. The local symmetry of the $Co^{II}$ ion is approximately $C_3$, broken by small differences in the equatorial bond angles (range = 118.62(5) to 113.07(6)°). The dihedral angles between pyridine rings range from 116.4° to 122.6° with an average of 119.997°. The closest intermolecular Co-Co contact is 7.863 Å. The thermal ellipsoid plot of [Co(TPMA)(CH$_3$CN)](BF$_4$)$_2$ is displayed in Figure 40 and Table 19 lists bond distances and angles.

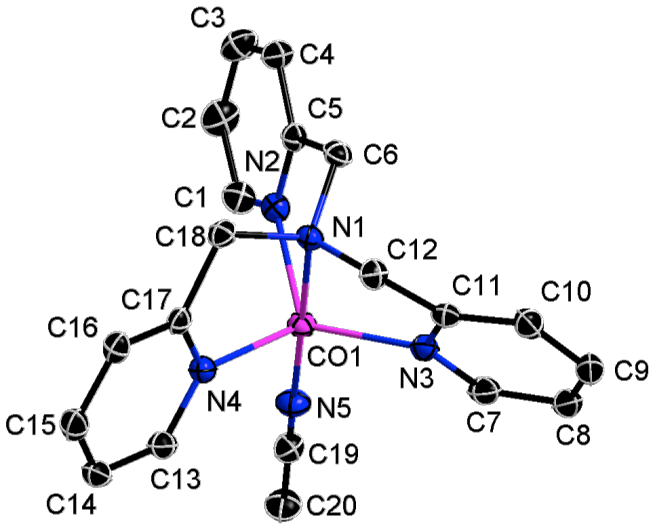


**Figure 40.** Thermal ellipsoid plot of the cationic unit of [Co(TPMA)(CH$_3$CN)](BF$_4$)$_2$. Ellipsoids are drawn at the 50% probability level; H atoms were omitted for the sake of clarity.

**Table 19.** Bond distances and angles for $[Co(TPMA)(CH_3CN)](BF_4)_2$.

| Atom | Atom | Length/Å | Atom | Atom | Length/Å |
|---|---|---|---|---|---|
| Co1 | N1 | 2.1705(16) | F3 | B1 | 1.395(2) |
| Co1 | N2 | 2.0434(17) | N3 | C11 | 1.345(2) |
| Co1 | N3 | 2.0383(17) | N3 | C7 | 1.339(2) |
| Co1 | N4 | 2.0315(15) | C3 | C4 | 1.385(2) |
| Co1 | N5 | 2.0373(17) | C11 | C12 | 1.501(2) |
| N1 | C12 | 1.472(2) | F4 | B1 | 1.386(2) |
| N1 | C6 | 1.467(2) | C4 | C5 | 1.379(2) |
| N1 | C18 | 1.475(2) | C21 | C22 | 1.455(3) |
| C1 | N2 | 1.345(2) | C20 | C19 | 1.444(2) |
| C1 | C2 | 1.373(3) | F5 | B2 | 1.394(2) |
| C10 | C11 | 1.384(2) | N5 | C19 | 1.139(2) |
| C10 | C9 | 1.379(3) | C5 | C6 | 1.502(2) |
| C17 | N4 | 1.340(2) | F6 | B2 | 1.376(2) |
| C17 | C16 | 1.379(2) | N6 | C22 | 1.136(3) |
| C17 | C18 | 1.502(2) | C15 | C14 | 1.375(3) |
| F1 | B1 | 1.383(2) | C15 | C16 | 1.380(2) |
| F2 | B1 | 1.375(2) | F7 | B2 | 1.398(2) |
| N2 | C5 | 1.345(2) | C7 | C8 | 1.383(3) |
| C2 | C3 | 1.380(3) | F8 | B2 | 1.384(2) |
| C13 | N4 | 1.340(2) | C8 | C9 | 1.376(3) |
| C13 | C14 | 1.378(2) | | | |

| Atom | Atom | Atom | Angle/° | Atom | Atom | Atom | Angle/° |
|---|---|---|---|---|---|---|---|
| N2 | Co1 | N1 | 78.53(6) | N3 | C11 | C12 | 115.50(14) |
| N3 | Co1 | N1 | 78.71(5) | C17 | N4 | Co1 | 116.64(10) |
| N3 | Co1 | N2 | 118.62(5) | C13 | N4 | Co1 | 124.20(11) |
| N4 | Co1 | N1 | 79.40(6) | C13 | N4 | C17 | 119.12(14) |
| N4 | Co1 | N2 | 113.07(6) | C5 | C4 | C3 | 118.89(16) |
| N4 | Co1 | N3 | 117.41(7) | N1 | C12 | C11 | 109.85(13) |
| N4 | Co1 | N5 | 101.20(6) | C19 | N5 | Co1 | 179.09(15) |
| N5 | Co1 | N1 | 178.34(5) | N2 | C5 | C4 | 121.89(15) |
| N5 | Co1 | N2 | 99.81(7) | N2 | C5 | C6 | 115.48(14) |
| N5 | Co1 | N3 | 102.31(6) | C4 | C5 | C6 | 122.59(14) |

**Table 19** Continued

| Atom | Atom | Atom | Angle/° | Atom | Atom | Atom | Angle/° |
|---|---|---|---|---|---|---|---|
| C12 | N1 | Co1 | 107.13(10) | N1 | C6 | C5 | 109.71(12) |
| C12 | N1 | C18 | 112.55(12) | C14 | C15 | C16 | 119.54(15) |
| C6 | N1 | Co1 | 106.22(10) | C15 | C14 | C13 | 118.71(15) |
| C6 | N1 | C12 | 111.86(12) | N3 | C7 | C8 | 122.21(17) |
| C6 | N1 | C18 | 112.25(12) | N5 | C19 | C20 | 179.38(19) |
| C18 | N1 | Co1 | 106.32(9) | C9 | C8 | C7 | 119.09(16) |
| N2 | C1 | C2 | 122.37(16) | C17 | C16 | C15 | 118.83(15) |
| C9 | C10 | C11 | 119.03(17) | C8 | C9 | C10 | 119.07(16) |
| N4 | C17 | C16 | 121.70(15) | N1 | C18 | C17 | 110.12(12) |
| N4 | C17 | C18 | 115.73(13) | N6 | C22 | C21 | 179.4(2) |
| C16 | C17 | C18 | 122.47(14) | F1 | B1 | F3 | 108.69(16) |
| C1 | N2 | Co1 | 124.86(11) | F1 | B1 | F4 | 108.73(16) |
| C5 | N2 | Co1 | 116.38(11) | F2 | B1 | F1 | 110.81(17) |
| C5 | N2 | C1 | 118.73(14) | F2 | B1 | F3 | 108.49(16) |
| C1 | C2 | C3 | 118.81(16) | F2 | B1 | F4 | 110.50(17) |
| N4 | C13 | C14 | 122.03(15) | F4 | B1 | F3 | 109.60(15) |
| C11 | N3 | Co1 | 117.05(10) | F5 | B2 | F7 | 107.85(14) |
| C7 | N3 | Co1 | 124.31(12) | F6 | B2 | F5 | 109.47(15) |
| C7 | N3 | C11 | 118.61(14) | F6 | B2 | F7 | 109.93(15) |
| C2 | C3 | C4 | 119.31(16) | F6 | B2 | F8 | 110.34(15) |
| C10 | C11 | C12 | 122.49(15) | F8 | B2 | F5 | 110.32(15) |
| N3 | C11 | C10 | 121.94(15) | F8 | B2 | F7 | 108.89(14) |

**[Co(TPMA)Cl]Cl**. The two phases of [Co(TPMA)Cl]Cl provide a unique opportunity to study the effects of symmetry on magnetic properties. The two phases are isostructural in that that both adopt a TBP coordination geometry. The bonding metrics are remarkable similar but the two compounds have dramatically different crystallographic symmetry.

For the triclinic phase there are three crystallographically independent molecules in the asymmetric unit with an average $N_{py}$-Co-$N_{py}$ angle of 115.6°. The dihedral angles between the pyridine rings range from 116.60° to 122.76° with an average of 120.0°. Similar to $[Co(TPMA)CH_3CN](BF_4)_2$, acute $N_{py}$-Co-$N_{amine}$ angles force the $Co^{II}$ ions to project out of the equatorial plane toward the coordinated chloride ion by an average of 0.435 Å, with an average Co-Cl bond length of 2.2707 Å. The closest intermolecular Co-Co contact is 6.119 Å. It needs to be mentioned that the location of the outer-sphere chloride ions and water molecules cannot be determined with certainty. During the structural refinement the main $[Co(TPMA)Cl]^+$ moieties and one outer-sphere chloride ion could be assigned definitively. None of the remaining electron density peaks were of sufficient intensity to warrant assignment as a fully occupied chloride ion. TGA and IR analysis (*vide infra*) demonstrated that at least some of the residual electron density was due to the presence of water molecules in the crystal structure. The refinement was conducted on the premise that any residual electron density peak of intensity greater than eight electrons per cubic angstrom was unlikely to be water. These peaks were assigned as partially occupied chloride ions. A site occupancy constraint was used to constrain the occupancy of the disordered chloride ions such that the total chloride occupancy of the unit cell was 12, the value needed to balance the charge of the six $Co^{II}$ ions in the unit cell. The highest remaining residual density peaks were assigned as partially occupied chloride ions until the thermal parameters for the chloride ions reached reasonable values and no chloride ion was occupied to a percentage greater than one. This strategy resulted in three positions being assigned as disordered chloride ions

with site occupancies of 78.8, 52.7, and 68.3%. The remaining residual density peaks were then assigned as water oxygen atoms using a methodology similar to that used for the chloride ions. A site occupancy constraint was used to constrain the site occupancy of the disordered oxygen atoms such that the total water oxygen occupancy of the unit cell was 12, resulting in a molecular formula of [Co(TPMA)Cl]Cl•2$H_2O$. A total of twelve oxygen atoms from water were assigned with site occupancies ranging from 25.3 to 75.1%. Attempts to refine the water oxygen occupancy of the unit cell to the fractional molecular content observed by TGA and elemental analysis resulted in convergence problems. While the structure refines well in this manner there is no way to be certain that all of the disordered chloride and water molecules are assigned to the correct positions. For example, the chloride ion occupied at 52.3% could be a fully occupied water oxygen atom. Additionally, it is possible that some of the assigned positions are partially occupied as chloride and partially occupied as water oxygen atoms. While this model is not ideal, it is a better description of the reality of the system than the structure published in literature[146] in which no water molecules were assigned. The unit cell determined in this work and in literature are the same, consistent with the same compound being formed. The authors of the literature procedure for this compound report no elemental analysis, IR data, or TGA results to support their assignment of the structure as anhydrous [Co(TPMA)Cl]Cl although they observed similarly disordered, partially occupied chloride ions in their single crystal structure refinement. Figure 41 displays a thermal ellipsoid plot of the asymmetric unit of the triclinic phase of [Co(TPMA)Cl]Cl and Table 20 lists bond distances and angles.

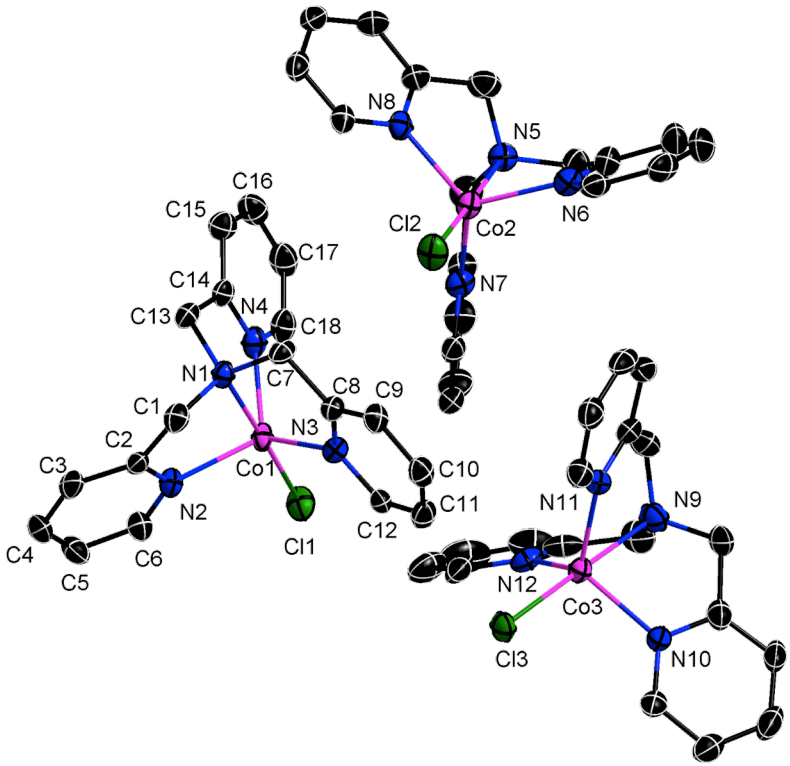


**Figure 41.** Thermal ellipsoid plot of the triclinic phase of [Co(TPMA)Cl]Cl depicting the three crystallographically independent molecules in the asymmetric unit. Ellipsoids are drawn at the 50% probability level; H atoms, outer-sphere Cl atoms, and water molecules were omitted for the sake of clarity.

**Table 20.** Bond distances and angles for the triclinic phase of [Co(TPMA)Cl]Cl.

| Atom | Atom | Length/Å | Atom | Atom | Length/Å |
|---|---|---|---|---|---|
| Co1 | Cl1 | 2.2757(17) | C10 | C11 | 1.376(9) |
| Co1 | N1 | 2.211(5) | N10 | C38 | 1.352(8) |
| Co1 | N2 | 2.050(5) | N10 | C42 | 1.328(8) |
| Co1 | N3 | 2.060(5) | C12 | C11 | 1.377(8) |
| Co1 | N4 | 2.058(5) | N12 | C50 | 1.339(9) |
| N1 | C1 | 1.470(8) | N12 | C54 | 1.348(9) |
| N1 | C7 | 1.475(7) | N11 | C44 | 1.344(8) |
| N1 | C13 | 1.472(7) | N11 | C48 | 1.353(8) |
| C1 | C2 | 1.504(8) | C13 | C14 | 1.496(8) |
| Co2 | Cl2 | 2.2630(17) | C14 | C15 | 1.386(9) |

**Table 20** Continued

| Atom | Atom | Length/Å | Atom | Atom | Length/Å |
|---|---|---|---|---|---|
| Co2 | N5 | 2.187(5) | C15 | C16 | 1.367(9) |
| Co2 | N6 | 2.051(5) | C16 | C17 | 1.371(10) |
| Co2 | N7 | 2.049(5) | C19 | C20 | 1.504(10) |
| Co2 | N8 | 2.069(5) | C18 | C17 | 1.387(9) |
| N2 | C2 | 1.334(8) | C21 | C20 | 1.376(10) |
| N2 | C6 | 1.358(8) | C21 | C22 | 1.359(11) |
| C2 | C3 | 1.389(8) | C22 | C23 | 1.366(11) |
| Co3 | Cl3 | 2.2704(17) | C23 | C24 | 1.389(10) |
| Co3 | N9 | 2.182(5) | C25 | C26 | 1.507(9) |
| Co3 | N10 | 2.059(5) | C26 | C27 | 1.386(10) |
| Co3 | N12 | 2.053(5) | C28 | C29 | 1.369(10) |
| Co3 | N11 | 2.050(5) | C28 | C27 | 1.373(10) |
| N3 | C8 | 1.358(7) | C29 | C30 | 1.371(9) |
| N3 | C12 | 1.343(7) | C31 | C32 | 1.504(10) |
| C3 | C4 | 1.387(10) | C32 | C33 | 1.384(9) |
| N4 | C14 | 1.354(8) | C33 | C34 | 1.365(10) |
| N4 | C18 | 1.344(8) | C34 | C35 | 1.368(10) |
| C4 | C5 | 1.379(10) | C35 | C36 | 1.378(9) |
| N5 | C19 | 1.452(8) | C37 | C38 | 1.498(9) |
| N5 | C25 | 1.465(8) | C38 | C39 | 1.369(9) |
| N5 | C31 | 1.471(8) | C39 | C40 | 1.367(11) |
| C5 | C6 | 1.364(9) | C40 | C41 | 1.384(11) |
| N6 | C20 | 1.337(8) | C41 | C42 | 1.378(9) |
| N6 | C24 | 1.337(8) | C43 | C44 | 1.490(10) |
| N7 | C26 | 1.346(8) | C44 | C45 | 1.394(9) |
| N7 | C30 | 1.349(8) | C45 | C46 | 1.394(10) |
| C7 | C8 | 1.494(8) | C46 | C47 | 1.359(10) |
| C9 | C8 | 1.379(8) | C47 | C48 | 1.374(9) |
| C9 | C10 | 1.378(9) | C49 | C50 | 1.498(11) |
| N9 | C37 | 1.458(9) | C50 | C51 | 1.380(11) |
| N9 | C43 | 1.486(8) | C51 | C52 | 1.359(13) |
| N9 | C49 | 1.474(9) | C52 | C53 | 1.372(13) |
| N8 | C32 | 1.328(8) | C53 | C54 | 1.366(10) |

**Table 20** Continued

| Atom | Atom | Length/Å |
|---|---|---|
| N8 | C36 | 1.333(8) |

| Atom | Atom | Atom | Angle/° | Atom | Atom | Atom | Angle/° |
|---|---|---|---|---|---|---|---|
| N1 | Co1 | Cl1 | 178.46(13) | C9 | C8 | N3 | 121.5(5) |
| N2 | Co1 | Cl1 | 100.76(14) | C9 | C8 | C7 | 123.6(5) |
| N2 | Co1 | N1 | 77.74(18) | C32 | N8 | Co2 | 116.9(4) |
| N3 | Co1 | Cl1 | 103.42(14) | C36 | N8 | Co2 | 124.5(4) |
| N3 | Co1 | N1 | 77.03(17) | C36 | N8 | C32 | 118.5(5) |
| N3 | Co1 | N2 | 114.51(19) | C11 | C10 | C9 | 120.0(6) |
| N4 | Co1 | Cl1 | 103.21(15) | C38 | N10 | Co3 | 116.2(4) |
| N4 | Co1 | N1 | 77.79(18) | C42 | N10 | Co3 | 124.6(4) |
| N4 | Co1 | N2 | 114.25(19) | C42 | N10 | C38 | 119.3(5) |
| N4 | Co1 | N3 | 117.62(19) | C11 | C12 | N3 | 122.3(6) |
| C1 | N1 | Co1 | 106.9(3) | C50 | N12 | Co3 | 116.5(5) |
| C7 | N1 | Co1 | 107.4(3) | C54 | N12 | Co3 | 124.1(5) |
| C7 | N1 | C1 | 112.1(5) | C54 | N12 | C50 | 119.2(6) |
| C13 | N1 | Co1 | 107.9(3) | C12 | C11 | C10 | 118.6(6) |
| C13 | N1 | C1 | 111.4(5) | C44 | N11 | Co3 | 117.6(4) |
| C13 | N1 | C7 | 110.9(5) | C48 | N11 | Co3 | 123.6(4) |
| C2 | C1 | N1 | 109.4(5) | C48 | N11 | C44 | 118.8(5) |
| N5 | Co2 | Cl2 | 178.90(14) | C14 | C13 | N1 | 109.6(5) |
| N6 | Co2 | Cl2 | 102.06(15) | C13 | C14 | N4 | 115.8(5) |
| N6 | Co2 | N5 | 78.08(19) | C15 | C14 | N4 | 121.6(6) |
| N7 | Co2 | Cl2 | 103.06(15) | C15 | C14 | C13 | 122.5(6) |
| N7 | Co2 | N5 | 77.85(19) | C16 | C15 | C14 | 119.2(6) |
| N7 | Co2 | N6 | 112.6(2) | C17 | C16 | C15 | 119.8(7) |
| N8 | Co2 | Cl2 | 101.39(14) | C20 | C19 | N5 | 110.3(5) |
| N8 | Co2 | N5 | 77.62(19) | C17 | C18 | N4 | 122.0(6) |
| N8 | Co2 | N6 | 118.2(2) | C18 | C17 | C16 | 118.9(6) |
| N8 | Co2 | N7 | 116.21(19) | C22 | C21 | C20 | 120.1(7) |
| C2 | N2 | Co1 | 117.9(4) | C19 | C20 | N6 | 115.5(6) |
| C6 | N2 | Co1 | 123.1(4) | C21 | C20 | N6 | 121.3(7) |
| C6 | N2 | C2 | 118.6(5) | C21 | C20 | C19 | 123.1(7) |

**Table 20** Continued

| Atom | Atom | Atom | Angle/° | Atom | Atom | Atom | Angle/° |
|---|---|---|---|---|---|---|---|
| N2 | C2 | C1 | 115.6(5) | C23 | C22 | C21 | 119.3(7) |
| C3 | C2 | C1 | 122.5(6) | C24 | C23 | C22 | 118.5(7) |
| C3 | C2 | N2 | 121.9(6) | C26 | C25 | N5 | 109.6(5) |
| N9 | Co3 | Cl3 | 178.57(15) | C23 | C24 | N6 | 122.1(7) |
| N10 | Co3 | Cl3 | 101.17(15) | C25 | C26 | N7 | 114.9(6) |
| N10 | Co3 | N9 | 78.0(2) | C27 | C26 | N7 | 121.4(6) |
| N12 | Co3 | Cl3 | 101.05(16) | C27 | C26 | C25 | 123.7(6) |
| N12 | Co3 | N9 | 78.3(2) | C27 | C28 | C29 | 119.1(7) |
| N12 | Co3 | N10 | 115.4(2) | C30 | C29 | C28 | 119.1(6) |
| N11 | Co3 | Cl3 | 103.95(15) | C29 | C30 | N7 | 122.7(6) |
| N11 | Co3 | N9 | 77.5(2) | C32 | C31 | N5 | 109.6(5) |
| N11 | Co3 | N10 | 115.9(2) | C31 | C32 | N8 | 116.0(6) |
| N11 | Co3 | N12 | 116.0(2) | C33 | C32 | N8 | 122.0(6) |
| C8 | N3 | Co1 | 118.2(4) | C33 | C32 | C31 | 122.0(6) |
| C12 | N3 | Co1 | 122.8(4) | C34 | C33 | C32 | 118.7(7) |
| C12 | N3 | C8 | 118.7(5) | C35 | C34 | C33 | 119.8(6) |
| C4 | C3 | C2 | 118.7(6) | C36 | C35 | C34 | 118.2(6) |
| C14 | N4 | Co1 | 117.6(4) | C35 | C36 | N8 | 122.6(6) |
| C18 | N4 | Co1 | 123.7(4) | C38 | C37 | N9 | 110.0(5) |
| C18 | N4 | C14 | 118.4(5) | C37 | C38 | N10 | 115.9(5) |
| C5 | C4 | C3 | 119.3(6) | C39 | C38 | N10 | 121.3(6) |
| C19 | N5 | Co2 | 107.5(4) | C39 | C38 | C37 | 122.8(6) |
| C25 | N5 | Co2 | 106.3(4) | C40 | C39 | C38 | 119.1(7) |
| C25 | N5 | C19 | 112.3(5) | C41 | C40 | C39 | 120.1(6) |
| C31 | N5 | Co2 | 106.9(4) | C42 | C41 | C40 | 117.8(7) |
| C31 | N5 | C19 | 111.7(5) | C41 | C42 | N10 | 122.4(6) |
| C31 | N5 | C25 | 111.7(5) | C44 | C43 | N9 | 109.5(5) |
| C6 | C5 | C4 | 119.1(6) | C43 | C44 | N11 | 115.8(6) |
| C20 | N6 | Co2 | 117.3(4) | C45 | C44 | N11 | 121.4(6) |
| C24 | N6 | Co2 | 124.1(4) | C45 | C44 | C43 | 122.8(6) |
| C24 | N6 | C20 | 118.6(6) | C46 | C45 | C44 | 118.3(6) |
| C5 | C6 | N2 | 122.4(6) | C47 | C46 | C45 | 120.2(6) |
| C26 | N7 | Co2 | 117.2(4) | C48 | C47 | C46 | 118.8(7) |

**Table 20** Continued

| Atom | Atom | Atom | Angle/° | Atom | Atom | Atom | Angle/° |
|---|---|---|---|---|---|---|---|
| C30 | N7 | Co2 | 124.8(4) | C47 | C48 | N11 | 122.5(6) |
| C30 | N7 | C26 | 118.0(5) | C50 | C49 | N9 | 111.4(6) |
| C8 | C7 | N1 | 109.6(5) | C49 | C50 | N12 | 116.2(6) |
| C10 | C9 | C8 | 118.9(6) | C51 | C50 | N12 | 120.7(8) |
| C37 | N9 | Co3 | 107.1(4) | C51 | C50 | C49 | 123.0(7) |
| C43 | N9 | Co3 | 107.2(4) | C52 | C51 | C50 | 120.1(8) |
| C43 | N9 | C37 | 111.7(5) | C53 | C52 | C51 | 119.0(8) |
| C49 | N9 | Co3 | 106.6(4) | C54 | C53 | C52 | 119.3(8) |
| C49 | N9 | C37 | 112.3(5) | C53 | C54 | N12 | 121.6(7) |
| C49 | N9 | C43 | 111.7(5) | C28 | C27 | C26 | 119.6(7) |
| C7 | C8 | N3 | 114.9(5) | | | | |

For the cubic phase, there is only one crystallographically independent molecule and it resides on a three-fold axis, thus enforcing strict *C*$_3$ symmetry with an $N_{py}$-Co-$N_{py}$ angle of 115.21(4)°. The dihedral angle formed by the pyridine rings is 120°. The projection of the $Co^{II}$ ion toward the coordinated chloride ion is 0.459 Å, with a Co-Cl bond length of 2.277(12) Å. The closest intermolecular Co-Co contact is 7.951 Å. Figure 42 displays a thermal ellipsoid plot of the cubic phase of [Co(TPMA)Cl]Cl and Table 21 lists bond distances and angles.

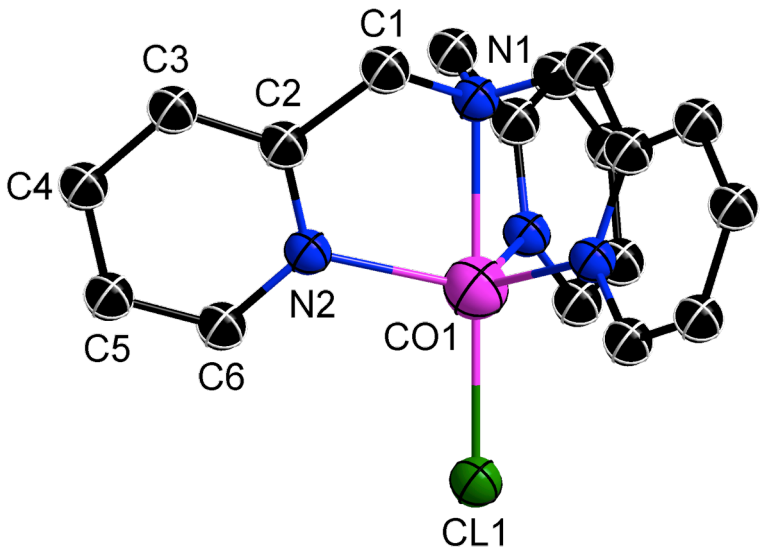


**Figure 42.** Thermal ellipsoid plot of the cationic unit of the cubic phase of [Co(TPMA)Cl]Cl. The atom numbers designate the asymmetric unit. Ellipsoids are drawn at the 50% probability level; H atoms were omitted for the sake of clarity.

**Table 21.** Bond distances and angles for the cubic phase of [Co(TPMA)Cl]Cl.

| Atom | Atom | Length/Å | Atom | Atom | Length/Å |
|---|---|---|---|---|---|
| Co1 | Cl1 | 2.2771(12) | C1 | C2 | 1.502(3) |
| Co1 | N1 | 2.214(3) | N2 | C2 | 1.351(3) |
| Co1 | N2[1] | 2.068(2) | N2 | C6 | 1.343(3) |
| Co1 | N2[2] | 2.068(2) | C2 | C3 | 1.381(3) |
| Co1 | N2 | 2.068(2) | C3 | C4 | 1.385(4) |
| N1 | C1 | 1.470(3) | C4 | C5 | 1.384(4) |
| N1 | C1[2] | 1.470(3) | C5 | C6 | 1.382(3) |
| N1 | C1[1] | 1.470(3) | | | |

[1]+Z,+X,+Y; [2]+Y,+Z,+X

| Atom | Atom | Atom | Angle/° | Atom | Atom | Atom | Angle/° |
|---|---|---|---|---|---|---|---|
| N1 | Co1 | Cl1 | 180.00(6) | C1[2] | N1 | C1[1] | 112.02(14) |
| N2[1] | Co1 | Cl1 | 102.83(6) | C1 | N1 | C1[1] | 112.02(14) |
| N2[2] | Co1 | Cl1 | 102.83(6) | N1 | C1 | C2 | 109.5(2) |
| N2 | Co1 | Cl1 | 102.83(6) | C2 | N2 | Co1 | 117.62(16) |

**Table 21** Continued

| Atom | Atom | Atom | Angle/° | Atom | Atom | Atom | Angle/° |
|---|---|---|---|---|---|---|---|
| N2 | Co1 | N1 | 77.17(6) | C6 | N2 | Co1 | 123.63(16) |
| N2[2] | Co1 | N1 | 77.17(6) | C6 | N2 | C2 | 118.6(2) |
| N2[1] | Co1 | N1 | 77.17(6) | N2 | C2 | C1 | 115.1(2) |
| N2 | Co1 | N2[2] | 115.21(4) | N2 | C2 | C3 | 121.9(2) |
| N2[2] | Co1 | N2[1] | 115.22(4) | C3 | C2 | C1 | 123.0(2) |
| N2 | Co1 | N2[1] | 115.21(4) | C2 | C3 | C4 | 119.3(2) |
| C1[2] | N1 | Co1 | 106.79(15) | C5 | C4 | C3 | 118.8(2) |
| C1[1] | N1 | Co1 | 106.79(15) | C6 | C5 | C4 | 119.0(2) |
| C1 | N1 | Co1 | 106.79(15) | N2 | C6 | C5 | 122.3(2) |
| C1 | N1 | C1[2] | 112.02(14) | | | | |

[1]+Z,+X,+Y; [2]+Y,+Z,+X

**[Co(TPMA)Br]Br**. The bromide analog also crystallizes in both triclinic and cubic phases. In the case of the triclinic phase there are three crystallographically independent molecules in the asymmetric unit with an average $N_{py}$-Co-$N_{py}$ angle of 114.9°. The dihedral angles formed by the pyridine rings of TPMA range from 116.62° to 123.11° with an average of 120.0°. The $Co^{II}$ ions project out of the equatorial plane toward the coordinated bromide ion by an average of 0.436 Å, with an average Co-Br bond length of 2.4151 Å. The closest intermolecular Co-Co contact is 6.289 Å. Similar to the triclinic chloride phase, one outer-sphere bromide ion is fully occupied with additional bromide ions being disordered over several positions. Using the same methodology as described previously for the triclinic chloride phase, a total of six additional bromide ions were assigned with partial occupancies ranging from 28.1 to 46.0%. The remaining residual density peaks were assigned as disordered water oxygen atoms, with the total

oxygen occupancy of the unit cell again constrained to 12.0 to be consistent with the nearest whole-number value of water molecules as determined by elemental analysis and TGA. A total of nine water oxygen atoms were assigned with site occupancies ranging from 27.5 to 98.7%. Analogous to the discussion presented for the triclinic chloride phase, the confidence in the placement of the bromide ions and water molecules cannot be considered unique, but the greater difference in electron density between oxygen and bromide as compared to oxygen and chloride makes the possibility of multiple refinement solutions somewhat less likely. Figure 43 displays a thermal ellipsoid plot of the asymmetric unit of the triclinic phase of [Co(TPMA)Br]Br and Table 22 lists bond distances and angles.

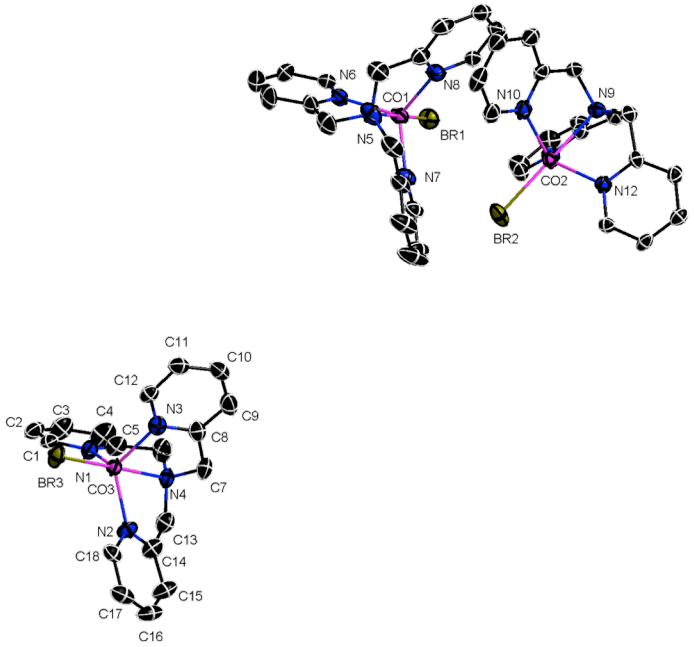


**Figure 43.** Thermal ellipsoid plot of the triclinic phase of [Co(TPMA)Br]Br depicting the three crystallographically independent molecules in the asymmetric unit. Ellipsoids are drawn at the 50% probability level; H atoms, outer-sphere Br atoms, and water molecules were omitted for the sake of clarity.

**Table 22.** Bond distances and angles for the triclinic phase of [Co(TPMA)Br]Br.

| Atom | Atom | Length/Å | Atom | Atom | Length/Å |
|---|---|---|---|---|---|
| Br1 | Co1 | 2.4131(12) | N10 | C48 | 1.334(10) |
| Co1 | N5 | 2.193(6) | C11 | C12 | 1.363(11) |
| Co1 | N6 | 2.053(6) | N11 | C50 | 1.347(9) |
| Co1 | N7 | 2.067(6) | N11 | C54 | 1.333(9) |
| Co1 | N8 | 2.057(6) | N12 | C38 | 1.345(8) |
| N1 | C1 | 1.341(9) | N12 | C42 | 1.343(8) |
| N1 | Co3 | 2.064(6) | C13 | C14 | 1.495(11) |
| N1 | C5 | 1.332(10) | C14 | C15 | 1.393(11) |
| C1 | C2 | 1.378(11) | C15 | C16 | 1.375(13) |
| Co2 | Br2 | 2.4222(12) | C16 | C17 | 1.376(13) |
| Co2 | N9 | 2.217(5) | C17 | C18 | 1.381(11) |
| Co2 | N10 | 2.064(6) | C19 | C20 | 1.499(12) |
| Co2 | N11 | 2.069(6) | C21 | C20 | 1.393(12) |
| Co2 | N12 | 2.065(5) | C21 | C22 | 1.359(15) |
| N2 | Co3 | 2.075(6) | C27 | C26 | 1.385(10) |
| N2 | C14 | 1.343(10) | C27 | C28 | 1.391(12) |
| N2 | C18 | 1.344(9) | C26 | C25 | 1.502(11) |
| C2 | C3 | 1.355(13) | C24 | C23 | 1.376(11) |
| Br3 | Co3 | 2.4093(12) | C23 | C22 | 1.382(13) |
| Co3 | N3 | 2.054(6) | C28 | C29 | 1.376(11) |
| Co3 | N4 | 2.189(5) | C29 | C30 | 1.374(10) |
| N3 | C8 | 1.347(9) | C31 | C32 | 1.490(12) |
| N3 | C12 | 1.340(9) | C32 | C33 | 1.384(11) |
| C3 | C4 | 1.384(14) | C33 | C34 | 1.378(15) |
| N4 | C6 | 1.457(10) | C34 | C35 | 1.386(14) |
| N4 | C7 | 1.478(9) | C35 | C36 | 1.370(11) |
| N4 | C13 | 1.463(10) | C37 | C38 | 1.509(9) |
| C4 | C5 | 1.396(12) | C38 | C39 | 1.383(9) |
| N5 | C19 | 1.468(10) | C39 | C40 | 1.383(10) |
| N5 | C25 | 1.478(10) | C40 | C41 | 1.373(10) |
| N5 | C31 | 1.477(11) | C41 | C42 | 1.391(9) |
| C5 | C6 | 1.518(12) | C43 | C44 | 1.497(10) |

**Table 22** Continued

| Atom | Atom | Length/Å | Atom | Atom | Length/Å |
|---|---|---|---|---|---|
| N6 | C20 | 1.343(9) | C44 | C45 | 1.383(10) |
| N6 | C24 | 1.340(10) | C45 | C46 | 1.392(12) |
| N7 | C32 | 1.340(10) | C46 | C47 | 1.371(13) |
| N7 | C36 | 1.337(10) | C47 | C48 | 1.387(12) |
| C7 | C8 | 1.503(11) | C49 | C50 | 1.507(10) |
| C9 | C8 | 1.394(11) | C50 | C51 | 1.386(10) |
| C9 | C10 | 1.386(12) | C51 | C52 | 1.375(11) |
| N9 | C37 | 1.473(8) | C52 | C53 | 1.385(11) |
| N9 | C43 | 1.473(8) | C53 | C54 | 1.386(10) |
| N9 | C49 | 1.472(9) | Br7 | O8[1] | 2.038(19) |
| N8 | C26 | 1.354(9) | Br10 | O3[2] | 0.964(9) |
| N8 | C30 | 1.354(9) | O3 | Br10[3] | 0.964(9) |
| C10 | C11 | 1.382(12) | O8 | Br7[1] | 2.038(19) |
| N10 | C44 | 1.360(9) | | | |

[1]1-X,1-Y,1-Z; [2]+X,1+Y,+Z; [3]+X,-1+Y,+Z

| Atom | Atom | Atom | Angle/° | Atom | Atom | Atom | Angle/° |
|---|---|---|---|---|---|---|---|
| N5 | Co1 | Br1 | 178.46(17) | N3 | C8 | C9 | 121.8(7) |
| N6 | Co1 | Br1 | 101.13(17) | C9 | C8 | C7 | 123.0(7) |
| N6 | Co1 | N5 | 77.9(2) | C26 | N8 | Co1 | 117.2(5) |
| N6 | Co1 | N7 | 115.1(2) | C26 | N8 | C30 | 118.7(6) |
| N6 | Co1 | N8 | 116.0(2) | C30 | N8 | Co1 | 124.0(5) |
| N7 | Co1 | Br1 | 101.47(17) | C11 | C10 | C9 | 118.3(7) |
| N7 | Co1 | N5 | 78.0(2) | C44 | N10 | Co2 | 116.9(5) |
| N8 | Co1 | Br1 | 103.95(16) | C48 | N10 | Co2 | 124.1(5) |
| N8 | Co1 | N5 | 77.6(2) | C48 | N10 | C44 | 118.7(6) |
| N8 | Co1 | N7 | 115.9(2) | C12 | C11 | C10 | 119.2(7) |
| C1 | N1 | Co3 | 125.1(5) | C50 | N11 | Co2 | 117.4(4) |
| C5 | N1 | C1 | 118.2(6) | C54 | N11 | Co2 | 123.1(5) |
| C5 | N1 | Co3 | 116.6(5) | C54 | N11 | C50 | 119.3(6) |
| N1 | C1 | C2 | 122.5(7) | N3 | C12 | C11 | 123.6(7) |
| N9 | Co2 | Br2 | 178.00(16) | C38 | N12 | Co2 | 117.8(4) |

**Table 22** Continued

| Atom | Atom | Atom | Angle/° | Atom | Atom | Atom | Angle/° |
|---|---|---|---|---|---|---|---|
| N10 | Co2 | Br2 | 103.12(16) | C42 | N12 | Co2 | 122.5(4) |
| N10 | Co2 | N9 | 78.3(2) | C42 | N12 | C38 | 119.4(6) |
| N10 | Co2 | N11 | 114.9(2) | N4 | C13 | C14 | 110.0(6) |
| N10 | Co2 | N12 | 116.4(2) | N2 | C14 | C13 | 115.7(7) |
| N11 | Co2 | Br2 | 100.49(15) | N2 | C14 | C15 | 121.7(8) |
| N11 | Co2 | N9 | 77.6(2) | C15 | C14 | C13 | 122.5(7) |
| N12 | Co2 | Br2 | 102.93(15) | C16 | C15 | C14 | 119.2(8) |
| N12 | Co2 | N9 | 77.6(2) | C15 | C16 | C17 | 119.6(7) |
| N12 | Co2 | N11 | 115.7(2) | C16 | C17 | C18 | 118.3(8) |
| C14 | N2 | Co3 | 116.6(5) | N2 | C18 | C17 | 123.2(8) |
| C14 | N2 | C18 | 118.1(6) | N5 | C19 | C20 | 110.6(6) |
| C18 | N2 | Co3 | 125.3(5) | C22 | C21 | C20 | 119.3(8) |
| C3 | C2 | C1 | 119.6(8) | N6 | C20 | C19 | 116.4(7) |
| N1 | Co3 | N2 | 118.5(2) | N6 | C20 | C21 | 120.9(8) |
| N1 | Co3 | Br3 | 102.46(16) | C21 | C20 | C19 | 122.6(7) |
| N1 | Co3 | N4 | 78.0(2) | C26 | C27 | C28 | 119.9(7) |
| N2 | Co3 | Br3 | 101.84(17) | N8 | C26 | C27 | 121.0(7) |
| N2 | Co3 | N4 | 77.5(2) | N8 | C26 | C25 | 115.4(6) |
| N3 | Co3 | N1 | 112.8(2) | C27 | C26 | C25 | 123.6(7) |
| N3 | Co3 | N2 | 116.0(2) | N5 | C25 | C26 | 109.9(6) |
| N3 | Co3 | Br3 | 101.91(17) | N6 | C24 | C23 | 122.7(7) |
| N3 | Co3 | N4 | 78.4(2) | C24 | C23 | C22 | 117.8(9) |
| N4 | Co3 | Br3 | 179.33(16) | C21 | C22 | C23 | 120.3(8) |
| C8 | N3 | Co3 | 116.7(5) | C29 | C28 | C27 | 118.6(7) |
| C12 | N3 | Co3 | 125.5(5) | C30 | C29 | C28 | 119.5(7) |
| C12 | N3 | C8 | 117.8(6) | N8 | C30 | C29 | 122.4(7) |
| C2 | C3 | C4 | 118.7(8) | N5 | C31 | C32 | 109.5(6) |
| C6 | N4 | Co3 | 107.9(4) | N7 | C32 | C31 | 117.1(6) |
| C6 | N4 | C7 | 111.3(6) | N7 | C32 | C33 | 120.5(8) |
| C6 | N4 | C13 | 112.7(6) | C33 | C32 | C31 | 122.4(8) |
| C7 | N4 | Co3 | 105.5(4) | C34 | C33 | C32 | 120.0(8) |
| C13 | N4 | Co3 | 107.0(4) | C33 | C34 | C35 | 118.9(8) |
| C13 | N4 | C7 | 111.9(6) | C36 | C35 | C34 | 118.2(9) |

**Table 22** Continued

| Atom | Atom | Atom | Angle/° | Atom | Atom | Atom | Angle/° |
|---|---|---|---|---|---|---|---|
| C3 | C4 | C5 | 119.0(9) | N7 | C36 | C35 | 122.9(8) |
| C19 | N5 | Co1 | 106.6(5) | N9 | C37 | C38 | 109.6(5) |
| C19 | N5 | C25 | 112.2(7) | N12 | C38 | C37 | 115.4(6) |
| C19 | N5 | C31 | 111.7(6) | N12 | C38 | C39 | 121.8(6) |
| C25 | N5 | Co1 | 106.8(4) | C39 | C38 | C37 | 122.8(6) |
| C31 | N5 | Co1 | 106.3(5) | C38 | C39 | C40 | 118.7(6) |
| C31 | N5 | C25 | 112.7(6) | C41 | C40 | C39 | 119.7(6) |
| N1 | C5 | C4 | 121.7(8) | C40 | C41 | C42 | 119.0(6) |
| N1 | C5 | C6 | 116.5(7) | N12 | C42 | C41 | 121.4(6) |
| C4 | C5 | C6 | 121.7(8) | N9 | C43 | C44 | 110.2(5) |
| C20 | N6 | Co1 | 116.4(5) | N10 | C44 | C43 | 115.8(6) |
| C24 | N6 | Co1 | 124.4(5) | N10 | C44 | C45 | 121.9(7) |
| C24 | N6 | C20 | 119.1(7) | C45 | C44 | C43 | 122.3(7) |
| N4 | C6 | C5 | 109.1(6) | C44 | C45 | C46 | 118.6(8) |
| C32 | N7 | Co1 | 115.8(5) | C47 | C46 | C45 | 119.1(8) |
| C36 | N7 | Co1 | 124.7(5) | C46 | C47 | C48 | 119.7(8) |
| C36 | N7 | C32 | 119.5(6) | N10 | C48 | C47 | 121.8(8) |
| N4 | C7 | C8 | 110.6(6) | N9 | C49 | C50 | 109.2(5) |
| C10 | C9 | C8 | 119.3(8) | N11 | C50 | C49 | 115.8(6) |
| C37 | N9 | Co2 | 107.3(4) | N11 | C50 | C51 | 121.2(6) |
| C43 | N9 | Co2 | 107.0(4) | C51 | C50 | C49 | 123.0(6) |
| C43 | N9 | C37 | 111.3(5) | C52 | C51 | C50 | 119.7(7) |
| C49 | N9 | Co2 | 107.4(4) | C51 | C52 | C53 | 118.8(7) |
| C49 | N9 | C37 | 111.3(5) | C52 | C53 | C54 | 118.8(7) |
| C49 | N9 | C43 | 112.2(5) | N11 | C54 | C53 | 122.2(7) |
| N3 | C8 | C7 | 115.3(6) | | | | |

In the cubic phase there is only one crystallographically independent molecule and it resides on a three-fold axis, enforcing strict $C_3$ symmetry with an $N_{py}$-Co-$N_{py}$ angle of 115.30(8)°. The dihedral angle formed by the TPMA pyridine rings is 120.0°.

The projection of the $Co^{II}$ ion toward the coordinated bromide ion is 0.455 Å, with a Co-Br bond distance of 2.427(16) Å. The closest intermolecular Co-Co contact is 8.079 Å. Figure 44 displays a thermal ellipsoid plot of the cubic phase of [Co(TPMA)Br]Br and Table 23 lists bond distances and angles.

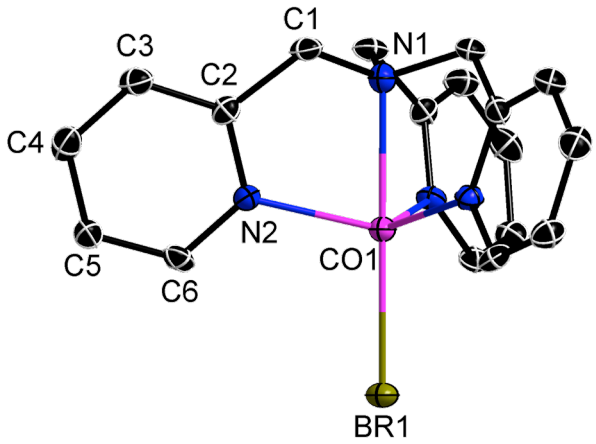


**Figure 44.** Thermal ellipsoid plot of the cationic unit of the cubic phase of [Co(TPMA)Br]Br. The atom numbers designate the asymmetric unit. Ellipsoids are drawn at the 50% probability level; H atoms were omitted for the sake of clarity.

**Table 23.** Bond distances and angles for the cubic phase of [Co(TPMA)Br]Br.

| Atom | Atom | Length/Å | Atom | Atom | Length/Å |
|---|---|---|---|---|---|
| Br1 | Co1 | 2.4276(16) | Co1 | $N2^{2}$ | 2.068(4) |
| N1 | $C1^{1}$ | 1.469(6) | N2 | C2 | 1.352(6) |
| N1 | $C1^{2}$ | 1.469(6) | N2 | C6 | 1.346(7) |
| N1 | C1 | 1.469(6) | C2 | C3 | 1.390(7) |
| N1 | Co1 | 2.214(7) | C4 | C3 | 1.380(8) |
| C1 | C2 | 1.497(7) | C4 | C5 | 1.387(8) |
| Co1 | N2 | 2.068(4) | C5 | C6 | 1.379(7) |
| Co1 | $N2^{1}$ | 2.068(4) | | | |

$^{1}$+Z,+X,+Y; $^{2}$+Y,+Z,+X

**Table 23** Continued

| Atom | Atom | Atom | Angle/° | Atom | Atom | Atom | Angle/° |
|---|---|---|---|---|---|---|---|
| $C1^1$ | N1 | $C1^2$ | 112.2(3) | N2 | Co1 | $N2^1$ | 115.30(8) |
| $C1^1$ | N1 | C1 | 112.2(3) | $N2^1$ | Co1 | $N2^2$ | 115.30(8) |
| $C1^2$ | N1 | C1 | 112.2(3) | N2 | Co1 | $N2^2$ | 115.30(8) |
| $C1^1$ | N1 | Co1 | 106.6(3) | C2 | N2 | Co1 | 117.5(3) |
| C1 | N1 | Co1 | 106.6(3) | C6 | N2 | Co1 | 123.8(3) |
| $C1^2$ | N1 | Co1 | 106.6(3) | C6 | N2 | C2 | 118.7(4) |
| N1 | C1 | C2 | 109.9(4) | N2 | C2 | C1 | 115.1(4) |
| N1 | Co1 | Br1 | 180.00(11) | N2 | C2 | C3 | 121.5(5) |
| N2 | Co1 | Br1 | 102.71(12) | C3 | C2 | C1 | 123.3(5) |
| $N2^1$ | Co1 | Br1 | 102.71(12) | C3 | C4 | C5 | 119.1(5) |
| $N2^2$ | Co1 | Br1 | 102.71(12) | C4 | C3 | C2 | 119.3(5) |
| $N2^2$ | Co1 | N1 | 77.29(12) | C6 | C5 | C4 | 119.0(5) |
| $N2^1$ | Co1 | N1 | 77.29(12) | N2 | C6 | C5 | 122.5(5) |
| N2 | Co1 | N1 | 77.29(12) | | | | |

$^1$+Y,+Z,+X; $^2$+Z,+X,+Y

**[Co(TPMA)I]I**. The iodide analog has only been isolated as a triclinic phase with two independent molecules in the asymmetric unit with an average $N_{py}$-Co-$N_{py}$ angle of 115.40°. The dihedral angles formed by the TPMA pyridine rings range from 115.93° to 122.49° with an average of 120.0°. The $Co^{II}$ ions project out of the equatorial plane toward the coordinated iodide ion by an average of 0.452 Å, with an average Co-I bond length of 2.645 Å. The closest intermolecular Co-Co contact is 6.601 Å. Figure 45 displays a thermal ellipsoid plot of [Co(TPMA)I]I and Table 24 lists bond distances and angles.

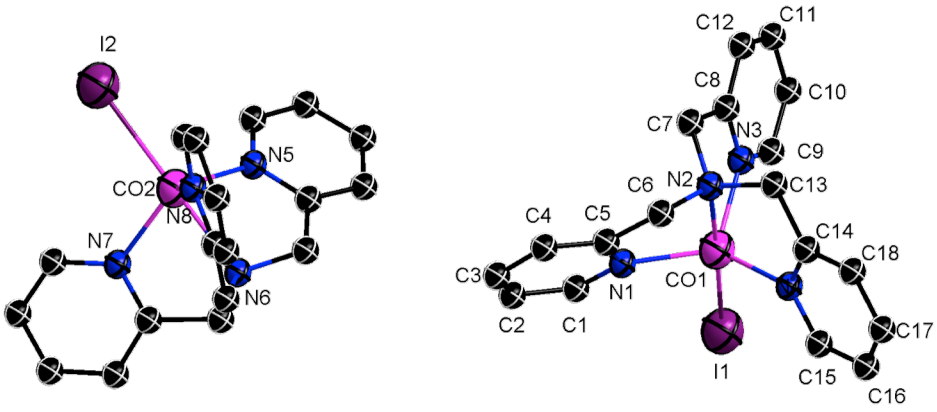


**Figure 45.** Thermal ellipsoid plot of [Co(TPMA)I]I depicting the two crystallographically independent molecules in the asymmetric unit. Ellipsoids are drawn at the 50% probability level; H atoms and outer-sphere I atoms were omitted for the sake of clarity.

**Table 24.** Bond distances and angles for [Co(TPMA)I]I.

| Atom | Atom | Length/Å | Atom | Atom | Length/Å |
|---|---|---|---|---|---|
| I1 | Co1 | 2.6355(8) | C2 | C3 | 1.383(8) |
| I2 | Co2 | 2.6550(8) | C3 | C4 | 1.386(8) |
| Co1 | N1 | 2.071(4) | C4 | C5 | 1.383(8) |
| Co1 | N2 | 2.195(4) | C5 | C6 | 1.508(8) |
| Co1 | N3 | 2.069(4) | C7 | C8 | 1.515(7) |
| Co1 | N4 | 2.072(5) | C8 | C12 | 1.386(7) |
| Co2 | N5 | 2.064(4) | C9 | C10 | 1.383(8) |
| Co2 | N6 | 2.193(4) | C10 | C11 | 1.395(8) |
| Co2 | N7 | 2.071(4) | C11 | C12 | 1.380(8) |
| Co2 | N8 | 2.077(4) | C13 | C14 | 1.498(9) |
| N1 | C1 | 1.338(6) | C14 | C18 | 1.390(8) |
| N1 | C5 | 1.349(7) | C15 | C16 | 1.381(9) |
| N2 | C6 | 1.477(7) | C16 | C17 | 1.369(10) |
| N2 | C7 | 1.472(7) | C17 | C18 | 1.364(10) |
| N2 | C13 | 1.473(7) | C19 | C20 | 1.510(7) |
| N3 | C8 | 1.344(7) | C19 | C33 | 1.385(8) |
| N3 | C9 | 1.345(6) | C21 | C22 | 1.504(7) |
| N4 | C14 | 1.362(7) | C22 | C26 | 1.397(7) |

**Table 24** Continued

| Atom | Atom | Length/Å | Atom | Atom | Length/Å |
|---|---|---|---|---|---|
| N4 | C15 | 1.348(7) | C23 | C24 | 1.374(7) |
| N5 | C19 | 1.351(7) | C24 | C25 | 1.387(8) |
| N5 | C36 | 1.348(7) | C25 | C26 | 1.374(8) |
| N6 | C20 | 1.483(7) | C27 | C28 | 1.497(7) |
| N6 | C21 | 1.474(7) | C28 | C32 | 1.396(7) |
| N6 | C27 | 1.483(6) | C29 | C30 | 1.374(8) |
| N7 | C22 | 1.345(7) | C30 | C31 | 1.385(9) |
| N7 | C23 | 1.353(7) | C31 | C32 | 1.390(8) |
| N8 | C28 | 1.351(7) | C33 | C34 | 1.386(8) |
| N8 | C29 | 1.340(7) | C34 | C35 | 1.386(8) |
| C1 | C2 | 1.388(8) | C35 | C36 | 1.374(8) |

| Atom | Atom | Atom | Angle/° | Atom | Atom | Atom | Angle/° |
|---|---|---|---|---|---|---|---|
| N1 | Co1 | I1 | 100.65(13) | C29 | N8 | C28 | 118.9(5) |
| N1 | Co1 | N2 | 77.29(17) | N1 | C1 | C2 | 123.3(5) |
| N1 | Co1 | N4 | 117.03(18) | C3 | C2 | C1 | 118.1(5) |
| N2 | Co1 | I1 | 176.89(12) | C2 | C3 | C4 | 119.2(5) |
| N3 | Co1 | I1 | 105.45(12) | C5 | C4 | C3 | 119.1(6) |
| N3 | Co1 | N1 | 117.65(17) | N1 | C5 | C4 | 122.2(5) |
| N3 | Co1 | N2 | 77.62(16) | N1 | C5 | C6 | 115.4(5) |
| N3 | Co1 | N4 | 111.99(17) | C4 | C5 | C6 | 122.4(5) |
| N4 | Co1 | I1 | 100.97(14) | N2 | C6 | C5 | 109.8(4) |
| N4 | Co1 | N2 | 78.10(18) | N2 | C7 | C8 | 109.4(4) |
| N5 | Co2 | I2 | 103.71(13) | N3 | C8 | C7 | 115.1(4) |
| N5 | Co2 | N6 | 77.14(17) | N3 | C8 | C12 | 122.2(5) |
| N5 | Co2 | N7 | 116.37(17) | C12 | C8 | C7 | 122.7(5) |
| N5 | Co2 | N8 | 113.82(17) | N3 | C9 | C10 | 122.2(5) |
| N6 | Co2 | I2 | 177.95(12) | C9 | C10 | C11 | 119.0(5) |
| N7 | Co2 | I2 | 103.86(12) | C12 | C11 | C10 | 118.7(5) |
| N7 | Co2 | N6 | 77.28(17) | C11 | C12 | C8 | 119.3(5) |
| N7 | Co2 | N8 | 115.55(17) | N2 | C13 | C14 | 110.5(5) |
| N8 | Co2 | I2 | 100.73(13) | N4 | C14 | C13 | 116.0(5) |
| N8 | Co2 | N6 | 77.22(17) | N4 | C14 | C18 | 120.8(6) |

**Table 24** Continued

| Atom | Atom | Atom | Angle/° | Atom | Atom | Atom | Angle/° |
|---|---|---|---|---|---|---|---|
| C1 | N1 | Co1 | 124.1(4) | C18 | C14 | C13 | 123.1(6) |
| C1 | N1 | C5 | 118.0(5) | N4 | C15 | C16 | 122.3(6) |
| C5 | N1 | Co1 | 117.8(4) | C17 | C16 | C15 | 118.8(7) |
| C6 | N2 | Co1 | 107.9(3) | C18 | C17 | C16 | 120.0(6) |
| C7 | N2 | Co1 | 105.9(3) | C17 | C18 | C14 | 119.6(7) |
| C7 | N2 | C6 | 111.0(4) | N5 | C19 | C20 | 115.7(5) |
| C7 | N2 | C13 | 112.7(4) | N5 | C19 | C33 | 121.7(5) |
| C13 | N2 | Co1 | 107.7(3) | C33 | C19 | C20 | 122.6(5) |
| C13 | N2 | C6 | 111.3(4) | N6 | C20 | C19 | 109.1(4) |
| C8 | N3 | Co1 | 116.8(3) | N6 | C21 | C22 | 109.0(4) |
| C8 | N3 | C9 | 118.6(4) | N7 | C22 | C21 | 116.0(4) |
| C9 | N3 | Co1 | 124.5(4) | N7 | C22 | C26 | 121.8(5) |
| C14 | N4 | Co1 | 116.6(4) | C26 | C22 | C21 | 122.1(5) |
| C15 | N4 | Co1 | 124.9(4) | N7 | C23 | C24 | 122.7(5) |
| C15 | N4 | C14 | 118.4(5) | C23 | C24 | C25 | 119.3(5) |
| C19 | N5 | Co2 | 117.8(4) | C26 | C25 | C24 | 118.6(5) |
| C36 | N5 | Co2 | 124.0(4) | C25 | C26 | C22 | 119.6(5) |
| C36 | N5 | C19 | 118.2(5) | N6 | C27 | C28 | 109.4(4) |
| C20 | N6 | Co2 | 108.0(3) | N8 | C28 | C27 | 116.9(4) |
| C20 | N6 | C27 | 111.5(4) | N8 | C28 | C32 | 121.5(5) |
| C21 | N6 | Co2 | 106.7(3) | C32 | C28 | C27 | 121.6(5) |
| C21 | N6 | C20 | 110.9(4) | N8 | C29 | C30 | 122.7(6) |
| C21 | N6 | C27 | 112.3(4) | C29 | C30 | C31 | 118.9(6) |
| C27 | N6 | Co2 | 107.2(3) | C30 | C31 | C32 | 119.3(5) |
| C22 | N7 | Co2 | 116.6(3) | C31 | C32 | C28 | 118.5(6) |
| C22 | N7 | C23 | 118.0(4) | C19 | C33 | C34 | 119.3(6) |
| C23 | N7 | Co2 | 125.4(4) | C33 | C34 | C35 | 119.2(5) |
| C28 | N8 | Co2 | 116.1(4) | C36 | C35 | C34 | 118.4(5) |
| C29 | N8 | Co2 | 125.0(4) | N5 | C36 | C35 | 123.2(6) |

*Powder X-ray Diffraction*

Given that the syntheses of the triclinic and cubic phases of [Co(TPMA)Cl]Cl and [Co(TPMA)Br]Br are somewhat similar and some difficulty was encountered while trying to isolate a phase-pure sample of [Co(TPMA)Cl]Cl, powder X-ray diffraction experiments were used to verify the phase purity of these four complexes prior to conducting magnetic measurements. The simulated powder patterns were generated from the single crystal structures using Mercury.

Figure 46 shows the powder X-ray diffraction patterns for the triclinic and cubic phases of [Co(TPMA)Cl]Cl compared with the powder patterns simulated from the single crystal structures. The experimental powder pattern of the cubic phase reproduces the simulated pattern very well; even the relative intensities of the peaks are similar. There is a very minor shift to lower angles in 2θ visible in the experimental powder pattern, consistent with a slightly larger unit cell at room temperature than at the temperature of the simulated powder pattern (110 K). As expected, there are many more peaks in the powder pattern of the triclinic phase. Overall the experimental pattern reproduces the simulated pattern quite well, with the slight shifts to lower 2θ values again visible for the low angle peaks.

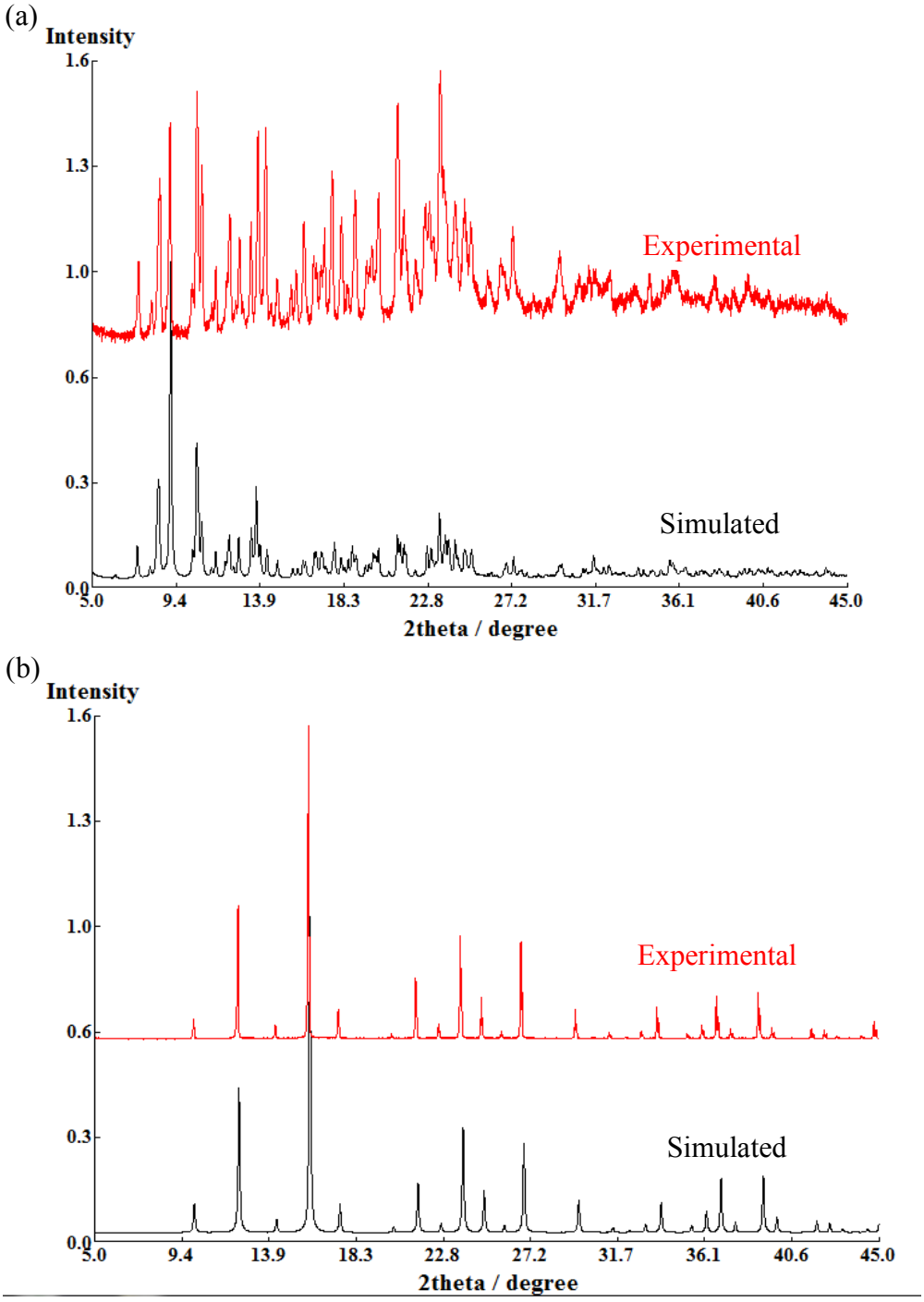


**Figure 46.** Powder patterns for the triclinic phase of [Co(TPMA)Cl]Cl (a) and the cubic phase (b).

Figure 47 depicts a comparison of the powder pattern of a sample of [Co(TPMA)Cl]Cl that was prepared in the dry box by slowly adding $Et_2O$ to an acetonitrile solution of [Co(TPMA)Cl]Cl to precipitate a green microcrystalline solid over the course of several minutes to powder patterns simulated from the single crystal triclinic and cubic phases of the complex. There are clearly two phases in the sample with one component matching the pattern for the simulated cubic phase and a second component that is consistent with the pattern for the simulated triclinic phase.

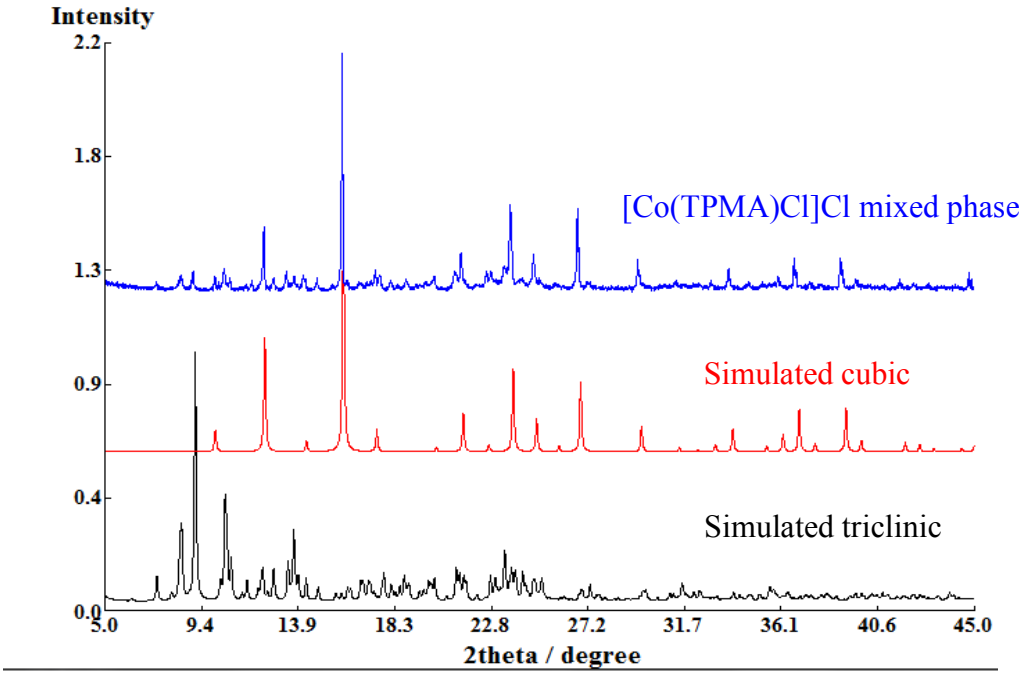


**Figure 47.** Powder pattern of a mixed phase of [Co(TPMA)Cl]Cl.

The phase purity of the bromide samples used for magnetic measurements was also verified by powder X-ray diffraction. In Figure 48 the experimental powder patterns of the triclinic and cubic phases of [Co(TPMA)Br]Br are compared with those

simulated from the single crystal structures. The experimental powder pattern of the cubic phase reproduces the simulated pattern very well with the relative intensities of the peaks being very similar. There is a very minor shift to lower angles in 2θ visible in the experimental powder pattern, consistent with a slightly larger unit cell at room temperature than at the temperature of the simulated powder pattern (110 K). As expected, there are many more peaks in the powder pattern of the triclinic phase. Overall the experimental pattern reproduces the simulated pattern quite well, with slight shifts to lower 2θ values again visible for the low angle peaks.

Even though the synthesis of the iodide compound never produced a single crystal structure other than the triclinic one, powder X-ray diffraction was used to demonstrate that the sample used for magnetic measurements was purely the triclinic phase. Figure 49 shows a comparison of the powder pattern simulated from the single crystal structure with the experimentally determined powder pattern of the sample used for SQUID measurements.

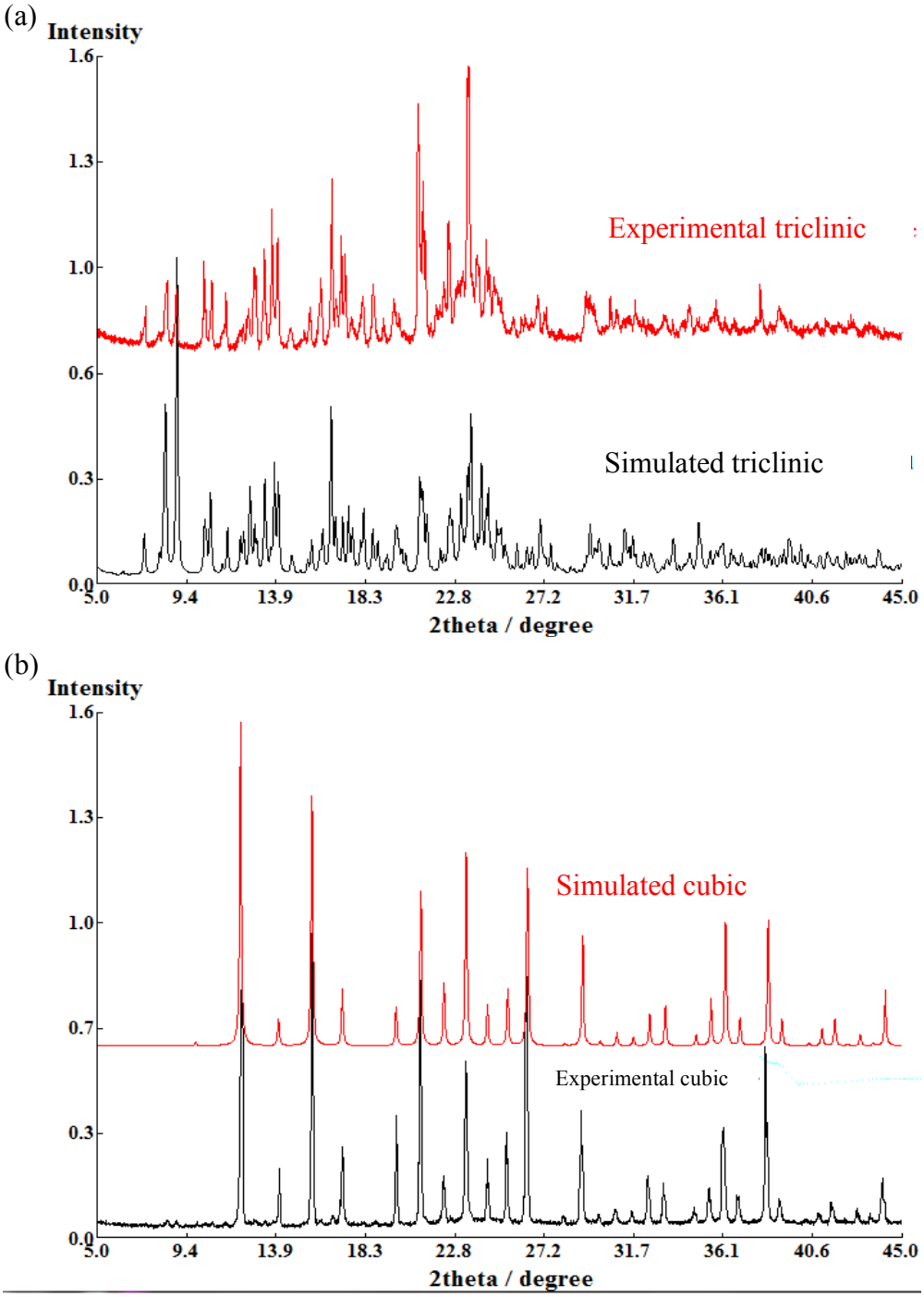


**Figure 48.** Powder patterns for the triclinic phase of [Co(TPMA)Br]Br (a) and the cubic phase (b).

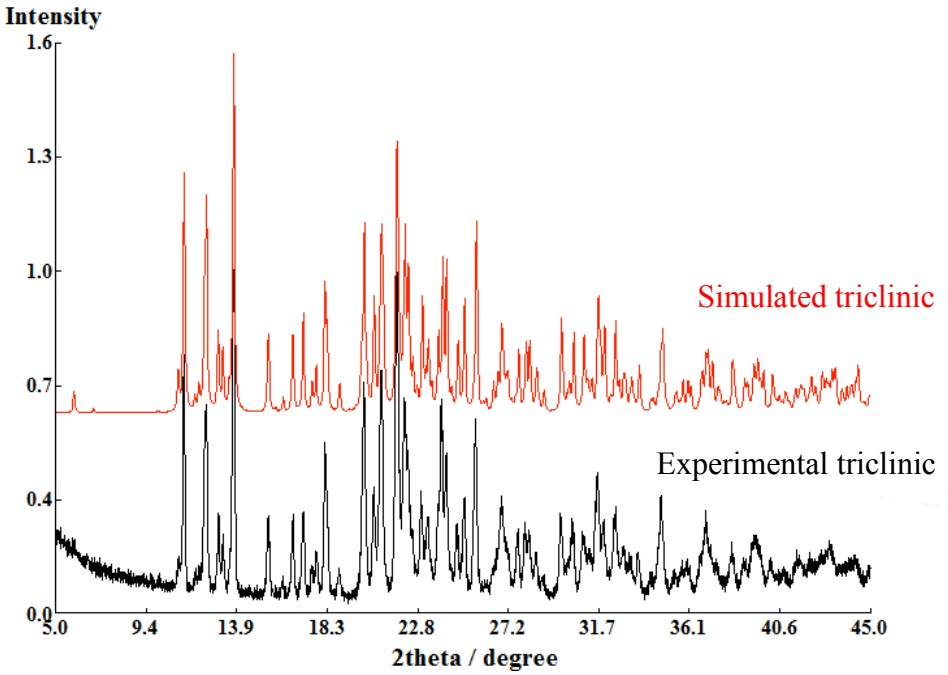


**Figure 49.** Powder pattern of the sample of [Co(TPMA)I]I used for magnetic measurements.

*Infrared Spectroscopy*

Due to the fact that the syntheses of the triclinic phases of [Co(TPMA)Cl]Cl and [Co(TPMA)Br]Br were performed in air using hexahydrate cobalt starting materials and that there was halide disorder in the crystal structures, IR spectroscopy was used to determine if the isolated crystalline material contains water molecules. The IR spectra of the triclinic phases of [Co(TPMA)Cl]Cl and [Co(TPMA)Br]Br both show a broad absorption centered at ~ 3400 $cm^{-1}$ which is indicative of the stretching frequency of hydrogen-bonded water molecules in the sample.

*TGA Measurements*

The IR spectra of the triclinic phases of [Co(TPMA)Cl]Cl and [Co(TPMA)Br]Br indicate the presence of water in both complexes but this technique does not help quantify the amount of water present or whether the water is surface bound or located in the interstices. TGA analysis was performed to aid in the corroboration of the results of the elemental analysis. Two separate TGA measurements were performed on each sample. The first measurement was performed on crystalline material freshly filtered from the mother liquor, washed with $Et_2O$, and briefly dried in air. While the TGA experiment was running, the remaining crystals were ground to a fine powder and used in a powder X-ray diffraction experiment to confirm the phase purity of the sample. After the powder X-ray results confirmed the identity of the product it was placed under vacuum on a Schlenk line for a period of 26 hours. Immediately after being isolated from vacuum a second TGA experiment was performed. The results of the two TGA experiments on the triclinic phase of [Co(TPMA)Cl]Cl are displayed in Figure 50. The two thermograms are essentially identical, consisting of two major mass loss events below 100 °C and another more gradual mass loss between 100 and approximately 140 °C before the onset of decomposition at approximately 250 °C. The striking similarity of the two TGA plots strongly suggests that the water is contained within the crystals and is not surface water. Total mass loss is consistent with 2.2 molecules of water per [Co(TPMA)Cl]Cl molecule for the freshly filtered sample and 2.3 molecules of water for the sample that had been under vacuum for 26 hours.

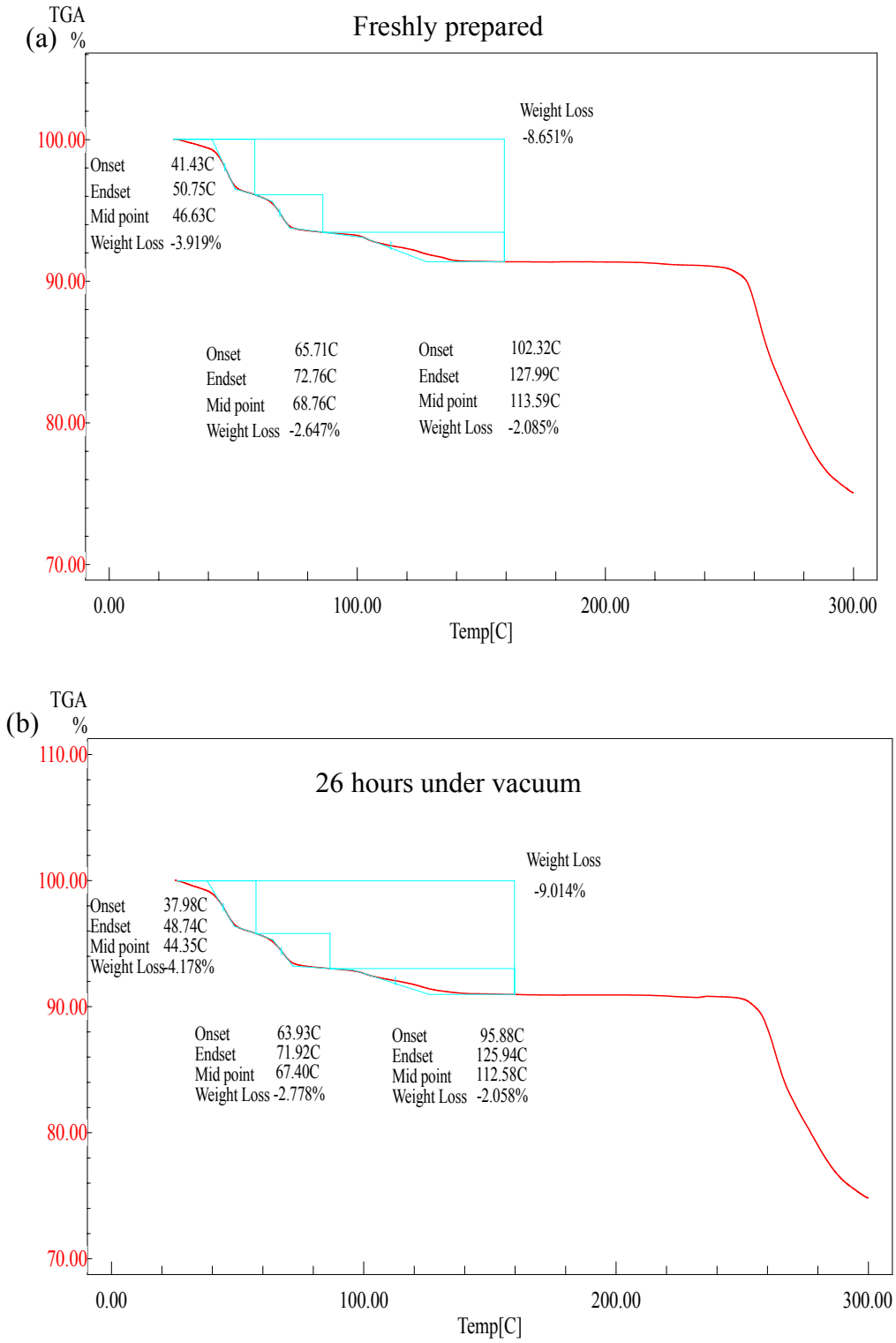


**Figure 50.** Thermograms of [Co(TPMA)Cl]Cl as a freshly filtered sample (a) and after being subjected to Schlenk line vacuum for 26 hours (b).

The TGA analysis of the triclinic phase of [Co(TPMA)Br]Br was carried out in an analogous manner to that of the triclinic phase of [Co(TPMA)Cl]Cl. The thermograms for [Co(TPMA)Br]Br are displayed in Figure 51. Unlike [Co(TPMA)Cl]Cl only one mass loss event was observed for [Co(TPMA)Br]Br before the onset of decomposition at approximately 260 °C. The thermograms before and after the sample was placed under vacuum are again very similar, suggesting that the water content is not due to surface water. For the freshly prepared sample, the total mass loss is consistent with 1.98 molecules of water per [Co(TPMA)Br]Br molecule. The TGA measurement for the sample that had been under vacuum was complicated by difficulty in stabilizing the balance on the instrument after the sample was loaded. As such, the error in this measurement is likely higher than the measurement for the freshly prepared sample. Total mass loss is consistent with 1.42 water molecules for the sample that had been under vacuum for 26 hours.

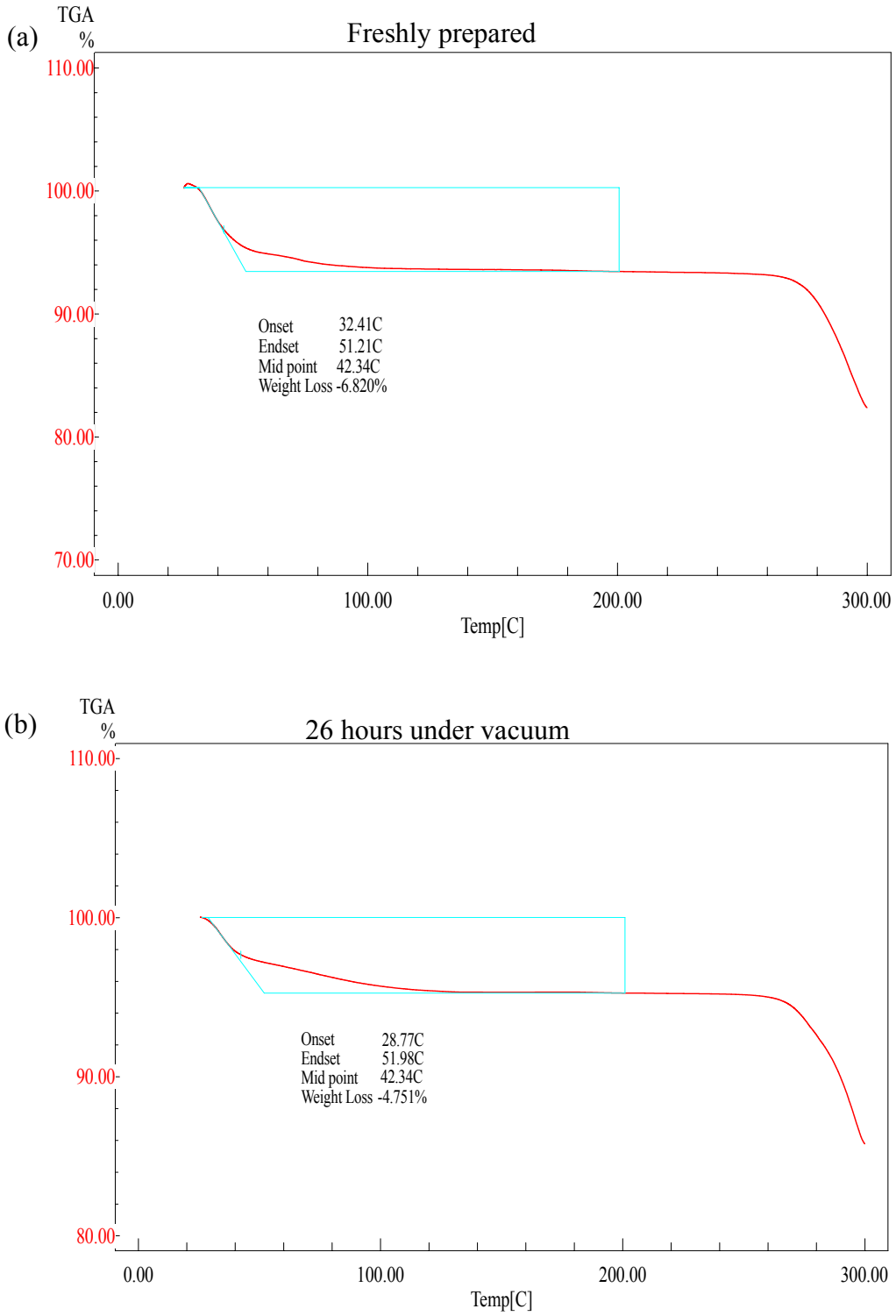


**Figure 51.** Thermograms of [Co(TPMA)Br]Br as a freshly filtered sample (a) and after being subjected to Schlenk line vacuum for 26 hours (b).

*Magnetic Measurements*

**[Co(TPMA)(CH$_3$CN)](BF$_4$)$_2$**. Static DC magnetic measurements were performed on crushed single crystals of [Co(TPMA)(CH$_3$CN)](BF$_4$)$_2$ between 1.8 and 300 K. The 300 K $\chi$T value of 2.38 emu K mol$^{-1}$ is significantly higher than the 1.875 emu K mol$^{-1}$ expected for an S = 3/2 system with g = 2 due to spin-orbit coupling. The value of $\chi$T slowly decreases until ~ 18 K, at which temperature it begins to decrease more rapidly until reaching a minimum of 1.54 emu K mol$^{-1}$ at 2.0 K (Figure 52a). The precipitous drop at low temperatures is due to zero-field splitting effects.

Further evidence of single ion anisotropy is indicated by low temperature magnetization experiments. At 1.8 K, the magnetization does not saturate at the highest available field of 7 T (Figure 52b). Additionally, field-dependent magnetization data between 1.8 and 4.0 K (reduced magnetization) reveal a non-superposition of the iso-field lines (Figure 52c). Fitting of the field-dependent magnetization data using ANISOFIT2.0[132] resulted in a D value of +9.6 cm$^{-1}$ with E = 0.008 cm$^{-1}$ and g = 2.38. Fitting using PHI gave a D value of +9.7 cm$^{-1}$ and g = 2.39. Attempts to fit the field-dependent magnetization data with negative values of D resulted in lower-quality fits of the data; the large positive value of D for Co$^{II}$ ions in a TBP environment is consistent with recent theoretical predictions using model geometries[48] and is also in accord with recent theoretical calculations that indicate D should be positive in the presence of an axially coordinated $\pi$-acceptor ligand.[137] The small value of the transverse anisotropy parameter E is appropriate for a molecule of $C_3$ symmetry.[137]

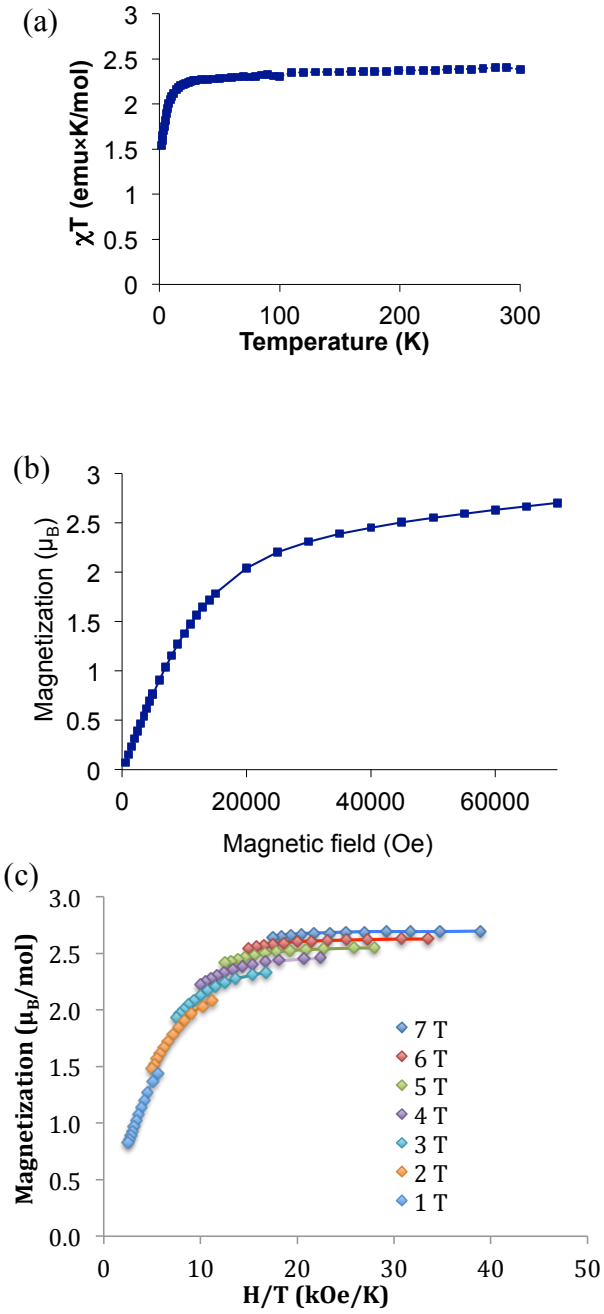


**Figure 52.** DC magnetic properties of $[Co(TPMA)(CH_3CN)](BF_4)_2$. (a) χT product under a 1000 Oe field. The solid line is a guide for the eye. (b) plot of M vs. H at 1.8 K. The solid line is merely a guide for the eye. (c) temperature and field dependence of the magnetization. Filled diamonds: experimental data. Solid lines: fitting of the experimental data using the parameters described in the main text for the ANISOFIT2.0 fitting.

AC susceptibility experiments were carried out in order to probe if $[Co(TPMA)(CH_3CN)](BF_4)_2$ behaves as a SMM. In the absence of an applied DC field, there is no appearance of an out-of-phase component ($\chi''$) to the susceptibility down to 1.8 K. In an applied DC field of 1000 Oe, frequency-dependent maxima in $\chi''$ were observed below 2.4 K (Figure 53a). A fitting of the Cole-Cole plot using a modified Debye function[111,112] allowed for the extraction of the $\tau$ and $\alpha$ parameters (Figure 53b). The $\tau$ values were used to construct an Arrhenius plot (Figure 53c), from which the relaxation parameters of $U_{eff}/k_b$ = 21 K and $\tau_o$ = 1.7 x $10^{-8}$ s were determined. The barrier to thermal relaxation in $[Co(TPMA)(CH_3CN)](BF_4)_2$ is slightly higher than the 18 K barrier reported for $[Co(Me_6tren)(OH_2)]^{2+}$ with $\tau_o$ = 9.6 x $10^{-9}$ s.[138] The $\alpha$ parameter varies between 0.14 and 0.16, indicating a relatively narrow distribution of relaxation times. What is intriguing about this complex is that there is no evidence of a crossover to a quantum tunneling regime at low temperatures. Among the previously reported mononuclear $Co^{II}$ SMMs the observation of a tunneling regime at low temperatures is more common than observing thermal spin relaxation down to the lowest measured temperature.[41,42,84,86,87,115,118,138-140,151-156] Application of a 1000 Oe DC bias field appears to be sufficient for blocking the tunneling pathway at all temperatures above 1.8 K. Since the splitting between the $M_s = \pm 1/2$ and $\pm 3/2$ sublevels is $2|D|$ in this case, a purely thermal relaxation pathway should lead to an energy barrier of 28 K, only slightly higher than the observed $U_{eff}/k_b$ of 21.0 K. This fact further supports that tunneling is not a major relaxation pathway above 1.8 K. Previous reports of $Co^{II}$ SMMs with a large rhombic term have put forth the hypothesis that slow relaxation is due to

the rhombic term establishing an "easy axis" within the easy plane.[116,157] As the rhombic term is very small in $[Co(TPMA)(CH_3CN)](BF_4)_2$ this does not seem to be a viable explanation for the SMM behavior in this case. A pseudo-tetrahedral mononuclear $Co^{II}$ complex with a positive D value and a low E value reported by Long and co-workers displays SMM behavior in an applied DC field in which thermal relaxation was observed instead of direct tunneling between the $M_s = \pm 1/2$ states which was attributed to a phonon bottleneck effect, namely there are not enough phonon modes of the proper frequency to allow for direct relaxation.[115] A more recent report from the Ruiz and Luis groups has demonstrated that coupling of the electron spin to the nuclear spin of cobalt ($I = 7/2$) governs the relaxation processes in $Co^{II}$ systems with easy-plane anisotropy.[49]

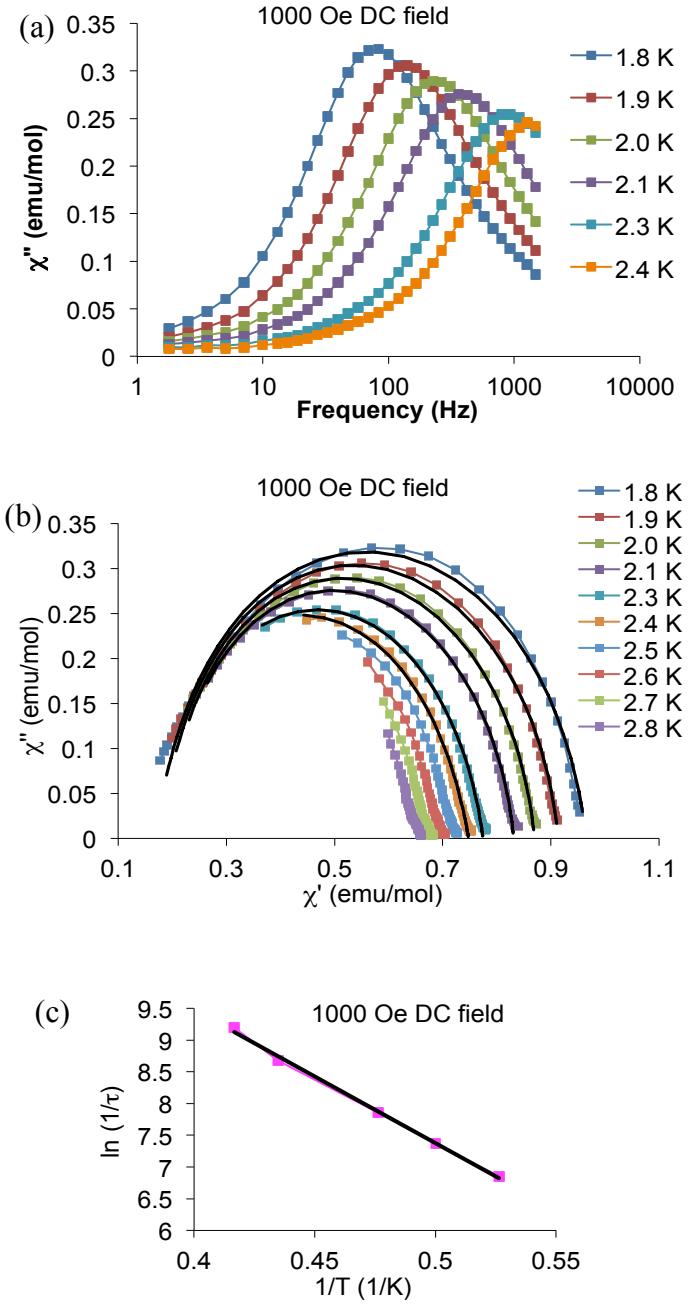


**Figure 53.** AC magnetic data for $[Co(TPMA)(CH_3CN)](BF_4)_2$. (a) frequency dependence of χ'' collected in a 1000 Oe DC field. Solid lines are guides for the eye. (b) Cole-Cole plot. The colored points and lines are experimental data and guides for the eye, respectively. The solid black lines are the results of fitting the data to a modified Debye function as discussed in the main text. (c) Arrhenius plot. The black line is a linear regression fit to the data which results in a barrier height of 21 K with $\tau_o = 1.74 \times 10^{-8}$ s as discussed in the main text.

**[Co(TPMA)Cl]Cl.** The molar magnetic susceptibility of the triclinic phase was calculated using the average water content as determined by elemental analysis and TGA. Static DC magnetic measurements on crushed single crystals of both phases of [Co(TPMA)Cl]Cl were conducted between 1.8 and 300 K. The 300 K $\chi T$ values of 2.46 emu K $mol^{-1}$ (triclinic) and 2.39 emu K $mol^{-1}$ (cubic) are significantly higher than the 1.875 emu K $mol^{-1}$ expected for an S = 3/2 system with g = 2 as expected for $Co^{II}$ ions due to spin-orbit coupling. The value of $\chi T$ slowly decreases until approximately 20 K for both phases, at which temperature it begins to decrease much more rapidly until reaching a minimum of 1.49 emu K $mol^{-1}$ (triclinic) and 1.51 emu K $mol^{-1}$ (cubic) at 2.0 K (Figure 54a).

For both the triclinic and cubic phases low-temperature magnetization experiments, M vs. H at 1.8 K (Figure 54b) and reduced magnetization (Figure 55), reveal behavior similar to the acetonitrile analog in that saturation is not observed at 7 T in the M vs. H plot and there is non-superposition of the isofield lines for the reduced magnetization measurements. Fittings with ANISOFIT2.0 yielded ZFS parameters of D = -8.18 $cm^{-1}$, E = 4 x $10^{-4}$ $cm^{-1}$, and g = 2.31 for the triclinic phase and D = -8.65 $cm^{-1}$, E = 6 x $10^{-4}$ $cm^{-1}$, and g = 2.25 for the cubic phase. Fittings with PHI yielded ZFS parameters of D = -8.01 $cm^{-1}$ and g = 2.30 for the triclinic phase and D = -8.49 $cm^{-1}$ and g = 2.24 for the cubic phase. Unlike the acetonitrile analog, the fits to the magnetization data are better with negative D values for these two complexes. The sign and magnitude of D as well as the g value are consistent with the ZFS parameters derived from EPR studies of $[Co(Me_6tren)Cl]^+$, which crystallizes in the trigonal space group *R3c*.[137] The

similarity in the ZFS parameters between the triclinic and cubic phases suggests that the electronic environment is not significantly affected by the pseudo-$C_3$ symmetry of the triclinic phase versus the rigorous $C_3$ symmetry of the cubic phase.

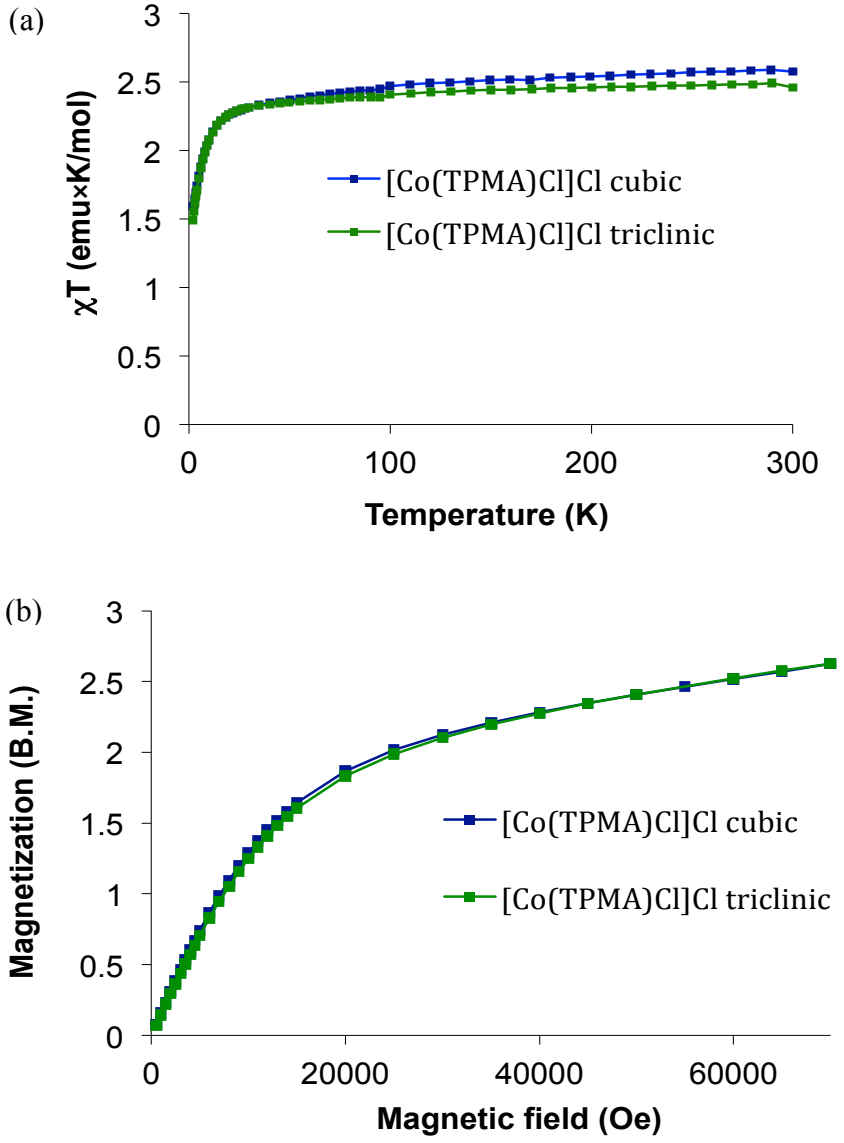


**Figure 54.** DC magnetic properties of [Co(TPMA)Cl]Cl. (a) the χT product under a 1000 Oe applied field. The solid line is a guide for the eye. (b) plot of M vs. H at 1.8 K with the solid line being merely a guide for the eye.

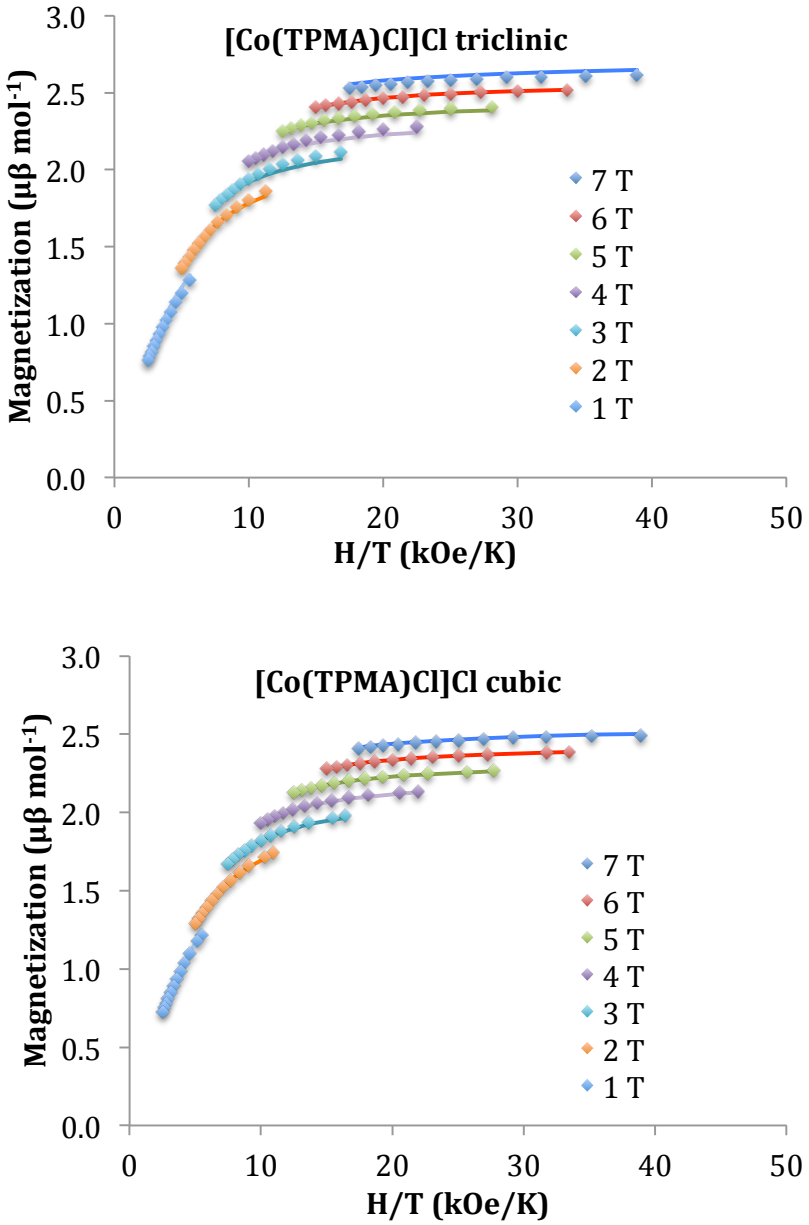


**Figure 55.** Temperature and field dependence of the magnetization for [Co(TPMA)Cl]Cl. Filled diamonds: experimental data. Solid lines: fitting of the experimental data using the parameters described in the main text for the ANISOFIT2.0 fitting.

Dynamic AC susceptibility measurements on both chloride phases were performed in order to determine the effect of changing from a coordinated acetonitrile molecule to a coordinated halide ion and to probe if the change in symmetry has any noticeable effect on the slow relaxation behavior. For the triclinic phase, there was no out-of-phase signal in a zero applied DC field. The beginnings of an out-of-phase signal is observed in a DC field but even in a 2000 Oe DC field no maximum in χ'' could be observed, even at 1.8 K, at any frequency (Figure 56). This behavior is indicative of the presence of a very fast relaxation process, which is likely quantum tunneling.

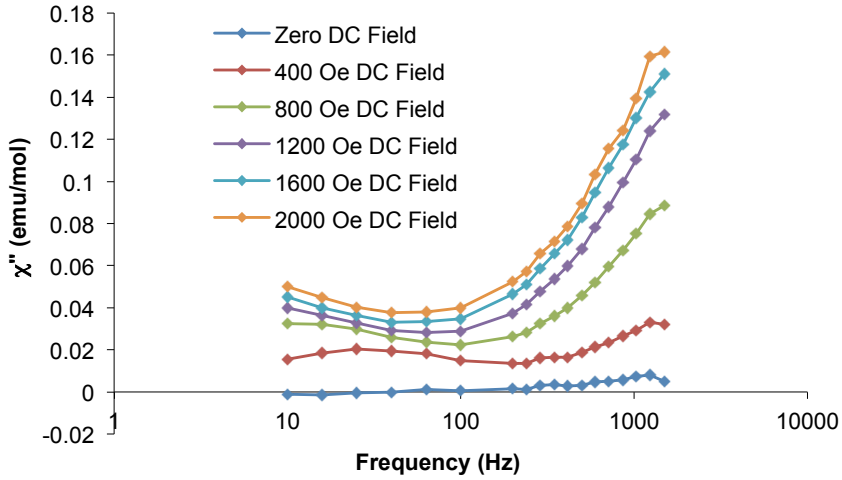


**Figure 56.** Out of phase AC susceptibility data for the triclinic phase of [Co(TPMA)Cl]Cl as a function of applied DC field at 1.8 K.

The cubic phase exhibits much more interesting AC behavior. In zero DC field there are the beginnings of an out-of-phase signal at 1.8 K but no maximum is observed

below the highest measurable frequencies. In a 400 Oe DC field there are frequency dependent maxima in χ'' for frequencies as low as 33 Hz at 1.8 K but there is also a distinct tail at high frequencies indicative of a second relaxation process (Figure 57a). This tail becomes less apparent at higher temperatures and by 2.3 K it has disappeared.

Attempts to use a single modified Debye function could not reproduce these tails and, in general, resulted in unsatisfactory fits to the data. Using CC-FIT,[104] both relaxation processes were fit simultaneously (Figure 57b). One of the relaxation processes, tau1 in Figure 57c, appears to be essentially temperature independent, consistent with quantum tunneling, but no further interpretation of this process is possible since no maximum in χ'' was observed. The second process, tau2, produces the linear Arrhenius plot shown in Figure 57c. This relaxation process is frequency dependent at all measured temperatures, consistent with a thermal relaxation process. The effective barrier extracted for this thermal process is 20.6 K with a pre-exponential factor of 4.43 x $10^{-8}$ s. The alpha values are all less than 0.07, indicating a narrow distribution of relaxation times. The observed barrier is consistent with the one calculated from $(S^2 - {}^1/_4)|D|$ (17 K); the barrier height is also consistent with the energy gap of $2|D|$ (17 K) between the $M_S = \pm {}^3/_2$ and $M_S = \pm {}^1/_2$ states, in accord with the relaxation pathway being via an Orbach process.

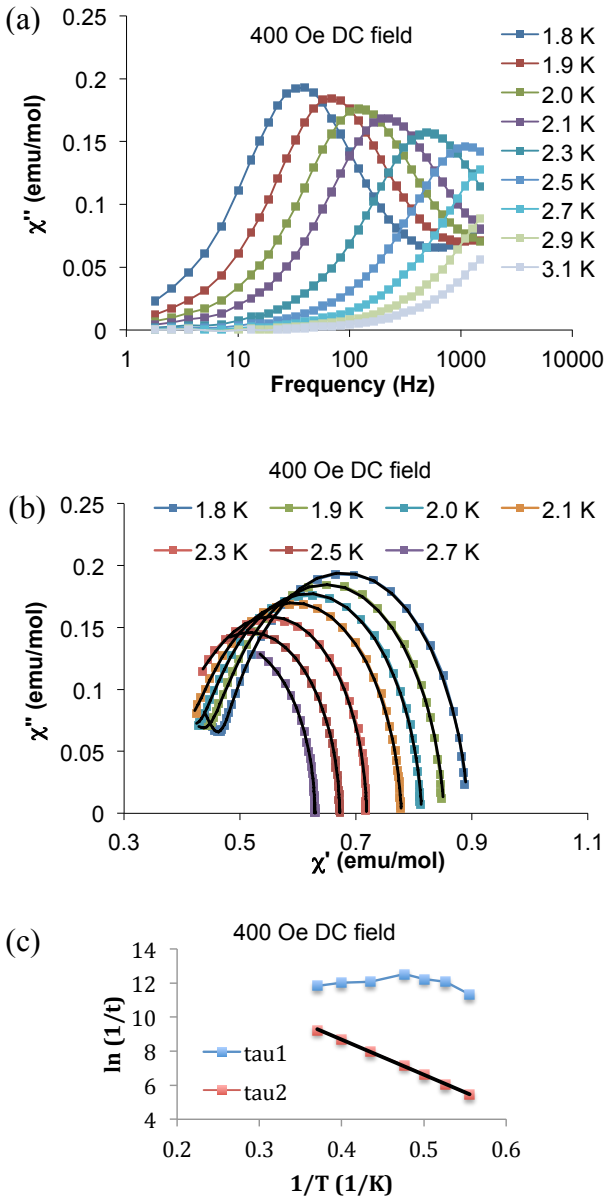


**Figure 57.** AC magnetic measurements for the cubic phase of [Co(TPMA)Cl]Cl in a 400 Oe DC field. (a) frequency dependence of χ''. Solid lines are guides for the eye. (b) Cole-Cole plot. The colored points and lines are experimental data and guides for the eye, respectively. The solid black lines are the results of fitting the data with CC-FIT using two relaxation processes as discussed in the main text. (c) Arrhenius plot. The black line is a linear regression fit to the data which results in the barrier height of 20.6 K with $\tau_o = 4.43 \times 10^{-8}$ s.

To further validate the fitted parameters for the thermal process, another fitting of the 400 Oe Cole-Cole data was performed with CC-FIT that did not include the five highest AC frequencies, which minimized the appearance of a tail in the Cole-Cole plot at 1.8 K and virtually eliminated the tail at all higher temperatures. The results of this fitting are shown in Figure 58. The value of $U_{eff}/k_b$ extracted from this fitting is 21.3 K with $\tau_o$ = 2.98 x $10^{-8}$ s. The alpha value ranges from 0.12 at 1.8 K to 0.02 at 2.7 K. These results are consistent with the values obtained from the fitting using two relaxation processes and demonstrate that the tail observed in the Cole-Cole plot is due to a second, fast relaxation process that has little effect on the thermal relaxation mechanism that is observed at high temperatures.

If the DC field is increased to 2000 Oe (Figure 59) the high-frequency tails are suppressed and the Cole-Cole plot can be fit with a single relaxation process using CC-FIT or a single modified Debye function to give $U_{eff}/k_b$ = 23.0 K and $\tau_o$ = 5.28 x $10^{-8}$ s. The alpha values are now less than 0.22 over the temperature range investigated, slightly higher than the alpha values observed in a 400 Oe DC field; the higher alpha values are likely due to the presence of a minor second relaxation process as can be seen in the very slight tails in the Cole-Cole plot. Attempts to fit the 2000 Oe data with two relaxation processes were unsuccessful. As with the measurements performed in a 400 Oe DC field the observed barrier is consistent with the $U_{eff}$ predicted by $(S^2 - {}^1/_4)|D|$ and the energy gap between $M_s$ states.

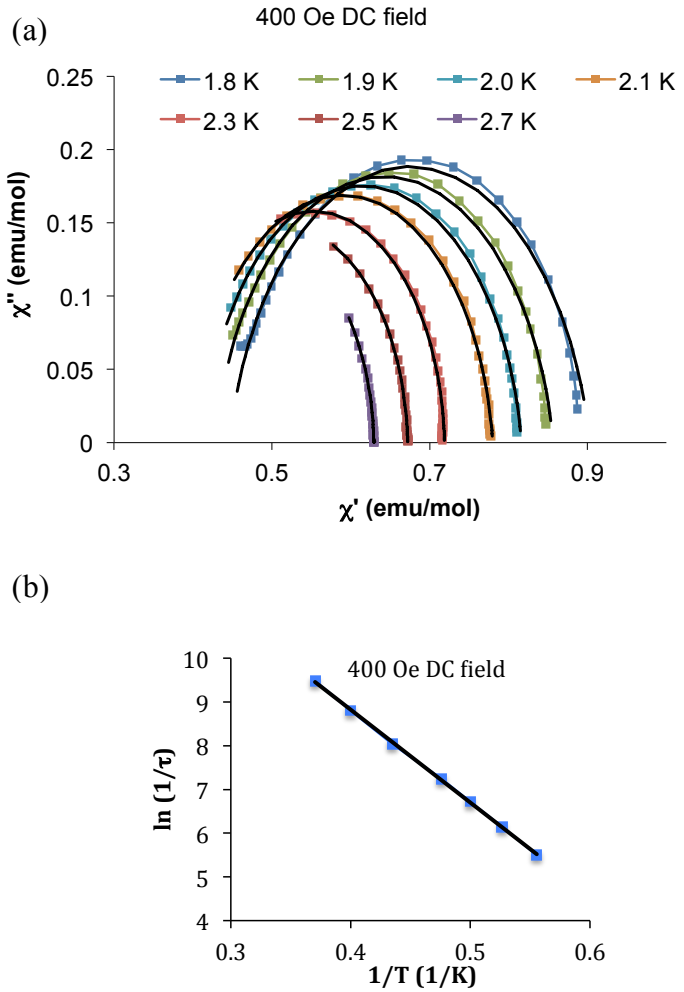


**Figure 58.** (a) Cole-Cole plot of the cubic phase of [Co(TPMA)Cl]Cl without the five highest frequency measurements. The colored points and lines are experimental data and guides for the eye, respectively. The solid black lines are the results of fitting the data with CC-FIT using one relaxation process as discussed in the main text. (b) Arrhenius plot using the parameters obtained from the fitting of the Cole-Cole plot. The black line is a linear regression fit to the data which resulted in the barrier height of 21.3 K with $\tau_o = 2.98 \times 10^{-8}$ s.

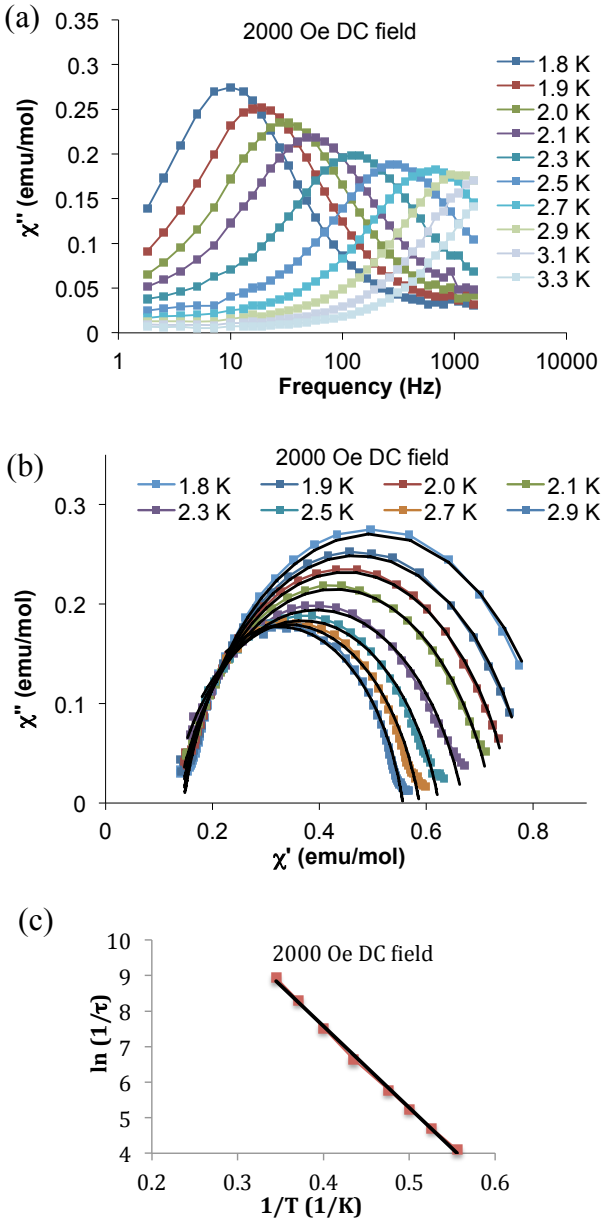


**Figure 59.** AC magnetic measurements for the cubic phase of [Co(TPMA)Cl]Cl in a 2000 Oe DC field. (a) frequency dependence of χ''. Solid lines are guides for the eye. (b) Cole-Cole plot. The colored points and lines are experimental data and guides for the eye, respectively. The solid black lines are the results of fitting the data with CC-FIT as discussed in the main text. (c) Arrhenius plot. The black line is a linear regression fit to the data which resulted in the barrier height of 23.0 K with $\tau_o = 5.28 \times 10^{-8}$ s.

If the applied DC field is further increased to 2800 Oe, the AC data become slightly noisy and begin to broaden out at higher temperatures (Figure 60) but a good fit can still be obtained, yielding $U_{eff}/k_b$ = 18.5 K with $\tau_o$ = 5.17 x $10^{-7}$ s and alpha values of less than 0.36, with the highest temperature having the largest alpha value. The observed energy barriers are consistent with those expected for an Orbach process. The lack of field dependence for the barriers rules out direct processes as a relaxation mechanism in this system. Raman processes are also field independent but scale as a power law in temperature and results in non-linearity of the Arrhenius plot which is not observed in this system, either. The combined observations lead to the conclusion that the major relaxation pathway in this system is an Orbach process.

It is tempting to ascribe the improved magnetic behavior to the strictly enforced 3-fold symmetry in the cubic phase since the rhombic term in the ZFS Hamiltonian should be zero in a molecule that possesses 3-fold symmetry[137,158] and the presence of a rhombic term is known to promote quantum tunneling,[115] but this would not explain the presence of SMM behavior in the acetonitrile analog which has a larger rhombic ZFS parameter. A more probable explanation can be found by examining the magnetic properties of the bromide and iodide congeners.

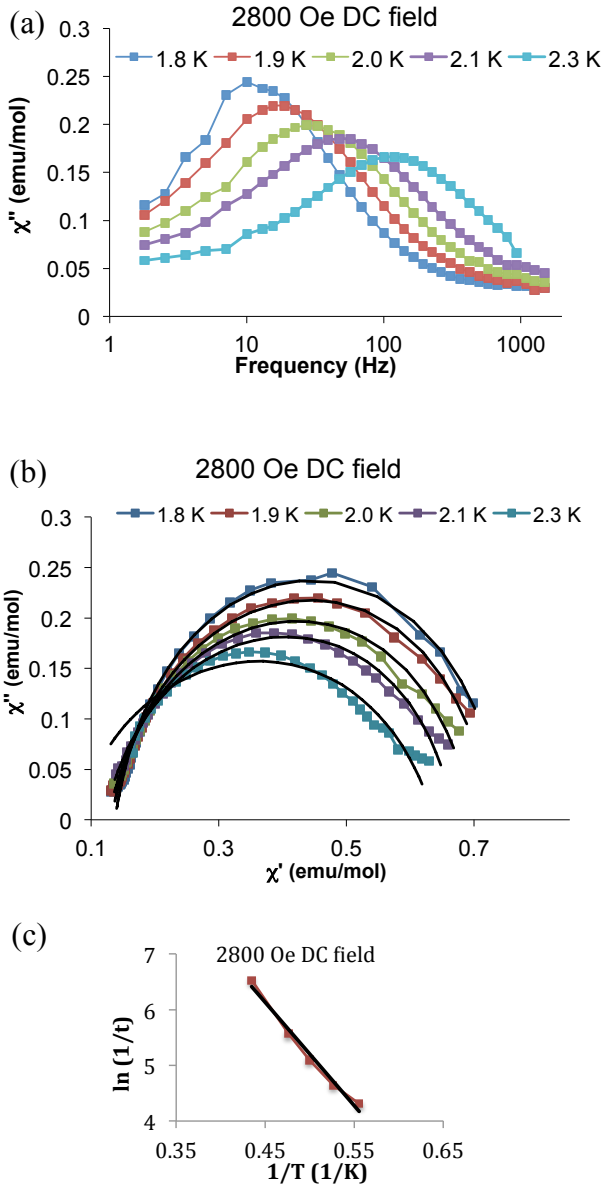


**Figure 60.** AC magnetic measurements for the cubic phase of [Co(TPMA)Cl]Cl in a 2800 Oe DC field. (a) frequency dependence of χ''. Solid lines are guides for the eye. (b) Cole-Cole plot. The colored points and lines are experimental data and guides for the eye, respectively. The solid black lines are the results of fitting the data with CC-FIT as discussed in the main text. (c) Arrhenius plot. The black line is a linear regression fit to the data which resulted in the barrier height of 18.5 K with $\tau_o = 5.17 \times 10^{-7}$ s.

**[Co(TPMA)Br]Br**. The molar magnetic susceptibility data of the triclinic phase was calculated using the average water content as determined by elemental analysis and TGA. Static DC magnetic measurements on crushed single crystals of both phases of [Co(TPMA)Br]Br were conducted between 1.8 and 300 K. The 300 K $\chi T$ values of 2.51 emu K $mol^{-1}$ (triclinic) and 2.31 emu K $mol^{-1}$ (cubic) are significantly higher than the 1.875 emu K $mol^{-1}$ expected for an S = 3/2 system with g = 2 due to spin-orbit coupling. The value of $\chi T$ slowly decreases down to ~ 20 K for both phases, after which temperature it begins to decrease much more rapidly until reaching a minimum of 1.61 emu K $mol^{-1}$ (triclinic) and 1.51 emu K $mol^{-1}$ (cubic) at 2.0 K (Figure 61a). The low-temperature magnetization of the two bromide phases is similar to the two chloride phases and the acetonitrile phase (Figure 61b, Figure 62). For these two complexes the best-fit parameters from ANISOFIT2.0 yielded D = -7.74 $cm^{-1}$, E = 1 x $10^{-3}$ $cm^{-1}$, and g = 2.43 for the triclinic phase and D = -7.29 $cm^{-1}$, E = 4 x $10^{-4}$ $cm^{-1}$, and g = 2.24 for the cubic phase. The best-fit parameters using PHI were D = -7.44 $cm^{-1}$ and g = 2.40 for the triclinic phase and D = -7.18 $cm^{-1}$ and g = 2.23 for the cubic phase. Similar to the chloride complexes, the fittings are of higher quality with negative versus positive D values. The sign of D for these two complexes is consistent with the sign of D reported for [Co($Me_6$tren)Br]Br as derived from EPR studies[137] and is larger in magnitude, namely -2.4 $cm^{-1}$ for [Co($Me_6$tren)Br]Br as compared to ~8 $cm^{-1}$ for the two TPMA complexes. The smaller D value for [Co($Me_6$tren)Br]Br as compared to [Co($Me_6$tren)Cl]$ClO_4$ was attributed to a stronger σ-donor effect from the equatorial amine nitrogen atoms of $Me_6$tren as evidenced by shortened Co-$N_{amine}$ bond lengths.

The authors provided computational evidence that this increase in σ donation has the effect of increasing the energy gap between the ($d_{xz}$,$d_{yz}$) and ($d_{xy}$,$d_{x^2-y^2}$) orbital sets, leading to a smaller D value. The TPMA ligand is more rigid than $Me_6$tren as evidenced by only minor changes in the Co-TPMA bonding metrics among all members of the family, thus making the energy gap between the ($d_{xz}$,$d_{yz}$) and ($d_{xy}$,$d_{x^2-y^2}$) orbital sets relatively constant across the series, leading to similar values for D across the series.

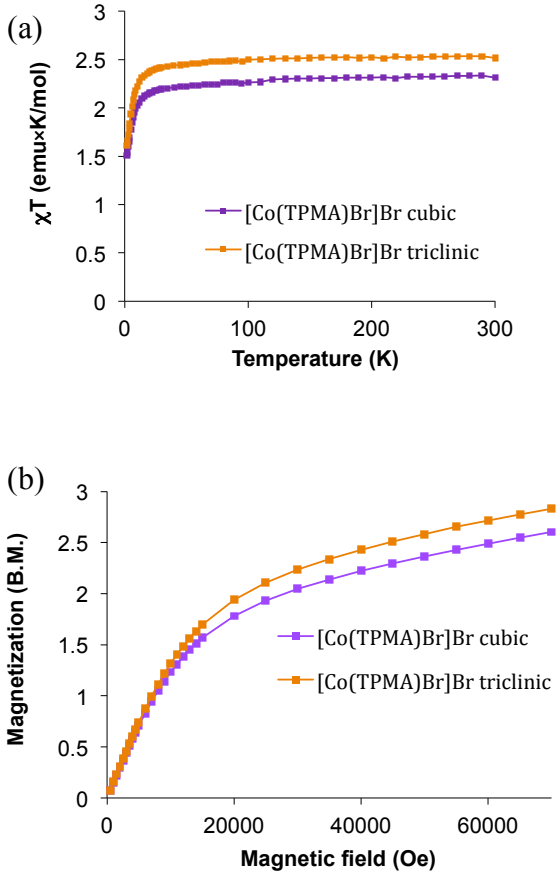


**Figure 61.** DC magnetic properties of [Co(TPMA)Br]Br. (a) the χT product under a 1000 Oe field. The solid line is a guide for the eye. (b) plot of M vs. H at 1.8 K. The solid line is merely a guide for the eye.

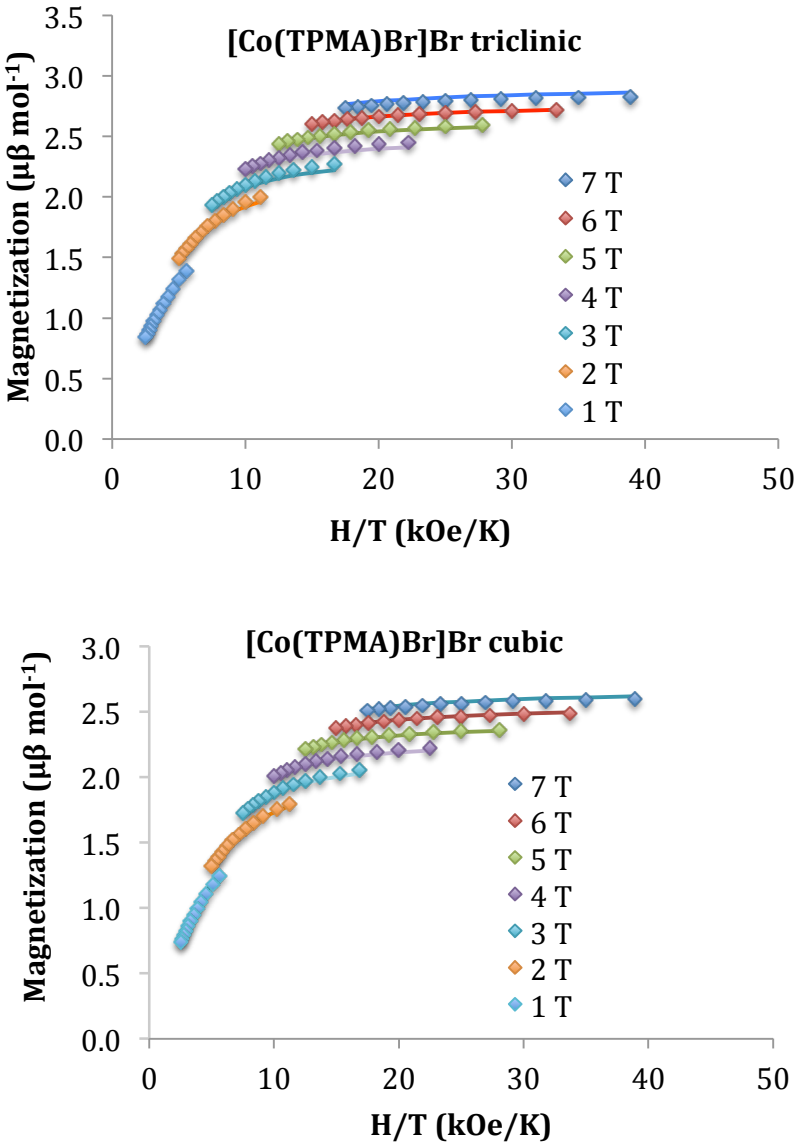


**Figure 62.** Temperature and field dependence of the magnetization for [Co(TPMA)Br]Br. Filled diamonds: experimental data. Solid lines: fitting of the experimental data using the parameters described in the main text for the ANISOFIT2.0 fitting.

The dynamic AC magnetic properties of the bromide phases are remarkably similar to the chloride phases. For the triclinic phase there is no out-of-phase signal in

zero applied DC field. At 1.8 K in DC fields of up to 2000 Oe, there is only a high-frequency tail visible in the χ'' data (Figure 63), signifying the presence of a fast relaxation process that is reasonably ascribed to quantum tunneling of the magnetization.

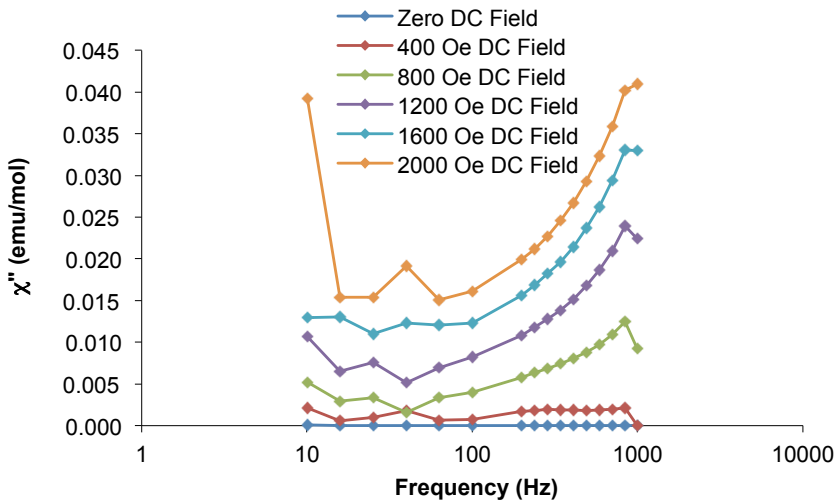


**Figure 63.** Out-of-phase AC susceptibility for the triclinic phase of [Co(TPMA)Br]Br as a function of applied DC field at 1.8 K.

The cubic phase was only investigated in an applied DC field of 1600 Oe, Figure 64, but displays behavior similar to the cubic chloride phase in a 2000 Oe DC field. There are slight tails in the Cole-Cole plot but fitting the data with two relaxation processes was unsuccessful. Using a single relaxation process, an Arrhenius plot was constructed that gives $U_{eff}/k_b$ = 17.2 K with $\tau_o$ = 8.06 x $10^{-8}$ s. The alpha values are less than 0.30 and the larger values are likely due to the presence of a second relaxation process. The magnitude of the observed barrier is consistent with an Orbach relaxation mechanism.

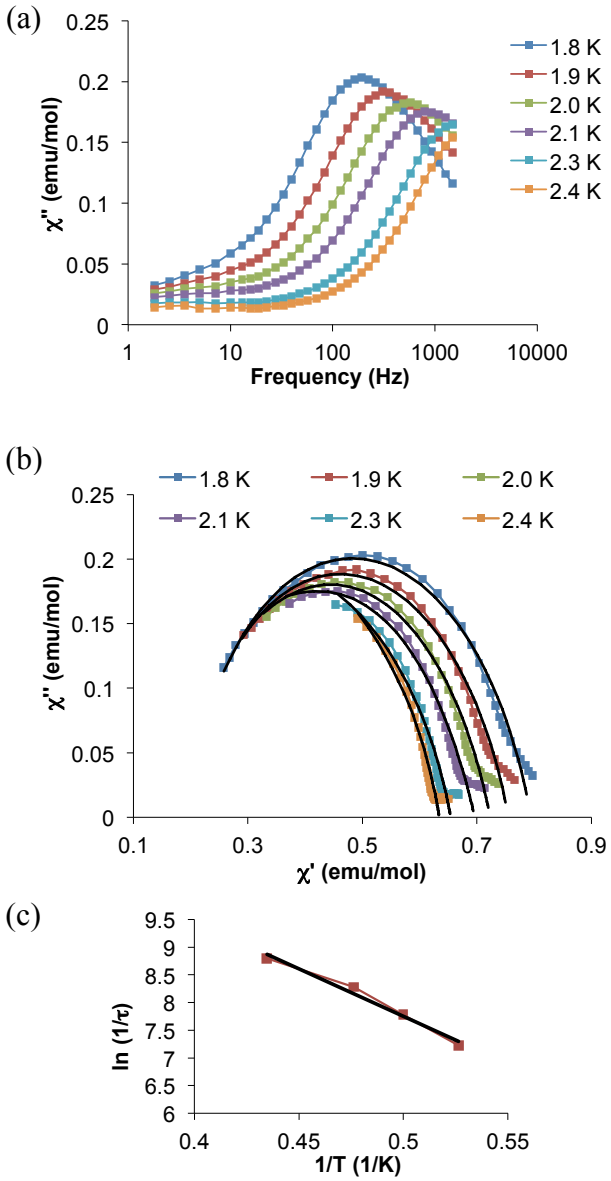


**Figure 64.** AC magnetic measurements for the cubic phase of [Co(TPMA)Br]Br in a 1600 Oe DC field. (a) frequency dependence of χ''. Solid lines are guides for the eye. (b) Cole-Cole plot. The colored points and lines are experimental data and guides for the eye, respectively. The solid black lines are the results of fitting the data with a modified Debye function as discussed in the main text. (c) Arrhenius plot. The black line is a linear regression fit to the data which resulted in the barrier height of 17.2 K with $\tau_o$ = 8.06 x $10^{-8}$ s.

**[Co(TPMA)I]I**. Static DC magnetic measurements on crushed single crystals of [Co(TPMA)I]I were conducted between 1.8 and 300 K. The 300 K $\chi T$ value of 2.32 emu K $mol^{-1}$ is, not unexpectedly, significantly higher than the 1.875 emu K $mol^{-1}$ expected for an S = 3/2 system with g = 2. The value of $\chi T$ slowly decreases until approximately 20 K, after which temperature it begins to decrease rapidly until reaching a minimum of 1.59 emu K $mol^{-1}$ at 2.0 K (Figure 65a).

The results of the low-temperature magnetization measurements are consistent with the previous complexes, Figure 65b, c. Fittings using ANISOFIT2.0 gave a D value of -8.28 $cm^{-1}$, E = -6 x $10^{-4}$ $cm^{-1}$, and g = 2.42. The best-fit parameters using PHI were D = -8.14 $cm^{-1}$ and g = 2.41. Unlike the previous cases the quality of the fits was equally good with a positive D value of similar magnitude and a slightly lower g value.

Consistent with the AC magnetic behavior of the triclinic phases of [Co(TPMA)Cl]Cl and [Co(TPMA)Br]Br, there is no out-of-phase signal for [Co(TPMA)I]I in a zero applied DC field. The relaxation dynamics of [Co(TPMA)I]I at 1.8 K were investigated with applied DC fields of up to 2800 Oe with no apparent maximum in the $\chi''$ data (Figure 66).

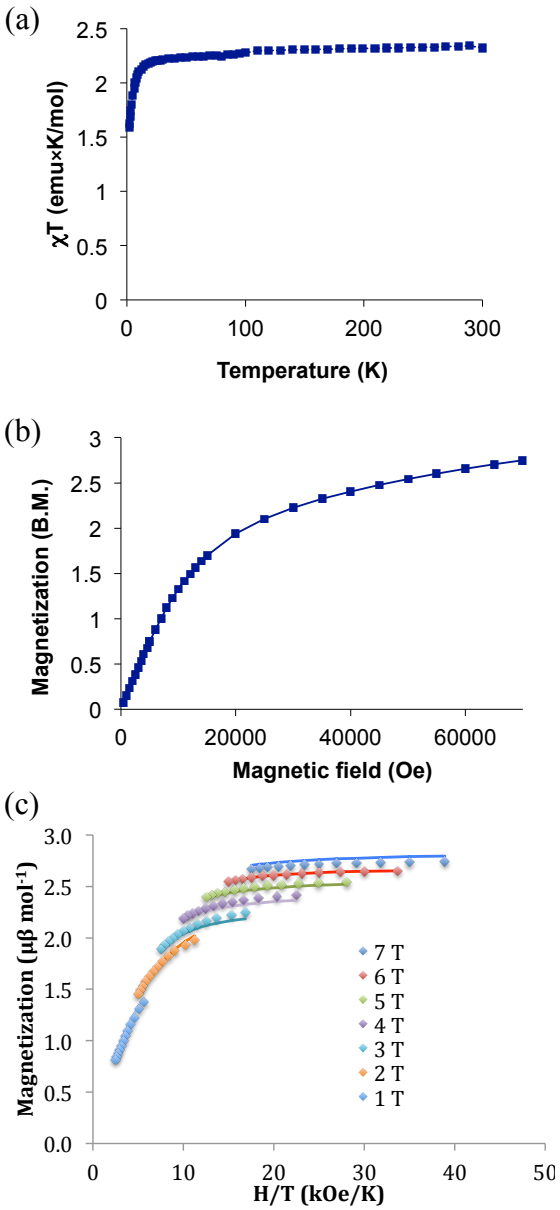


**Figure 65.** DC magnetic data for [Co(TPMA)I]I. (a) the χT product under a 1000 Oe field. The solid line is a guide for the eye. (b) plot of M vs. H at 1.8 K. The solid line is a guide for the eye. (c) temperature and field dependence of the magnetization. Filled diamonds: experimental data. Solid lines: fitting of the experimental data using the parameters described in the main text for the ANISOFIT2.0 fitting.

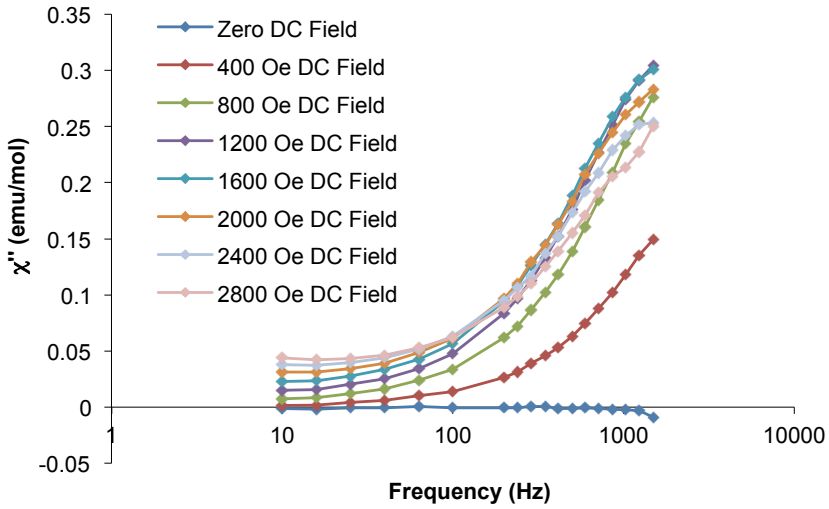


**Figure 66.** Out of phase AC susceptibility for [Co(TPMA)I]I as a function of applied DC field at 1.8 K.

As mentioned previously, if one considers only the halide series of compounds, it is reasonable to ascribe the SMM behavior of the cubic phases to the presence of strict 3-fold symmetry and the lack thereof in the triclinic phases. This symmetry argument, however, does not explain the SMM behavior of the acetonitrile complex. In order to gain more insight into the reasons behind the differences in magnetic behavior, *ab initio* calculations were conducted by Dr. Silvia Gomez-Coca, a postdoctoral researcher in our laboratories, and Dr. Eliseo Ruiz from the Departament de Química Inorganica and Institut de Recerca de Química Teòrica I Computacional, University of Barcelona. The results of those calculations, along with the ZFS parameters obtained by fitting the magnetization data, are summarized in Table 25. The ZFS parameters are similar for all six compounds with the exception of the positive D value for the acetonitrile complex,

**Table 25.** ZFS parameters for the members of the $[Co(TPMA)X]^{1+/2+}$ family from both magnetic measurements and ab initio calculations.

| | Magnetic Measurements | | | | |
|---|---|---|---|---|---|
| | PHI | | Anisofit | | |
| **Compound** | g | D ($cm^{-1}$) | g | D ($cm^{-1}$) | \|E\| ($cm^{-1}$) |
| $[Co(TPMA)CH_3CN](BF_4)_2$ | 2.39 | 9.69 | 2.38 | 9.63 | $8 \times 10^{-3}$ |
| [Co(TPMA)Cl]Cl triclinic | 2.30 | -8.01 | 2.31 | -8.18 | $4 \times 10^{-4}$ |
| [Co(TPMA)Cl]Cl cubic | 2.24 | -8.49 | 2.25 | -8.65 | $6 \times 10^{-4}$ |
| [Co(TPMA)Br]Br triclinic | 2.40 | -7.44 | 2.43 | -7.74 | $1 \times 10^{-3}$ |
| [Co(TPMA)Br]Br cubic | 2.23 | -7.18 | 2.24 | -7.29 | $4 \times 10^{-4}$ |
| [Co(TPMA)I]I triclinic | 2.41 | -8.14 | 2.42 | -8.28 | $6 \times 10^{-4}$ |

| | Orca | | | | |
|---|---|---|---|---|---|
| | CASSCF | | NEVPT2 | | |
| **Compound** | D ($cm^{-1}$) | E/D | D ($cm^{-1}$) | E/D | $g_{iso}$ |
| $[Co(TPMA)CH_3CN](BF_4)_2$ | 8.86 | 0.11 | 8.22 | 0.09 | 2.17 |
| [Co(TPMA)Cl]Cl triclinic | -7.47 | 0.06 | -4.82 | 0.07 | 2.19 |
| [Co(TPMA)Cl]Cl cubic | -8.63 | 0.0 | -5.75 | 0.0 | 2.20 |
| [Co(TPMA)Br]Br triclinic | -4.83 | 0.08 | -2.80 | 0.11 | 2.20 |
| [Co(TPMA)Br]Br cubic | -5.30 | 0.0 | -3.27 | 0.0 | 2.20 |
| [Co(TPMA)I]I triclinic | -2.97 | 0.22 | -1.66 | 0.22 | 2.20 |

which is expected based on the π-accepting character of the $CH_3CN$ ligand. The agreement between the experimental and theoretical ZFS parameters is fairly good for all members of the series. *Ab inito* calculations of this type are known to accurately predict the sign of D,[142,159] thus lending support to the sign of D determined from the magnetization experiments. The ground and first four excited states of all of the complexes are highly multiconfigurational, with five separate determinants contributing significantly to the ground state. Four determinants are heavily involved in the first excited state, five in the second excited state, and three in the third and fourth excited states. This multiconfigurational nature makes correlating the wave functions to the

changes in the ZFS parameters a challenging task, one that is still ongoing. There is no evidence of the heavy-halide effect[160-163] on the ZFS parameters as derived from magnetization measurements; the calculations show a trend of decreasing D for the heavier halides. This difference could be due to the limitations on the accuracy of D values as obtained from powder magnetization measurements or slight inaccuracies in the treatment of the heavier halides in the calculations. The bond metrics also support a very similar electronic structure for all of the members of this family (Table 26).

**Table 26.** Bond distances and angles for the members of the $[Co(TPMA)X]^{1+/2+}$ family obtained from the single crystal X-ray structures.

| **Compound** | Co-X (Å)[a] | Co-$N_{py}$ plane (Å)[b] | $N_{py}$-Co-$N_{py}$ (°)[c] | Co-$N_{py}$ (Å)[d] | Co-$N_{am}$ (Å)[e] | Co-Co (Å)[f] |
|---|---|---|---|---|---|---|
| $[Co(TPMA)(CH_3CN)](BF_4)_2$ | 2.037(17) | 0.395 | 115.9 | 2.0378 | 2.1705(16) | 7.863 |
| [Co(TPMA)Cl]Cl triclinic | 2.2707 | 0.435 | 115.6 | 2.058 | 2.193 | 6.119 |
| [Co(TPMA)Cl]Cl cubic | 2.277(12) | 0.459 | 115.21(4) | 2.068(2) | 2.214(3) | 7.951 |
| [Co(TPMA)Br]Br triclinic | 2.4151 | 0.436 | 114.9 | 2.061 | 2.200 | 6.289 |
| [Co(TPMA)Br]Br cubic | 2.427(16) | 0.455 | 115.30(8) | 2.068(4) | 2.214(7) | 8.079 |
| [Co(TPMA)I]I triclinic | 2.645 | 0.452 | 115.40 | 2.071 | 2.194 | 6.601 |

[a]distance between the $Co^{II}$ ion and the coordinated $CH_3CN$/halide ion.
[b]distance the $Co^{II}$ ion projects out of the mean plane of the three pyridine N atoms of TPMA.
[c]average angle formed by two of the three pyridine N atoms of TPMA and the $Co^{II}$ ion.
[d]average distance between the $Co^{II}$ ion and the pyridine N atoms of TPMA.
[e]distance between the $Co^{II}$ ion and the bridgehead amine N atom of TPMA.
[f]closest intermolecular Co-Co distance.

The bond distances between the $Co^{II}$ ion and the atom coordinated to the open site left by TPMA follow a reasonable trend, *vis*., lengthening from $CH_3CN$ to iodide. The projection of the $Co^{II}$ ion out of the equatorial N3 plane is similar for all of the members of the family, as are the distances and angles between the $Co^{II}$ ion and the TPMA ligand. What is different, however, is the nearest-neighbor distance between cobalt ions. For the three triclinic halide analogs that do not display SMM behavior, the shortest Co-Co distance is 6.6 Å or less. For the acetonitrile and two cubic halide analogs that display SMM behavior, the shortest Co----Co intermolecular distance is in the range of 7.863 to 8.079 Å, much longer than in the triclinic halide phases. These increased cobalt distances, taken together with the narrow distribution of distances for the analogs that display similar SMM behavior, strongly suggest that dipolar interactions are the source of fast relaxation in the members of the family that do not display SMM behavior.

As discussed in Chapter I, transverse magnetic fields caused by the internal field of neighboring molecules can dramatically increase the tunneling probability in SMMs. All of the members of this series display less than ideal packing arrangements in this respect. As can be seen in Figure 67, the $C_3$ axes of neighboring molecules are not co-linear in any of these molecules. Figure 68 displays packing diagrams of the different members of the series as viewed down the crystallographic *c* axis. The transverse dipolar fields generated by these packing arrangements will promote quantum tunneling, which explains why a DC field is needed to observe SMM behavior even in the cubic analogs, for which E is vanishingly small.

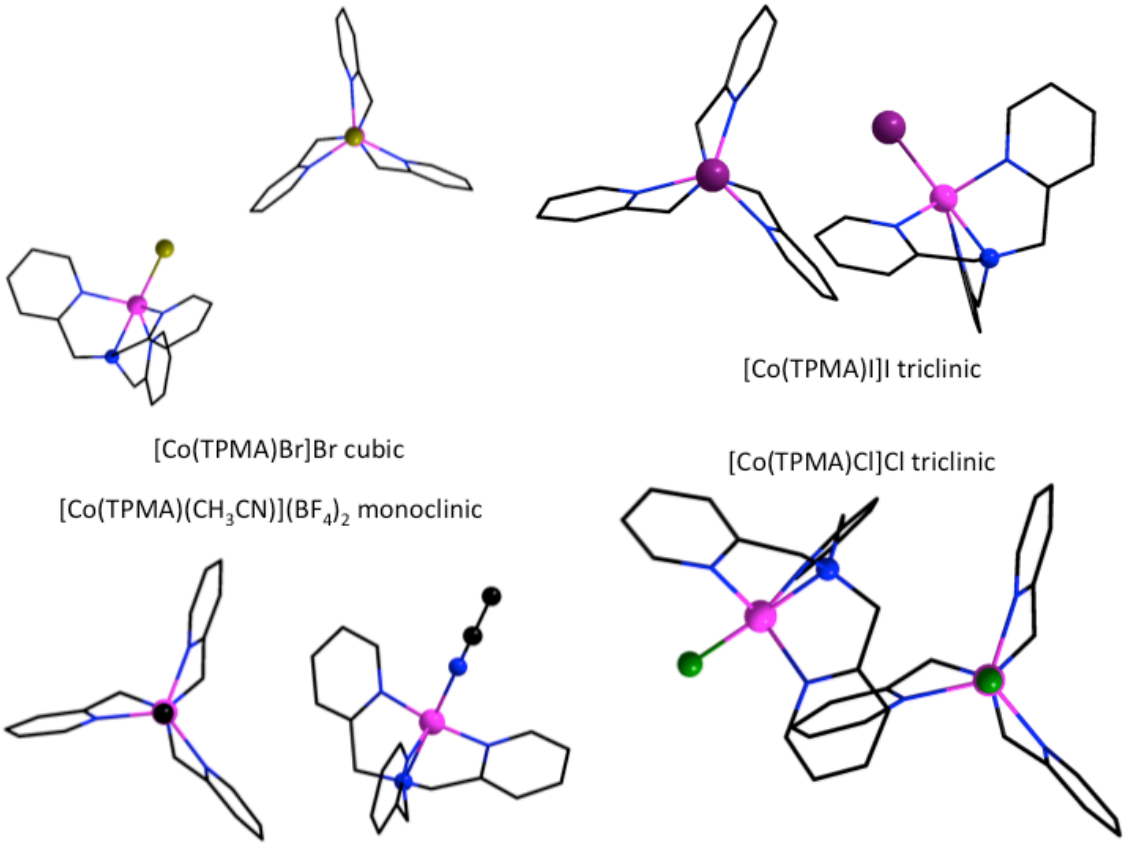


**Figure 67.** Relative orientation of the $C_3$ axes for members of the $[Co(TPMA)X]^{n+}$ series. The cubic phase of [Co(TPMA)Cl]Cl is identical to the cubic bromide phase pictured. The triclinic phase of [Co(TPMA)Br]Br is identical to the triclinic chloride phase pictured. Color code: C, black; N, blue; Co, pink; Cl, green; Br, yellow; I, purple.

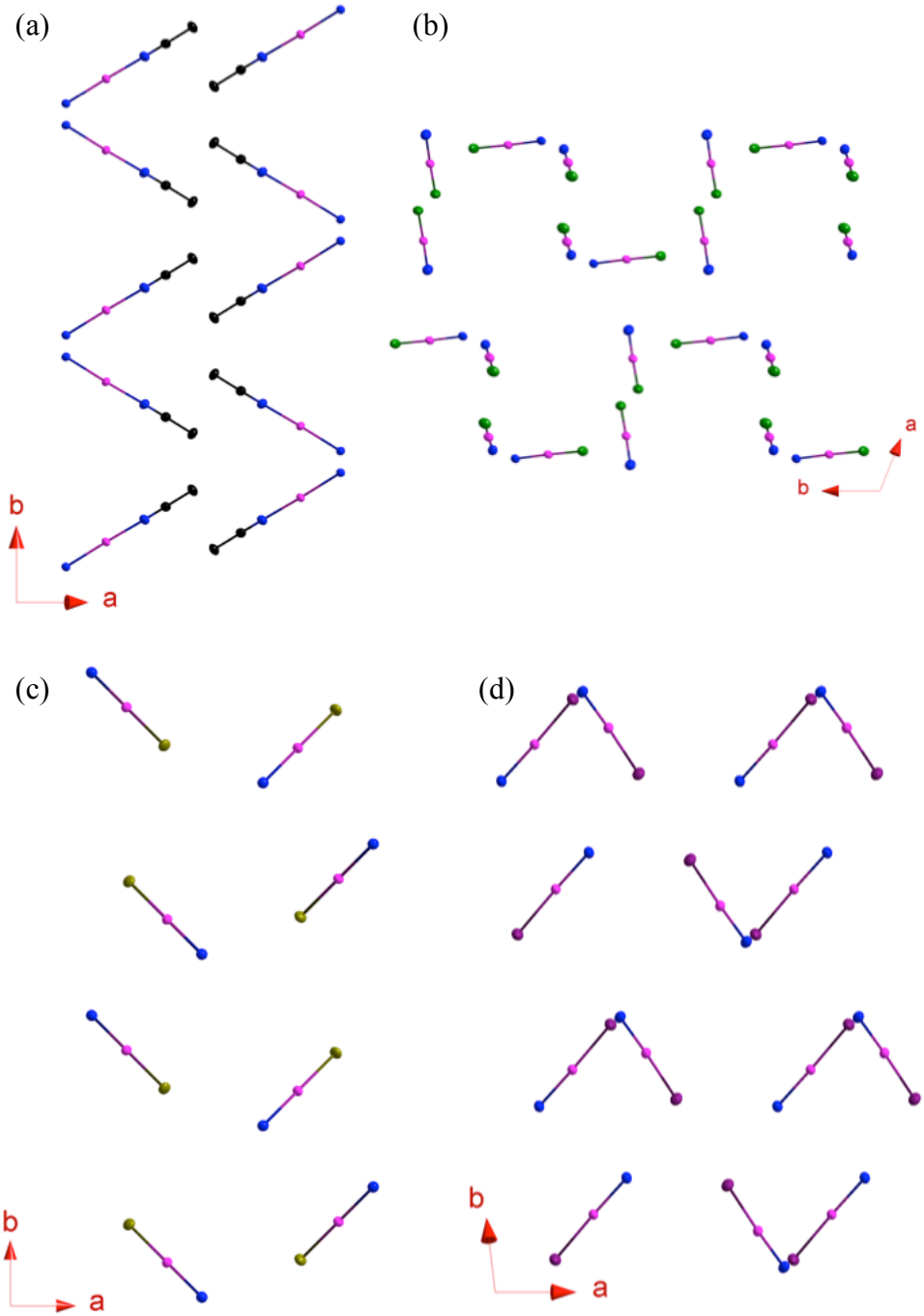


**Figure 68.** Packing arrangement of members of the $[Co(TPMA)X]^{n+}$ family. Only the atoms defining the $C_3$ axes are shown for the sake of clarity. (a) $[Co(TPMA)(CH_3CN)](BF_4)_2$. (b) triclinic phase of [Co(TPMA)Cl]Cl. Note that the triclinic phase of [Co(TPMA)Br]Br exhibits identical packing. (c) cubic phase of [Co(TPMA)Br]Br. Note that the cubic phase of [Co(TPMA)Cl]Cl exhibits identical packing. (d) [Co(TPMA)I]I. Color code: C, black; N, blue; Co, pink; Cl, green; Br, yellow; I, purple.

**Conclusions**

The results of the present study performed on an isostructural family of $Co^{II}$ complexes provide convincing evidence of the importance of dipolar relaxation pathways in mononuclear SMM systems. In the present family, the relatively minor differences in the coordination environment around the $Co^{II}$ ion have been found to have minor effects on the electronic structure as evidenced by the similarity in the ZFS parameters. These findings suggest that, at least in some cases, minor distortions from an ideal symmetry can be considered sufficiently close to the ideal symmetry to generate the desired SMM properties when targeting that symmetry. This realization greatly increases the scope of ligands that the synthetic inorganic chemist can consider when designing new SMMs based on ideal geometries. The most pronounced differences in the solid-state structures are the intermolecular Co----Co distances, where an interatomic distance of approximately eight angstroms correlates with improved SMM behavior. In the $[Co(Me_6tren)Cl]ClO_4$ and $[Co(Me_6tren)Br]Br$ complexes[137] the closest Co----Co contact is 7.95 Å for the chloride complex and 8.155 Å for the bromide complex, similar to the Co-Co distances in this study. No AC susceptibility experiments were performed in this report, making a direct comparison of the SMM properties to the ones in this study impossible, but micro-SQUID measurements displayed open hysteresis loops below 1 K, thus confirming the SMM behavior of the $Me_6$tren complexes. A dilution study with Co:Zn ratios of 0.1:0.9 and 0.05:0.95 demonstrated that dipolar interactions were not involved in the relaxation pathway, lending support to the hypothesis that Co----Co contacts of ~8 Å are sufficient to minimize dipolar

relaxation. Recently the AC magnetic behavior of $[Co(Me_6tren)Cl](ClO_4)$ was reported.[164] The complex displayed weak out-of-phase signals in a zero applied DC field and a spin reversal barrier of ~20 K across a range of applied DC fields from 2000 to 8000 Oe. This behavior is remarkable similar to that observed in the cubic phase of [Co(TPMA)Cl]Cl. In $[Co(Me_6tren)H_2O](NO_3)_2$ the closest Co----Co contact is 7.791 Å[138] but no maximum in $\chi''$ is observable at 1.9 K, even at DC fields as high as 7000 Oe, consistent with a very fast relaxation mechanism. No investigation of the mechanism of the fast relaxation was reported. This Co-Co distance is only 0.072 Å shorter than in $[Co(TPMA)(CH_3CN)](BF_4)_2$, the SMM with the shortest Co----Co distance in this study. Since the magnitude of the dipole interaction scales as $r^{-3}$ it is possible that this small difference in intermolecular distance is responsible for the different magnetic behavior but this seems unlikely. It has recently been shown that the interaction between the electron spin and the nuclear spin of cobalt can also have a significant impact on the relaxation properties in these types of systems,[49] as can vibronic coupling.[165] In the absence of further experimental and theoretical studies the presence of the water protons in $[Co(Me_6tren)H_2O](NO_3)_2$ leading to an increase in vibronic coupling is a much more viable explanation for the faster relaxation observed in $[Co(Me_6tren)H_2O](NO_3)_2$ as compared to $[Co(Me_6tren)Cl](ClO_4)$, [Co(Me6tren)Br]Br, and the $[Co(TPMA)X]^+$ complexes described in this work. The coordinated water molecule forms hydrogen bonds to the nitrate counteranions in that molecule. There are no classic hydrogen bonds between the coordinated $CH_3CN$ molecule and the tetrafluoroborate counteranions in $[Co(TPMA)(CH_3CN)](BF_4)_2$.The

greater flexibility of the $Me_6$tren ligand as compared to TPMA may also be responsible for the differences in magnetic behavior but is not thought to be a major influence given the similarity in the AC magnetic behavior of [Co($Me_6$tren)Cl]($ClO_4$) and the cubic phase of [Co(TPMA)Cl]Cl.

# CHAPTER IV

# SINGLE CRYSTAL X-RAY AND NEUTRON DIFFRACTION STUDIES OF A SERIES OF TRANSITION METAL FLUORIDE CAGES

## Introduction

The field of cyanide[166]- and oxide[167]-based molecular magnetic materials is well established and quite vast. In contrast, molecular magnetic materials containing fluoride ligands are relatively scarce,[168-170] leaving a large area of coordination chemistry unexplored from a magnetism perspective. The work of Winpenny[171-182] and Bendix[168,169,183-185] in recent years has shown that the fluoride ligand is a viable alternative to other bridging ligands for the synthesis of magnetic molecules. In these relatively few examples, however, the fluoride ion is not the only ligand present in the metal coordination sphere. In Winpenney's homologous series of antiferromagnetically coupled "wheels" of general formula $[NR_2H_2][M_7M'F_8(O_2CR')_{16}]$, which have been synthesized for a wide range of R, M, M′, and R′, the metal centers are bridged by a mixture of fluoride ions and carboxylate derivatives. In unrelated work, Bendix has recently published several reports of lanthanide-containing complexes containing unsupported bridging fluoride ligands but again the ligand system is mixed, with a combination of organic ligands and fluoride filling the coordination sphere of the lanthanide ions. In the last several years the Bendix group has also reported paramagnetic transition metal compounds containing unsupported fluoride bridges, namely *catena*-MnF(salen),[168] the 3d-4f compound

$[Cr_2Nd_2F_4(NO_2)_8(phen)_4]\cdot 4CH_3OH\cdot H_2O$ (phen = 1,10-phenanthroline),[184] and a $[Ni(vis)_4(ReF_6)]_\infty$ (vis = 1-vinylimidazole) chain based on $[ReF_6]^{2-}$.[186] Of the fluoride-bridged molecular magnets that are known, the coupling constants span a wide range. In the compound $[\{Cu^{II}(dmpz)_2(mpz)\}_2(\mu\text{-}F)_2](BF_4)_2$ (dmpz = 3,5-dimethylpyrazole, mpz = 5(3)-methylpyrazole) the exchange coupling is so weak it is essentially zero.[187] In contrast, the exchange coupling in $[\{Cu^{II}(\mu\text{-}L_m)\}2(\mu\text{-}F)](BF_4)_3\bullet 2.25((CH_3)_2CO)$ ($L_m$ = *m*-bis[bis(1-pyrazolyl)methyl]benzene) is >-300 $cm^{-1}$ (-2J Hamiltonian).[188] This range of exchange coupling constants is similar to those observed for compounds with bridging oxide ligands[189] and cyanide ligands[166] making fluoride a viable alternative to cyanide and oxide for the synthesis of molecular magnets.[170]

The high stability of polyoxometallates piqued our interest as to whether similar structures could be formed with isoelectronic fluoride ligands in place of oxide ligands. Precedent for these types of anionic compounds was established in 2002 with the synthesis of the first open-shell Keggin ion, which is also the first report of a Keggin ion containing terminal or bridging fluoride ligands.[190] This compound consists of a polyfluorometallate core with $[O]^{2-}$ and $[F]^-$ groups acting as bridging and terminal ligands. Prior to the current thesis work a postdoctoral student in the Dunbar group, Dr. Xinyi Wang, demonstrated in preliminary studies that a mixed-valence iron-fluoride cage that resembles the classic Keggin ion[190] of formula $[XM_{12}O_{40}]^{3-}$ forms in a very simple one-pot reaction. By using $(Et_4N)_3[M_2F_9]$ ($M = V^{III}$, $Cr^{III}$, $Fe^{III}$) as fluoride sources and reacting this precursor with divalent transition metal salts Xinyi prepared an isostructural series of complexes that comprise the majority of the first row transition

metals (Table 27). Xinyi's efforts to refine the crystal structures did not lead to publishable results. While these compounds likely contain exclusively fluoride ligands in the bridging and terminal positions, Xinyi's elemental analysis and mass spectrometry experiments were unable to confirm that composition. In particular, elemental analysis indicated that a large amount of oxygen is present in the crystals, which was attributed to DMF solvent molecules in the unit cell. Inductively Coupled Plasma Mass Spectrometry (ICP-MS) and Neutron Activation Analysis (NAA) established a M:M' ratio of 2:1 in the crystals, consistent with the stoichiometry of the reaction. For the $(Et_4N)_8[Co_4Fe_8F_{40}]$ and $(Et_4N)_8[Ni_4Fe_8F_{40}]$ cages the isotope patterns of the mass spectrometry data could only be reproduced by formulae involving heterometallic cages, making the existence of "whole-molecule" disorder in which the crystals are composed of a mixture of homometallic cages unlikely. The current work focused on the use of synchrotron X-ray and single crystal neutron diffraction experiments to assist in determining the nature of this series of complexes. It should be noted that the true composition of these cage molecules is still ambiguous so all formulae presented herein are approximations based on the information available.

**Table 27.** Known metal combinations for the polyfluorometallate complexes. Nomenclature: MM'F, where M originates from the $M^{II}$ precursor and M' from the $[M_2F_9]^{3-}$ starting material.

| Compound | *a* (Å) | Volume (Å$^3$) | Crystal Color |
|---|---|---|---|
| VFeF | 27.2308(16) | 20192(2) | reddish brown |
| CrFeF | 27.1969(18) | 20117(39) | brown |
| FeF | 27.2957(47) | 20337(14) | red |
| CoFeF | 27.2252(10) | 20179(4) | pink |
| NiFeF | 27.1451(6) | 19990(4) | light green |
| CuFeF | 27.0673(31) | 19830(8) | light green |
| ZnFeF | 27.1550(39) | 20024(9) | colorless |
| FeCrF | 26.7931(19) | 19291(6) | brown |
| NiCrF | 26.6789(27) | 18989(8) | brown |
| NiVF | 27.0129(24) | 19711(8) | yellow |
| CoVF | 26.9500(31) | 19573(8) | red |

**Experimental Section**

All manipulations were carried out under an inert atmosphere of Ar or $N_2$ using standard glove box and Schlenk line techniques unless otherwise noted. The salts $(Et_4N)_3[Fe_2F_9]$,[191] $[Co(CH_3CN)_6](BF_4)_2$,[96] and $[Ni(CH_3CN)_6](BF_4)_2$[96] were prepared by literature procedures. The compound $[Cr(CH_3CN)_4](BF_4)_2$ was prepared according to a literature procedure[192] with the substitution of $Cr_2(O_2CCF_3)_4$ for $Cr_2(O_2CCH_3)_4$. The reagent $(Et_4N)F{\bullet}xH_2O$ (Alfa Aesar) was used as received and stored in a vacuum desiccator. The precursors $VCl_3$ (Aldrich), $CrCl_2$ (Alfa Aesar), $NaBPh_4$ (Aldrich), $NaO_2CCF_3$ (Aldrich), $NOBF_4$ (Alfa Aesar), cobalt metal (Alfa Aesar), and nickel metal (Alfa Aesar) were used as received. The oxidizing agent $Et_3OBF_4$ was purchased from Aldrich as a 1 M solution in $CH_2Cl_2$ and used as received. The $CH_3CN$ was pre-dried by storage over 3 Å molecular sieves and distilled from 3 Å molecular sieves under an $N_2$ atmosphere. The EtOH was purified by distillation from Mg/I under an $N_2$ atmosphere.

The $CH_2Cl_2$ was purified by distillation from $P_2O_5$ under an $N_2$ atmosphere. Benzene was purified using an MBRAUN solvent purification system. Anhydrous THF (Aldrich) and anhydrous DMF (Alfa Aesar) were used as received. The solutions used for the syntheses of the fluoride cages were prepared in an MBRAUN dry box under an $N_2$ atmosphere using glassware coated with Glassclad®-18. These solutions were then removed from the dry box and used on a Schlenk line under an Argon atmosphere for further manipulations. Elemental analysis was performed by Atlantic Microlabs, Inc., Norcross, GA. Infrared spectra were recorded on a Nicolet Nexus 470 FT-IR under an $N_2$ atmosphere as Nujol mulls on KBr plates.

*Syntheses*

**$[V(CH_3CN)_6](BPh_4)_2$.** This salt was synthesized using a modification of a previously published procedure.[193,194] The reaction was carried out under an atmosphere of dry Argon using Schlenk line techniques. A quantitiy of $VCl_3$ (3 g, 19.2 mmol) was stirred in 200 mL of dry $CH_3CN$ at 75 °C for three days yielding a green solution. Upon cooling to room temperature, a solution of $NaBPh_4$ (19.8 g, 57.8 mmol) in 40 mL of $CH_3CN$ was added with a metal cannula. The instantaneous formation of a white precipitate was observed. The slurry was stirred for three hours, after which time the solvent was removed under vacuum to obtain a green solid. The green solid was continuously extracted with boiling $CH_3CN$ using a Soxhlet extractor for three days to obtain a bright green solution. Upon cooling, green crystals and white powder precipitated. The solution was heated to 85 °C to re-dissolve the green crystals and filtered while hot. Green crystals formed upon cooling. The solution was further chilled

to -10 °C and left overnight. The solution was filtered and the green crystals were stored under $N_2$ in the dry box. (Yield 8.454 g, 47%)

**$(Et_4N)_8[V_4Fe_8F_{40}]$.** A solution of $(Et_4N)_3[Fe_2F_9]$ (0.0999 g, 0.148 mmol) in $CH_3CN$ (6 mL) was placed in a Schlenk tube. To a second Schlenk tube was added $[V(CH_3CN)_6](BPh_4)_2$ (0.1390 g, 0.149 mmol) in $CH_3CN$ (5 mL) and DMF (1 mL). A solution consisting of 5 mL of $CH_3CN$ and 1 mL of DMF was prepared in a third Schlenk tube. The three solutions were installed on a Schlenk line and used to layer a series of thin glass tubes under an Argon atmosphere. The bottom layer of each thin tube contained 1 mL of the brown $V^{II}$ solution, followed by 0.5 mL of the 5:1 $CH_3CN$:DMF solution, and finally 1 mL of the colorless $(Et_4N)[Fe_2F_9]$ solution. The thin tube was flame sealed under reduced pressure. Reddish brown crystals formed in three days. If the tubes were allowed to stand undisturbed for several months, crystals of approximately 1 mm in size, suitable for neutron diffraction, were present.

**$(Et_4N)_8[Cr_4Fe_8F_{40}]$.** A solution of $(Et_4N)_3[Fe_2F_9]$ (0.1007 g, 0.150 mmol) in $CH_3CN$ (6 mL) was placed in a Schlenk tube. To a second Schlenk tube was added $[Cr(CH_3CN)_4](BF_4)_2$ (0.0608 g, 0.156 mmol) in $CH_3CN$ (5 mL) and DMF (1 mL). A solution consisting of 5 mL of $CH_3CN$ and 1 mL of DMF was prepared in a third Schlenk tube. The three solutions were installed on a Schlenk line and used to layer a series of thin glass tubes under an Argon atmosphere. The bottom layer of each thin tube contained 1 mL of the blue-green $Cr^{II}$ solution, followed by 0.5 mL of the 5:1 $CH_3CN$:DMF solution, and finally 1 mL of the colorless $(Et_4N)[Fe_2F_9]$ solution. The thin tube was then flame sealed under reduced pressure. Brown, block-shaped crystals

formed in three days. If the tubes were allowed to stand undisturbed for several months, crystals of approximately 1 mm in size, suitable for neutron diffraction, were present. Analysis calculated (found) for $(Et_4N)_9[Cr_4Fe_8F_{35}(OH)_6]$ ($C_{72}H_{186}N_9F_{35}O_6Cr_4Fe_8$): C: 33.34% (23.80%), H: 7.23% (4.82%), N: 4.86% (6.18%) F: 25.63% (27.27%).

**$(Et_4N)_8[Co_4Fe_8F_{40}]$.** A solution of $(Et_4N)_3[Fe_2F_9]$ (0.1000 g, 0.148 mmol) in $CH_3CN$ (6 mL) was placed in a Schlenk tube. To a second Schlenk tube was added $[Co(CH_3CN)_6](BF_4)_2$ (0.0711 g, 0.148 mmol) in $CH_3CN$ (5 mL) and DMF (1 mL). A solution consisting of 5 mL of $CH_3CN$ and 1 mL of DMF was prepared in a third Schlenk tube. The three solutions were installed on a Schlenk line and used to layer a series of thin glass tubes under an Argon atmosphere. The bottom layer of each thin tube contained 1 mL of the pink $Co^{II}$ solution, followed by 0.5 mL of the 5:1 $CH_3CN$:DMF solution, and finally 1 mL of the colorless $(Et_4N)[Fe_2F_9]$ solution. The thin tube was then flame sealed under reduced pressure. Pink crystals formed in three days. If the tubes were allowed to stand undisturbed for several months, crystals of approximately 1 mm in size, suitable for neutron diffraction, were present.

**$(Et_4N)_8[Ni_4Fe_8F_{40}]$.** A solution of $(Et_4N)_3[Fe_2F_9]$ (0.0996 g, 0.148 mmol) in $CH_3CN$ (6 mL) was placed in a Schlenk tube. To a second Schlenk tube was added $[Ni(CH_3CN)_6](BF_4)_2$ (0.0708 g, 0.148 mmol) in $CH_3CN$ (5 mL) and DMF (1 mL). A solution consisting of 5 mL of $CH_3CN$ and 1 mL of DMF was prepared in a third Schlenk tube. The three solutions were installed on a Schlenk line and used to layer a series of thin glass tubes under an Argon atmosphere. The bottom layer of each thin tube contained 1 mL of the pale green $Ni^{II}$ solution, followed by 0.5 mL of the 5:1

$CH_3CN$:DMF solution, and finally 1 mL of the colorless $(Et_4N)[Fe_2F_9]$ solution. The thin tube was then flame sealed under reduced pressure. Pale green crystals formed in three days. If the tubes were allowed to stand undisturbed for several months, crystals of approximately 1 mm in size, suitable for neutron diffraction, were present.

*X-ray Crystallographic Measurements*

Single crystal X-ray data for $(Et_4N)_8[Cr_4Fe_8F_{40}]$ and $(Et_4N)_8[Ni_4Fe_8F_{40}]$ were collected on a Bruker APEXII (Mo $K_\alpha$) diffractometer equipped with a CCD detector. A suitable crystal was affixed to a nylon loop with Paratone® oil and placed in a cold stream of $N_{2(g)}$ at 110 K. The frames were integrated with the Bruker APEXII software package[99] and a semi-empirical absorption correction was applied using SADABS as contained within the Bruker APEXII software suite. The structure was solved using SHELXS[100] and refined using SHELXL-2014[101] as implemented in ShelXle, a graphical interface for the SHELX suite of programs.[102] The remaining non-hydrogen atoms were located by alternating cycles of least-squares refinements and difference Fourier maps. All hydrogen atoms were placed in calculated positions. The final refinements were carried out with anisotropic thermal parameters for all non-hydrogen atoms unless otherwise specified. All of the crystals studied were found to be merohedral twins, with twin ratios of close to 50% for all crystals.

All of the structures, including the ones previously collected by Dr. Xinyi Wang and the ones reported here, exhibit similar disorder of the metal ions and fluoride ligands. The methods used to model this disorder will be discussed further in the remainder of this chapter. In addition, only one $[Et_4N]^+$ cation could be located in the

difference map, which is not sufficient to balance any reasonable charge on the anionic cage. Further pertinent details of the X-ray refinements are given in Table 28.

**Table 28.** X-ray crystal and structural refinement data for $(Et_4N)_8[Cr_4Fe_8F_{40}]$ and $(Et_4N)_8[Ni_4Fe_8F_{40}]$.

| Identification code | Ni-Fe-F | Cr-Fe-F |
|---|---|---|
| Empirical formula | $C_{18}HN_3F_{40.05}Fe_8Ni_4$ | $C_{18}H_{42}N_{1.5}F_{40}Cr_6Fe_6$ |
| Formula weight | 1700.80 | 1686.63 |
| Temperature/K | 110.15 | 110.15 |
| Crystal system | cubic | cubic |
| Space group | Im-3 | Im-3 |
| a/Å | 27.0487(19) | 27.197(18) |
| b/Å | 27.0487(19) | 27.197(18) |
| c/Å | 27.0487(19) | 27.197(18) |
| α/° | 90 | 90 |
| β/° | 90 | 90 |
| γ/° | 90 | 90 |
| Volume/Å$^3$ | 19790(4) | 20117(39) |
| Z | 8 | 8 |
| $\varrho_{calc}$g/cm$^3$ | 1.142 | 1.114 |
| μ/mm$^{-1}$ | 1.962 | 1.541 |
| F(000) | 6476.0 | 6564.0 |
| Crystal size/mm$^3$ | 0.250 × 0.250 × 0.170 | 0.308 × 0.29 × 0.235 |
| Radiation | MoKα (λ = 0.71073 Å) | MoKα (λ = 0.71073 Å) |
| 2Θ range for data collection/° | 3.012 to 43.914 | 2.118 to 46.374 |
| Index ranges | -27 ≤ h ≤ 28, -28 ≤ k ≤ 28, -28 ≤ l ≤ 4 | -30 ≤ h ≤ 29, -30 ≤ k ≤ 26, -30 ≤ l ≤ 25 |
| Reflections collected | 18690 | 41272 |
| Independent reflections | 2191 [$R_{int}$ = 0.0505, $R_{sigma}$ = 0.0271] | 2569 [$R_{int}$ = 0.0433, $R_{sigma}$ = 0.0166] |
| Data/restraints/parameters | 2191/0/90 | 2569/0/103 |
| Goodness-of-fit on F$^{2\ c}$ | 2.284 | 2.567 |
| Final R indexes [I>=2σ (I)] | $R_1{}^a$ = 0.0921, $wR_2{}^b$ = 0.2772 | $R_1{}^a$ = 0.0973, $wR_2{}^b$ = 0.2908 |
| Final R indexes [all data] | $R_1{}^a$ = 0.1018, $wR_2{}^b$ = 0.2859 | $R_1{}^a$ = 0.1058, $wR_2{}^b$ = 0.2996 |
| Largest diff. peak/hole / e Å$^{-3}$ | 1.15/-0.77 | 1.62/-1.10 |

$^a R_1 = \Sigma \left| \left| F_o \right| - \left| F_c \right| \right| / \Sigma \left| F_o \right|$. $^b wR_2 = \{\Sigma [w(F_o^2 - F_c^2)^2] / \Sigma w(F_o^2)^2]\}^{1/2}$. $^c$Goodness-of-fit $= \{\Sigma [w(F_o^2 - F_c^2)^2]/(n-p)\}^{1/2}$, where $n$ is the number of reflections and $p$ is the total number of parameters refined.

X-ray anomalous dispersion experiments were conducted on $(Et_4N)_8[V_4Fe_8F_{40}]$, $(Et_4N)_8[Co_4Fe_8F_{40}]$, and $(Et_4N)_8[Ni_4Fe_8F_{40}]$ using beam line 15-ID-B at the Advanced Photon Source, Argonne National Laboratory. A suitable crystal was mounted on a nylon loop with Paratone® oil and placed in a cold stream of $N_{2(g)}$ at 100 K. Data were collected at wavelengths of 0.41328 Å and 1.7433 Å (Fe K edge) for $(Et_4N)_8[V_4Fe_8F_{40}]$, 0.41328 Å, 1.6083 Å (Co K edge), and 1.7433 Å (Fe K edge) for $(Et_4N)_8[Co_4Fe_8F_{40}]$, and 0.41328 Å, 1.4879 Å (Ni K edge), and 1.7433 Å (Fe K edge) for $(Et_4N)_8[Ni_4Fe_8F_{40}]$. The frames were integrated with the Bruker APEXII software package[99] and a semi-empirical absorption correction was applied using SADABS as contained within the Bruker APEXII software suite. The structures were solved using SHELXS[100] and refined using SHELXL-2014[101] as implemented within ShelXle, a graphical interface for the SHELX suite of programs.[102] The dispersion corrections to the scattering factors for the elements at non-standard wavelengths were obtained from WinGX.[195] The 0.41328 Å data set was used for overall structure determination. After a suitable refinement was obtained the atomic coordinates of the 0.41328 Å structure were refined against the intensity data from the K edge data sets. The dispersion corrections for the metal edge of interest were left at the 0.41328 Å values; all others were adjusted to the values appropriate for the wavelength under study.

*Single Crystal Neutron Diffraction Measurements*

Single crystal neutron diffraction experiments on $(Et_4N)_8[V_4Fe_8F_{40}]$, $(Et_4N)_8[Cr_4Fe_8F_{40}]$, $(Et_4N)_8[Co_4Fe_8F_{40}]$, and $(Et_4N)_8[Ni_4Fe_8F_{40}]$ were conducted at the TOPAZ beam line (BL-12) at the Spallation Neutron Source, Oak Ridge National

Laboratory. A suitable crystal was mounted on a MiTeGen loop with an aluminum pin using Krytox™ grease and positioned onto the goniometer. Data collection was conducted at 100 K using neutrons with wavelengths in the range of 0.6 to 3.3 Å. Sample orientations were optimized with CRYSTALPLAN.[196] Data were collected with 21 detectors and used 11 crystal orientations, with collection times of approximately 8 h per sample orientation. The integrated raw Bragg intensities were obtained using the 3D ellipsoidal Q-space integration method.[197] Data reduction including Lorentz, absorption, time-of-flight spectrum, and detector efficiency corrections were carried out with the ANVRED3 program.[198] The reduced data were merged and saved in SHELX HKLF 4 format. Initial models were based on the single crystal X-ray diffraction refinement results, and the neutron refinements were carried out using SHELXL-2014.[101] ShelXle[102] was used as a graphical interface. Data collection on $(Et_4N)_8[Ni_4Fe_8F_{40}]$ did not finish before the allotted beam time was exhausted. Attempts were made to refine the $(Et_4N)_8[Ni_4Fe_8F_{40}]$ structure using the available data but were unsuccessful. Further pertinent details of the neutron refinements are given in Table 29.

**Table 29.** Neutron crystal and structural refinement data for the fluoride cages.

| | | |
|---|---|---|
| Identification code | V-Fe-F | Cr-Fe-F |
| Empirical formula | $C_{18}H_{42}N_{1.5}F_{41.35}V_{4.26}Fe_{7.8}$ | $C_{18}H_{48}N_{1.5}F_{35.35}Cr_{3.91}Fe_{8.07}O_6$ |
| Formula weight | 1718.28 | 1707.39 |
| Temperature/K | 100.15 | 100.15 |
| Crystal system | cubic | cubic |
| Space group | Im-3 | Im-3 |
| a/Å | 27.1661(11) | 27.190(19) |
| b/Å | 27.1661(11) | 27.190(19) |
| c/Å | 27.1661(11) | 27.190(19) |
| α/° | 90 | 90 |
| β/° | 90 | 90 |
| γ/° | 90 | 90 |
| Volume/Å$^3$ | 20048(2) | 20100(43) |
| Z | 8 | 8 |
| $\varrho_{calc}$g/cm$^3$ | 1.139 | 1.128 |
| μ/mm$^{-1}$ | 0.018 | 0.019 |
| F(000) | 6669.0 | 6691.0 |
| Crystal size/mm$^3$ | 1.3 × 1.3 × 1.1 | 1.5 × 1.5 × 1.3 |
| Radiation | neutrons (λ = 0.60 – 3.29 Å) | neutrons (λ = 0.60 – 3.29 Å) |
| 2Θ range for data collection/° | 2.756 to 21.62 | 4.238 to 37.73 |
| Index ranges | -24 ≤ h ≤ 24, -24 ≤ k ≤ 22, -23 ≤ l ≤ 24 | -21 ≤ h ≤ 24, -24 ≤ k ≤ 24, -23 ≤ l ≤ 21 |
| Reflections collected | 11955 | 10803 |
| Independent reflections | 1396 [$R_{int}$ = 0.1713, $R_{sigma}$ = 0.1078] | 1400 [$R_{int}$ = 0.1781, $R_{sigma}$ = 0.1297] |
| Data/restraints/parameters | 1396/76/64 | 1400/7/38 |
| Goodness-of-fit on F$^{2\ c}$ | 4.458 | 3.099 |
| Final R indexes [I>=2σ (I)] | $R_1{}^a$ = 0.3099, $wR_2{}^b$ = 0.5996 | $R_1{}^a$ = 0.2665, $wR_2{}^b$ = 0.4961 |
| Final R indexes [all data] | $R_1{}^a$ = 0.3138, $wR_2{}^b$ = 0.6011 | $R_1{}^a$ = 0.2757, $wR_2{}^b$ = 0.4979 |
| Largest diff. peak/hole / e Å$^{-3}$ | 1.79/-1.03 | 2.06/-0.89 |

**Table 29** Continued

| | |
|---|---|
| Identification code | Co-Fe-F |
| Empirical formula | $C_{18}H_{47.52}N_{1.5}O_{5.53}F_{35.8}Fe_{7.97}Co_{4.04}$ |
| Formula weight | 1737.00 |
| Temperature/K | 100.15 |
| Crystal system | cubic |
| Space group | Im-3 |
| a/Å | 27.0709(14) |
| b/Å | 27.0709(14) |
| c/Å | 27.0709(14) |
| α/° | 90 |
| β/° | 90 |
| γ/° | 90 |
| Volume/Å$^3$ | 19838(3) |
| Z | 8 |
| $\varrho_{calc}$g/cm$^3$ | 1.163 |
| μ/mm$^{-1}$ | 0.019 |
| F(000) | 6790.0 |
| Crystal size/mm$^3$ | 1.5 × 1.5 × 1.0 |
| Radiation | neutrons (λ = 0.60 – 3.29 Å) |
| 2Θ range for data collection/° | 2.474 to 21.662 |
| Index ranges | -23 ≤ h ≤ 24, -24 ≤ k ≤ 24, -24 ≤ l ≤ 24 |
| Reflections collected | 12636 |
| Independent reflections | 1406 [$R_{int}$ = 0.1797, $R_{sigma}$ = 0.1380] |
| Data/restraints/parameters | 1406/78/134 |
| Goodness-of-fit on F$^2$ [c] | 2.906 |
| Final R indexes [I>=2σ (I)] | $R_1$[a] = 0.2501, $wR_2$[b] = 0.4654 |
| Final R indexes [all data] | $R_1$[a] = 0.2566, $wR_2$[b] = 0.4672 |
| Largest diff. peak/hole / e Å$^{-3}$ | 1.16/-0.95 |

[a]$R_1 = \Sigma \big| \, |F_o| - |F_c| \, \big| / \Sigma |F_o|$. [b]$wR_2 = \{\Sigma [w(F_o^2 - F_c^2)^2] / \Sigma w(F_o^2)^2]\}^{1/2}$. [c]Goodness-of-fit $= \{\Sigma [w(F_o^2 - F_c^2)^2]/(n-p)\}^{1/2}$, where $n$ is the number of reflections and $p$ is the total number of parameters refined.

**Results and Discussion**

*Syntheses*

The syntheses of all of the members of the cage family are similar. The starting materials and final products are generally air- and water-sensitive. Another member of the family, namely $(Et_4N)_8[Cr_4Fe_8F_{40}]$, was added in this work so that in conjunction with the $(Et_4N)_3[Fe_2F_9]$ precursor the cage molecules were prepared for all divalent first row transition metals from vanadium to zinc, with the exception of $Mn^{II}$. There is preliminary crystallographic evidence that $Mn^{II}$ does form the same type of cage molecule but the X-ray data are not of a sufficient quality to be definitive. The synthesis of the cage molecules proceeds regardless of the source of the divalent metal. The majority of the syntheses were performed with $[BF_4]^-$ salts of the divalent metal; Xinyi Wang was able to synthesize the $(Et_4N)_8[Cu_4Fe_8F_{40}]$ cage using $CuBr_2$ and use of either $ZnI_2$ or $[Zn(CH_3CN)_4](BF_4)_2$ produced crystals of $(Et_4N)_8[Zn_4Fe_8F_{40}]$. In the current work, it was shown that either $[Ni(CH_3CN)_6](BF_4)_2$ or $[Ni(CH_3CN)_6](SbF_6)_2$ can be used to synthesize $(Et_4N)_8[Ni_4Fe_8F_{40}]$. It is possible to grow crystals of the cages in bulk in a Schlenk tube instead of multiple thin tubes as long as a large enough $CH_3CN$:DMF layer is used. A typical yield from thin tube crystallization is approximately 30%. The yield from bulk layering crystallizations is similar. The $(Et_4N)_8[Fe_4Fe_8F_{40}]$ analog has proven to be the most difficult for the growth of bulk crystals.

Attempts to synthesize derivatives of the cage with a lower crystal symmetry have proven to be unsuccessful. Previous work from our group has shown that reacting $FeCl_2$ with two equivalents of tmphen (tmphen = 3,4,7,8-tetramethyl-1,10-

phenanthroline) results in a solution of "$[Fe(tmphen)_2]^{2+}$" that can then be used directly as a reactive precursor for the synthesis of trigonal bipyramidal molecules.[199] In this vein, $[Fe(CH_3CN)_6][BF_4]_2$ was reacted with two equivalents of tmphen in a 3:1 $CH_3CN$:DMF mixed solvent system. This solution, assumed to contain $[Fe(tmphen)_2(solvent)_2]^{2+}$, was then reacted with a $CH_3CN$ solution of $(Et_4N)_3[Fe_2F_9]$ and layered in thin tubes in a manner analogous to that used to form the polyfluorometallate cages. The goal was to make a derivative of the cage unit with tmphen, which would serve two functions. Assuming the tmphen remained coordinated to the $Fe^{II}$ ions it would then be easier to differentiate the $Fe^{II}$ and $Fe^{III}$ ions in the crystal structure. Also, the cage derivative would most likely crystallize in a crystal system of lower than cubic symmetry, which would diminish the disorder problems for the $[Et_4N]^+$ counter ions. After three weeks reddish-brown crystals were observed in the thin tubes. Single crystal X-ray diffraction analysis provided no evidence of tmphen in the crystal. Remarkably, the product is the same $(Et_4N)_8[Fe_4Fe_8F_{40}]$ cage product that forms in the absence of tmphen.

Post-synthetic metathesis of the $[Et_4N]^+$ counterion with a large cation that would be easier to locate in the crystal structure and perhaps lead to a lowering of the crystallographic symmetry also proved unsuccessful. Once formed, the crystals of the cage molecules are only very sparingly soluble in all solvents investigated. Due to the solubility issues, attempts were also made to incorporate a larger anion directly during the synthesis of the cages. Large excesses of $[AsPh_4](BF_4)$ or $[MePPh_3](BF_4)$ were included in the solution of the divalent metal precursor and bulk layering reactions were

performed. No crystalline material was obtained from these reactions but IR analysis of the resulting solid was consistent with the formation of the $[Et_4N]^+$ salts of the cages with no evidence of resonances from $[AsPh_4]^+$ or $[MePPh_3]^+$ cations.

*Infrared Spectroscopy*

The IR spectra of $(Et_4N)_8[Cr_4Fe_8F_{40}]$, $(Et_4N)_8[Fe_4Fe_8F_{40}]$, and $(Et_4N)_8[Zn_4Fe_8F_{40}]$ all have a stretching frequency at approximately 3542 $cm^{-1}$, indicative of an $[OH]^-$ stretch. All three spectra also contain resonances at approximately 2250 $cm^{-1}$ and 1650 $cm^{-1}$, consistent with the C≡N stretching mode of $CH_3CN$ and the carbonyl stretching mode of DMF, respectively. These data indicate that the crystals of $(Et_4N)_8[Cr_4Fe_8F_{40}]$, $(Et_4N)_8[Fe_4Fe_8F_{40}]$, and $(Et_4N)_8[Zn_4Fe_8F_{40}]$ contain $CH_3CN$ and DMF solvent molecules and at least partial substitution of $[F]^-$ ligands for $[OH]^-$.

*Single Crystal X-ray Diffraction*

All of the cage molecules crystallize in the cubic space group $Im\bar{3}$ with eight cages in the unit cell. Every crystal of these compounds that was investigated was found to be merohedrally twinned by a two-fold rotation about [110] and twin fractions of approximately 0.5:0.5, indicating almost perfect merohedral twinning. For simplicity, the following discussion will focus on the $(Et_4N)_8[Ni_4Fe_8F_{40}]$ analog as a representative example of the refinement strategy for all of the structures. Two metal atom sites are crystallographically unique and reside on general positions, for a total of 96 metal atom sites in the unit cell. The fluoride ligands reside on general and special positions.

The $[Et_4N]^+$ cation that can be located in the structure was found to be disordered between two positions, with each position additionally disordered across a mirror plane. The ratio between the two symmetry independent orientations was allowed to refine freely and converged to 0.63:0.37 for the two orientations. Each of the two heavy atom sites is partially occupied by $Ni^{II}$ and $Fe^{III}$. The site occupancy for each position was fixed at 0.666 $Fe^{III}$ and 0.333 $Ni^{II}$ to establish the 2:1 ratio Xinyi determined by ICP-MS and NAA. The atomic coordinates of the $Ni^{II}$ and $Fe^{III}$ ions were initially constrained to be the same but during later stages of the refinement this constraint was released to allow the metal atoms to occupy slightly different locations in the unit cell. The bridging fluoride ligands are disordered between two positions. One position results in Fe-F bond lengths of approximately 1.8 Å, appropriate for a bridging $Fe^{III}$-F-$Fe^{III}$ bond. The second position results in bond lengths of approximately 2.1 Å, appropriate for a bridging $Ni^{II}$-F-$Ni^{II}$ bond. Initially the site occupancy of the two bridging fluoride sites was fixed at 0.5. The terminal fluoride ligands were modeled as disordered over two positions, both with a fixed occupancy of 0.5. At this point the structural refinement was found to be stable. The site occupancy of the disordered fluoride ligands was then allowed to freely refine, with the occupancy of all of the positions corresponding to 1.8 Å bridging bond distances constrained to be equal and likewise for all of the positions corresponding to 2.1 Å bridging bond distances. The total occupancy was constrained to 1.0. The site occupancy converged to a value of approximately 0.55:0.45 for the sites corresponding to $Fe^{III}$ coordination and $Ni^{II}$ coordination, respectively. The other members of the family displayed similar site

occupancies when freely refining the fluoride occupancies. At this point the metal atoms and fluoride ligands could be refined anisotropically. The $[Et_4N]^+$ cation could only be refined isotropically. This refinement strategy led to decent final refinement parameters, with an $R_1$ value of 9.2%. Figure 69 displays a thermal ellipsoid plot of the disordered anionic cage, as well as views of the Fe and Ni components. Figure 70 displays the atom numbering scheme for the asymmetric unit and Table 30 lists bond distances and angles.

Large voids of disordered electron density were still present in the structure at this stage. This residual density could not be refined as additional $[Et_4N]^+$ cations, even with numerous constraints and restraints. The residual density also could not be refined as $CH_3CN$ or DMF, the two solvents identified by IR spectroscopy. In an attempt to determine the identity of the molecules contained in this void space, the PLATON program SQUEEZE[120] was used to remove this residual density. The $[Et_4N]^+$ cation that could be located was removed prior to running SQUEEZE so that the only assigned density was due to the cage molecule. Using this approach SQUEEZE removed a total of 7435 electrons from the 13,978 $Å^3$ of void space found in the unit cell. These values are consistent with 8 $[Et_4N]^+$ cations, 4 $CH_3CN$ molecules, and 6 DMF molecules per cage. This is not a unique solution, though. Calculations involving as few as 6 $[Et_4N]^+$ cations and 15-20 solvent molecules per cage also give total electron and void space values close to those removed by SQUEEZE. It is encouraging, nonetheless, that the available void space and residual electron density support at least 8 $[Et_4N]^+$ cations, enough to balance the charge of a $[Ni^{II}_4Fe^{III}_8F_{40}]^{8-}$ formula.

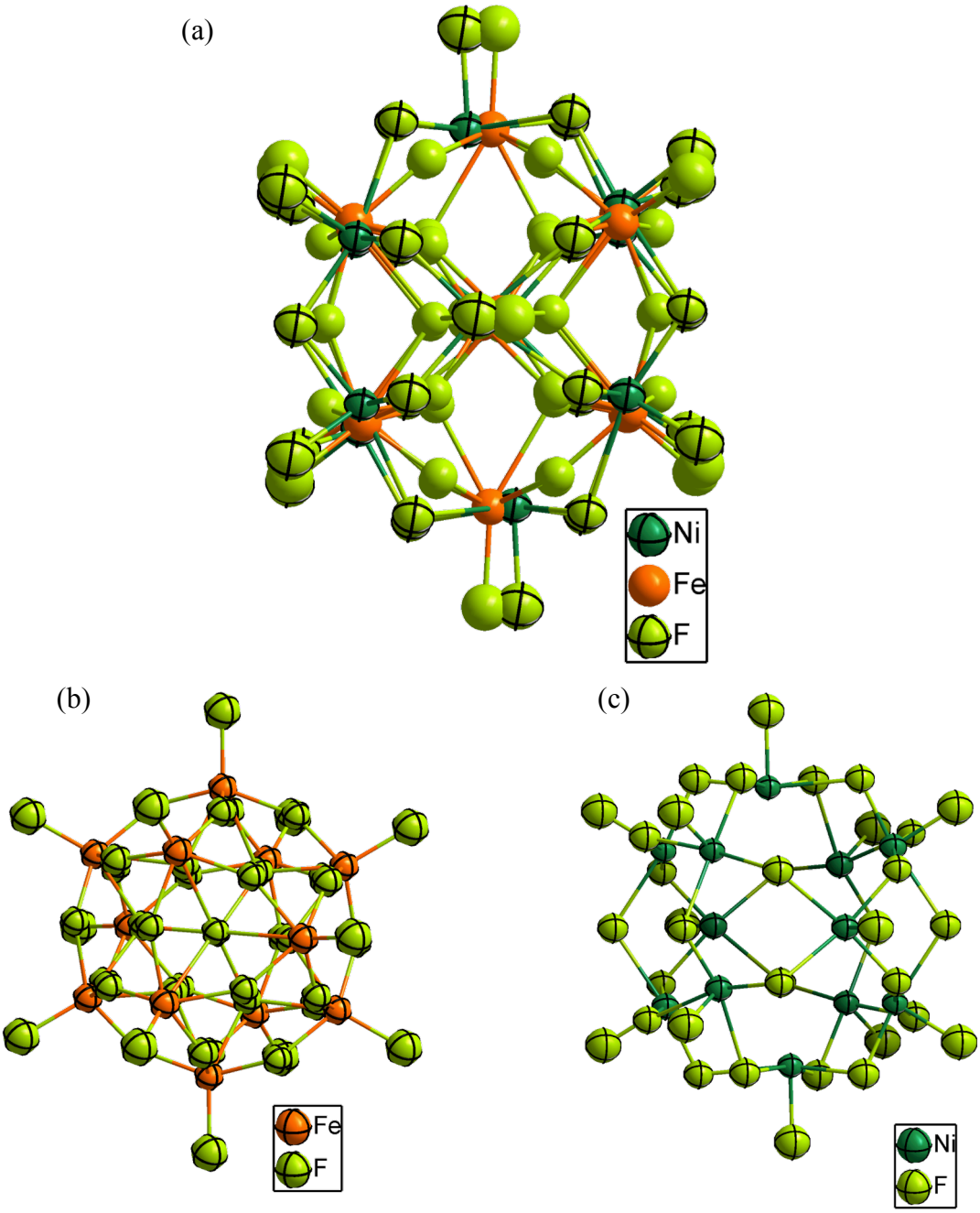


**Figure 69.** Structure of $(Et_4N)_n[Ni_4Fe_8F_{40}]$. Ellipsoids are drawn at the 50% probability level. (a) disordered model of the structure. Ni ions and the $[F]^-$ ligands bound to Ni are drawn as thermal ellipsoids. Fe ions and the $[F]^-$ ligands bound to Fe are drawn as spheres. (b) thermal ellipsoid plot of the Fe-F connectivity. (c) thermal ellipsoid plot of the Ni-F connectivity.

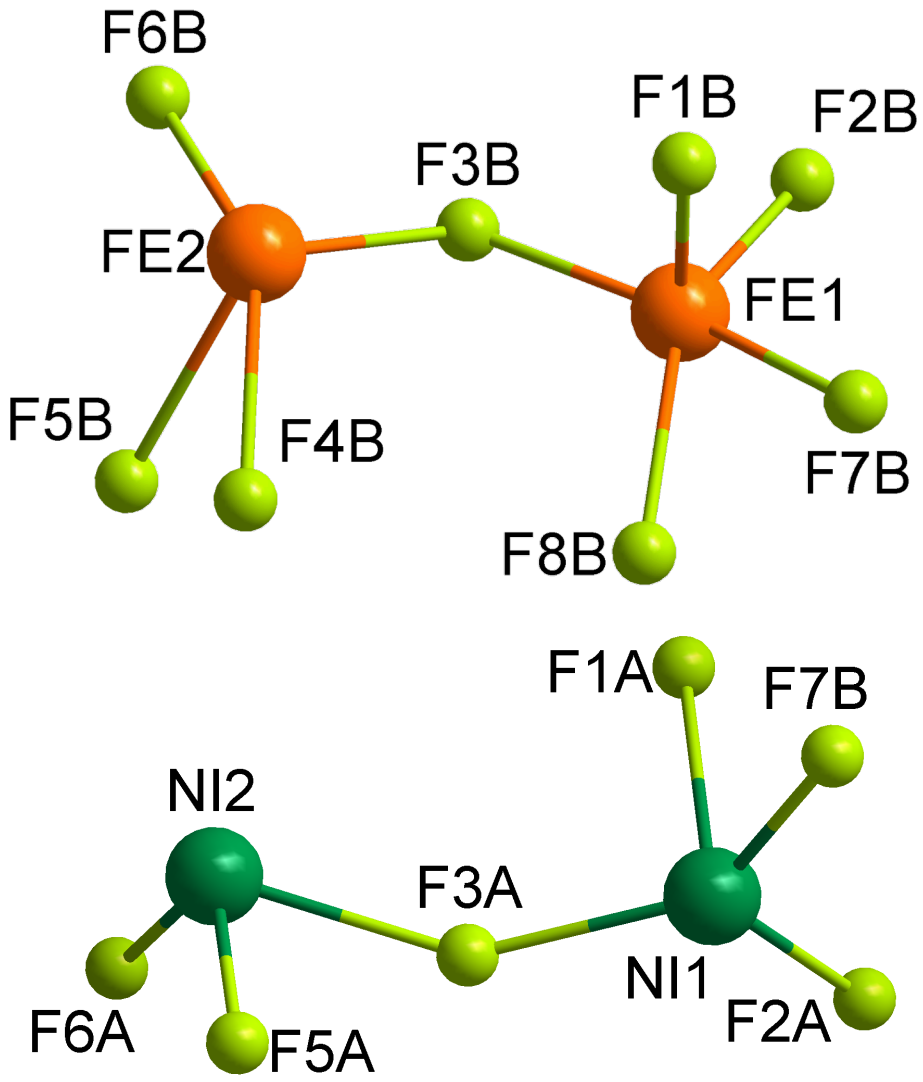


**Figure 70.** Atom numbering scheme for the asymmetric unit of $(Et_4N)_n[Ni_4Fe_8F_{40}]$. The asymmetric unit is separated into the iron and nickel sections for the sake of clarity.

**Table 30.** Bond distances and angles for $(Et_4N)_n[Ni_4Fe_8F_{40}]$.

| Atom | Atom | Length/Å | Atom | Atom | Length/Å |
|---|---|---|---|---|---|
| Ni1 | F1A | 2.327(17) | F7B | Ni1[4] | 1.658(15) |
| Ni1 | F2A | 1.87(2) | F1B | Fe2[2] | 1.923(15) |
| Ni1 | F3A | 1.985(15) | F5B | Fe2[3] | 2.012(15) |
| Ni1 | F7B[1] | 1.659(15) | F7A | Fe1[4] | 2.265(16) |
| Ni1 | F7B | 1.689(15) | F8B | Fe1[4] | 2.278(9) |
| Fe1 | F1B | 1.774(15) | F8B | Fe1[1] | 2.281(9) |
| Fe1 | F2B | 1.85(2) | F4B | Fe1[3] | 2.122(14) |
| Fe1 | F3B | 1.945(16) | F4B | Fe2[3] | 2.103(13) |
| Fe1 | F7A | 2.236(17) | N1A | C1A | 1.530(19) |
| Fe1 | F7A[1] | 2.265(16) | N1A | C3A | 1.528(19) |
| Fe1 | F8B | 2.282(9) | N1A | C4A | 1.508(18) |
| Fe1 | F4B[2] | 2.122(14) | N1A | C5A | 1.518(18) |
| Ni2 | F1A[3] | 1.874(16) | C1A | C2A | 1.70(2) |
| Ni2 | F3A | 2.015(15) | C3A | C7A | 1.82(2) |
| Ni2 | F5A[2] | 1.990(13) | C4A | C8A | 1.71(2) |
| Ni2 | F5A | 1.697(13) | C5A | C6A | 1.72(2) |
| Ni2 | F6A | 1.82(2) | N1B | C1B | 1.27(3) |
| Fe2 | F1B[3] | 1.923(15) | N1B | C3B | 1.54(3) |
| Fe2 | F3B | 1.962(15) | N1B | C5B | 1.59(4) |
| Fe2 | F5B | 2.238(14) | N1B | C7B | 1.62(4) |
| Fe2 | F5B[2] | 2.012(15) | C1B | C2B | 1.69(4) |
| Fe2 | F6B | 1.84(2) | C1B | C5B | 1.93(4) |
| Fe2 | F4B[2] | 2.103(13) | C1B | C6B | 1.92(4) |
| Fe2 | F4B | 2.281(13) | C3B | C4B | 1.50(3) |
| F1A | Ni2[2] | 1.874(16) | C5B | C6B | 1.32(3) |
| F5A | Ni2[3] | 1.990(13) | C7B | C8B | 1.67(4) |

[1]+Z,+X,+Y; [2]3/2-Z,3/2-X,3/2-Y; [3]3/2-Y,3/2-Z,3/2-X; [4]+Y,+Z,+X

| Atom | Atom | Atom | Angle/° | Atom | Atom | Atom | Angle/° |
|---|---|---|---|---|---|---|---|
| F2A | Ni1 | F1A | 85.7(8) | F5B | Fe2 | F4B | 69.4(5) |
| F2A | Ni1 | F3A | 108.2(9) | F5B[2] | Fe2 | F4B[2] | 77.4(5) |
| F3A | Ni1 | F1A | 84.7(6) | F6B | Fe2 | F1B[3] | 108.0(9) |

**Table 30** Continued

| Atom | Atom | Atom | Angle/° | Atom | Atom | Atom | Angle/° |
|---|---|---|---|---|---|---|---|
| F7B | Ni1 | F1A | 86.8(6) | F6B | Fe2 | F3B | 83.0(9) |
| F7B[1] | Ni1 | F1A | 155.1(7) | F6B | Fe2 | F5B[2] | 79.6(9) |
| F7B | Ni1 | F2A | 106.8(9) | F6B | Fe2 | F5B | 89.5(7) |
| F7B[1] | Ni1 | F2A | 108.3(9) | F6B | Fe2 | F4B[2] | 149.3(8) |
| F7B | Ni1 | F3A | 143.2(7) | F6B | Fe2 | F4B | 152.2(8) |
| F7B[1] | Ni1 | F3A | 71.5(7) | F4B[2] | Fe2 | F5B | 115.2(5) |
| F7B[1] | Ni1 | F7B | 107.7(9) | F4B[2] | Fe2 | F4B | 58.4(6) |
| F1B | Fe1 | F2B | 101.6(8) | Ni2[2] | F1A | Ni1 | 108.2(8) |
| F1B | Fe1 | F3B | 102.0(7) | Ni1 | F3A | Ni2 | 146.5(8) |
| F1B | Fe1 | F7A[1] | 158.4(7) | Ni2 | F5A | Ni2[3] | 139.6(8) |
| F1B | Fe1 | F7A | 86.1(6) | Ni1[4] | F7B | Ni1 | 132.1(9) |
| F1B | Fe1 | F8B | 91.4(7) | Fe1 | F1B | Fe2[2] | 137.5(8) |
| F1B | Fe1 | F4B[2] | 60.5(6) | Fe1 | F3B | Fe2 | 109.4(8) |
| F2B | Fe1 | F3B | 83.8(9) | Fe2[3] | F5B | Fe2 | 108.0(7) |
| F2B | Fe1 | F7A[1] | 91.0(8) | Fe1 | F7A | Fe1[4] | 108.6(8) |
| F2B | Fe1 | F7A | 86.3(8) | Fe1[4] | F8B | Fe1[1] | 106.6(6) |
| F2B | Fe1 | F8B | 152.7(10) | Fe1 | F8B | Fe1[4] | 106.6(6) |
| F2B | Fe1 | F4B[2] | 148.6(9) | Fe1 | F8B | Fe1[1] | 106.5(6) |
| F3B | Fe1 | F7A[1] | 96.7(6) | Fe1[3] | F4B | Fe2 | 103.0(5) |
| F3B | Fe1 | F7A | 168.3(7) | Fe2[3] | F4B | Fe1[3] | 98.0(5) |
| F3B | Fe1 | F8B | 117.0(6) | Fe2[3] | F4B | Fe2 | 103.4(5) |
| F3B | Fe1 | F4B[2] | 76.0(6) | C3A | N1A | C1A | 102.8 |
| F7A | Fe1 | F7A[1] | 77.3(8) | C4A | N1A | C1A | 132.2 |
| F7A[1] | Fe1 | F8B | 70.2(6) | C4A | N1A | C3A | 98.5 |
| F7A | Fe1 | F8B | 70.7(6) | C4A | N1A | C5A | 91.1 |
| F4B[2] | Fe1 | F7A[1] | 114.7(6) | C5A | N1A | C1A | 106.7 |
| F4B[2] | Fe1 | F7A | 115.5(6) | C5A | N1A | C3A | 129.5 |
| F4B[2] | Fe1 | F8B | 58.3(6) | N1A | C1A | C2A | 116.2 |
| F1A[3] | Ni2 | F3A | 169.8(7) | N1A | C3A | C7A | 101.4 |
| F1A[3] | Ni2 | F5A[2] | 90.7(7) | N1A | C4A | C8A | 98.4 |
| F5A | Ni2 | F1A[3] | 107.9(7) | N1A | C5A | C6A | 107.9 |
| F5A | Ni2 | F3A | 70.1(6) | C1B | N1B | C3B | 113.1 |
| F5A[2] | Ni2 | F3A | 86.0(6) | C1B | N1B | C5B | 84.1 |

**Table 30** Continued

| Atom | Atom | Atom | Angle/° | Atom | Atom | Atom | Angle/° |
|---|---|---|---|---|---|---|---|
| F5A | Ni2 | F5A[2] | 143.1(9) | C1B | N1B | C7B | 150.4 |
| F5A | Ni2 | F6A | 107.7(9) | C3B | N1B | C5B | 130.7 |
| F6A | Ni2 | F1A[3] | 83.0(9) | C3B | N1B | C7B | 89.2 |
| F6A | Ni2 | F3A | 107.2(9) | C5B | N1B | C7B | 96.2 |
| F6A | Ni2 | F5A[2] | 105.9(9) | N1B | C1B | C2B | 104.3 |
| F1B[3] | Fe2 | F3B | 167.4(7) | N1B | C1B | C5B | 55.1 |
| F1B[3] | Fe2 | F5B[2] | 88.1(6) | N1B | C1B | C6B | 86.0 |
| F1B[3] | Fe2 | F5B | 88.7(6) | C2B | C1B | C5B | 81.5 |
| F1B[3] | Fe2 | F4B | 55.6(5) | C2B | C1B | C6B | 97.0 |
| F1B[3] | Fe2 | F4B[2] | 91.3(6) | C6B | C1B | C5B | 40.0 |
| F3B | Fe2 | F5B[2] | 87.7(6) | C4B | C3B | N1B | 118.6 |
| F3B | Fe2 | F5B | 97.9(6) | N1B | C5B | C1B | 40.8 |
| F3B | Fe2 | F4B | 116.7(6) | C6B | C5B | N1B | 99.4 |
| F3B | Fe2 | F4B[2] | 76.1(6) | C6B | C5B | C1B | 69.6 |
| F5B[2] | Fe2 | F5B | 167.1(6) | C5B | C6B | C1B | 70.4 |
| F5B[2] | Fe2 | F4B | 118.3(6) | N1B | C7B | C8B | 108.2 |

[1]+Z,+X,+Y; [2]3/2-Z,3/2-X,3/2-Y; [3]3/2-Y,3/2-Z,3/2-X; [4]+Y,+Z,+X

*Anomalous Dispersion X-ray Experiments*

The goal of this study was to determine if one of the metal ions in the mixed-metal cages occupied one of the heavy atom sites preferentially over the other. The similarity in X-ray scattering factors between the first row transition metals makes refining the site occupancy of the heavy atom sites problematic and, ultimately, unreliable. X-ray Anomalous Dispersion, a technique that has been used to quantitatively determine the site occupancy in mixed-metal Kagomé-type compounds,[200] zinc-doped gallium phosphates,[201] heterobimetallic Mn, Fe, and Co

complexes,[202] and a mixed Mn-Ti perovskite,[203] takes advantage of the ability of synchrotrons to produce X-rays of variable wavelength. When single crystal X-ray diffraction data is collected at a wavelength that corresponds to the K edge absorption energy of the atom of interest that atom will no longer contribute to the diffraction pattern. Instead, it will absorb most of the incoming X-ray radiation. This absorption leads to the appearance of regions of negative electron density, or "holes", in the difference Fourier map that can be used to determine the location of the atom type of interest. Previous studies of this type have led to quantitative determination of site occupancy. The accuracy of such determinations is largely dependent on the quality of the starting model. Due to the large regions of disordered electron density in the cage structures no attempts to perform a quantitative site occupancy determination were undertaken; the results presented here are qualitative in nature.

**$(Et_4N)_8[V_4Fe_8F_{40}]$.** Data were collected at X-ray wavelengths of 0.41328 Å and 1.7433 Å (Fe K edge). The vanadium K edge is not an accessible wavelength at this beam line so only iron K edge data were collected; 0.41328 Å is far from the absorption edge of any element in the sample and data collected at this wavelength were refined in a manner analogous to that described above for the refinement of $(Et_4N)_8[Ni_4Fe_8F_{40}]$ using data collected on a Bruker APEXII diffractometer. This model was used as the starting point for the refinement of the data collected at the Fe K edge wavelength. The results of the Fe edge refinement are shown in Figure 71. Only the asymmetric unit is pictured for simplicity. The red surfaces denote regions of negative residual density, or

"holes". The negative surfaces appear to be equally distributed between the sites labeled Fe1 and Fe2, indicating no preference for one site over the other.

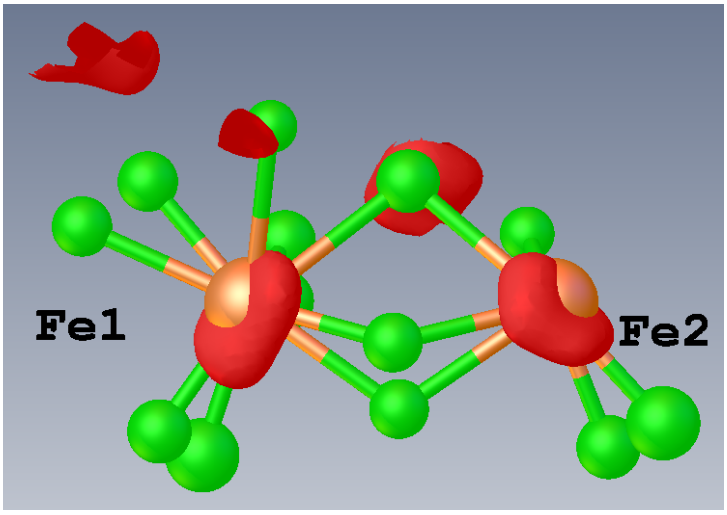


**Figure 71.** Difference map of $(Et_4N)_8[V_4Fe_8F_{40}]$ as refined against the Fe K edge data. The red surface represents areas of negative electron density. The surface contour is drawn at the -2.2 e/Å$^3$ level.

**$(Et_4N)_8[Co_4Fe_8F_{40}]$.** Data were collected at X-ray wavelengths of 0.41328 Å, 1.6083 Å (cobalt K edge), and 1.7433 Å (iron K edge). As was the case for $(Et_4N)_8[V_4Fe_8F_{40}]$, the 0.41328 Å model was used as the starting point for the refinement of the data collected at the iron and cobalt K edge wavelengths. The results of the Fe edge refinement are shown in Figure 72a. There is significant negative density at both the Fe1 and Fe2 sites. There might be a slight preference for the Fe1 site but that cannot be determined definitively. The results of the Co edge refinement are shown in Figure 72b. The larger negative density surface associated with the Co2 site is consistent with a higher percentage of Co character at the Co2 site as compared to the Co1 site.

(a)

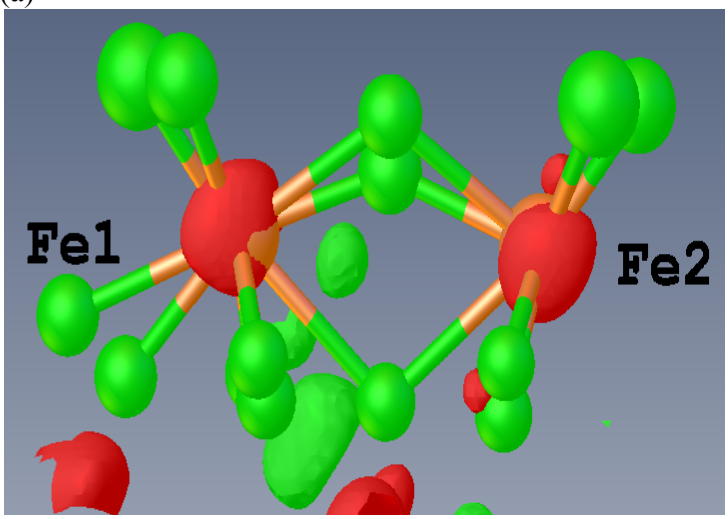


(b)

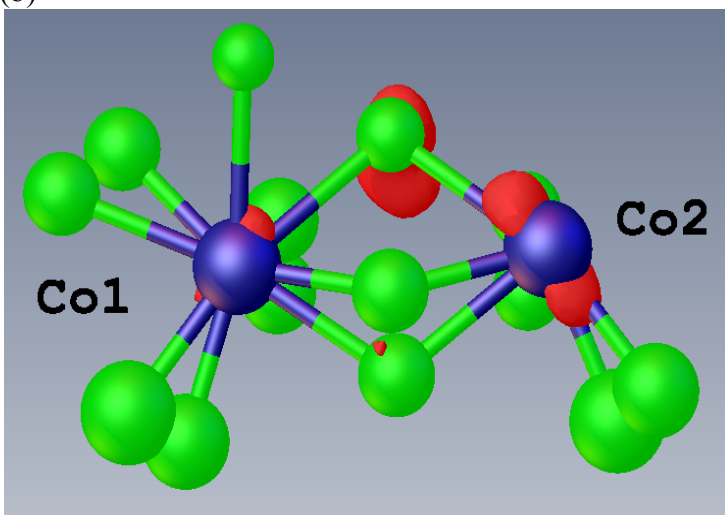


**Figure 72.** Difference map of $(Et_4N)_8[Co_4Fe_8F_{40}]$. (a) as refined against the Fe K edge data. The red surface represents areas of negative electron density. The surface contour is drawn at the -5.2 e/Å$^3$ level. (b) as refined against the Co K edge data. The red surface represents areas of negative electron density. The surface contour is drawn at the -2.4 e/Å$^3$ level.

**$(Et_4N)_8[Ni_4Fe_8F_{40}]$.** Data were collected at X-ray wavelengths of 0.41328 Å, 1.4879 Å (nickel K edge), and 1.7433 Å (iron K edge). As for $(Et_4N)_8[V_4Fe_8F_{40}]$, the 0.41328 Å model was used as the starting point for the refinement of the data collected at the iron and nickel K edge wavelengths. The results of the Fe edge refinement are shown in Figure 73a. There is significant negative density at both the Fe1 and Fe2 sites. There is less negative density at the Fe1 site compared to Fe2, indicating a preference for iron to locate at the Fe2 site. The results of the Ni edge refinement are shown in Figure 73b. There does not seem to be a preference for Ni to locate at one site over the other.

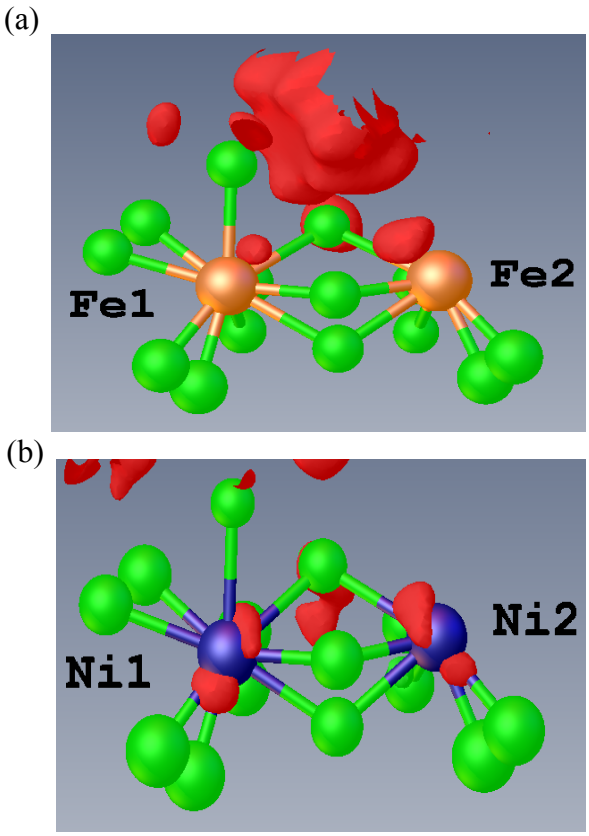


**Figure 73.** Difference map of $(Et_4N)_8[Ni_4Fe_8F_{40}]$. (a) as refined against the Fe K edge data. The red surface represents areas of negative electron density. The surface contour is drawn at the -7.7 e/Å$^3$ level. (b) as refined against the Ni K edge data. The red surface represents areas of negative electron density. The surface contour is drawn at the -2.4 e/Å$^3$ level.

*Single Crystal Neutron Diffraction Experiments*

Unlike X-ray scattering factors, neutron scattering lengths do not scale with atomic number. Instead, they vary somewhat randomly across the periodic table. For example, carbon and nitrogen diffract neutrons almost as strongly as iron. This makes neutron diffraction ideally suited to gain additional information about the location of metal atoms in the fluoride cage molecules. It was our hope that the increased scattering power of carbon and nitrogen would also assist in locating additional $[Et_4N]^+$ cations in the structure. Structural determination from neutron diffraction has the added benefit of being able to confidently locate protons in the structure. Ideally, crystals used for neutron diffraction have a low hydrogen content to minimize background noise due to the large incoherent scattering cross section of hydrogen. Preferably, hydrogen is replaced by deuterium for neutron diffraction; deuterium has a very low incoherent scattering cross section. The fluoride cages are less than ideal in this sense, containing roughly 40 atom percent hydrogen that was not able to be replaced by deuterium. As such, the neutron diffraction data has a large incoherent background, which limits the quality of the data sets obtained but some general conclusions can still be drawn.

**$(Et_4N)_8[V_4Fe_8F_{40}]$.** Of the data sets that were able to be refined, $(Et_4N)_8[V_4Fe_8F_{40}]$ provides the least useful information. Vanadium is not a strong scatterer of neutrons. The absence of diffraction can still be used to refine the site occupancy of vanadium, but a positional constraint had to be used to keep the x, y, z coordinates of the vanadium atom the same as the corresponding iron atom. If this constraint was removed the vanadium atom's position diverged, making the refinement unstable. Each heavy atom

site was partially occupied by vanadium and partially occupied by iron, resulting in a total of four free variables being used to describe the metal content of the cage. Site occupancy constraints were used to constrain the total occupancy of each of the heavy atom sites to 1 and the V:Fe ratio to 1:2, the ratio established by ICP-MS and NAA for $(Et_4N)_8[Co_4Fe_8F_{40}]$ and $(Et_4N)_8[Ni_4Fe_8F_{40}]$. The site occupancy restraints were formulated in such a way that the total charge of the two heavy atom sites was +5.333, the charge expected from a 2:1 ratio of $Fe^{III}$ to $V^{II}$. While there is no direct evidence that the charge of the metal atoms remains the same throughout the formation of the cage molecules, there is also no evidence that a change in oxidation state of either metal has occurred. As such, the refinements proceeded on the assumption that $V^{II}$ remains $V^{II}$ and $Fe^{III}$ remains $Fe^{III}$. After several refinement cycles, one of the heavy atom positions converged to 64% iron and 36% vanadium, with the other heavy atom site being occupied by 66% iron and 34% vanadium. The fluoride ligand disorder was modeled in the same manner as in the X-ray structures. Only the one $[Et_4N]^+$ cation that could be refined in the X-ray structure was visible in the neutron data.

**$(Et_4N)_8[Cr_4Fe_8F_{40}]$**. The data obtained for $(Et_4N)_8[Cr_4Fe_8F_{40}]$ are of somewhat higher quality than the V-Fe analog due to the increased scattering power of chromium. The scattering power of iron is approximately 2.5 times that of chromium, providing good contrast between the two metals. The data still suffers from a high hydrogen background, which limits the overall resolution of the data set. The refinement of the site occupancy of the heavy atom sites was conducted in a manner analogous to that described for $(Et_4N)_8[V_4Fe_8F_{40}]$. Initially a positional restraint was used to maintain the

coordinates of the crystallographically equivalent metal atoms the same. Later in the refinement this constraint was removed. The metal atoms did not shift positions nearly as dramatically as in the V-Fe analog but, overall, the refinement was more stable if this constraint was kept. After several refinement cycles, one of the heavy atom positions converged to 58% iron and 42% chromium, with the other heavy atom site being occupied by 76% iron and 24% chromium. The fluoride ligand disorder was modeled in the same manner as in the X-ray structures. Similar to $(Et_4N)_8[V_4Fe_8F_{40}]$, no additional $[Et_4N]^+$ cations could be located in the structure.

Although a low hydrogen content is preferred for neutron diffraction studies, there is one characteristic of hydrogen that makes it appealing to use hydrogenated samples – hydrogen has a negative neutron scattering length. This has the effect of protons producing negative observed intensity in the diffraction experiment. Normally, X-ray diffraction is not ideal for differentiating an $[F]^-$ ligand from $[OH]^-$ due to their similarity in electron density. Neutron diffraction does not have this limitation. Even though the neutron scattering power of oxygen and fluorine are very similar, a proton is easily located in the structure because it appears as a region of negative density. Upon completion of the refinement of the metal site occupancy, modeling of the fluoride ligand disorder, and refinement of the one $[Et_4N]^+$ cation that could be located, an examination of the $F_{obs}$ map revealed significant negative density near both positions of one of the disordered bridging fluoride ligands. This negative density was in a reasonable position for an $[OH]^-$ proton. Attempts to refine these positions as mixed $[F]^-$ /$[OH]^-$ occupancy were unsuccessful. The best structural model that could be obtained

had both of these positions occupied as $[OH]^-$ ligands with 50% occupation of each position. This result is consistent with the IR data (*vide supra*). A bond distance restraint was used to restrict the O-H bond to a reasonable distance. Figure 74a displays the $F_{obs}$ map, highlighting the negative density surrounding the $[OH]^-$ protons. Figure 74b displays the anionic cage, emphasizing the positions of the $[OH]^-$ ligands. Based on these results, the best formula for this cage is found to be $(Et_4N)_9[Cr_4Fe_8F_{35}(OH)_6]$.

What is difficult at this stage of the problem is the lack of consistency between the proposed formula and the C, H, N, F, and O elemental analysis. The current elemental analysis results for $(Et_4N)_9[Cr_4Fe_8F_{35}(OH)_6]$ are consistent with what Dr. Xinyi Wang obtained for the $[Fe_{12}F_{40}]^{n-}$, $[Co_4Fe_8F_{40}]^{n-}$, and $[Ni_4Fe_8F_{40}]^{n-}$ analogs. There is a large disparity between the expected and found values for all of the elements analyzed. This discrepancy cannot be resolved by assuming some DMF and/or $CH_3CN$ molecules were lost from the crystal prior to the elemental analysis being performed and remains unexplained.

(a)

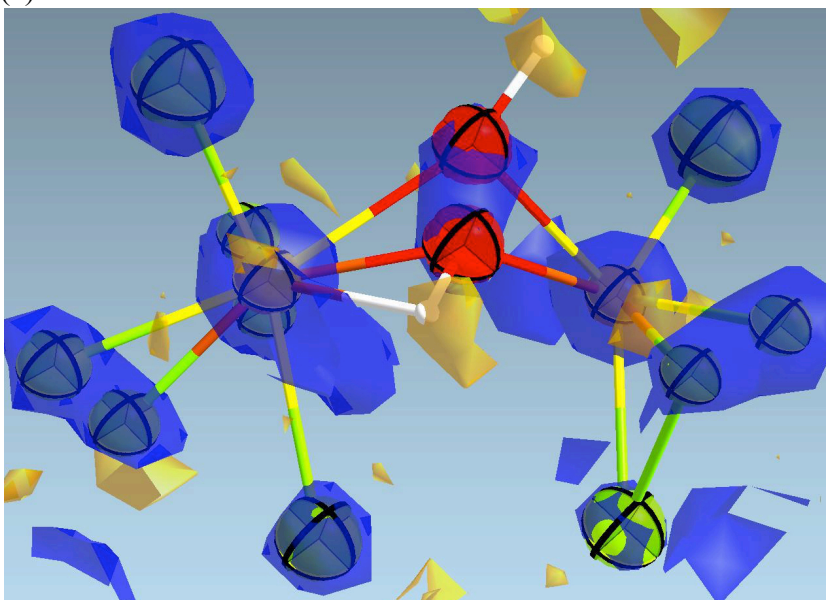

(b)

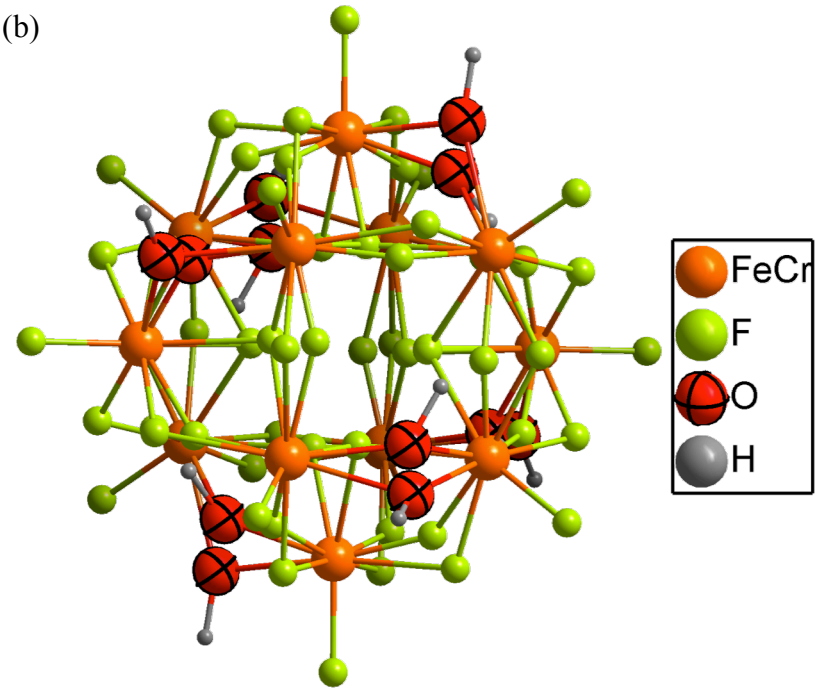


**Figure 74.** (a) map of $F_{obs}$ for $(Et_4N)_9[Cr_4Fe_8F_{35}(OH)_6]$. Blue surfaces are positive observed density, yellow surfaces are negative observed density. Color code: O, red; F, green; Fe, orange; Cr, yellow. (b) ball-and-stick model of the anionic cage. Oxygen atoms are drawn as ellipsoids at the 50% probability level for emphasis.

**$(Et_4N)_8[Co_4Fe_8F_{40}]$.** The data obtained for $(Et_4N)_8[Co_4Fe_8F_{40}]$ are of similar quality to $(Et_4N)_8[Cr_4Fe_8F_{35}(OH)_6]$. The scattering power of iron is approximately 4 times that of cobalt, providing good contrast between the two metals. The data still suffers from a high hydrogen background, which limits the overall resolution of the data set. The refinement of the site occupancy of the heavy atom sites was conducted in a manner analogous to that described for $(Et_4N)_8[V_4Fe_8F_{40}]$. Initially a positional constraint was used to maintain the coordinates of the crystallographically equivalent metal atoms to be the same. Similar to the $(Et_4N)_9[Cr_4Fe_8F_{35}(OH)_6]$ case, the positional constraint could be removed in later refinement cycles without causing major issues but the refinement was more stable if this constraint was kept. After several refinement cycles, one of the heavy atom positions converged to 61% iron and 39% cobalt, with the other heavy atom site being occupied by 72% iron and 28% cobalt. The fluoride ligand disorder was modeled in the same manner as in the X-ray structures. Similar to $(Et_4N)_8[V_4Fe_8F_{40}]$ and $(Et_4N)_9[Cr_4Fe_8F_{35}(OH)_6]$, no additional $[Et_4N]^+$ cations could be located in the structure.

Negative density due to $[OH]^-$ protons was visible in the $F_{obs}$ map during the later stages of refinement. Unlike the $(Et_4N)_9[Cr_4Fe_8F_{35}(OH)_6]$ case, for $(Et_4N)_8[Co_4Fe_8F_{40}]$ the $[OH]^-$ ligands were found to occupy two different bridging positions. Both $[OH]^-$ groups were found in the position on the exterior of the cage, with the position on the interior of the cage occupied by $[F]^-$. The $[OH]^-/[F]^-$ ratio was refined, with one site converging to 0.52:0.48 and the other converging to 0.41:0.59. Figure 75a displays the $F_{obs}$ map, highlighting the negative density surrounding the $[OH]^-$ protons. Figure 75b displays the anionic cage, highlighting the positions of the

$OH^-$ ligands. Based on these results, the best formula for this cage is found to be $(Et_4N)_9[Co_4Fe_8F_{36}(OH)_5]$.

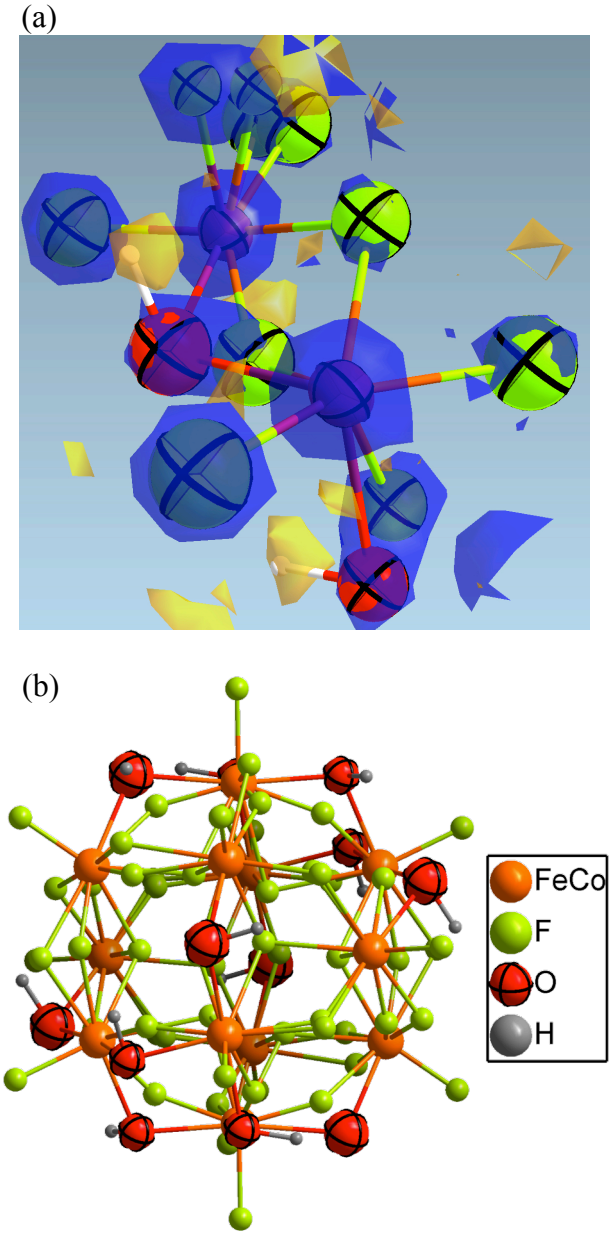


**Figure 75.** (a) map of $F_{obs}$ for $(Et_4N)_9[Co_4Fe_8F_{36}(OH)_5]$. Blue surfaces are positive observed density, yellow surfaces are negative observed density. Color code: O, red; F, green; Fe, orange; Co, pink. (b) ball-and-stick model of the anionic cage. Oxygen atoms are drawn as ellipsoids at the 50% probability level for emphasis.

**Conclusions**

The experiments described herein have increased our knowledge of the formulae for these cages. The anomalous dispersion experiments showed that there is indeed a statistical distribution of the two metals at the heavy atom sites in the mixed-metal cages. The neutron diffraction experiments revealed the presence of $[OH]^-$ ligands in the cages, consistent with the IR spectra. Refinement of the X-ray and neutron diffraction data sets with the metal ratios found by ICP-MS and NAA leads to stable convergence of site occupancy factors. A SQUEEZE analysis shows that there is sufficient void space and disordered electron density to account for the required number of $[Et_4N]^+$ cations, as well as the DMF and $CH_3CN$ solvent molecules identified by IR spectroscopy. While no $[OH]^-$ ligands were found in the neutron refinement of $(Et_4N)_8[V_4Fe_8F_{40}]$, the data were not of high enough quality to completely discount the presence of $[OH]^-$ in the structure. All of these data points together provide significant support for a general formula of $(Et_4N)_9[M_4Fe_8F_{35\text{-}36}(OH)_{5\text{-}6}]\bullet x CH_3CN\bullet y DMF$ (M = V, Cr, Co, $x$ = ~4, $y$ = ~6). Based on the different locations that $[OH]^-$ ligands were found to occupy in the neutron structures it is not yet clear if the number and location of $[OH]^-$ ligands is consistent between samples or varies from crystal to crystal. The $[OH]^-$ content could also vary between different syntheses of the same complex. Definitive proof of the oxidation state of the metals is also still lacking. Progress has been made, however, and a model that explains the elemental analysis results satisfactorily would also allow the assignment of the metal oxidation states and provide the final piece of the puzzle as to the identity of these cage molecules.

# CHAPTER V

# SUMMARY AND FUTURE OUTLOOK

The quest for SMMs with higher blocking temperatures continues, with new insights into the physics governing this behavior providing guidelines for the synthetic chemist when deciding what ligand sets and metal ions to use when synthesizing new molecules. The work presented in this dissertation provides further information on how the structure of a molecule, as well as the solid-state packing arrangement, can produce drastic changes in the magnetic properties.

In Chapter II, a series of transition metal complexes bridged by a radical ligand were presented. The radical ligand promoted the desired strong exchange interactions between the metal ions but the SMM behavior was not as impressive as hoped, due largely to structural distortions that introduced transverse anisotropy into the system. Modification of the capping ligand to provide a more symmetric ligand environment for the metal ion should further improve the SMM properties of compounds of this type.

Chapter III presented a large, isostructural family of mononuclear $Co^{II}$ complexes. From this study we learned that crystallographically enforced 3-fold symmetry is not a requirement to suppress transverse anisotropy; approximate 3-fold symmetry was sufficient to limit the magnitude of E. The most intriguing finding of this study was that the SMM behavior of these compounds was strongly influenced by the solid-state packing, specifically the intermolecular Co-Co distance. Larger Co-Co distances led to much improved SMM behavior, regardless of the overall symmetry

about the $Co^{II}$ ion. While the importance of minimizing dipole-dipole interactions when attempting to synthesize SMMs is well known, this study is the first to provide such evidence across a large family of isostructural compounds. Changing the identity of the coordinated terminal ligand from various halides to a $CH_3CN$ solvent molecule, the presence or absence of solvent molecules in the unit cell, and the variation of crystallographic symmetry about the $Co^{II}$ center had minimal impact on the SMM properties. The closest Co-Co contact was found to be the controlling parameter in determining the SMM behavior of these compounds.

In Chapter IV a series of isostructural polyfluorometallate cages were investigated by X-ray Anomalous Dispersion and single crystal neutron diffraction. While the exact chemical composition of the cages remains unclear these experiments provided important information about the cages, most notably the presence of $[OH]^-$ bridging ligands in the cage molecules evidenced by the neutron diffraction experiments. While no magnetic characterization was presented due to the unknown composition of the cage molecules, preliminary magnetic measurements were performed on $(Et_4N)_8[Fe_{12}F_{40}]$, $(Et_4N)_8[Co_4Fe_8F_{40}]$, and $(Et_4N)_8[Zn_4Fe_8F_{40}]$. These measurements indicate that very strong antiferromagnetic coupling is present in these cages, providing further support for the fluoride ligand's usefulness as a means of generating large exchange coupling constants.

Ultimately, SMMs need to be incorporated into devices if they are going to be used as magnetic storage units, in quantum computers, or spintronics. Investigation of SMMs deposited on surfaces is the first step in realizing device-based applications, and

is an active area of research.[204-207] These initial studies have demonstrated that some SMMs retain their magnetic properties when deposited on a surface, while others do not. Studies have also been done in which molecules that do not behave as SMMs have been deposited on surfaces or in single molecule junctions that demonstrate the ability to read out the magnetic state of the molecule or to influence the magnetic state of the molecule with an external stimulus such as pressure from an STM tip.[205,208-211] These studies have demonstrated that it is possible to manipulate magnetic molecules when incorporated into a device, another important step in the eventual incorporation of SMMs into device technologies. More studies of this type are needed to fully understand how these molecules will behave when adhered to a surface or inserted into a molecular junction, at which point true device applications will be realized.

REFERENCES


1. Lis, T. *Act Crystallogr., Sect. B: Struct. Sci., Cryst. Eng. Mater.* **1980**, *36*, 2042.

2. Milios, C.; Winpenny, R. P. Cluster-Based Single-Molecule Magnets, In *Structure and Bonding*; Springer Berlin Heidelberg, 2014; Vol. 164.

3. Caneschi, A.; Gatteschi, D.; Sessoli, R.; Barra, A. L.; Brunel, L. C.; Guillot, M. *J. Am. Chem. Soc.* **1991**, *113*, 5873.

4. Sessoli, R.; Tsai, H. L.; Schake, A. R.; Wang, S.; Vincent, J. B.; Folting, K.; Gatteschi, D.; Christou, G.; Hendrickson, D. N. *J. Am. Chem. Soc.* **1993**, *115*, 1804.

5. Sessoli, R.; Gatteschi, D.; Caneschi, A.; Novak, M. A. *Nature* **1993**, *365*, 141.

6. Thomas, L.; Lionti, F.; Ballou, R.; Gatteschi, D.; Sessoli, R.; Barbara, B. *Nature* **1996**, *383*, 145.

7. Barbara, B.; Wernsdorfer, W.; Sampaio, L. C.; Park, J. G.; Paulsen, C.; Novak, M. A.; Ferré, R.; Mailly, D.; Sessoli, R.; Caneschi, A.; Hasselbach, K.; Benoit, A.; Thomas, L. *J. Magn. Magn. Mater.* **1995**, *140–144, Part 3*, 1825.

8. Friedman, J. R.; Sarachik, M. P.; Tejada, J.; Ziolo, R. *Phys. Rev. Lett.* **1996**, *76*, 3830.

9. Bogani, L.; Wernsdorfer, W. *Nat. Mater.* **2008**, *7*, 179.

10. Qian, K.; Huang, X.-C.; Zhou, C.; You, X.-Z.; Wang, X.-Y.; Dunbar, K. R. *J. Am. Chem. Soc.* **2013**, *135*, 13302.

11. Christou, G. *Polyhedron* **2005**, *24*, 2065.

12. Tasiopoulos, A. J.; Vinslava, A.; Wernsdorfer, W.; Abboud, K. A.; Christou, G. *Angew. Chem. Int. Ed.* **2004**, *43*, 2117.

13. Sun, Z.; N. Hendrickson, D.; Sun, Z.; M. Grant, C.; L. Castro, S.; Christou, G. *Chem. Commun.* **1998**, 721.

14. Aubin, S. M. J.; Wemple, M. W.; Adams, D. M.; Tsai, H.-L.; Christou, G.; Hendrickson, D. N. *J. Am. Chem. Soc.* **1996**, *118*, 7746.

15. Barra, A. L.; Caneschi, A.; Cornia, A.; Fabrizi de Biani, F.; Gatteschi, D.; Sangregorio, C.; Sessoli, R.; Sorace, L. *J. Am. Chem. Soc.* **1999**, *121*, 5302.

16. Oshio, H.; Hoshino, N.; Ito, T. *J. Am. Chem. Soc.* **2000**, *122*, 12602.

17. Sangregorio, C.; Ohm, T.; Paulsen, C.; Sessoli, R.; Gatteschi, D. *Phys. Rev. Lett.* **1997**, *78*, 4645.

18. Boudalis, A. K.; Donnadieu, B.; Nastopoulos, V.; Clemente-Juan, J. M.; Mari, A.; Sanakis, Y.; Tuchagues, J.-P.; Perlepes, S. P. *Angew. Chem. Int. Ed.* **2004**, *43*, 2266.

19. Powell, G. W.; Lancashire, H. N.; Brechin, E. K.; Collison, D.; Heath, S. L.; Mallah, T.; Wernsdorfer, W. *Angew. Chem. Int. Ed.* **2004**, *43*, 5772.

20. Benelli, C.; Cano, J.; Journaux, Y.; Sessoli, R.; Solan, G. A.; Winpenny, R. E. P. *Inorg. Chem.* **2001**, *40*, 188.

21. Yang, E.-C.; Hendrickson, D. N.; Wernsdorfer, W.; Nakano, M.; Zakharov, L. N.; Sommer, R. D.; Rheingold, A. L.; Ledezma-Gairaud, M.; Christou, G. *J. Appl. Phys.* **2002**, *91*, 7382.

22. Murrie, M.; Teat, S. J.; Stœckli-Evans, H.; Güdel, H. U. *Angew. Chem. Int. Ed.* **2003**, *42*, 4653.

23. Cadiou, C.; Murrie, M.; Paulsen, C.; Villar, V.; Wernsdorfer, W.; Winpenny, R. E. P. *Chem. Commun.* **2001**, 2666.

24. Ochsenbein, S. T.; Murrie, M.; Rusanov, E.; Stoeckli-Evans, H.; Sekine, C.; Güdel, H. U. *Inorg. Chem.* **2002**, *41*, 5133.

25. Sokol, J. J.; Hee, A. G.; Long, J. R. *J. Am. Chem. Soc.* **2002**, *124*, 7656.

26. Osa, S.; Kido, T.; Matsumoto, N.; Re, N.; Pochaba, A.; Mrozinski, J. *J. Am. Chem. Soc.* **2004**, *126*, 420.

27. Ako, A. M.; Hewitt, I. J.; Mereacre, V.; Clérac, R.; Wernsdorfer, W.; Anson, C. E.; Powell, A. K. *Angew. Chem. Int. Ed.* **2006**, *45*, 4926.

28. Milios, C. J.; Vinslava, A.; Wernsdorfer, W.; Moggach, S.; Parsons, S.; Perlepes, S. P.; Christou, G.; Brechin, E. K. *J. Am. Chem. Soc.* **2007**, *129*, 2754.

29. Waldmann, O. *Inorg. Chem.* **2007**, *46*, 10035.

30. Ruiz, E.; Cirera, J.; Cano, J.; Alvarez, S.; Loose, C.; Kortus, J. *Chem. Commun.* **2008**, 52.

31. Neese, F.; Pantazis, D. A. *Faraday Discuss.* **2011**, *148*, 229.

32. Lampropoulos, C.; Hill, S.; Christou, G. *ChemPhysChem* **2009**, *10*, 2397.

33. Ishikawa, N.; Sugita, M.; Ishikawa, T.; Koshihara, S.-y.; Kaizu, Y. *J. Am. Chem. Soc.* **2003**, *125*, 8694.

34. Chen, Y.-C.; Liu, J.-L.; Ungur, L.; Liu, J.; Li, Q.-W.; Wang, L.-F.; Ni, Z.-P.; Chibotaru, L. F.; Chen, X.-M.; Tong, M.-L. *J. Am. Chem. Soc.* **2016**, *138*, 2829.

35. Liu, J.; Chen, Y.-C.; Liu, J.-L.; Vieru, V.; Ungur, L.; Jia, J.-H.; Chibotaru, L. F.; Lan, Y.; Wernsdorfer, W.; Gao, S.; Chen, X.-M.; Tong, M.-L. *J. Am. Chem. Soc.* **2016**, *138*, 5441.

36. Freedman, D. E.; Harman, W. H.; Harris, T. D.; Long, G. J.; Chang, C. J.; Long, J. R. *J. Am. Chem. Soc.* **2010**, *132*, 1224.

37. Henderson, J. J.; Koo, C.; Feng, P. L.; del Barco, E.; Hill, S.; Tupitsyn, I. S.; Stamp, P. C. E.; Hendrickson, D. N. *Phys. Rev. Lett.* **2009**, *103*, 017202.

38. Friedman, J. R. *Resonant magnetization tunneling in molecular magnets*, Exploring the Quantum/Classical Frontier: Recent Advances in Macroscopic and Mesoscopic Quantum Phenomena. Nova Science Publishers, Inc.: Huntington, NY, 2002.

39. Gatteschi, D.; Sessoli, R. *Angew. Chem. Int. Ed.* **2003**, *42*, 268.

40. Glaser, T.; Hoeke, V.; Gieb, K.; Schnack, J.; Schröder, C.; Müller, P. *Coord. Chem. Rev.* **2015**, *289–290*, 261.

41. Zadrozny, J. M.; Long, J. R. *J. Am. Chem. Soc.* **2011**, *133*, 20732.

42. Zhu, Y.-Y.; Cui, C.; Zhang, Y.-Q.; Jia, J.-H.; Guo, X.; Gao, C.; Qian, K.; Jiang, S.-D.; Wang, B.-W.; Wang, Z.-M.; Gao, S. *Chem. Sci.* **2013**, *4*, 1802.

43. Fataftah, M. S.; Zadrozny, J. M.; Rogers, D. M.; Freedman, D. E. *Inorg. Chem.* **2014**, *53*, 10716.

44. Novikov, V. V.; Pavlov, A. A.; Nelyubina, Y. V.; Boulon, M.-E.; Varzatskii, O. A.; Voloshin, Y. Z.; Winpenny, R. E. P. *J. Am. Chem. Soc.* **2015**, *137*, 9792.

45. Rechkemmer, Y.; Breitgoff, F. D.; van der Meer, M.; Atanasov, M.; Hakl, M.; Orlita, M.; Neugebauer, P.; Neese, F.; Sarkar, B.; van Slageren, J. *Nat. Commun.* **2016**, *7*.

46. Carl, E.; Demeshko, S.; Meyer, F.; Stalke, D. *Chem. Eur. J.* **2015**, *21*, 10109.

47. Zadrozny, J. M.; Xiao, D. J.; Atanasov, M.; Long, G. J.; Grandjean, F.; Neese, F.; Long, J. R. *Nat. Chem.* **2013**, *5*, 577.

48. Gomez-Coca, S.; Cremades, E.; Aliaga-Alcalde, N.; Ruiz, E. *J. Am. Chem. Soc.* **2013**, *135*, 7010.

49. Gómez-Coca, S.; Urtizberea, A.; Cremades, E.; Alonso, P. J.; Camón, A.; Ruiz, E.; Luis, F. *Nat. Commun.* **2014**, *5*.

50. Graham, M. J.; Zadrozny, J. M.; Shiddiq, M.; Anderson, J. S.; Fataftah, M. S.; Hill, S.; Freedman, D. E. *J. Am. Chem. Soc.* **2014**, *136*, 7623.

51. Zadrozny, J. M.; Atanasov, M.; Bryan, A. M.; Lin, C.-Y.; Rekken, B. D.; Power, P. P.; Neese, F.; Long, J. R. *Chem. Sci.* **2013**, *4*, 125.

52. Dong, Y.; Yan, P.; Zou, X.; Liu, T.; Li, G. *J. Mater. Chem. C.* **2015**, *3*, 4407.

53. Vostrikova, K. E. *Coord. Chem. Rev.* **2008**, *252*, 1409.

54. Tsukerblat, B. S.; Palii, A. V.; Ostrovsky, S. M.; Kunitsky, S. V.; Klokishner, S. I.; Dunbar, K. R. *J. Chem. Theory Comput.* **2005**, *1*, 668.

55. Langley, S. K.; Wielechowski, D. P.; Vieru, V.; Chilton, N. F.; Moubaraki, B.; Chibotaru, L. F.; Murray, K. S. *Chem. Sci.* **2014**, *5*, 3246.

56. Jeon, I.-R.; Park, J. G.; Xiao, D. J.; Harris, T. D. *J. Am. Chem. Soc.* **2013**, *135*, 16845.

57. Dhers, S.; Costes, J.-P.; Guionneau, P.; Paulsen, C.; Vendier, L.; Sutter, J.-P. *Chem. Commun.* **2015**, *51*, 7875.

58. Manriquez, J. M.; Yee, G. T.; McLean, R. S.; Epstein, A. J.; Miller, J. S. *Science* **1991**, *252*, 1415.

59. Caneschi, A.; Gatteschi, D.; Lalioti, N.; Sangregorio, C.; Sessoli, R.; Venturi, G.; Vindigni, A.; Rettori, A.; Pini, M. G.; Novak, M. A. *Angew. Chem. Int. Ed.* **2001**, *40*, 1760.

60. Gatteschi, D.; Sessoli, R.; Villain, J. *Molecular Nanomagnets*; Oxford University Press, Inc.: New York, 2006.

61. Sanvito, S. *Chem. Soc. Rev.* **2011**, *40*, 3336.

62. Clemente-Juan, J. M.; Coronado, E.; Gaita-Arino, A. *Chem. Soc. Rev.* **2012**, *41*, 7464.

63. Troiani, F.; Affronte, M. *Chem. Soc. Rev.* **2011**, *40*, 3119.

64. Ratera, I.; Veciana, J. *Chem. Soc. Rev.* **2012**, *41*, 303.

65. Rinehart, J. D.; Fang, M.; Evans, W. J.; Long, J. R. *Nat. Chem.* **2011**, *3*, 538.

66. Rinehart, J. D.; Fang, M.; Evans, W. J.; Long, J. R. *J. Am. Chem. Soc.* **2011**, *133*, 14236.

67. Zhu, M.; Li, Y.-G.; Ma, Y.; Li, L.-C.; Liao, D.-Z. *Inorg. Chem.* **2013**, *52*, 12326.

68. Fortier, S.; Le Roy, J. J.; Chen, C.-H.; Vieru, V.; Murugesu, M.; Chibotaru, L. F.; Mindiola, D. J.; Caulton, K. G. *J. Am. Chem. Soc.* **2013**, *135*, 14670.

69. Wu, J.; MacDonald, D. J.; Clérac, R.; Jeon, I.-R.; Jennings, M.; Lough, A. J.; Britten, J.; Robertson, C.; Dube, P. A.; Preuss, K. E. *Inorg. Chem.* **2012**, *51*, 3827.

70. Demir, S.; Zadrozny, J. M.; Nippe, M.; Long, J. R. *J. Am. Chem. Soc.* **2012**, *134*, 18546.

71. Pierpont, C. G.; Lange, C. W. The Chemistry of Transition Metal Complexes Containing Catechol and Semiquinone Ligands; John Wiley & Sons, Inc.: 2007.

72. Kaizaki, S. *Coord. Chem. Rev.* **2006**, *250*, 1804.

73. Brook, D. J. R. *Comments Inorg. Chem.* **2014**, 1.

74. Freedman, D. E.; Bennett, M. V.; Long, J. R. *Dalton Trans.* **2006**, 2829.

75. Song, Y.; Zhang, P.; Ren, X.-M.; Shen, X.-F.; Li, Y.-Z.; You, X.-Z. *J. Am. Chem. Soc.* **2005**, *127*, 3708.

76. Yoshihara, D.; Karasawa, S.; Koga, N. *J. Am. Chem. Soc.* **2008**, *130*, 10460.

77. Liu, Y.; Chen, Z.; Ren, J.; Zhao, X.-Q.; Cheng, P.; Zhao, B. *Inorg. Chem.* **2012**, *51*, 7433.

78. Mondal, K. C.; Sundt, A.; Lan, Y.; Kostakis, G. E.; Waldmann, O.; Ungur, L.; Chibotaru, L. F.; Anson, C. E.; Powell, A. K. *Angew. Chem. Int. Ed.* **2012**, *51*, 7550.

79. Guedes, G. P.; Soriano, S.; Mercante, L. A.; Speziali, N. L.; Novak, M. A.; Andruh, M.; Vaz, M. G. F. *Inorg. Chem.* **2013**, *52*, 8309.

80. Towatari, M.; Nishi, K.; Fujinami, T.; Matsumoto, N.; Sunatsuki, Y.; Kojima, M.; Mochida, N.; Ishida, T.; Re, N.; Mrozinski, J. *Inorg. Chem.* **2013**, *52*, 6160.

81. Yamaguchi, T.; Costes, J.-P.; Kishima, Y.; Kojima, M.; Sunatsuki, Y.; Bréfuel, N.; Tuchagues, J.-P.; Vendier, L.; Wernsdorfer, W. *Inorg. Chem.* **2010**, *49*, 9125.

82. Kanegawa, S.; Karasawa, S.; Nakano, M.; Koga, N. *Bull. Chem. Soc. Jpn.* **2006**, *79*, 1372.

83. Kanegawa, S.; Karasawa, S.; Nakano, M.; Koga, N. *Chem. Commun.* **2004**, 1750.

84. Karasawa, S.; Nakano, K.; Tanokashira, J.-i.; Yamamoto, N.; Yoshizaki, T.; Koga, N. *Dalton Trans.* **2012**, *41*, 13656.

85. Karasawa, S.; Yoshihara, D.; Watanabe, N.; Nakano, M.; Koga, N. *Dalton Trans.* **2008**, 1418.

86. Karasawa, S.; Koga, N. *Inorg. Chem.* **2011**, *50*, 5186.

87. Karasawa, S.; Nakano, K.; Yoshihara, D.; Yamamoto, N.; Tanokashira, J.-i.; Yoshizaki, T.; Inagaki, Y.; Koga, N. *Inorg. Chem.* **2014**, *53*, 5447.

88. Kanegawa, S.; Karasawa, S.; Maeyama, M.; Nakano, M.; Koga, N. *J. Am. Chem. Soc.* **2008**, *130*, 3079.

89. Karasawa, S.; Zhou, G.; Morikawa, H.; Koga, N. *J. Am. Chem. Soc.* **2003**, *125*, 13676.

90. Tobinaga, H.; Suehiro, M.; Ito, T.; Zhou, G.; Karasawa, S.; Koga, N. *Polyhedron* **2007**, *26*, 1905.

91. Kaim, W.; Fees, J. *Z. Naturforsch., B: J. Chem. Sci.* **1995**, *50*, 123.

92. Glockle, M.; Hubler, K.; Kummerer, H. J.; Denninger, G.; Kaim, W. *Inorg. Chem.* **2001**, *40*, 2263.

93. Glockle, M.; Kaim, W.; Fiedler, J. *Z. Anorg. Allg. Chem.* **2001**, *627*, 1441.

94. Frantz, S.; Kaim, W.; Fiedler, J.; Duboc, C. *Inorg. Chim. Acta* **2004**, *357*, 3657.

95. Tyeklar, Z.; Jacobson, R. R.; Wei, N.; Murthy, N. N.; Zubieta, J.; Karlin, K. D. *J. Am. Chem. Soc.* **1993**, *115*, 2677.

96. Hathaway, B. J.; Holah, D. G.; Underhill, A. E. *J. Chem. Soc.* **1962**, 2444.

97. Heintz, R. A.; Smith, J. A.; Szalay, P. S.; Weisgerber, A.; Dunbar, K. R. *Inorg. Synth.* **2002**, *33*, 75.

98. Bain, G. A.; Berry, J. F. *J. Chem. Educ.* **2008**, *85*, 532.

99. APEX2 v2013.10-0, Bruker AXS, **2013.**

100. Sheldrick, G. M. *Acta Crystallogr. Sect. A: Found. Crystallogr.* **2008**, *A64*, 112.

101. Sheldrick, G. *Acta Crystallogr., Sect. C: Struct. Chem.* **2015**, *71*, 3.

102. Hubschle, C. B.; Sheldrick, G. M.; Dittrich, B. *J. Appl. Crystallogr.* **2011**, *44*, 1281.

103. Chilton, N. F.; Anderson, R. P.; Turner, L. D.; Soncini, A.; Murray, K. S. *J. Comput. Chem.* **2013**, *34*, 1164.

104. CC-FIT, Nicholas F. Chilton, http://nfchilton.com/cc-fit.html, **2014.**

105. Orbach, R. *Proc. R. Soc. London, Ser. A* **1961**, *264*, 458.

106. Schmitz, M.; Seibel, M.; Kelm, H.; Demeshko, S.; Meyer, F.; Krüger, H.-J. *Angew. Chem. Int. Ed.* **2014**, *53*, 5988.

107. Park, J. G.; Jeon, I.-R.; Harris, T. D. *Inorg. Chem.* **2015**, *54*, 359.

108. Shen, F.-X.; Huang, W.; Yamamoto, T.; Einaga, Y.; Wu, D. *New J. Chem.* **2016**.

109. Halcrow, M. A. *Chem. Soc. Rev.* **2011**, *40*, 4119.

110. Martinho, P. N.; Gildea, B.; Harris, M. M.; Lemma, T.; Naik, A. D.; Müller-Bunz, H.; Keyes, T. E.; Garcia, Y.; Morgan, G. G. *Angew. Chem. Int. Ed.* **2012**, *51*, 12597.

111. Cole, K. S.; Cole, R. H. *J. Chem. Phys.* **1941**, *9*, 341.

112. Aubin, S. M. J.; Sun, Z.; Pardi, L.; Krzystek, J.; Folting, K.; Brunel, L.-C.; Rheingold, A. L.; Christou, G.; Hendrickson, D. N. *Inorg. Chem.* **1999**, *38*, 5329.

113. Lines, M. E. *J. Chem. Phys.* **1971**, *55*, 2977.

114. Khan, O. *Molecular Magnetism*; VCH Publishers: New York, 1993.

115. Zadrozny, J. M.; Liu, J.; Piro, N. A.; Chang, C. J.; Hill, S.; Long, J. R. *Chem. Commun.* **2012**, *48*, 3927.

116. Vallejo, J.; Castro, I.; Ruiz-García, R.; Cano, J.; Julve, M.; Lloret, F.; De Munno, G.; Wernsdorfer, W.; Pardo, E. *J. Am. Chem. Soc.* **2012**, *134*, 15704.

117. Colacio, E.; Ruiz, J.; Ruiz, E.; Cremades, E.; Krzystek, J.; Carretta, S.; Cano, J.; Guidi, T.; Wernsdorfer, W.; Brechin, E. K. *Angew. Chem. Int. Ed.* **2013**, *52*, 9130.

118. Herchel, R.; Váhovská, L.; Potočňák, I.; Trávníček, Z. *Inorg. Chem.* **2014**, *53*, 5896.

119. Habib, F.; Korobkov, I.; Murugesu, M. *Dalton Trans.* **2015**, *44*, 6368.

120. Spek, A. *Acta Crystallogr., Sect. C: Struct. Chem.* **2015**, *71*, 9.

121. Janiak, C. *J. Chem. Soc.-Dalton Trans.* **2000**, 3885.

122. Carlin, R. L. *Magnetochemistry*; Springer-Verlag: Berlin, 1986.

123. Barclay, T. M.; Hicks, R. G.; Lemaire, M. T.; Thompson, L. K.; Xu, Z. *Chem. Commun.* **2002**, 1688.

124. Hicks, R. G.; Lemaire, M. T.; Thompson, L. K.; Barclay, T. M. *J. Am. Chem. Soc.* **2000**, *122*, 8077.

125. Barclay, T. M.; Hicks, R. G.; Lemaire, M. T.; Thompson, L. K. *Inorg. Chem.* **2003**, *42*, 2261.

126. Barclay, T. M.; Hicks, R. G.; Lemaire, M. T.; Thompson, L. K. *Inorg. Chem.* **2001**, *40*, 5581.

127. Caneschi, A.; Dei, A.; Lee, H.; Shultz, D. A.; Sorace, L. *Inorg. Chem.* **2000**, *40*, 408.

128. Tzeng, Y.-W.; Lin, C.-J.; Nakano, M.; Yang, C.-I.; Wan, W.-L.; Lai, L.-L. *Dalton Trans.* **2014**, *43*, 3044.

129. Poulten, R. C.; Page, M. J.; Algarra, A. G.; Le Roy, J. J.; López, I.; Carter, E.; Llobet, A.; Macgregor, S. A.; Mahon, M. F.; Murphy, D. M.; Murugesu, M.; Whittlesey, M. K. *J. Am. Chem. Soc.* **2013**, *135*, 13640.

130. Lin, W.; Bodenstein, T.; Mereacre, V.; Fink, K.; Eichhöfer, A. *Inorg. Chem.* **2016**, *55*, 2091.

131. Miklovic, J.; Valigura, D.; Boca, R.; Titis, J. *Dalton Trans.* **2015**, *44*, 12484.

132. Shores, M. P.; Sokol, J. J.; Long, J. R. *J. Am. Chem. Soc.* **2002**, *124*, 2279.

133. Giles, I. D.; Chifotides, H. T.; Shatruk, M.; Dunbar, K. R. *Chem. Commun.* **2011**, *47*, 12604.

134. Aravena, D.; Ruiz, E. *Inorg. Chem.* **2013**, *52*, 13770.

135. Sorace, L.; Benelli, C.; Gatteschi, D. *Chem. Soc. Rev.* **2011**, *40*, 3092.

136. Woodruff, D. N.; Winpenny, R. E. P.; Layfield, R. A. *Chem. Rev.* **2013**, *113*, 5110.

137. Ruamps, R.; Batchelor, L. J.; Guillot, R.; Zakhia, G.; Barra, A.-L.; Wernsdorfer, W.; Guihery, N.; Mallah, T. *Chem. Sci.* **2014**, *5*, 3418.

138. Pinero Cruz, D. M.; Woodruff, D. N.; Jeon, I.-R.; Bhowmick, I.; Secu, M.; Hillard, E. A.; Dechambenoit, P.; Clerac, R. *New J. Chem.* **2014**, *38*, 3443.

139. Eichhöfer, A.; Lan, Y.; Mereacre, V.; Bodenstein, T.; Weigend, F. *Inorg. Chem.* **2014**, *53*, 1962.

140. Boča, R.; Miklovič, J.; Titiš, J. *Inorg. Chem.* **2014**, *53*, 2367.

141. Bar, A. K.; Pichon, C.; Sutter, J.-P. *Coord. Chem. Rev.* **2016**, *308, Part 2*, 346.

142. Gómez-Coca, S.; Aravena, D.; Morales, R.; Ruiz, E. *Coord. Chem. Rev.* **2015**, *289–290*, 379.

143. Huang, X.-C.; Zhou, C.; Shao, D.; Wang, X.-Y. *Inorg. Chem.* **2014**, *53*, 12671.

144. Chen, L.; Wang, J.; Wei, J.-M.; Wernsdorfer, W.; Chen, X.-T.; Zhang, Y.-Q.; Song, Y.; Xue, Z.-L. *J. Am. Chem. Soc.* **2014**, *136*, 12213.

145. Mossin, S.; Tran, B. L.; Adhikari, D.; Pink, M.; Heinemann, F. W.; Sutter, J.; Szilagyi, R. K.; Meyer, K.; Mindiola, D. J. *J. Am. Chem. Soc.* **2012**, *134*, 13651.

146. Chan, S. L.-F.; Lam, T. L.; Yang, C.; Yan, S.-C.; Cheng, N. M. *Chem. Commun.* **2015**, *51*, 7799.

147. Neese, F. *WIREs Comput. Mol. Sci.* **2012**, *2*, 73.

148. Schäfer, A.; Huber, C.; Ahlrichs, R. *J. Chem. Phys.* **1994**, *100*, 5829.

149. Weigend, F. *Phys. Chem. Chem. Phys.* **2006**, *8*, 1057.

150. Atwood, D.; Hutchison, A.; Zhang, Y. Compounds Containing Five-Coordinate Group 13 Elements, In *Structure and Bonding*; Roesky, H., Atwood, D., Eds.; Springer Berlin Heidelberg: 2003; Vol. 105.

151. Zadrozny, J. M.; Telser, J.; Long, J. R. *Polyhedron* **2013**, *64*, 209.

152. Huang, W.; Liu, T.; Wu, D.; Cheng, J.; Ouyang, Z. W.; Duan, C. *Dalton Trans.* **2013**, *42*, 15326.

153. Habib, F.; Luca, O. R.; Vieru, V.; Shiddiq, M.; Korobkov, I.; Gorelsky, S. I.; Takase, M. K.; Chibotaru, L. F.; Hill, S.; Crabtree, R. H.; Murugesu, M. *Angew. Chem. Int. Ed.* **2013**, *52*, 11290.

154. Buchholz, A.; Eseola, A. O.; Plass, W. *Comptes Rendus Chimie* **2012**, *15*, 929.

155. Yoshihara, D.; Karasawa, S.; Koga, N. *Polyhedron* **2011**, *30*, 3211.

156. Jurca, T.; Farghal, A.; Lin, P.-H.; Korobkov, I.; Murugesu, M.; Richeson, D. S. *J. Am. Chem. Soc.* **2011**, *133*, 15814.

157. Wu, D.; Zhang, X.; Huang, P.; Huang, W.; Ruan, M.; Ouyang, Z. W. *Inorg. Chem.* **2013**, *52*, 10976.

158. Palii, A. V.; Clemente-Juan, J. M.; Coronado, E.; Klokishner, S. I.; Ostrovsky, S. M.; Reu, O. S. *Inorg. Chem.* **2010**, *49*, 8073.

159. Atanasov, M.; Aravena, D.; Suturina, E.; Bill, E.; Maganas, D.; Neese, F. *Coord. Chem. Rev.* **2015**, *289–290*, 177.

160. Karunadasa, H. I.; Arquero, K. D.; Berben, L. A.; Long, J. R. *Inorg. Chem.* **2010**, *49*, 4738.

161. Busey, R. H.; Sonder, E. *J. Chem. Phys.* **1962**, *36*, 93.

162. Desrochers, P. J.; Telser, J.; Zvyagin, S. A.; Ozarowski, A.; Krzystek, J.; Vicic, D. A. *Inorg. Chem.* **2006**, *45*, 8930.

163. Duboc, C.; Phoeung, T.; Zein, S.; Pécaut, J.; Collomb, M.-N.; Neese, F. *Inorg. Chem.* **2007**, *46*, 4905.

164. Packová, A.; Miklovič, J.; Boča, R. *Polyhedron* **2015**, *102*, 88.

165. Atanasov, M.; Zadrozny, J. M.; Long, J. R.; Neese, F. *Chem. Sci.* **2013**, *4*, 139.

166. Shatruk, M.; Avendano, C.; Dunbar, K. R. Cyanide-Bridged Complexes of Transition Metals: A Molecular Magnetism Perspective; John Wiley & Sons, Inc.: 2009.

167. Gatteschi, D.; Fittipaldi, M.; Sangregorio, C.; Sorace, L. *Angew. Chem. Int. Ed.* **2012**, *51*, 4792.

168. Birk, T.; Pedersen, K. S.; Piligkos, S.; Thuesen, C. A.; Weihe, H.; Bendix, J. *Inorg. Chem.* **2011**, *50*, 5312.

169. Birk, T.; Pedersen, K. S.; Thuesen, C. A.; Weyhermuller, T.; Schau-Magnussen, M.; Piligkos, S.; Weihe, H.; Mossin, S.; Evangelisti, M.; Bendix, J. *Inorg. Chem.* **2012**, *51*, 5435.

170. Pedersen, K. S.; Sørensen, M. A.; Bendix, J. *Coord. Chem. Rev.* **2015**, *299*, 1.

171. Timco, G. A.; Faust, T. B.; Tuna, F.; Winpenny, R. E. P. *Chem. Soc. Rev.* **2011**, *40*, 3067.

172. Schlegel, C.; van Slageren, J.; Timco, G.; Winpenny, R. E. P.; Dressel, M. *Phys. Rev. B* **2011**, *83*.

173. McRobbie, A.; Sarwar, A. R.; Yeninas, S.; Nowell, H.; Baker, M. L.; Allan, D.; Luban, M.; Muryn, C. A.; Pritchard, R. G.; Prozorov, R.; Timco, G. A.; Tuna, F.; Whitehead, G. F. S.; Winpenny, R. E. P. *Chem. Commun.* **2011**, *47*, 6251.

174. Baker, M. L.; Piligkos, S.; Bianchi, A.; Carretta, S.; Collison, D.; McDouall, J. J. W.; McInnes, E. J. L.; Mutka, H.; Timco, G. A.; Tuna, F.; Vadivelu, P.; Weihe, H.; Gudel, H. U.; Winpenny, R. E. P. *Dalton Trans.* **2011**, *40*, 8533.

175. Baker, M. L.; Bianchi, A.; Carretta, S.; Collison, D.; Docherty, R. J.; McInnes, E. J. L.; McRobbie, A.; Muryn, C. A.; Mutka, H.; Piligkos, S.; Rancan, M.; Santini, P.; Timco, G. A.; Tregenna-Piggott, P. L. W.; Tuna, F.; Gudel, H. U.; Winpenny, R. E. P. *Dalton Trans.* **2011**, *40*, 2725.

176. Cianchi, L.; Del Giallo, F.; Lantieri, M.; Moretti, P.; Spina, G.; Timco, G.; Winpenny, R. *Solid State Commun.* **2010**, *150*, 903.

177. Piligkos, S.; Weihe, H.; Bill, E.; Neese, F.; El Mkami, H.; Smith, G. M.; Collison, D.; Rajaraman, G.; Timco, G. A.; Winpenny, R. E. P.; McInnes, E. J. L. *Chem.--Eur. J.* **2009**, *15*, 3152.

178. Kozlowski, P.; Kamieniarz, G.; Antkowiak, M.; Tuna, F.; Timco, G. A.; Winpenny, R. E. P. *Polyhedron* **2009**, *28*, 1852.

179. Boeer, A. B.; Collison, D.; Muryn, C. A.; Timco, G. A.; Tuna, F.; Winpenny, R. E. P. *Chem.--Eur. J.* **2009**, *15*, 13150.

180. Ochsenbein, S. T.; Waldmann, O.; Sieber, A.; Carver, G.; Bircher, R.; Gudel, H. U.; Davies, R. S. G.; Timco, G. A.; Winpenny, R. E. P.; Mutka, H.; Fernandez-Alonso, F. *Epl* **2007**, *79*.

181. Guidi, T.; Copley, J. R. D.; Qiu, Y.; Carretta, S.; Santini, P.; Amoretti, G.; Timco, G.; Winpenny, R. E. P.; Dennis, C. L.; Caciuffo, R. *Phys. Rev. B* **2007**, *75*.

182. Affronte, M.; Carretta, S.; Timco, G. A.; Winpenny, R. E. P. *Chem. Commun.* **2007**, 1789.

183. Thuesen, C. A.; Pedersen, K. S.; Schau-Magnussen, M.; Evangelisti, M.; Vibenholt, J.; Piligkos, S.; Weihe, H.; Bendix, J. *Dalton Trans.* **2012**, *41*, 11284.

184. Birk, T.; Schau-Magnussen, M.; Weyhermuller, T.; Bendix, J. *Acta Crystallogr., Sect. E: Struct. Rep. Online* **2011**, *67*, m1561.

185. Dreiser, J.; Pedersen, K. S.; Piamonteze, C.; Rusponi, S.; Salman, Z.; Ali, M. E.; Schau-Magnussen, M.; Thuesen, C. A.; Piligkos, S.; Weihe, H.; Mutka, H.; Waldmann, O.; Oppeneer, P.; Bendix, J.; Nolting, F.; Brune, H. *Chem. Sci.* **2012**, *3*, 1024.

186. Pedersen, K. S.; Sigrist, M.; Sørensen, M. A.; Barra, A.-L.; Weyhermüller, T.; Piligkos, S.; Thuesen, C. A.; Vinum, M. G.; Mutka, H.; Weihe, H.; Clérac, R.; Bendix, J. *Angew. Chem. Int. Ed.* **2014**, *53*, 1351.

187. Rietmeijer, F. J.; De Graaff, R. A. G.; Reedijk, J. *Inorg. Chem.* **1984**, *23*, 151.

188. Reger, D. L.; Foley, E. A.; Watson, R. P.; Pellechia, P. J.; Smith, M. D.; Grandjean, F.; Long, G. J. *Inorg. Chem.* **2009**, *48*, 10658.

189. Weihe, H.; Güdel, H. U. *J. Am. Chem. Soc.* **1998**, *120*, 2870.

190. Bino, A.; Ardon, M.; Lee, D.; Spingler, B.; Lippard, S. J. *J. Am. Chem. Soc.* **2002**, *124*, 4578.

191. Kramer, K. W.; Schenker, R.; Hauser, J.; Weihe, H.; Gudel, H. U.; Burgi, H. B. *Zeitschrift Fur Anorganische Und Allgemeine Chemie* **2001**, *627*, 2511.

192. Hein, F.; Herzog, S. SECTION 24 - Chromium, Molybdenum, Tungsten, Uranium A2 - BRAUER, GEORG; Academic Press: 1965.

193. Casey, A. T.; Clark, R. J. H.; Nyholm, R. S.; Scaife, D. E.; Boyd, T. E.; Rhine, W.; Stucky, G. Tetraphenylarsonium Tetrachlorovanadate (III); John Wiley & Sons, Inc.: 2007.

194. Anderson, S. J.; Wells, F. J.; Willkinson, G.; Hussain, B.; Hursthouse, M. B. *Polyhedron* **1988**, *7*, 2615.

195. Farrugia, L. *J. Appl. Crystallogr.* **2012**, *45*, 849.

196. Zikovsky, J.; Peterson, P. F.; Wang, X. P.; Frost, M.; Hoffmann, C. *J. Appl. Crystallogr.* **2011**, *44*, 418.

197. Schultz, A. J.; Jorgensen, M. R. V.; Wang, X.; Mikkelson, R. L.; Mikkelson, D. J.; Lynch, V. E.; Peterson, P. F.; Green, M. L.; Hoffmann, C. M. *J. Appl. Crystallogr.* **2014**, *47*, 915.

198. Schultz, A. J.; Srinivasan, K.; Teller, R. G.; Williams, J. M.; Lukehart, C. M. *J. Am. Chem. Soc.* **1984**, *106*, 999.

199. Funck, K. E.; Prosvirin, A. V.; Mathonière, C.; Clérac, R.; Dunbar, K. R. *Inorg. Chem.* **2011**, *50*, 2782.

200. Freedman, D. E.; Han, T. H.; Prodi, A.; Müller, P.; Huang, Q.-Z.; Chen, Y.-S.; Webb, S. M.; Lee, Y. S.; McQueen, T. M.; Nocera, D. G. *J. Am. Chem. Soc.* **2010**, *132*, 16185.

201. Cowley, A. R.; Jones, R. H.; Teat, S. J.; Chippindale, A. M. *Microporous and Mesoporous Materials* **2002**, *51*, 51.

202. Tereniak, S. J.; Carlson, R. K.; Clouston, L. J.; Young, V. G.; Bill, E.; Maurice, R.; Chen, Y.-S.; Kim, H. J.; Gagliardi, L.; Lu, C. C. *J. Am. Chem. Soc.* **2014**, *136*, 1842.

203. Battle, P. D.; Blundell, S. J.; Coldea, A. I.; Cussen, E. J.; Rosseinsky, M. J.; Singleton, J.; Spring, L. E.; Vente, J. F. *J. Mater. Chem.* **2001**, *11*, 160.

204. Malavolti, L.; Poggini, L.; Margheriti, L.; Chiappe, D.; Graziosi, P.; Cortigiani, B.; Lanzilotto, V.; de Mongeot, F. B.; Ohresser, P.; Otero, E.; Choueikani, F.; Sainctavit, P.; Bergenti, I.; Dediu, V. A.; Mannini, M.; Sessoli, R. *Chem. Commun.* **2013**, *49*, 11506.

205. Vincent, R.; Klyatskaya, S.; Ruben, M.; Wernsdorfer, W.; Balestro, F. *Nature* **2012**, *488*, 357.

206. Gonidec, M.; Biagi, R.; Corradini, V.; Moro, F.; De Renzi, V.; del Pennino, U.; Summa, D.; Muccioli, L.; Zannoni, C.; Amabilino, D. B.; Veciana, J. *J. Am. Chem. Soc.* **2011**, *133*, 6603.

207. del Carmen Giménez-López, M.; Moro, F.; La Torre, A.; Gómez-García, C. J.; Brown, P. D.; van Slageren, J.; Khlobystov, A. N. *Nat. Commun.* **2011**, *2*, 407.

208. Li, J.-J.; Bai, M.-L.; Chen, Z.-B.; Zhou, X.-S.; Shi, Z.; Zhang, M.; Ding, S.-Y.; Hou, S.-M.; Schwarzacher, W.; Nichols, R. J.; Mao, B.-W. *J. Am. Chem. Soc.* **2015**, *137*, 5923.

209. Heinrich, B. W.; Braun, L.; Pascual, J. I.; Franke, K. J. *Nano Lett.* **2015**, *15*, 4024.

210. Frisenda, R.; Gaudenzi, R.; Franco, C.; Mas-Torrent, M.; Rovira, C.; Veciana, J.; Alcon, I.; Bromley, S. T.; Burzurí, E.; van der Zant, H. S. J. *Nano Lett.* **2015**, *15*, 3109.

211. Wagner, S.; Kisslinger, F.; Ballmann, S.; Schramm, F.; Chandrasekar, R.; Bodenstein, T.; Fuhr, O.; Secker, D.; Fink, K.; Ruben, M.; Weber, H. B. *Nat. Nanotechnol.* **2013**, *8*, 575